# NEW WIND TUNNEL FACILITY FOR ICING EXPERIMENTS ON MODELS OF TURBOFAN COMPRESSOR SURFACES

A Thesis submitted by

Ramiz Ibraheem Saeed Candidate, M Eng

For the award of

Doctor of Philosophy

2019

# Abstract

Compressors of modern turbofan engines are often sensitive to ice crystal accretion which can occur if aircraft fly through cloud regions associated with storm complexes. Such flight paths are occasionally necessary, and if ice accretion within the compressor does occur, the ensuing engine performance degradation can range from a mild reduction of efficiency through to a complete loss of power. Many parameters influence the initiation and rate of ice accretion but the physical processes and parameters governing the sensitivity of compressor surfaces to ice accretion are not fully understood. To develop reliable engineering models that can be used to aid the design and operation of compressors under icing conditions, further experimental data is needed. Existing icing wind tunnels around the world are very capable, but the operating costs for these wind tunnels are typically very high. The objective of this work is to establish a new icing wind tunnel that has modest operating costs and yet can also facilitate hardware testing, instrumentation development, and fundamental studies of ice crystal icing at compressor-relevant flow conditions.

A wind tunnel arrangement was proposed involving water droplet freeze-out using liquid nitrogen evaporation followed by natural particle melting through dilution with warm air. The viability of the arrangement was demonstrated theoretically using a conservation of energy analysis. Thermodynamic performance of the facility is dictated largely by the availability of the liquid nitrogen and the proposed operating concept specified using a maximum of 20 litre of liquid nitrogen per run in the facility within 2 minutes to achieve the target operating conditions for the facility: flow speed around 50 m/s, temperatures around 0 °C, and total water content up to 10 g/m$^3$ with melting ratio up to 0.2.

The hardware developed for the facility includes an icing jet generator with nozzle

exit diameter of 170 mm, and an open circuit wind tunnel. Ice particles are generated by injecting water from atomiser nozzles into a mixture of recently-evaporated liquid nitrogen and air which provides a low-temperature medium for the freezing process. A liquid nitrogen receiver and valve system was designed to supply the liquid nitrogen into the evaporator at a metered and controllable rate. The suspended ice particle mixture is then delivered to a diffuser with perforated walls through which further air is injected for the purpose of raising the temperature of the mixture, and generating some natural melting of the ice particles. The icing jet nozzle contraction, which is attached to the downstream end of the diffuser chamber increased the flow velocity and decreased the non-uniformity of the flow velocity at the exit of the jet.

The performance targets for the facility have mostly been achieved, and this has been confirmed through experimentation with individual components and with the facility working as a combined unit. Experimental results have demonstrated a generally favourable agreement with the energy equation analysis, and with results from Computational Fluid Dynamics (CFD) simulations. The probe traversing system developed for the icing jet nozzle exit flow enabled quantification of the velocity uniformity at the exit of the icing jet generator. Within a core flow diameter of 140 mm, the flow speed was $28.1 \pm 1.1$ m/s. This speed is somewhat lower than the target figure of 50 m/s, but it is expected that this can be readily rectified through installation of a higher power blower. The jet exit temperature uniformity was also reasonable: over the same jet core flow region at one particular operating condition, the temperature was $-9.1 \pm 1.9\,^{\circ}$C. However, results from the isokinetic total water content probe developed for this work indicate that improvements in the uniformity of the water distribution are needed.

Initial experiments with a 12.7 mm diameter cylindrical test article have demonstrated some ice accretion at glaciated conditions, and more significant accretion was registered with a non-zero melting ratio operating condition. However, additional improvements are needed in the facility and in the instrumentation used to quantify the facility performance. The introduction of humidity control, melting ratio control, temperature control, and more extensive instrumentation having a faster-response time is achievable in the near term and is expected to have significant impact on the quality of data derived from the new icing wind tunnel in the near future.

# Certification of Thesis

This Thesis is entirely the work of Ramiz Ibraheem Saeed except where otherwise acknowledged. The work is original and has not previously been submitted for any other award, except where acknowledged.

Principal Supervisor: Prof. David Buttsworth

Associate Supervisor: Dr. Khalid Saleh

Associate Supervisor: Dr. Ray Malpress

Student and supervisors signatures of endorsement are held at the University.

# Acknowledgments

First and foremost, I would like to thank and praise God, my Lord Jesus, for giving me the knowledge, strength and perseverance to complete this research. Without His blessings I would have not been able to go through this journey.

Then, I wish to express my deep appreciation to my supervisor Prof. David Buttsworth for his support and guidance throughout my Ph.D. I am grateful that he gave me the opportunity to work on this research project. Along the course of 4 years, his vision, sincerity and guidance deeply inspired me and broadened my knowledge.

Also, I would like to express my gratitude to my supervisors: Dr. Khalid Saleh and Dr. Ray Malpress. Through their patient guidance, encouragement and useful critiques the Ph.D. came into fruition. Particularly their willingness to give their time, expertise and creditable ideas have greatly contributed to the successful completion of this Ph.D.

I would like to extend my acknowledgements to the technical staff of the engineering workshop of the University of Southern Queensland for their contributions and special thanks to the laboratory technicians Mr. Brian Lenske and Mr. Wayne Crowell who helped in the fibreglass work.

This research was made possible through the financial assistance of the Iraqi Government represented by the Ministry of Higher Education and Scientific Research (MoHESR), and the Australian Government represented by the Research Training Program (RTP), *thank you*!

Finally, my acknowledgement would not be complete without thanking my biggest source of strength: my family. With special acknowledgement to my father and mother who have raise me to become who I am today. My deep and sincere appreciation goes to my dear wife Mrs. Mirna Keasou who provided overwhelming unselfish love and sacrifice. Willingly she accepted to be my companion through this challenging Ph.D. journey. Together with my son Nawar and daughter Merai, they gave me every hope and reason to complete the research. Finally, I would never forget the moral and emotional support of my brother and sisters who have helped me to get to this stage.

Ramiz Ibraheem Saeed

*University of Southern Queensland*

*November 2019*

# Contents

# List of Figures

# List of Tables

# Notation

| | |
|---|---|
| $A$ | Internal surface area of the probe in $mm^2$ |
| $A_{c,max}$ | Maximum limit area of the valve when full open in $mm^2$ |
| $A_e$ | Cross sectional area at the tank exit in $mm^2$ |
| $A_i$ | Open area in the perforated plate entrance |
| $A_t$ | Tank base area in $m^2$ |
| $C_d$ | Discharge coefficient for the orifice |
| $C_{H_2O,l}$ | Specific heat at constant pressure for water in liquid form in J/kg.K |
| $C_{H_2O,s}$ | Specific heat at constant pressure for water in solid form in J/kg.K |
| $C_{p,air}$ | Specific heat at constant pressure of air in J/kg.K |
| $C_{pe}$ | Pressure coefficient at nozzle jet outlet |
| $C_{pi}$ | Pressure coefficient at nozzle jet inlet |
| $C_{p,N_2}$ | Specific heat at constant pressure of nitrogen J/kg.K |
| $CR$ | Contraction Ratio |
| $D$ | Pipe internal diameter of the probe intake in mm |
| $d_e$ | Exit hole diameter of the valve in mm |
| $d_j$ | Hole diameter in the perforated plate entrance in mm |
| $f_{lam}$ | Flow friction factor in laminar flow |
| $f_{trans}$ | Flow friction factor in transitional flow |
| $f_{turb}$ | Flow friction factor in turbulent flow |
| $g$ | Acceleration due to gravity in $m/s^2$ |
| $h$ | Heat transfer coefficient in the internal flow region of probe in $W/m^2K$ |
| $h_{air,1}$ | Enthalpy of air at Station 1 in J/kg |
| $h_{air,e}$ | Enthalpy of evaporator air at Station 0 in J/kg |
| $h_{air,e,2}$ | Enthalpy of evaporator air at Station 2 in J/kg |

| | |
|---|---|
| $h_{air,inj}$ | Enthalpy of injection air in J/kg |
| $h_{air,inj2}$ | Enthalpy of injection air at Station 2 in J/kg |
| $h_{cf}$ | Heat transfer coefficient in co-flow region in W/m$^2$K |
| $h_{fg}$ | Heat of evaporation in J/kg |
| $h_{fg,N_2}$ | Heat of evaporation of the liquid nitrogen in J/kg |
| $h_{H_2O,2}$ | Enthalpy of water injection at Station 2 in J/kg |
| $h_{H_2O}$ | Enthalpy of water injection in J/kg |
| $h_{if,H_2O}$ | Heat of fusion of water in J/kg |
| $h_j$ | Heat transfer coefficient in jet flow region in W/m$^2$K |
| $h_{LN_2}$ | Enthalpy of liquid nitrogen in J/kg |
| $h_{N_2,1}$ | Enthalpy of nitrogen (liquid+gas) at Station 1 in J/kg |
| $I$ | Current in A |
| $k$ | Thermal conductivity of air flow within the IKP in W/m.K |
| $K_\infty$ | Thermal conductivity of flow in W/m.K |
| $\dot{m}_{a,f}$ | Mass flow rate delivered from the fan in kg/s |
| $m_{air,e}$ | Evaporator air mass flow rate at Station 0 in kg/s |
| $m_{air,inj}$ | Injection air mass flow rate within atomiser nozzle in kg/s |
| $\dot{m}_{d,wall}$ | Mass flow rate through the perforated diffuser in kg/s |
| $\dot{m}_{H_2O}$ | Mass flow rate of injection water within atomiser nozzle in kg/s |
| $\dot{m}_{H_2O,l}$ | Mass flow rate of liquid water in kg/s |
| $\dot{m}_{H_2O,s}$ | Mass flow rate of solid water in kg/s |
| $\dot{m}_{N_2}$ | Liquid nitrogen mass flow rate in kg/s |
| $n_j$ | Number of jet orifices in the perforated diffuser wall |
| $N_j$ | Number of holes in the perforated plate entrance |
| $Nu_D$ | Nusselt number based on the diameter of the cylinder |
| $P_{atm}$ | Atmospheric pressure in Pa |
| $Ph$ | Pitch between holes in mm |
| $Pr$ | Prandtl number |
| $Pr_s$ | Prandtl number based on the surface temperature of the cylinder |
| $P_s$ | Saturation pressure at saturation temperature in Pa |
| $p_s$ | Static pressure measured around of the perimeter of pitot probe in Pa |
| $p_t$ | Total pressure measured in the central hole of the pitot probe in Pa |
| $P_w$ | Water vapour pressure in Pa |

| | |
|---|---|
| $Q_{cf}$ | Heat transfer from the portion of the cylinder in co-flow in W |
| $Q_{conv}$ | Convective heat transfer from the surface of the cylinder in W |
| $Q_{corr}$ | Heat transfer correlation in W |
| $Q_{elec}$ | Electrical power for test article or IKP in W |
| $Q_{exp}$ | Experimental heat transfer in W |
| $Q_j$ | Heat transfer from the portion of the cylinder in jet flow in W |
| $Re_D$ | Reynolds number based on the diameter of the cylinder |
| $RH$ | Relative humidity in % |
| $t$ | Time in s |
| $T_1$ | Temperature of mixture (air+nitrogen) at Station 1 in K |
| $T_2$ | Temperature of mixture at Station 2 in K |
| $T_3$ | Temperature of mixture at Station 3 in K |
| $T_\infty$ | Free stream flow temperature in °C |
| $T_{air,1}$ | Temperature of air at Station 1 in K |
| $T_{air,d}$ | Temperature of air before entering the perforated diffuser in K |
| $T_{air,d,3}$ | Temperature of diffuser air at Station 3 in K |
| $T_{air,e}$ | Temperature of evaporator air at Station 0 in K |
| $T_{air,e,3}$ | Temperature of evaporator air at Station 3 in K |
| $T_{air,inj,3}$ | Temperature of injection air at Station 3 in K |
| $T_{amb}$ | Ambient temperature in °C |
| $T_{cf}$ | Temperature of co-flowing in °C |
| $T_{core}$ | Temperature of jet flow in °C |
| $T_{H_2O,2}$ | Temperature of injection water at Station 2 in K |
| $T_{H_2O,3}$ | Temperature of water at Station 3 in K |
| $T_L$ | Flow temperature within the probe after heating length in °C |
| $T_{N_2,l}$ | Temperature of nitrogen (liquid+gas) at Station 1 in K |
| $T_{N_2,3}$ | Temperature of nitrogen at Station 3 in K |
| $T_{norm}$ | Normalised temperature |
| $T_p$ | Thickness of plate entrance in mm |
| $T_s$ | Surface temperature of the test article in °C |
| $T_{sat,N_2}$ | Saturation temperature of liquid nitrogen in K |
| $T_w$ | Probe surface temperature in °C |
| $\tilde{u}_2$ | Non uniformity at the nozzle exit |

| | |
|---|---|
| $u_\infty$ | Flow speed in wind tunnel in m/s |
| $U_{co}$ | Flow velocity in the co-flow region in m/s |
| $u_e$ | Velocity of the liquid drainage from the tank in m/s |
| $u_j$ | Flow velocity through each orifice of the perforated diffuser in m/s |
| $U_j$ | Flow velocity in the jet flow region in m/s |
| $V$ | Voltage in V |
| $\dot{V}_{a,f}$ | Air volume flow rate delivered from the fan in $m^3/s$ |
| $\dot{V}_{air,N_2}$ | Mixture volumetric flow rate (air+$N_2$) in $m^3/s$ |
| $\dot{v}_e$ | Liquid volume flow rate from the receiver in litre/s |
| $\dot{v}_{exp}$ | Experimental liquid volume flow rate delivered from the receiver in litre/s |
| $v_{flow}$ | Liquid volume flow from liquid nitrogen receiver in litre |
| $V_i$ | Velocity through the holes in perforated plate entrance in m/s |
| $v_{th}$ | Theoretical liquid volume flow rate delivered from the receiver in litre/s |
| $y_l$ | Instantaneous height of liquid in the tank in m |
| $y_{sh}$ | Gap height between the piston and hole surface in the valve of the receiver in mm |
| $\gamma$ | Empirical fragmentation factor |
| $\varepsilon$ | Pipe roughness in mm |
| $\phi$ | Relative humidity measured by IKP |
| $\omega$ | Specific humidity in g of water/ kg of dry air |
| $\theta$ | Conical half angle of the diffuser in $^\circ$ |
| $\tau$ | Time constant in s |
| $\rho_a$ | Air flow density in $kg/m^3$ |
| $\rho_\infty$ | Free stream flow density in $kg/m^3$ |
| $\rho_{air\&N_2}$ | Flow mixture density (air+$N_2$) in $kg/m^3$ |
| $\Delta P_{d,wall}$ | Pressure drop through the perforated diffuser in Pa |
| $\Delta P_i$ | Pressure drop through the holes in perforated plate entrance in Pa |
| $\mu_\infty$ | Free stream flow dynamic viscosity in $N.s/m^2$ |

# Acronyms & Abbreviations

| | |
|---|---|
| AIWT | Altitude Icing Wind Tunnel |
| BRAIT | Boeing Research Aerodynamic Icing Tunnel |
| CIRA | Italian Aerospace Research Centre |
| FAA | Federal Aviation Administration |
| HSV | Hue Saturation Value |
| IGS | Icing Generation System |
| IKP | Isokinetic Probe |
| IRT | Icing Research Tunnel |
| IWC | Ice Water Content |
| JKR | Johnson, Kendal and Robert |
| LIRL | LeClerc Icing Research Laboratory |
| LWC | Liquid Water Content |
| NRC | National Research Council |
| PSD | Particle Size Distribution |
| RATFac | Research Altitude Test Facility |
| TU | Technische University |
| TWC | Total Water Content |

# Chapter 1

# Introduction

## 1.1 Motivation

Pilots of commercial airliners and transport aircraft are normally directed not to fly through the most intense region of thunderstorms. But occasionally flights through cloud regions associated with storm complexes are necessary, and can result in solid phase ice accretion in the compressors of the jet engines.

Clouds associated with storm complexes can contain sufficient concentrations of ice particles to cause a blockage effect in the turbofan compressor in a very short period of time. Such blockages can cause a gradual loss of engine power, engine surge, stall, roll back (loss of engine control), a sudden flameout, or severe damage to the engine if the accumulated ice is shed as a mass and ingested by the combustion chamber (Mason et al., 2006). Therefore, ice accretion on aircraft engine components is a significant hazard for modern aviation because of the increasing demand for flights in the vicinity of storm complexes and because of the potential for loss of life.

In the more general case of ice accretion on aircraft components, temperatures at/or below freezing are generally required and the severity of the accretion depends on several specific factors such as: air speed, droplet size, Liquid Water Content (LWC), ambient temperature, the geometry of the surface, droplet collection efficiency and cloud extent

(Gent et al., 2000; Paraschivoiu and Saeed, 2004; Politovich, 2000).

For aircraft flying in very cold weather (−40 to −10 °C) at high altitude and moderate speed, and in air with low liquid water content ($0.05\,\mathrm{g/m^3}$), supercooled droplets rapidly freeze when they impinge on the surface of aircraft components and the accreted ice can form rapidly in an almost dry growth process because the latent heat of fusion released from droplets is not sufficient to generate large volumes of liquid water on the surface (Politovich, 2000). This form of accretion is the 'rime' type of ice accretion (Gent et al., 2000; Mingione et al., 1997), and as shown in Figure 1.1, rime ice has a milky white, opaque appearance because the rapid freezing leads to trapped air between the droplets. The profile of rime accretion can sometimes take on a pointed or spearhead shape (Gent et al., 2000).

If the aircraft is flying in warmer temperatures (−18 to 0 °C), with high speed in a cloud with high liquid water content ($1\,\mathrm{g/m^3}$) and large droplet sizes, a wet growth process occurs because there is insufficient frozen phase and temperature margin below 0 °C to fully absorb the heat of fusion. Thus the freezing process does not happen immediately when the droplets impinge the aircraft surfaces, but water droplets run back (flowing on the aircraft surface) until freezing at the surface occurs and forms the 'glaze' ice accretion. Glaze icing tends to be hard and translucent in appearance (Gent et al., 2000), and the glaze accretion can form the profile of two ice horns in the case of accretion on an aircraft wing (Gent et al., 2000), as illustrated in Figure 1.1. Rime ice typically has a freezing fraction (the fraction of impinging water that freezes on impact) higher than that of glaze ice, it may approach to 1.0. Also, rime ice tends to adhere to surfaces more strongly glaze ice even though the rime ice density is lower.

In the case of engine icing which occurs within clouds primarily containing only solid phase particles (ice crystal icing), another important factor is the melting ratio (Struk et al., 2012) which is the ratio of LWC to Total Water Content (TWC). Partial melting of the particles occurs when the particles enter the compressor. Struk et al. (2012) demonstrated that for aircraft engine icing, the amount of ice accretion will vary with the melting ratio as illustrated in Figure 1.2. The optimum regime for ice crystal ice accretion will occur between two limits: the upper limit occurs for conditions where there is insufficient Ice Water Content (IWC) to cool the surface to the freezing point


(a)

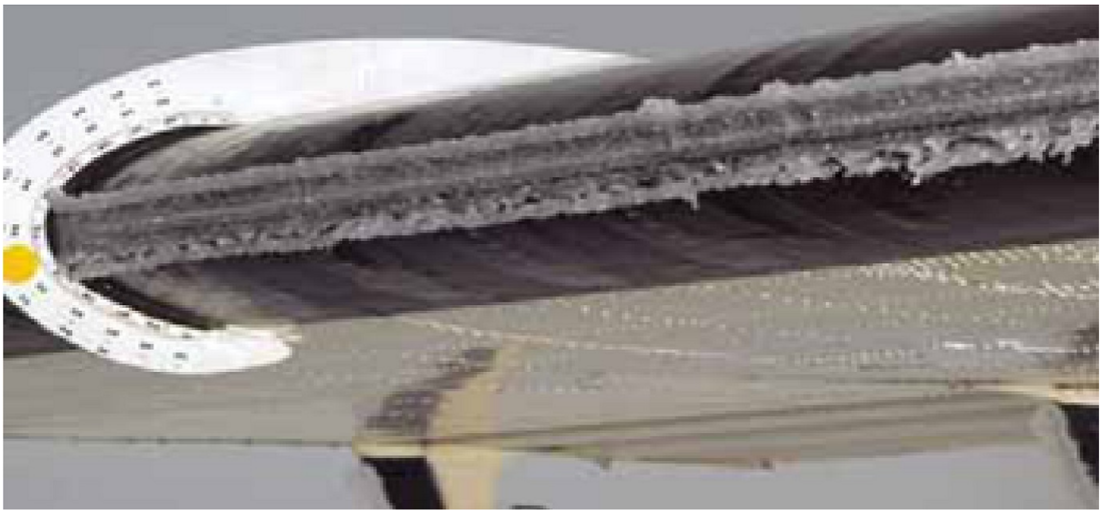

(b)

Figure 1.1: Types of aircraft ice accretion: (a) Rime ice accretion (Shields, 2011); and (b) Glaze ice accretion (Aircraft Icing. Safety Advisor 2002).

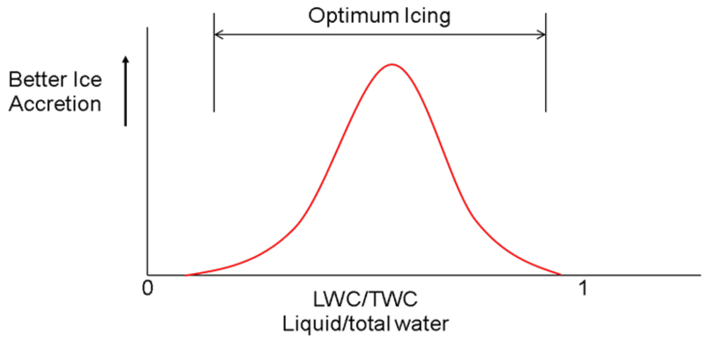


Figure 1.2: Conceptual curve showing optimal ice-crystal icing conditions (Struk et al., 2012).

because there is too much liquid, and the lower limit where there is insufficient LWC to adhere the impacting ice to the surface and to allow the heat transfer from the warm surface to happen because there is too little liquid.

Ice accretion on both the external surfaces of an aircraft (Figure 1.1) and within the engine flow path (Figure 1.3) represents a significant hazard for flight. For the case of the icing on external surfaces, the hazard arises from aerodynamic performance degradation: the icing leads to changes in roughness and shape of the aircraft surfaces resulting in reduced lift force, increased drag force, and decreased stall angle of attack (Balakrishna and Ketha, 2014). For the case of aircraft engine icing, similar degradation of aerodynamic performance of the engine can occur resulting in blockage of the flow path and significant or total loss of engine power. From a certain perspective, turbofan engines can be viewed being more sensitive to ice accretion than the external aircraft surfaces such as wings (Dong et al., 2015) because of the axial temperature gradient: at some point along the engine flow path, the optimum melting ratio will be achieved if fully glaciated conditions are initially present in the cloud.

Many flow variables can potentially play an important role in the ice crystal icing process including: flow speed, pressure, temperature, humidity, melting ratio, total water content, particle size distribution, and ice particle morphology. Surface variables such as surface shape, roughness, wetting, temperature and other thermal properties can also impact the sensitivity of a particular configuration to ice crystal icing. While significant progress towards understanding the ice crystal icing process has been made over the last decade, reliable and broadly-applicable engineering models that can be


Figure 1.3: Ice accretion on compressor surfaces tested in the NASA PSL facility (Tsao, 2019).

used to accurately simulate ice crystal icing sensitivity of turbofan compressors are yet to be established. Additional experimental data is needed.

There already exist several icing wind tunnels around the world which can physically simulate elements of the relevant flow and surface conditions needed to investigate the ice crystal icing problem. However, the charge-out rates for experiments in these facilities are typically very high, making the development of a broad database for engineering model development unlikely. Furthermore, new instrumentation to probe the complex interacting physical processes could provide valuable insight for the analysis of the problem, but such instruments could only make contributions once their reliability has been firmly established. Applying the highly sophisticated well-established icing wind tunnels to the task of instrument development is difficult to justify.

## 1.2 Aim

If an ice crystal icing wind tunnel facility were available with moderate operating costs, it could be used for: (1) investigation of fundamental problems in ice cryctal icing; (2) instrumentation development activities; and (3) the testing of new physical models prior to deployment in other icing wind tunnel facilities. The aim of this research has been to investigate the feasibility of developing such a facility at the University of Southern Queensland, and if possible, to develop a suitable wind tunnel concept into a viable, operating facility.

## 1.3 Objectives

The objectives of the present work have been:

1. Assess the viability of potential icing wind tunnel concepts within the University of Southern Queensland context through application of conservation of energy analyses.

2. Design and develop new and/or modified hardware and instrumentation suitable for the new icing wind tunnel facility through application of engineering analysis and computational simulation where appropriate.

3. Demonstrate the success or otherwise of the new hardware through facility performance measurements with data assessed against required performance specifications. Iterate through the design and assessment process until success is demonstrated.

4. Perform experiments on a test article to further assess the facility performance.

## 1.4 Thesis outline

**Chapter 2** Literature Review

This chapter provides the reader an overview of the cloud conditions associated with the ice crystal icing problem, aircraft engine icing conditions, relevant icing experimental work and a general description of the capabilities and features of several significant icing wind tunnels around the globe.

**Chapter 3** Concept Development

This chapter explores the viability of a new wind tunnel concept for the University of Southern Queensland using a steady flow conservation of energy analysis.

**Chapter 4** Facility Design and Arrangement

Hardware designed and developed for the new facility is described and operational characteristics of the individual components are presented.

**Chapter 5** Performance of Facility.

The performance of the facility as an integrated unit is presented and discussed for different operating conditions with reference to the energy equation analysis presented in Chapter 3.

**Chapter 6** Computational Fluid Dynamics Simulations.

Computational fluid dynamics simulations of the wind tunnel, icing generator and combination of new icing bell mouth with wind tunnel are discussed and assessed within the context of the measured performance of the facility.

**Chapter 7** Preliminary Testing.

Initial experiments have been performed on a cylindrical test article with an internal heating element. Results from these experiments are presented and discussed.

**Chapter 8** Conclusion.

The work is drawn to a conclusion through the presentation of summaries of motivations and outcomes from the work, plus suggestions for future development activities.

# Chapter 2

# Literature Review

## 2.1 Introduction

An overview of the ice crystal icing which can compromise the performance of the turbofan compressors has been introduced in Chapter 1. The present chapter presents the conditions associated with ice crystal icing, a description of the ice crystal icing process identified through experimental work, and several major icing wind tunnel facilities from around the world.

Figure 2.1 illustrates the components in a turbofan engine which are exposed to ice accretion problems. An extensive range of previous studies have indicated that the engine inlet, spinner, fan and first stages of the core are sensitive to supercooled liquid accretion; the stators within the low pressure compressor and the inter-compressor duct are more likely to be expose to ice crystal accretion problems (Mason et al., 2006).

## 2.2 Engine icing conditions

Since the 1990s, according to a Boeing database (Bravin et al., 2015), a large number of jet engines have experienced engine power losses during aircraft flight in certain types of clouds, especially the anvil region of thunderstorms which exist at high altitudes.

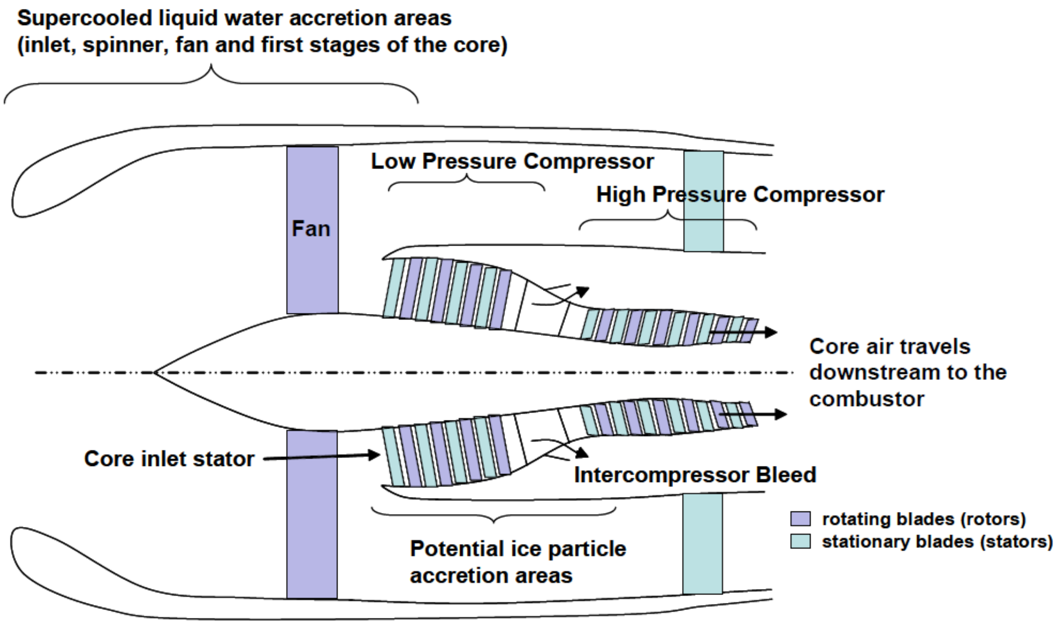


Figure 2.1: Schematic diagram of a typical turbofan engine illustrating the sites of potential ice accretion (Mason et al., 2006).

Most commercial and commuter aircraft travel at altitudes higher than 7 km above sea level. The ambient temperature at such altitudes can reach values less than $-40\,^{\circ}$C, making the existence of supercooled water droplets unlikely. In the anvil region of thunderstorms, concentration of ice particles may reach up to $3\,\mathrm{g/m^3}$ in the more intense anvil region (Lawson et al., 1998). The ingestion of the high concentration of those ice particles into a turbofan engine may cause a thrust loss incident (Lawson et al., 1998).

At temperatures less than $-40\,^{\circ}$C, water particles in the atmosphere are in a solid phase and exist as ice particles, graupel, and hail. It was thought that flying within clouds containing small ice particles was safe because the ice particles seem to 'bounced off' wings and other structures of the aircraft without observed accretion. Nevertheless, accretion can occur inside the jet engine compressor stages because the elevated air and surface temperatures causes partial melting of the particles so the potential for particle adhesion to surfaces is greatly increased. Such accretion can cause engine power loss and in certain cases, when a high mass of ice is ingested and the accreted mass is suddenly released from the compressor and enters to the combustion chamber, an engine flame out and permanent damage can occur (Mason et al., 2006).

A catalogue of 100 engine icing events at different sites across the globe was analysed by Grzych and Mason (2010) to understand the conditions which are leading to engine power loss. Within this catalogue of incidents, 12 different types of engine were involved. The majority of the events have been recorded in northern Australia, Indonesia and South-east Asia. The analysis of meteorological data indicated these events have occurred at altitudes from 2.7 km up to 12.5 km, and all occurred in the anvil region clouds. It was found that 50 % of the events occurred at an ambient temperature around $-29\,^{\circ}$C, and 26 % of them happened at less than $-40\,^{\circ}$C. It was concluded that the Ice Water Content (IWC), the ice crystal size and morphology are important parameters in engine icing, and additional effort should be put towards characterization of the atmospheric conditions relevant to these events (Grzych and Mason, 2010).

A consortium consisting of 37 partners representing 14 European countries and their aeronautical industries collaborated to study High Altitude Ice Crystals (HAIC). The main goal of the HAIC project is to characterise the atmospheric icing conditions which may help in developing and designing icing detection technologies (Dezitter et al., 2013). The statistical properties of 14 years of Tropical Rainfall Measuring Mission data have been documented, and three bands of conditions have been defined. In the first, at altitudes about 10 km, which is the usual flight altitude for commercial jet aircraft, the representative temperature is $-50 \pm 3\,^{\circ}$C and all water particle content will be fully frozen because of homogeneous nucleation and the smallest ice particles can exist (20 to 40 $\mu$m). The second band is at the mid-altitude around 10 km in which the representative temperature is $-30 \pm 3\,^{\circ}$C, and here intermediate sized particles may be present (50 to 200 $\mu$m). The low flight level is the last one at around 7 km, where the ambient temperature is around $-10 \pm 3\,^{\circ}$C and supercooled mixed-phase droplets can be found (Protat et al., 2014; Lawson et al., 1998).

## 2.3 Ice crystal icing experimental work

### 2.3.1 Humidity

Experiments have been performed by Struk et al. (2012) to investigate the physical mechanism of ice accretion on representative engine surfaces that are susceptible to glaciated and mixed phase conditions. A single wedge aerofoil was mounted inside a cascade rig facility (Section 2.4.5) that has the ability to create suitable ice-crystal and mixed-phase conditions with a variety of simulated altitudes. The experiments have been performed at Mach numbers ranging from 0.2 to 0.3, total temperatures from 5 to 15 °C, total pressure of 45 and 93 kPa, and LWC and IWC up to 3 and 20 g/m$^3$, respectively. It was observed that there was a strong adhesion between the ice and the surface for the 45 kPa case, and the thickness of ice formation on the leading edge reached 15 mm in only three minutes. However, there were minimal deposits observed in the highest pressure case (93 kPa): the ice accretion was usually limited over a small area in the vicinity of the stagnation line on the leading edge. The results indicated that the ice accretion behaviour was linked to the wet bulb temperature in both pressure cases, which was below the freezing temperature in all tests at the low pressure and above freezing temperature in all tests at the high pressure case.

To investigate the sensitivity of the ice accretion to wet bulb temperature (dependent on humidity, total temperature, and total pressure), Currie et al. (2012) extended the earlier work of Struk et al. (2012). The experiments were conducted on the same aerofoil used by Struk et al. (2012) and the wet bulb temperature was controlled between −2 °C and +2 °C by controlling the total pressure, temperature, and Relative Humidity (RH). The results of this study have confirmed the effect of wet bulb temperature on the accretion. To obtain strongly adhered ice accretion, $T_{wb} < 0\,°C$ is required at least on the un-cooled surface. It was also noticed that the ice accumulation on the aerofoil surface appeared weakly adhered, slushy, and regularly shed at $T_{wb} > 0\,°C$. However, for $T_{wb} < 0\,°C$, the ice formation looked like strongly adhered glaze ice, and clear or semitransparent. A large amount of ice accumulation was detected at high IWC in the case of $T_{wb} > 0\,°C$.

### 2.3.2 Melting ratio (LWC/TWC)

Currie et al. (2013) conducted an experimental study to investigate the significance of the LWC/TWC ratio on ice accretion. A small wind tunnel, the RATFac wind tunnel (Section 2.4.5) was used to perform the experiments on a test article comprised of a nose attached to a conical body. The melting ratio (LWC/TWC) was controlled (up to 25 %) at constant TWC and at two different absolute pressures of 34.5 kPa and 69 kPa. It was concluded that the ice accretion size and ice growth rate were very sensitive to the melting ratio and both the size and growth rate increase when the melting ratio increased from 6 to 12 %. However, the ice accretion size and ice growth rate decreased with increasing melting ratio for the higher melting ratios, between 20 and 25 %. The results have also indicated that the TWC plays an important role in accretion growth. For any melting ratio, the largest accretions were observed when the authors used small particles (up to 45 $\mu$m).

Currie et al. (2014) developed a particle sticking efficiency correlation and Currie and Fuleki (2016) subsequently published and a new sticking efficiency correlation based on additional experiments with much smaller particles (28 $\mu m$ MVD), similar in size to those expected in compressors. These particles were produced with a grinder and natural melting of the particles in warm air was used to generate a range of liquid water fractions. The results of this study showed that large ice accretion was obtained at Mach numbers up to 0.65 and the largest accretion was generated for melting ratios between 10 and 17 %. The sticking efficiency correlation published by Bucknell et al. (2018a) was similar to those previously published, but was not limited to a single particle size distribution.

An experimental study by Struk et al. (2015) has been conducted on two different models – a NACA0012 aerofoil, and a wedge model – at flow speeds of 85 and 135 m/s in the RATAFac wind tunnel (described in Section 2.4.5). Measurements focused on ice accretion shape and the influence of the surface temperature. A thin heater was attached to edges of the NACA0012 airfoil to improve the view of the central portion of the model while a cooling mixture blowing across the wedge was used to reduce the surface temperature below the freezing point in some experiments. In other experiments the cooling was not used, resulting in nominally adiabatic icing surface. Thermocouples were embedded on both models. The wet bulb temperature was adjusted by varying the total air temperature, total pressure and humidity in the test flow. The NACA0012 experiments were performed using only injected ice particles which naturally melted in the warm airflow with no additional liquid water injected. It was found that at the higher flow speed of 135 m/s, for the icing to start, a melting ratio larger than 7% was required. The rate of ice accretion initially increased with melting ratio (at 85 m/s), but then decreased with a peak growth rate ($\sim$ 0.018 mm/s) somewhere between melting ratios of 6 % and 12 %. At the higher flow speed, no ice accretion was observed at 7 %, but at a melting ratio of 14 %, an ice growth rate of $\sim$ 0.0069 mm/s was measured. This study concluded that with active surface cooling, ice accretion without shedding occurred and the growth rate increased with melting ratio (Struk et al., 2015).

To estimate the sticking efficiency of the ice and water to the surface, Bucknell et al. (2018a) conducted an experimental study on an axisymmetric conical test article in the RATFac tunnel (Section 2.4.5). Three interchangeable cone faces with half angles of 20°, 35°, and 45° were used. The study was performed with Mach numbers between 0.25 and 0.5, wet bulb temperature from −6.5 to +5.5 °C, and TWC up to 12 g/m$^3$. The results showed the particle melting ratio played an important role in the net sticking efficiency for fixed Mach number and particle size distribution. The maximum sticking efficiency occurred for melting ratios between 9 and 13 %. The results also indicated that increasing Mach number increased the erosion effect at a fixed melting ratio. With increasing angle cone, the net sticking efficiency increased and the maximum sticking efficiency values are expected at the cone tip.

### 2.3.3 Particle sizes and distribution

An experimental study by Knezevici et al. (2012) was conducted to investigate the effects of ice particle size on the ice accretion on an inter-compressor duct bleed slot. The results showed that under mixed phase conditions, the amount of ice accretion is affected significantly by the ice crystal particle size. It was also shown that smaller ice particles are more affected by the natural melting than the larger particles, whereas the larger ice particles have more ability to remove ice accretion and cause erosion effects (Knezevici et al., 2012). In Knezevici et al. (2013), the ice particle melting and particle size distribution were also shown to affect the accretion. The amount of ice accretion is highly sensitive to particle size distribution for wet bulb temperatures above and below freezing for the same LWC, and the same melting ratio. The ice formation rate on the leading edge was found to be lower than theoretical ice formation rate by factors between 0.11 and 0.25. In this case the theoretical growth rate was computed by assuming all of the ice and water flux at the stagnation point adheres. The difference between the observed and the theoretical results was attributed to mechanisms such as particle bounce, erosion, and splashing.

Struk et al. (2018) showed that for the case of small particle size clouds (28 $\mu$m) and a Mach number of 0.4, the ice accumulation rate increased and then decreased with increasing melting ratio. In contrast, for the case of large particle size clouds (50 $\mu$m) and at the same Mach number of 0.4, no ice accretion was observed due to the smaller melting ratios achieved compared with the lower Mach case 0.25. The Particle Size Distribution (PSD) also impacts the net sticking efficiency and the highest efficiency value was observed when $D_{v50} = 34\,\mu$m, while sticking efficiency was less than 2 % when $D_{v50} = 50\,\mu$m. The net sticking efficiency decreases by at least 60% in case of 40 $\mu$m compared with 34 $\mu$m particles (Bucknell et al., 2018a).

Bucknell et al. (2018b) analysed the thermodynamic and mechanical process of ice crystals impacting a warm surface for the purpose of defining heat transfer enhancement under different convective and icing conditions (Mach number, angle of attack, dynamic pressure, TWC, and particle diameter). The results showed that increasing both TWC and particle diameter cause an increase of heat transfer enhancement. Also, having a Stokes number larger than unity was identified as important for a high rate of impingement and heat transfer enhancement. Adding an empirical fragmentation factor ($\gamma$) to the analysis showed that increasing impact time might be another factor affecting the heat transfer. The results also showed that the heat transfer enhancement was independent of Reynolds and Mach number for particles were ballistic fragmentation was expected.

Hauk et al. (2015) performed an experimental and theoretical study of ice crystal impact onto a dry solid wall. The diameter of the spherical particles ranged from approximately

260 to 3500 $\mu$m. The ambient temperature, ice particle temperature and target temperature were between $-10\,^{\circ}$C and $-20\,^{\circ}$C. The experiment classified four main sorts of fragmentation: no fragmentation, minor, major and catastrophic fragmentation. The study showed that the transition from minor to major/catastrophic fragmentation typically occurred around 4.6 m/s. The study also indicated that particle splitting is possibly the main mechanism producing major and catastrophic fragmentation.

### 2.3.4 Flow speed effect

The flow speed plays an important role in two respects. (1) The rate of ice particle interception by the body depends on the speed of the body within the cloud, the collection efficiency of the body, and the concentration of ice particles in the cloud. At higher flow speeds, particle momentum will increase making impact with the surface near the stagnation point more likely, leading to more particles impacting on the body. As a result, the ice accretion growth has potential to be greater than at lower speed. However at higher speeds, particle bounce and/or fracture may also become more significant and can increase the erosion effect (Bucknell et al., 2018a). (2) Convection and evaporation are stronger at high flow speeds so the re-freezing of any liquid present on the surface is likely to be enhanced by flow speed. The heat and mass transfer is essentially governed by speed, geometry, roughness of the surface, and the temperature and humidity difference between the surface and local air (Gent et al., 2000; Paraschivoiu and Saeed, 2004).

The experiments of Saleh (2013) at the low speed of approximately 10 m/s revealed that there is ice accretion at sub-zero temperatures for glaciated ice conditions in the vicinity of the stagnation point on the surface of the test article. This result is very different to other observations such as those by Mason, Chow and Fuleki (2011), and Al-Khalil (2003). Mason et al. (2011) used an ice jet with an exit velocity of 90 m/s to produce glaciated conditions at temperatures from $-15$ to $-10\,^{\circ}$C. No ice accretion was observed on an aerofoil at sub-zero temperatures, but accretion did occur at warm surface temperatures. Al-Khalil (2003) also conducted experiments with a flow speed of 120 mph (53.6 m/s) within glaciated and mixed phase conditions. In the case of an unheated surface in glaciated conditions, just a thin layer of frost was observed on the surface with no additional ice deposition (Al-Khalil, 2003). The flow speed used in the work of Saleh (2013) differs from that of Al-Khalil (2003) and Mason et al. (2011) by more than a factor of 5.

### 2.3.5 Summary of ice crystal accretion

Ice accretion inside the compressors of aircraft engines flying at conditions where the external air temperature is low (around $-40\,^{\circ}\mathrm{C}$ or less) is attributed to ice particles because at these conditions, supercooled droplets will be absent.

When ice particles impinge on the external surface of the aircraft at freezing temperatures, the particles are likely to bounce off and leave the aircraft body without ice accretion. However, when the ice particles are ingested into the turbofan engine compressor, the temperature of the air flow within the compressor increases above the freezing point and at these conditions, a fraction of the ice crystals particles will melt due to elevated air and surface temperatures within the compressor stages. The liquid component of the ingested cloud of particles which has been created through melting can entrap crystals on the compressor surfaces. Under certain conditions, the partially melted particles on the surface can re-freeze and the ice accretion process can continue with additional layers building up.

Accretion can cause engine surges and roll back and if shedding of the bodies of ice also occurs, flame-outs are possible and permanent engine damage may also be sustained. The literature review identified that many parameters and effects may play an important role in ice accretion. These include the shape of the surface, its roughness, wetting, temperature and other thermal characteristics, and flow parameters such as speed, pressure, temperature, relative humidity, wet bulb temperature, melting ratio, total water content, particle size distribution, ice particle morphology, sticking efficiency, and erosion.

## 2.4 Icing wind tunnels

### 2.4.1 Overview

Icing wind tunnels have been used extensively, and they have similar shapes and characteristics to traditional wind tunnels except the icing wind tunnels necessarily contain refrigeration and spray and ice generation systems. First, the refrigeration system is required to reduce the temperature of air flow below the freezing temperature of water. Second, the spray and ice generation system is responsible for producing and injecting the small water droplets and ice particles into the airflow stream to simulate the cloud conditions.

Major icing wind tunnels can be found over the world and they are typically owned by research centres and companies such as NASA (Ide and Sheldon, 2008), the Canadian National Research Council (Currie et al., 2013), the Boeing Company (Chintamani, Delcarpio and Langmeyer, 1997), Cox and Co. (AI-Khalil and Salamon, 1998), and Centro Italiano Ricerche Aerospaziali (Bellucci, 2007). In these existing icing wind tunnels, a wide range for different parameters such as liquid water content, water droplet diameters and flow temperatures can be generated. However, the operating cost of these major facilities is very high. For example, the operating cost of the NASA-IRT wind tunnel is around 34,000 USD/day and the scheduling is required at least nine months in advance (Rios Pabon, 2012).

### 2.4.2 The Icing Research Tunnel (IRT)

The IRT tunnel is located at Cleveland, Ohio and is reported as the longest test duration, and the second largest icing tunnel in the world according to the NASA-IRT website. The facility first started operating in 1944, and research and development work relating to different icing problems has been conducted from that time until now. This tunnel has a good ability to replicate in-flight icing conditions representative of the actual conditions experienced by aircraft engines and external aircraft surfaces. Experiments conducted in IRT target various aspects including icing simulation validation,

Table 2.1: NASA-IRT wind tunnel specification (https://www1.grc.nasa.gov).

| | |
|---|---|
| Type | Closed-loop wind tunnel |
| Test section specification | 1.83 m heigh × 2.74 m wide × 6.1 m long |
| Air speed | 25.7 - 167.2 m/s |
| LWC | 0.15 - 4 g/m$^3$ |
| Temperature | $-30\,°C$ |
| Icing cloud | 1.37 m × 1.83 m |
| Water droplet diameter | 15 - 275 $\mu$m |
| Refrigeration capacity | 7385 kW |
| Test cost | 34,000 USD/ day (Rios Pabon, 2012) |

the mitigation of icing, and the research and development of aircraft ice protection systems. IRT is a closed loop, atmospheric icing wind tunnel with a refrigeration capacity of 7385 kW. This facility also has the capability to produce both supercooled droplet and icing cloud condition by using water spray bars. Because this facility has a long test section (6.1 m), it can accommodate a variety of full-scale components. The test section also contains a 2.62 m diameter turntable to rotate the test component through angles of $\pm\,20°$. Table 2.1 presents more details and operation conditions for this facility, and Figure 2.2 provides a schematic diagram of NASA-IRT wind tunnel.

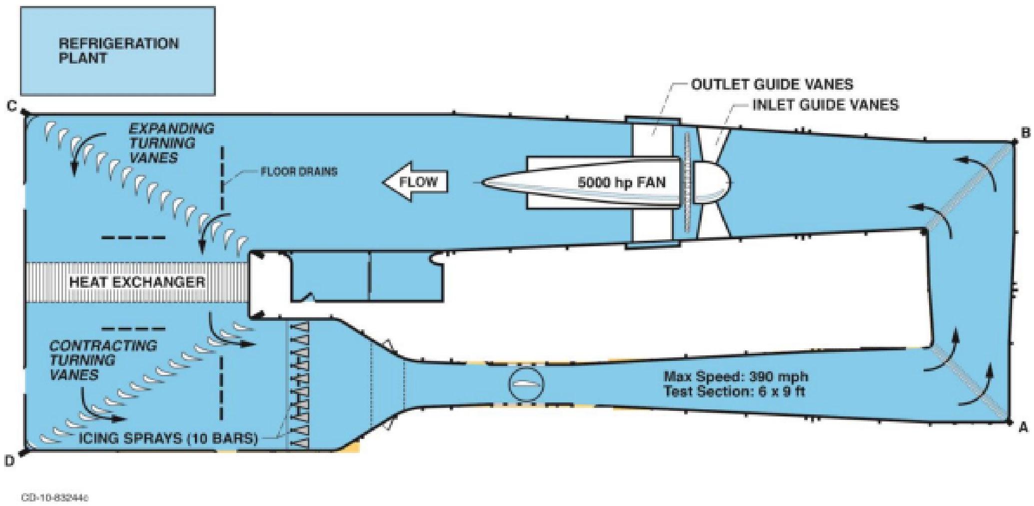


Figure 2.2: Plan view of the NASA-Glenn Icing Research Tunnel (Steen et al., 2015).

### 2.4.3 The Cox LIRL tunnel

The Cox LeClerc Icing Research Laboratory (LIRL) tunnel is also a closed loop icing tunnel, but it is smaller than the NASA-IRT. Figure 2.3 illustrates this facility which is located in New York. It was designed to support the development and certification process of Cox and Company's components and products. The facility has two test sections: the smaller size ($0.71 \times 1.17 \times 2\,\mathrm{m}$) for higher air speeds of $89.4\,\mathrm{m/s}$ and the larger size ($1.22 \times 1.22 \times 1.52\,\mathrm{m}$) for lower air speeds of $53.64\,\mathrm{m/s}$. The facility is provided with an air scavenging system to simulate engine inlets. This facility has the ability to generate both supercooled water cloud, and ice particle (glaciated) cloud conditions. Liquid clouds are produced by 6 horizontal spray bars while the glaciated cloud conditions are created by either a snow gun or an ice shaver system. The facility's refrigeration system has a cooling capacity of $281\,\mathrm{kW}$ at $-30\,°\mathrm{C}$. Table 2.2 presents details and conditions of LIRL tunnel (Al-Khalil and Salamon, 1998).

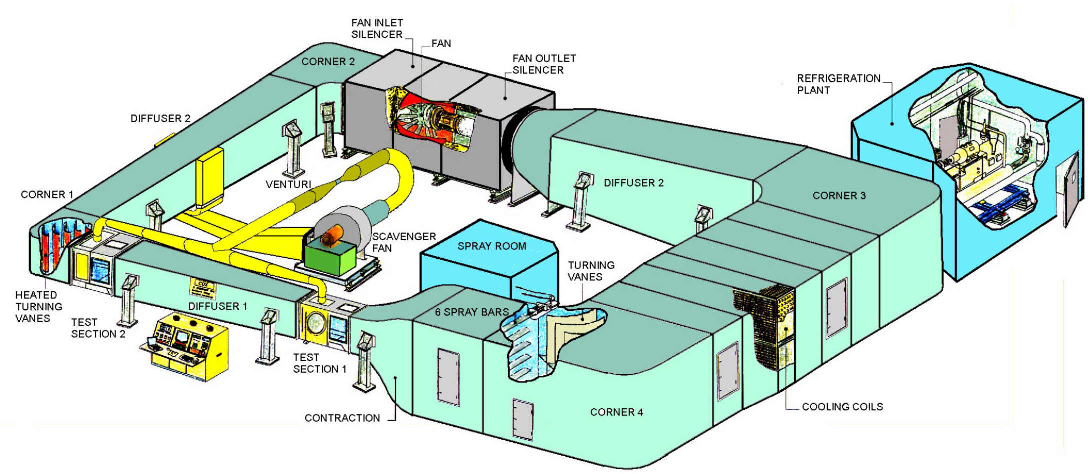


Figure 2.3: Cox Icing Research Laboratory Wind Tunnel (Al-Khalil, Salamon and Tenison 1998).

Table 2.2: LIRL wind tunnel specifications (Al-Khalil and Salamon, 1998).

| | |
|---|---|
| Type | Closed-loop wind tunnel |
| Test section 1 | 1.17 m heigh × 0.71 m wide × 2 m long<br>Turntable for dynamic angle of attack variations |
| Test section 2 | 1.22 m heigh × 1.22 m wide × 1.52 m long |
| Air speed | Test section 1 ∼ 89.4 m/s<br>Test section 2 ∼ 53.64 m/s |
| LWC | 0.25 - 3.0 g/m$^3$ |
| Temperature | −30 °C |
| Water droplet diameter<br>Ice particle size (MVD) | 13 - 50 $\mu$m<br>150 - 200 $\mu$m |
| Refrigeration capacity | 281 kW at −30 °C |
| Test cost | 9,000 USD/ day (Rios Pabon, 2012) |

### 2.4.4 Altitude Icing Wind Tunnel (AIWT)

This facility has been operated since 1930 by the National Research Council, Canada (NRC). It is also a closed loop wind tunnel. It has a square test section of 570 mm and 610 mm long. The air speed in the test section can be increased by inserting a throat to change the test section of cross sectional dimensions. The air flow is cooled by a refrigeration system with a total cooling capacity of 420 kW at −13 °C. The supercooled water droplets are generated by spray bars and recently, liquid nitrogen has been used in this facility to freeze water droplets which are generated by atomizer

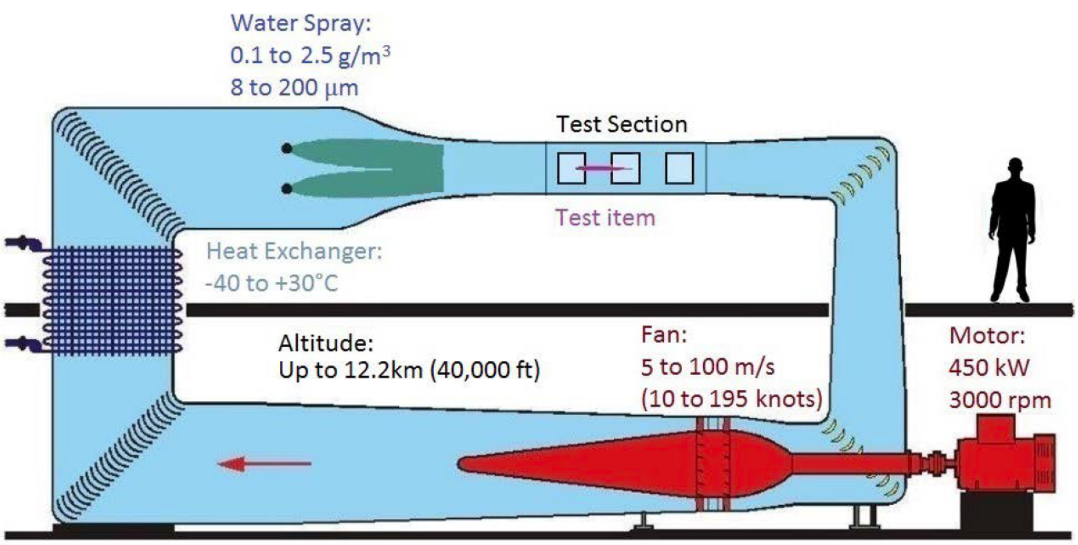


Figure 2.4: Schematic of the Altitude Icing Wind Tunnel (AIWT-NRC) (Clark et al., 2018).

Table 2.3: AIWT-NRC tunnel specifications (www.nrc-cnrc.gc.ca).

| | |
|---|---|
| Type | Closed-loop wind tunnel |
| Test section and Insert | Test 0.57 m heigh × 0.57 m wide × 1.83 m long<br>Insert 0.33 m heigh × 0.52 m wide × 0.60 m long |
| Air speed | Test section 5 - 100 m/s (Mach 0.015- 0.29)<br>With insert 8 - 180 m/s (Mach 0.025- 0.53) |
| Altitude | Up to 12.2 km |
| LWC | 0.1 - 2.5 $g/m^3$<br>With reducer 0.1 to 3.5 $g/m^3$ |
| Temperature | +35 to $-40\,°C$ |
| Water droplet diameter | 8 - 200 $\mu m$ |
| Refrigeration capacity | 420 kW at $-13\,°C$ |

nozzles (Bucknell et al., 2017). Figure 2.4 illustrates the schematic of AIWT facility and Table 2.3 present the condition and details according to National Research Council Canada website (www.nrc-cnrc.gc.ca).

### 2.4.5 Research Altitude Test Facility (RATFac)

This facility consists of a cold side and a hot side separated by a partition. The icing wind tunnel is placed in the hot side and an ice grinder and injection duct are located in cold side as shown in Figure 2.5. The grinder can be arranged to generate a variety of particle sizes. The temperature of the cold flow of air delivered from the injection duct can be around $-15\,°C$ with a $-50\,°C$ dew point. Warm air is also drawn into the test section from the chamber through a bell mouth. The air introduced into the test section of the chamber is drawn from ambient conditions on the roof of the building when warm test temperatures are required, and the working air can also be supplied from the refrigeration system which can provide a cold flow with dew point of $-50\,°C$. The air entering the test section passes a humidity regulation system so the moisture content can be controlled. This means the wet bulb temperature can be adjusted at a given pressure by varying both the temperature and relative humidity. Arrays of spray nozzles can be used to increase the LWC when required. Table 2.4 introduces more details about this facility.

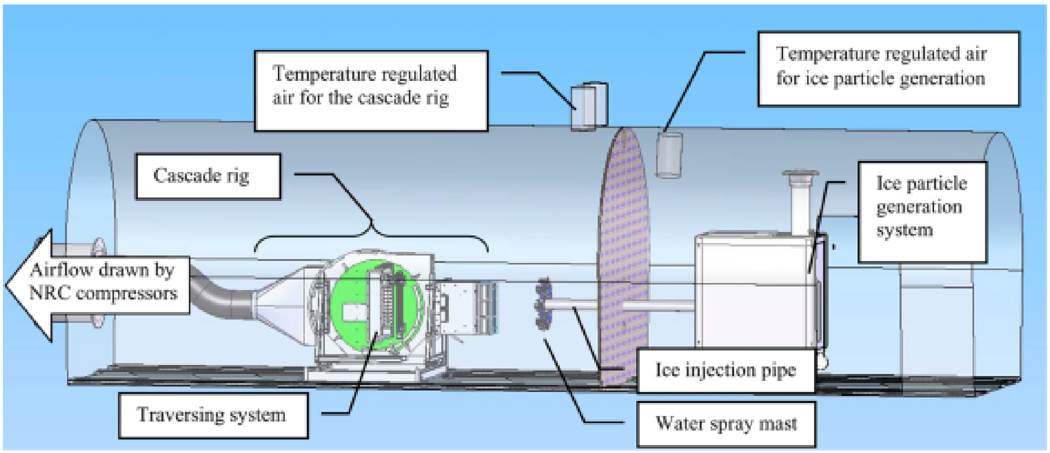


Figure 2.5: RATFac altitude chamber with icing tunnel (cascade rig) (Knezevici et al., 2012).

Table 2.4: RATFac altitude chamber specifications (Knezevici et al., 2013).

| | |
|---|---|
| Type | Open circuit |
| Tunnel cross section downstream bellmouth | 0.132 m wide × 0.254 m heigh |
| Distance from injection duct to bellmouth | 0.803 m |
| Mach no. | 0.15 - 0.8 |
| Total pressure | 27.6 - 93.1 kPa |
| LWC | 0.5 to 4 g/m$^3$ |
| IWC | 2 to 10 g/m$^3$ |
| Temperature | +35 to −40 °C |
| Water droplet diameter | MVD 20 - 40 $\mu$m |
| Ice particle size | MVD 100 - 300 $\mu$m |

### 2.4.6 The Italian Centre for Aerospace research (CIRA)

This facility is a closed loop icing wind tunnel. It has three changeable test sections, and the dimensions of the main test section are 2.35 × 2.24 × 8 m. One of the test sections provides the possibility to install either spray bars for generating icing clouds for icing tests or a screen module when lower turbulence airflow is required for high quality aerodynamic tests. The other test section provides an open jet arrangement. This facility accommodates model components reaching to 1.0 m diameter.

The CIRA facility can simulate altitudes up to 7000 m and has the capability of relative humidity control from 70 to 100 %. The simulation of altitude can be achieved by an evacuation/pressurisation system while the relative humidity can be regulated with the aid of a heat exchanger (Vecchione and De Matteis, 2003). The maximum velocity in this facility is governed by the chosen configuration but the highest Mach number is 0.7. The lowest temperature that can be achieved in main and additional test section is around $-32\,°C$ and in the secondary test section, the lowest achievable temperature is $-40\,°C$ (Bellucci, 2007; Vecchione and De Matteis, 2003). The CIRA Icing wind tunnel layout is shown in Figure 2.6 and some of the key tunnel operating parameters are presented in Table 2.5.

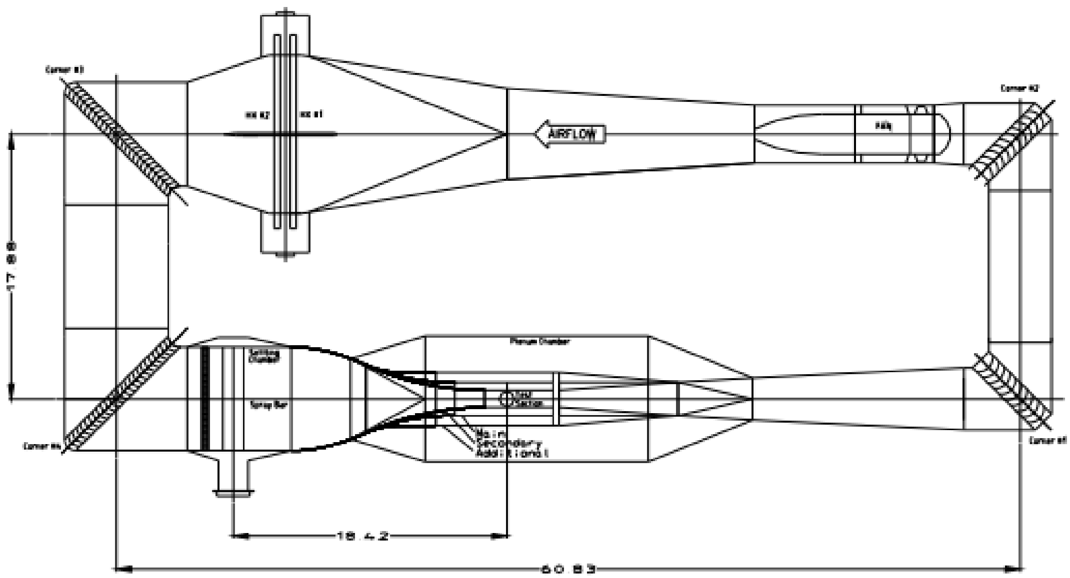


Figure 2.6: CIRA icing wind tunnel layout (Vecchione and De Matteis, 2003).

Table 2.5: CIRA icing wind tunnel specifications (Bellucci, 2007; Vecchione and De Matteis, 2003)

| | |
|---|---|
| Type | Closed circuit wind tunnel |
| Main test section<br>Secondary test section<br>Additional test section | 2.25 m wide × 2.35 m height × 7 m long<br>1.15 m wide × 2.35 m height × 5 m long<br>3.60 m wide × 2.35 m height × 8.3 m long |
| Distance from spray bar to test section | 18.42 m |
| Mach no. | Up to 0.4 main test section<br>Up to 0.7 secondary test section<br>Up to 0.25 additional test section |
| Total pressure | 93000 Pa (abs) down to 14500 Pa (abs) |
| Altitude | Up to 7000 m |
| LWC | Up to 3.5 $g/m^3$ |
| Turntable | 2 m diameter rotating platform |
| Temperature | Down to $-40\,°C$ |
| Water droplet diameter | 5 - 300 $\mu m$ |
| Refrigeration capacity | 4 compressors (1700 kW motor power each) |

### 2.4.7 The Boeing Research Aerodynamic Icing Tunnel (BRAIT)

For research development and airworthiness certification purposes, the Boeing wind tunnel has been developed to include icing test facilities as well. It is a closed loop tunnel and includes three test sections and the largest one has a 1.52 m × 2.44 m cross section area with a maximum flow speed of 130 m/s. The BRAIT was designed to simulate flight altitudes of 4600 m. The minimum temperature that can be achieved is −40 °C. The water droplets are generated by a spray bar system with droplet sizes between 15 and 40 $\mu$m and LWC from 0.25 to 3.0 g/m$^3$ (Chintamani et al., 1997). Figure 2.7 illustrates the schematic of the BRAIT facility.

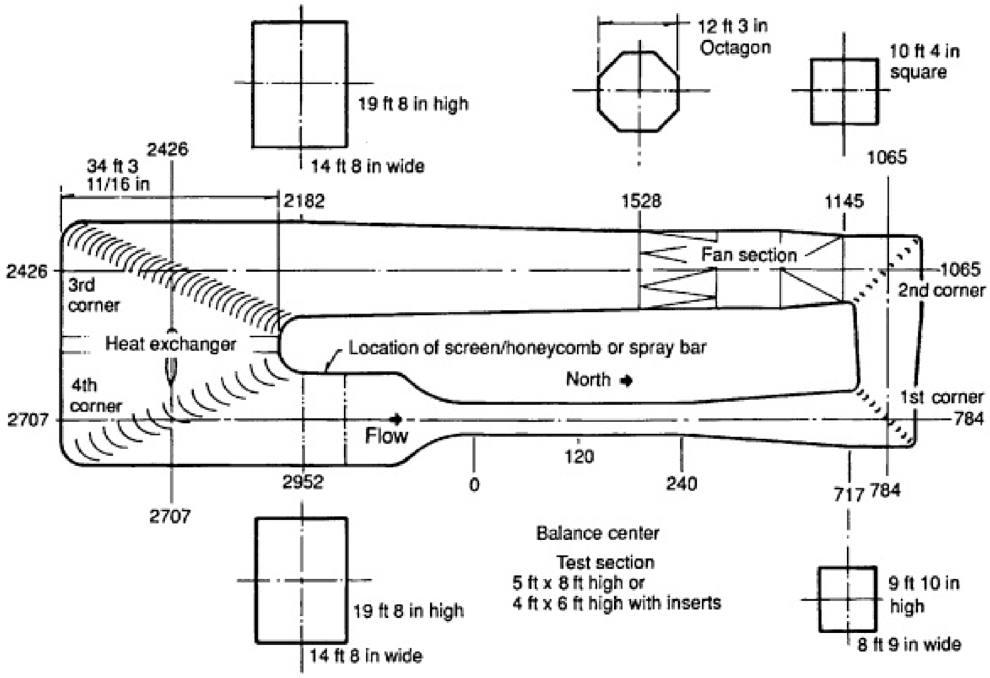


Figure 2.7: Schematic of Boeing Research Aerodynamic Icing Wind tunnel (Chintamani et al., 2003).

### 2.4.8 Braunschweig Icing Wind Tunnel Facility

The Technische University (TU) Braunschweig icing wind tunnel facility is located in the Institute of Fluid Mechanics of the TU Braunschweig in Germany. This facility comprises two main facilities. The first is a low speed wind tunnel and the second is the Icing Generation and conveyance System (IGS), as shown in Figure 2.8. The

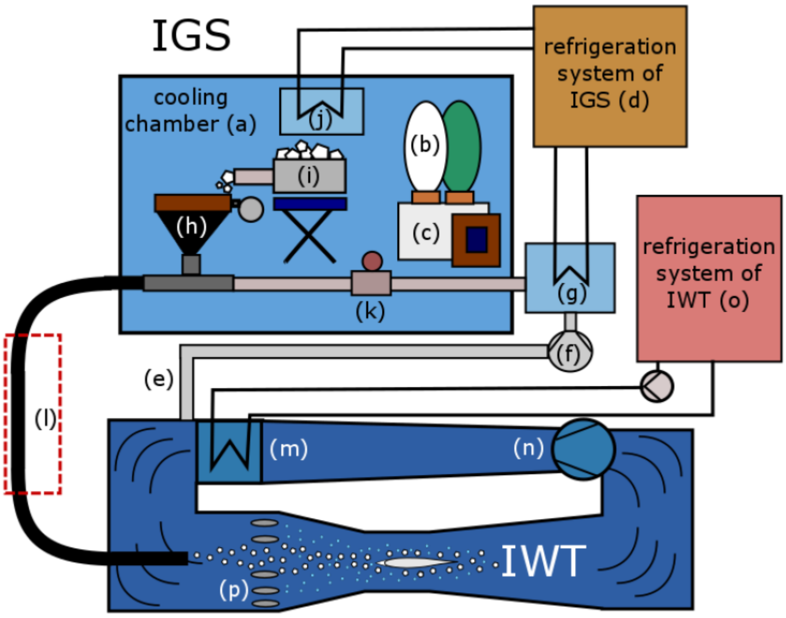


Figure 2.8: Illustration of TU Braunschweig icing wind tunnel facility (Baumert et al. 2016). (a) Cooling chamber. (b) Cloud chambers. (c) Chest freezer. (d) Refrigeration system. (e) Piping system. (f) Fan. (g) Heat exchanger. (h) Sieving machine (i) volumetric dosing machine. (j) Evaporator. (k) Swirl flow meter. (l) Mixing chamber into piping system. (m) Heat exchanger. (n) Fan of wind tunnel. (o) External refrigeration system. (p) Spray bar system.

low speed tunnel is a closed-loop atmospheric tunnel. It has a closed test section of $0.5 \times 0.5$ m cross section area. A flow speed of 40 m/s can be achieved in this test section. The tunnel has also a heat exchanger connected with a refrigeration system of cooling capacity of 30 kW to achieve test temperatures in a range from $-20$ to 20 °C. A spray bar is installed in the tunnel to generate a supercooled water cloud. Recently, Baumert et al. (2015) improved this tunnel to include the IGS system to contribute to fundamental icing research. Many modifications have been made to the facility for the icing work. The important improvements include the building of the cloud chamber technology, establishing storage of ice particles in chest freezer ($-60$ to $-70$ °C) prior facility operation, sieving ice particles and installing a conveyance system to transfer the particles into the tunnel. The facility also has an additional refrigeration system to keep the cooling chamber of the IGS in the temperatures range from 0 to $-20$ °C. In 2016, an additional cloud chamber and chest freezer were added to provide around 25 kg of ice particles per day (Baumert et al., 2016). More details and conditions of

TU icing wind tunnel are presented in Table 2.6.

Table 2.6: TU Braunschweig icing wind tunnel specifications (Baumert et al., 2016).

| | |
|---|---|
| Type | Closed circuit wind tunnel |
| Test section | 0.5 m wide × 0.5 m heigh |
| Air speed | Up to 40 m/s |
| Static temperature | −20 to +20 °C |
| LWC | Up to 3.0 g/m$^3$ |
| IWC | 3 to 19 g/m$^3$ |
| Water droplet diameter (MVD) | 30 $\mu$m by spray water bar |
| Ice particle size (MVD) | 25 - 300 $\mu$m |
| Capability of ice generation | 25 kg/day |
| Storing particles temperature | −60 to −70 °C |
| Refrigeration capacity (tunnel only) | 30 kW |

### 2.4.9 The Propulsion Systems Laboratory

The Propulsion Systems Laboratory (PSL) at the NASA Glenn Research Centre (GRC) has operated since 1952. PSL1 and PSL2 were initially used for ramjet and rocket engine studies and by the end of the 1960s, they were also used for turbojets tests. From 1973, an extra two chambers, PSL3 and PSL4 were added to the facility for turbofan engine research and both chambers are approximately 7.32 m in diameter, and 11.9 m long (Jones Jr, 2015). A wide variety of propulsion systems including commercial and military turbofan engines have been tested in these chambers. Recently, the facility has been upgraded to replicate Ice Crystals Icing (ICI) conditions and mixed phase clouds. In 2012 additional modifications and calibrations were performed to achieve the PSL icing design requirements (Griffin et al., 2014; Van Zante et al., 2018). The facility has been provided with spray bar, icing spray system, steam system (to control the relative humidity), and a temperature controller to simulate a wide range of flight conditions and cloud properties. Pressure conditions for altitudes up to 12.2 km, Mach number between 0.15 and 3 for PSL3 and between 0.15 and 6 for PSL4, and total temperatures from −51 to −9 °C can be simulated in this facility. Figure 2.9 illustrates PSL3 and Table 2.7 presents the facility operating conditions and details according to Griffin et al. (2014).

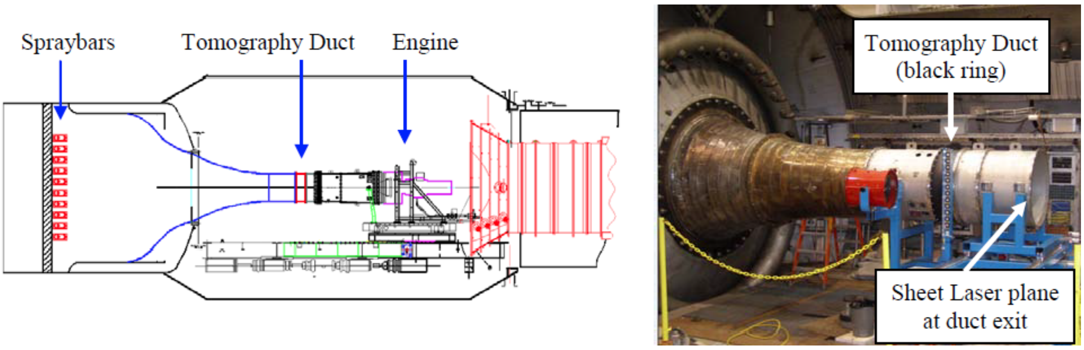


Figure 2.9: Illustration of NASA Propulsion Systems Laboratory (PSL) icing facility (Bencic et al., 2013).

Table 2.7: PSL icing chamber specifications (Van Zante et al., 2018).

| | |
|---|---|
| Type | Open circuit |
| Test section | Circular diameter 0.9144 m |
| Air flow rate | 4.5-150 kg/s |
| Mach number | 0.15-0.8 |
| Altitude | 1.22-12.2 km |
| Temperature | $-51$ to $-9\,^{\circ}$C |
| IWC | 0.5 to 9 g/m$^3$ |
| Ice particle size (MVD) | 40 - 60 $\mu$m |
| Run time | Up to 45 min. |

### 2.4.10 DGA Aero-engine testing

The General Armaments Directorate (DGA) Aero-engine testing division located in France has four icing test facilities: PAG, S1, R6, and A06 and facility S1 is illustrated in Figure 2.10. PAG is a relatively small icing wind tunnel, while S1 and R6 are large altitude test facilities while A06 is a small altitude test facility. S1 and R6 have been used for engine testing, but could be used for testing wings and rotor blades after some proposed modification to these facilities. A06 is a small altitude test facility which was designed to test combustors at low temperature, but recently the facility has been developed to include an icing test capability. Table 2.8 presents the characteristics of the DGA Aero-engine facilities according to Hervy (2011), Hervy et al. (2015), and Jérôme et al. (2016).

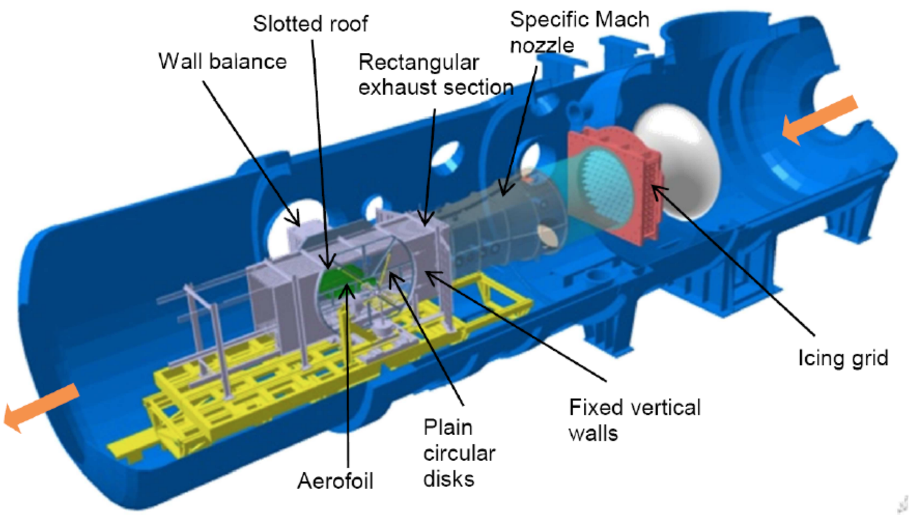


Figure 2.10: Illustration of the DGA Aero-engine altitude test facility S1 (Jérôme et al., 2016)

.

Table 2.8: DGA Aero-engine facilities characteristics (Hervy, 2011, Hervey et al., 2015).

| Facility Name | Type | Test section (m) | Mach No. | Altitude (km) | Max. mass flowrate (kg/s) | Total temp. (°C) | LWC (g/m$^3$) | MVD ($\mu$m) |
|---|---|---|---|---|---|---|---|---|
| PAG | Icing wind tunnel | 0.2×0.2<br>0.2×0.2 | 0.1-0.3<br>0.2-0.6 | Sea level | 12 | -40-0<br>-40-0 | 0.1-3 | 15-50 |
| S1 | Altitude test facility | $\phi$ 0.7<br>$\phi$ 0.82<br>$\phi$ 1.3<br>0.8×0.7 | 0.03-0.85<br>0.03-0.8<br>0.03-0.4<br>0.03-0.7 | 0-20 | 100 | -50-0 | 0.15-3 | 15-300 |
| R6 | Altitude test facility | $\phi$ 1.3<br>$\phi$ 1.8<br>2×0.7 | 0.03-0.6<br>0.03-0.3<br>0.03-0.7 | 0-20 | 140 | -50-0 | 0.2-3 | 15-50 |
| A06 | Altitude test facility | $\phi$ 0.1 | 0.03-0.85 | 0-11 | 4.2 | -45 | 6 | ~20 |

### 2.4.11 Central Institution of Aviation Motors facility

The Central Institution of Aviation Motors (CIAM) in Moscow has a high altitude test facility as illustrated in Figure 2.11. Altitudes up to 15 km, Mach number up to 0.85, flow total temperature around −40 °C, and mass flow rate up to 250 kg/s, can be produced in this test cell. The test section diameter of the wind tunnel in this rig is 1.02 m. A shaving method is adopted in this facility to generate ice particles and the shaver system is placed in a freezer room. The facility has the capability to produce both ice crystal icing and mixed phase conditions. The facility is still under calibration and experimental analysis for measuring ice crystal cloud uniformity to achieve icing condition requirements (Goriachev et al., 2019).

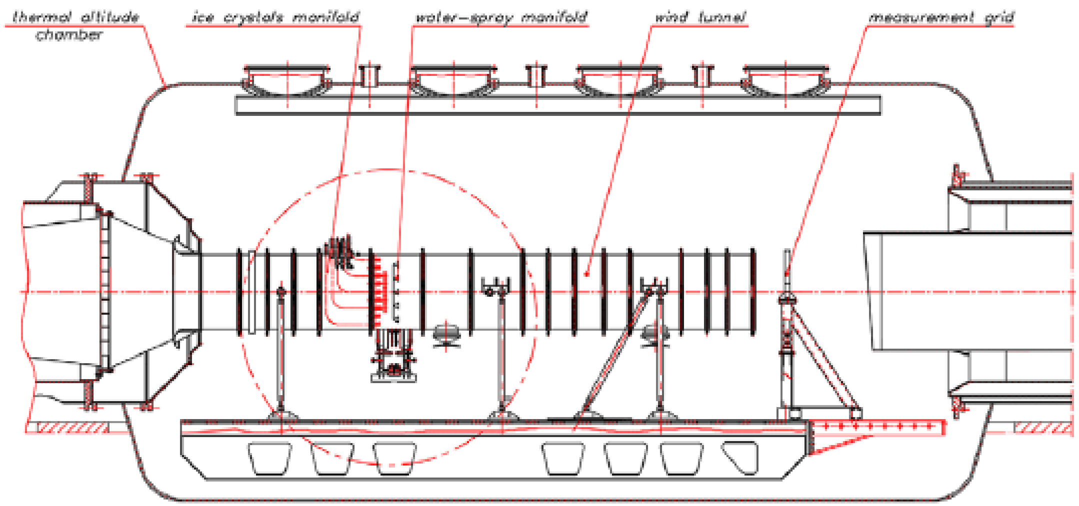


Figure 2.11: Schematic diagram illustrating the CIAM ice crystal facility (Goriachev et al., 2019).

## 2.5 Conclusion

A large number of jet engine power loss incidents have occurred during aircraft flight in the anvil region of thunderstorms, a cloud region containing large concentrations of ice particles but little, if any, liquid water particles. In such cases, partial melting of the ingested ice particles occurs during transit through the low pressure stages of the compressor because of the elevated air and surface temperatures. The potential for particles to adhere to compressor surfaces, and for the re-freezing of liquid water is greatly increased under such conditions. The presence of ice bonded onto compressor surfaces corrupts the performance of the compressor and will typically cause some degree of power loss from the engine.

Many inter-related parameters affect the severity of ice accretion on compressor surfaces and the influence of several of these parameters has already been examined in previous studies by operating representative hardware in icing wind tunnel facilities. Examples of the important parameters include:

- Humidity. The higher the humidity, the lower the capacity for evaporative cooling to contribute to the re-freezing of liquid water during ice accretion. In one study it was observed that for wet bulb temperature ($T_{wb}$) higher than 0°C, the ice was shed regularly, being only weakly adhered and of a slushy appearance, whereas strongly adhered semitransparent glaze ice formations occurred for $T_{wb}$ below 0°C.
- Melting ratio. The ratio of LWC-to-TWC, known as the melting ratio, strongly affects ice accretion. Particle sticking efficiency is linked to the melting ratio and ice growth rates and volumes reach peak values for melting ratios around 10 % with very little ice accretion occurring for values approaching 0 % and 20 %.
- Flow speed. The erosion effect, in which particles on the surface are removed through the impact by other particles, increases with flow speed.
- Particle size. The erosion effect is also sensitive to the particle size distribution, and both are linked with the melting ratio because natural melting occurs more readily for smaller particles.

However, a complete understanding of the ice crystal ice accretion processes has not yet been achieved and the wind tunnel experiments are expected to continue to play a significant role in establishing the knowledge needed for the development of reliable engineering models for the accretion processes.

A full duplication of all parameters which influence ice accretion is not currently achieved in wind tunnels. Icing wind tunnels do not generally offer humidity control, though a notable exception is the RATFac altitude icing chamber and wind tunnel of the National Research Council in Canada. The melting ratio in existing wind tunnels can be controlled through natural particle melting or through supplemental spray water addition. Icing wind tunnels offer speed control from very low speeds up to around 100 m/s and in some cases, Mach numbers as high as 0.8 can be achieved. Particles sizes in wind tunnels vary from 8 $\mu$m up to approximately 300 $\mu$m, reflecting the range of sizes that have been observed in natural clouds. However, icing wind tunnel facilities do not generally seek to reproduce the cloud ice particle morphology: wind tunnel ice particles are generally formed by the freezing of water droplets or through ice shaving techniques.

# Chapter 3

# Concept Development

## 3.1 Introduction

A new wind tunnel facility for ice crystal icing research could provide a useful platform for fundamental experimental investigations and for development of theoretical models and simulation tools. The facility might also become a useful 'proving - ground' for new physical models and experimental techniques that are planned for application in major international icing wind tunnels. However, the facility should produce relevant flow speeds and thermal conditions that are somewhat representative of the turbofan compressor environment or at least similar to conditions achieved in the major icing wind tunnels. This chapter explores the viability of one such wind tunnel concept using a steady flow conservation of energy analysis. To provide context for the presentation of the new facility, a summary of a small facility which previously existed at USQ is first introduced.

## 3.2 Motivation for improving previous icing wind tunnel

There are many challenges that should be overcome to analyse the initiation of ice accretion experimentally. Providing a suitable facility that correctly simulates the important flow parameters including the flow speed, pressure, temperature, humidity, melting ratio, total water content, particle size distribution, and ice particle morphology is a major challenge. Producing a sufficiently uniform distribution of these parameters within the available flow cross section is also necessary if meaningful flow conditions are to be specified for theoretical model development work.

A small experimental facility at USQ was previously designed to produce a relatively slow cold air stream, up to a maximum speed of 12 m/s. The tunnel duct had a 72 mm inner diameter. As illustrated in Figure 3.1, the main parts of this apparatus were: a compressed air vessel, pressurised water tank, ultrasonic atomiser, spray guide tube, particle transfer volume, liquid nitrogen dewar, liquid nitrogen plenum, settling chamber, Perspex vertical wind tunnel, and the test specimen (Saleh, 2013). The

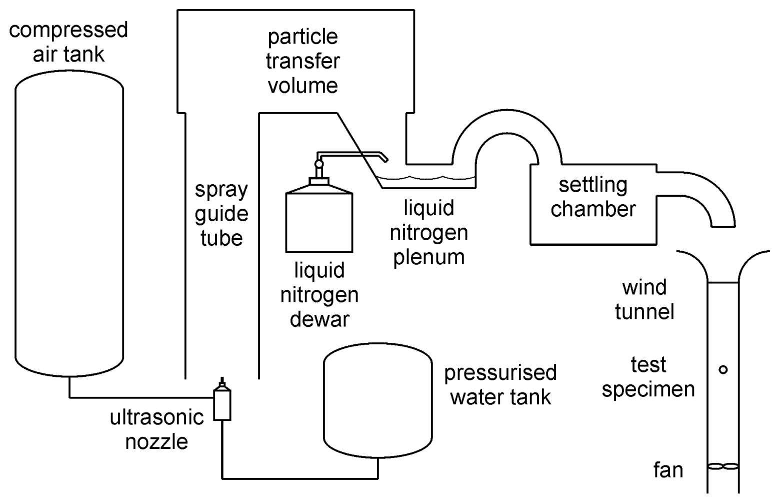


Figure 3.1: Schematic diagram of the previous icing wind tunnel (Saleh, 2013).

previous work demonstrated the use of liquid nitrogen as a refrigerant to generate a flow of fully glaciated ice particles in a ground testing facility with an Ice Water Content (IWC) of 0.42 g/m$^2$ and particle size of approximately 50 $\mu$m. The test flow duration of the previous USQ facility was up to 3 minutes, which is a reasonable period for icing initiation experiments.

In 2016, researchers from the University of Oxford conducted tests in the USQ icing wind tunnel facility as a preliminary assessment of their methods and model article which was designed to study aspects of the thermodynamic and mechanical processes which happen when ice crystals impact the warm surface of the test article. A set of experiments was conducted on the small test article within the available test section at USQ as a step in preparing for other experiment on a larger test article that was used at the NRC in Ottawa, Canada (Bucknell et al., 2018*b*). Although the preliminary experiments in the USQ icing tunnel by Bucknell et al (2018*b*) proved useful for troubleshooting, enhancement of the facility was required to enable engine-relevant ice crystal icing research.

There are several limitations of the Saleh (2013) USQ icing wind tunnel facility. First, because it has a small test section, it can not accommodate models with dimensions comparable to those being tested in other wind tunnel facilities. Second, the low flow speed is not representative of the speed within turbofan compressors. To simultaneously increase the test section size and flow speed while the same flow duration is maintained, the required volume of cold air and liquid nitrogen would far exceed the safe working capacity of the cold room in which the previous facility operated. Therefore, a new arrangement and/or operating environment must be developed to produce an icing wind tunnel with significantly higher flow speeds that can accommodate larger model sizes.

To develop an improved icing wind tunnel, this study will focus on several challenges. The first challenge to be resolved is, how to achieve a significant increase in the speed of the ice particle suspension in the test section. The second challenge concerns the ice production: how to produce a sufficient flow rate of ice particles and cold air. The third: how to achieve and measure the uniformity of velocity, temperature and water concentration in the test section. Finally: how to generate particle melting effects that are representative of the turbofan compressor environment.

## 3.3 Proposed new facility

### 3.3.1 Arrangement

To achieve flow speeds and test article sizes comparable to those currently being used in other icing research facilities, the application of a conventional wind tunnel that was no longer being used in faculty teaching was considered. The flow speeds achieved in this facility were around 35 m/s and the test section size was 305 × 305 mm. In the work of Saleh (2013), liquid nitrogen gave the cooling capacity to generate the ice particles, but only at the low speed of around 10 m/s. To use the newly-available conventional wind tunnel, a new ice production technique would be required. The liquid nitrogen cooling concept of Saleh (2013) remained appealing because calculations demonstrated that 20 litres of liquid nitrogen (the volume of a standard dewar) has sufficient cooling capacity to establish cold flows of nitrogen-air mixtures (at about 0 °C) at a speed of around 50 m/s within a core flow region of the wind tunnel measuring 202 × 202 mm. Thus, to take advantage of the existing facility and its test section, a configuration involving cold icing jet surrounded by a co-flowing stream would be required. The liquid nitrogen cooling concept was also appealing because it provided a technique to ensure glaciated particles would be generated. For the higher flow rates to be generated in the new facility, additional injection of water would also be required. The atomizing nozzle used by Saleh (2013) was attractive for droplet generation because its performance had already been characterised. It was proposed that the amount of water injected would be increased by increasing the number of nozzles used.

Figure 3.2 shows the injection, mixing, and flow acceleration processes proposed for the new facility. Firstly, the evaporation of the liquid nitrogen occurs through the introduction of evaporator air which is delivered through Station 0 to create a very cold stream of an air and nitrogen mixture at Station 1. Injection of water droplets into the air/nitrogen vapour occurs downstream of Station 1. It is necessary to ensure the liquid-nitrogen-to-evaporator-air-mixture-ratio is sufficiently high that the mixture temperature is less than −40 °C for freezing of the injected water, which occurs between Station 1 and Station 2.

To raise the temperature of the glaciated cloud flow towards the melting point, an air flow is introduced through a perforated diffuser, the physical extent of which is defined by Station 2 on the upstream end, and Station 3 on the downstream end. In the aeroengine compressor, the temperature and pressure of the icing cloud flow is raised through thermodynamic work input. In the icing wind tunnel facility concept, the elevation of the thermal state is achieved through a dilution/mixing process. The amount of air added and the residence time in the perforated diffuser is crucial as the

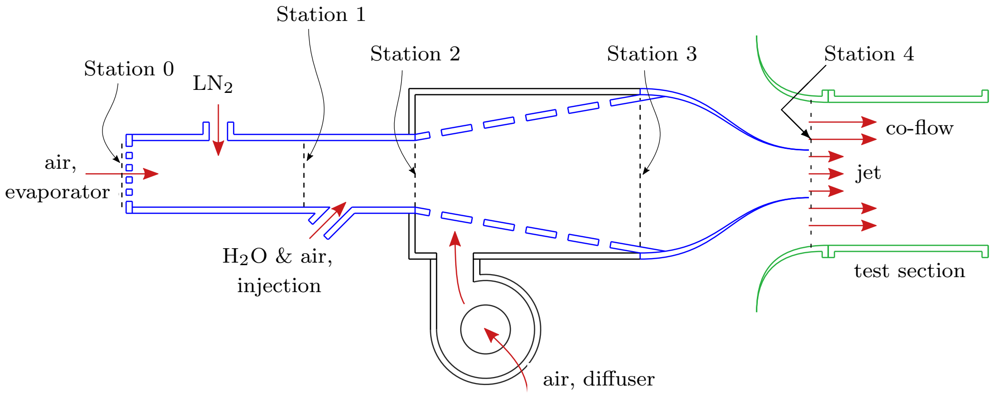


Figure 3.2: Illustration of arrangement for the conservation of energy analysis performed on the icing wind tunnel configuration.

ice particles should not completely melt before the test section is reached.

To increase the flow speed, and to improve the spatial uniformity of the flow delivered to the test section, the contraction is used to accelerate the mixture of the cold air and suspended ice particles from Station 3 to Station 4. The flow speed increases through the nozzle contraction, but because the flow remains essentially incompressible, the thermodynamic (fully-mixed, equilibrium) temperature of the flow at Station 3 and 4 will be approximately the same.

### 3.3.2 Turbofan compressor and facility target conditions

There are many parameters that could have a significant role in the icing process within the compressor of the turbofan engine. To determine which of these parameters are significant at any particular operating condition, it is important for icing wind tunnel facilities to have the capability to simulate as many of these parameters as possible.

In general, the flow speed in the compressor has a maximum value around Mach 0.5 (Gudmundsson, 2013), but the near-surface Mach number over the compressor blades can vary between 0.2 to 0.8 (Schnoes et al., 2018; Dixon and Hall, 2013), and in stagnation regions near the blade leading edge, the surface Mach number can obviously be less than 0.2. The Mach number is given by,

$$M_a = \frac{U}{\sqrt{\gamma_a R_a T_a}} \tag{3.1}$$

The maximum flow speed that can be achieved in a given wind tunnel cross section can be estimated using the power consumption of the main fan, however when considering the overall energy consumption of an icing wind tunnel, the limiting factor is likely to be the cooling power cost (Bansmer et al., 2018) which could be in excess of 20 times the fan power cost. Therefore, in order to keep the facility operating costs sufficiently low to enable operation within a modestly-funded university laboratory, it is necessary to target wind tunnel operation at the lower end of compressor flow speeds: Mach numbers of up to 0.2. When operating at a representative static temperature of around 273 K (0°C), the target flow speed is therefore around 66 m/s.

Viscous effects are characterised by the Reynolds number,

$$Re_a = \frac{\rho_a U d}{\mu_a} \tag{3.2}$$

In this equation, $d$ represents either the diameter of the model if it is a cylinder or the double radius of leading edge if the model is an aerofoil. Because the ice accretion often happens in the region near to the leading edge, it is necessary to select a length scale representative of the leading-edge region (Bond and Anderson, 2004). However the Reynolds number often is not included in the scaling analysis when the ice accretion occurs at the leading edge of the body where the boundary layer is thin and flow viscosity does not impact the accretion process. In other cases where the surface water run-back effect is significant, the Reynolds number should be included in the analysis.

Another important parameter in the icing process is the water content. Typical values for atmospheric liquid water content (LWC) vary from 0.1 to 3 g/m$^3$ according to measurements in convective systems (Lawson et al., 1998; Wendisch et al., 2016; Braga et al., 2017). In glaciated ice conditions, values for the ice water content (IWC) larger than 1 g/m$^3$ have been observed within 55 km of continental and oceanic convective system and peaks values in deep convective system of up to 6 g/m$^3$ can occur (Gayet et al., 2014). The range of total water content (TWC, which is sum of LWC and IWC) of relevance to the icing problem, has been specified elsewhere as being from 0.5 to 9 g/m$^3$ for MVD from 40 to 60 $\mu$m (Bencic et al., 2013).

Ice crystals can enter the core of an engine where they will melt partially and impinge on the warm surfaces of the compressor. These ice particles will reduce the temperature of the compressor surfaces and can begin to accrete on these surfaces if the aerodynamic and thermodynamic balance allows (Knezevici et al., 2012). Ice accretion can occur at flow temperatures both above and below 0°C (Mason et al., 2011), and ice accretion is sensitive to the wet bulb temperature with a range of between $-2$ and $+2$°C being indicative (Struk et al., 2012). To achieve the above range of wet bulb temperature in a wind tunnel facility with a relative humidity of around 40 %, the flow temperature should be in the range between 2 and 7°C.

Surface temperature and heat flux for the representative surface model also plays an important role in icing process. The ice accretion is driven by heat loss from these surfaces by convection and evaporation. Heat transfer by convection depends on the flow speed, surface shape, and temperature difference between the surface and the air stream. The evaporative cooling will drive the surface temperature towards the wet bulb temperature. Previous work in a small wind tunnel showed that over a surface temperature range between $-9$ and 5°C, no ice accretion was observed for surface temperatures above 0°C (Saleh, 2013). The heat flux from the icing surface to the overlying ice layer has an effect on growth rates of ice accretion. It was found that when using a cooling heat flux to decrease the surface temperature to slightly below freezing (typically $-4$°C), the adhesion of wet deposits formed at wet bulb temperatures above freezing was promoted and therefore ice accretion occurred without shedding and the growth rate increased with melting ratio (Struk et al., 2015).

### 3.3.3 Summary of target operating conditions

The target operating parameters and flow conditions for the new icing wind tunnel are summarised below with a brief justification in each case.

- Consumption of liquid nitrogen per run: $\leq$ 20 litres. This figure corresponds to the maximum size of a standard liquid nitrogen dewar that can be readily handled manually. By constraining the design to operate with this volume of liquid nitrogen, it was anticipated that the facility could be operated by a single person, for the most part, and that modest facility operating costs could therefore also be achieved.

- Operating period of the facility: $\leq 2$ minutes. Significant ice accretion thicknesses ($> 10$ mm) have been registered in previous studies in short periods ($\sim 3$ minutes). It was thought that a period of 2 minutes would be sufficient to assess initiation and initial growth rates.

- Flow speed: $\leq 50$ m/s. This figure is on the lower speed end of the capabilities of existing icing wind tunnels and is even slightly less than the figure of 66 m/s identified in Section 3.3.2. Nevertheless this figure is chosen as an achievable target value that is within the constraints of existing, or likely-to-be-sourced hardware that can be operated in the available laboratory area at the University of Southern Queensland.

- Flow temperature: $-10 \leq T \leq 10$°C. Flow temperatures close to the water freezing point are of interest in the ice crystal icing problem, but having a capability to produce flow temperatures a few degrees higher and lower than this point offers capability for parametric studies.

- Model size: chord $\sim 100$ mm, span $\sim 100$ mm. Indicative of models sizes used in the NRC icing wind tunnel facilities and sufficiently large for incorporation of internal heating elements, thermocouples and other instrumentation.

- Total water content: $\leq 10\,\mathrm{g/m^3}$. This maximum figure is on the higher end of conditions used in other icing wind tunnels, but it was thought that having this capability would be readily achievable and could offer flexibility in experiment design that offsets, to some degree, the ice accretion growth constraint associated with the specified 2 minutes maximum flow duration.

- Particle diameters: $\leq 200\,\mu$m. Particle diameters up to $300\,\mu$m have been used in other work, though a maximum figure of $\sim 200\,\mu$m seems to be more commonly quoted for other wind tunnel facilities.

- Melting ratios: $\leq 0.2$. Values slightly higher than 0.2 have occasionally been used in other facilities, but peak ice growth rates have generally been achieved for lower melting ratio values.

## 3.4 Conservation of energy analysis

To assess the viability of the proposed concept, a conservation of energy analysis was performed. The analysis presented in this section is somewhat approximate because it treats the air temperature as the equilibrium temperature of the particles whereas the wet bulb temperature will actually be the temperature of the particles in the equilibrium limit. For temperatures around 0°C which are of interest in this work, the wet bulb temperature is within about three degrees Celsius of the air temperature for relative humidity values of 40% or more, which are representative of the present operating conditions for the facility. Therefore the approximate treatment presented herein is considered adequate for the intended purpose of assessing the engineering viability of the icing wind tunnel configuration.

### 3.4.1 Temperature at Station 1

Referring to Figure 3.2, and ignoring boundary heat transfer, the conservation of energy equation for the system up to Station 1 gives

$$\dot{m}_{air,e}\left(h_{air,e} - h_{air,1}\right) + \dot{m}_{N_2}\left(h_{LN2} - h_{N_2,1}\right) = 0. \tag{3.3}$$

Provided $T_{sat,N_2} \leq T_{1,N_2}$, the energy balance for the facility up to Station 1 can be written as

$$\dot{m}_{air,e}C_{p,air}\left(T_{air,e} - T_{air,1}\right) + \dot{m}_{N_2}\left[C_{p,N_2}\left(T_{sat,N_2} - T_{N_2,1}\right) - h_{fg,N_2}\right] = 0, \tag{3.4}$$

on the assumption of constant specific heats.

For fully-mixed flow conditions at Station 1 such that

$$T_{air,1} = T_{N_2,1} = T_1, \tag{3.5}$$

the temperature at station 1 can be calculated as

$$T_1 = \frac{\dot{m}_{air,e}C_{p,air}T_{air,e} + \dot{m}_{N_2}\left(C_{p,N_2}T_{sat,N_2} - h_{fg,N_2}\right)}{\dot{m}_{air,e}C_{p,air} + \dot{m}_{N_2}C_{p,N_2}}. \tag{3.6}$$

In the limiting case where all of the liquid nitrogen is only just evaporated such that $T_{sat,N_2} = T_{air,1} = T_{N_2,1} = T_1$,

$$\frac{\dot{m}_{air,e}}{\dot{m}_{N_2}} = \frac{h_{fg,N_2}}{C_{p,air}\left(T_{air,e} - T_{sat,N_2}\right)}. \tag{3.7}$$

The above equation specifies the minimum amount of air required for complete evaporation of the liquid nitrogen.

### 3.4.2 Temperature at Station 2

For the atomizing water injection nozzles used in this work, a small amount of air is also injected. Details of the nozzles and their performance are presented in Section 4.2.8. The energy conservation analysis proceeds by denoting this amount of air as $\dot{m}_{air,inj}$, and again ignoring boundary heat transfer. Under these conditions, an energy balance for the system up to Station 2 gives

$$\dot{m}_{air,e}\left(h_{air,e}-h_{air,e,2}\right)+\dot{m}_{N_2}\left(h_{LN2}-h_{N_2,2}\right)+\dot{m}_{H_2O}\left(h_{H_2O,inj}-h_{H_2O,2}\right)+ \\ \dot{m}_{air,inj}\left(h_{air,inj}-h_{air,inj,2}\right)=0. \quad (3.8)$$

Assuming all of the water freezes and $T_{H_2O,2} \leq T_{freeze}$, and that constant specific heats apply, the energy balance can be written as

$$\dot{m}_{air,e}C_{p,air}\left(T_{air,e}-T_{air,2}\right)+ \\ \dot{m}_{N_2}\left[C_{p,N_2}\left(T_{sat,N_2}-T_{N_2,2}\right)-h_{fg,N_2}\right]+ \\ \dot{m}_{H_2O}\left[C_{H_2O,l}\left(T_{H_2O,inj}-T_{freeze}\right)+h_{if,H_2O}+C_{H_2O,s}\left(T_{freeze}-T_{H_2O,2}\right)\right]+ \\ \dot{m}_{air,inj}C_{p,air}\left(T_{air,inj}-T_{air,inj,2}\right)=0. \quad (3.9)$$

Assuming thermal equilibrium between constituents at Station 2,

$$T_{air,e,2}=T_{N_2,2}=T_{H_2O,2}=T_{air,inj,2}=T_2, \quad (3.10)$$

the temperature of the flow at Station 2 can be written

$$T_2=\frac{\dot{m}_{air}C_{p,air}T_{air}+\dot{m}_{N_2}\left(C_{p,N_2}T_{sat,N_2}-h_{fg,N_2}\right)}{\left(\dot{m}_{air}C_{p,air}+\dot{m}_{N_2}C_{p,N_2}+\dot{m}_{H_2O}C_{H_2O,s}\right)}+ \\ \frac{\dot{m}_{H_2O}\left[C_{H_2O,l}\left(T_{H_2O,inj}-T_{freeze}\right)+h_{if,H_2O}+C_{H_2O,s}T_{freeze}\right]}{\left(\dot{m}_{air}C_{p,air}+\dot{m}_{N_2}C_{p,N_2}+\dot{m}_{H_2O}C_{H_2O,s}\right)} \quad (3.11)$$

where

$$\dot{m}_{air}C_{p,air}T_{air}=\left(\dot{m}_{air,e}T_{air,e}+\dot{m}_{air,inj}T_{air,inj}\right)C_{p,air} \quad (3.12)$$

and

$$\dot{m}_{air}C_{p,air}=\left(\dot{m}_{air,e}+\dot{m}_{air,inj}\right)C_{p,air} \quad (3.13)$$

In the limiting case where $T_{freeze} = T_{air,e,2} = T_{N_2,2} = T_{H_2O,2} = T_{air,inj,2} = T_2$ and all of the water is frozen,

$$\frac{\dot{m}_{H_2O}}{\dot{m}_{N_2}} = \frac{\left[C_{p,N_2}\left(T_{freeze} - T_{sat,N_2}\right) + h_{fg,N_2}\right]}{\left[C_{H_2O,l}\left(T_{H_2O,inj} - T_{freeze}\right) + h_{if,H_2O}\right]} - \frac{\dot{m}_{air,e}}{\dot{m}_{N_2}} \frac{C_{p,air}\left(T_{air,e} - T_{freeze}\right)}{\left[C_{H_2O,l}\left(T_{H_2O,inj} - T_{freeze}\right) + h_{if,H_2O}\right]} - \frac{\dot{m}_{air,inj}}{\dot{m}_{N_2}} \frac{C_{p,air}\left(T_{air,inj} - T_{freeze}\right)}{\left[C_{H_2O,l}\left(T_{H_2O,inj} - T_{freeze}\right) + h_{if,H_2O}\right]}. \tag{3.14}$$

The above equation specifies the maximum amount of water that can be injected while still achieving glaciated conditions.

### 3.4.3 Temperature at Station 3

For the energy conservation of the system up to Station 3, it is noted that the only difference from the energy conservation of the system up to Station 2 is the introduction of additional air in the diffuser, $\dot{m}_{air,d}$. Again, ignoring heat transfer at the boundaries and assuming thermal equilibrium of the constituents at Station 3,

$$T_{air,e,3} = T_{N_2,3} = T_{H_2O,3} = T_{air,inj,3} = T_{air,d,3} = T_3, \tag{3.15}$$

and requiring the injected water to remain frozen and the temperature at Station 3 to be $T_3 \leq T_{freeze}$, now allows the temperature at Station 3 to be written as

$$T_3 = \frac{\dot{m}_{air} C_{p,air} T_{air} + \dot{m}_{N_2}\left(C_{p,N_2} T_{sat,N_2} - h_{fg,N_2}\right)}{\left(\dot{m}_{air} C_{p,air} + \dot{m}_{N_2} C_{p,N_2} + \dot{m}_{H_2O} C_{H_2O,s}\right)} + \frac{\dot{m}_{H_2O}\left[C_{H_2O,l}\left(T_{H_2O,inj} - T_{freeze}\right) + h_{if,H_2O} + C_{H_2O,s} T_{freeze}\right]}{\left(\dot{m}_{air} C_{p,air} + \dot{m}_{N_2} C_{p,N_2} + \dot{m}_{H_2O} C_{H_2O,s}\right)} \tag{3.16}$$

where

$$\dot{m}_{air} C_{p,air} T_{air} = \left(\dot{m}_{air,e} T_{air,e} + \dot{m}_{air,inj} T_{air,inj} + \dot{m}_{air,d} T_{air,d}\right) C_{p,air} \tag{3.17}$$

and

$$\dot{m}_{air} C_{p,air} = \left(\dot{m}_{air,e} + \dot{m}_{air,inj} + \dot{m}_{air,d}\right) C_{p,air} \tag{3.18}$$

In the limiting case where $T_{freeze} = T_{air,e,3} = T_{N_2,3} = T_{H_2O,3} = T_{air,inj,3} = T_{air,d,3} = T_3$ and all of the water is frozen,

$$\frac{\dot{m}_{air,d}}{\dot{m}_{N_2}} = \frac{\left[C_{p,N_2}\left(T_{freeze} - T_{sat,N_2}\right) + h_{fg,N_2}\right]}{C_{p,air}\left(T_{air,d} - T_{freeze}\right)} - \frac{\dot{m}_{H_2O}}{\dot{m}_{N_2}} \frac{\left[C_{H_2O,l}\left(T_{H_2O,inj} - T_{freeze}\right) + h_{if,H_2O}\right]}{C_{p,air}\left(T_{air,d} - T_{freeze}\right)} - \frac{\dot{m}_{air,e}}{\dot{m}_{N_2}} \frac{\left(T_{air,e} - T_{freeze}\right)}{\left(T_{air,d} - T_{freeze}\right)} - \frac{\dot{m}_{air,inj}}{\dot{m}_{N_2}} \frac{\left(T_{air,inj} - T_{freeze}\right)}{\left(T_{air,d} - T_{freeze}\right)}. \quad (3.19)$$

The above equation specifies the maximum amount of air that can be introduced through the diffuser while still maintaining glaciated conditions in the test flow.

### 3.4.4 Effect of Melting Ratio

The previous conservation of energy analyses were performed on the assumption that all water injected into the system freezes and remains in a frozen state. It is known that substantial ice accretion rarely occurs under fully glaciated conditions, so target wind tunnel flow conditions should include states with some liquid water present in the flow. We can expect at least partial melting of ice if sufficient warm air enters through the perforated diffuser, so an additional parameter, the melting ratio is introduced for the analysis. The melting ratio is defined using flow parameter values within the icing jet nozzle flow at the test section location (Station 4) as

$$MR = \frac{\dot{m}_{H_2O,l}}{\dot{m}_{H_2O}} = \frac{\dot{m}_{H_2O,l}}{\dot{m}_{H_2O,l} + \dot{m}_{H_2O,s}}. \quad (3.20)$$

In the conservation of energy analysis, the possibility that not all of the water at Station 4 is in a frozen state is accommodated by treating the flow rates of the solid water $\dot{m}_{H_2O,s}$ and the liquid water $\dot{m}_{H_2O,l}$ separately. Again, ignoring heat transfer effects, an energy balance for the system up to Station 3 should be essentially the same as that up to Station 4 and gives

$$\dot{m}_{air,e}\left(h_{air,e} - h_{air,e,3}\right) + \dot{m}_{N_2}\left(h_{LN2} - h_{N_2,3}\right) + \dot{m}_{air,inj}\left(h_{air,inj} - h_{air,inj,3}\right) + \dot{m}_{H_2O,s}\left(h_{H_2O,inj} - h_{H_2O,s,3}\right) + \dot{m}_{H_2O,l}\left(h_{H_2O,inj} - h_{H_2O,l,3}\right) + \dot{m}_{air,d}\left(h_{air,d} - h_{air,d,3}\right) + = 0. \quad (3.21)$$

Converting from the enthalpy-based format to a temperature-based format on the assumption of constant values of specific heats, we have

$$\begin{aligned}
&\dot{m}_{air,e}C_{p,air}\left(T_{air,e}-T_{air,3}\right)+\\
&\qquad\dot{m}_{N_2}\left[C_{p,N_2}\left(T_{sat,N_2}-T_{N_2,3}\right)-h_{fg,N_2}\right]+\\
&\dot{m}_{H_2O,s}\left[C_{H_2O,l}\left(T_{H_2O,inj}-T_{freeze}\right)+h_{if,H_2O}+C_{H_2O,s}\left(T_{freeze}-T_{H_2O,s,3}\right)\right]+\\
&\qquad\dot{m}_{H_2O,l}C_{H_2O,l}\left(T_{H_2O,inj}-T_{H_2O,l,3}\right)+\\
&\qquad\dot{m}_{air,inj}C_{p,air}\left(T_{air,inj}-T_{air,inj,3}\right)+\\
&\qquad\qquad\dot{m}_{air,d}C_{p,air}\left(T_{air,d}-T_{air,d,3}\right)=0. \qquad (3.22)
\end{aligned}$$

The gaseous components of the mixture should be well mixed by Station 3 and should be in thermal equilibrium so that,

$$T_{air,e,3}=T_{N_2,3}=T_{air,inj,3}=T_{air,d,3}=T_3. \qquad (3.23)$$

However the solid and liquid components may not be in thermal equilibrium with the gaseous mixture, so some further assumptions are needed.

**Case 1.** If $T_3 < T_{freeze}$, we assume that if any liquid water is present, it will be in a supercooled state such that $T_{H_2O,l,3} = T_3$ and any ice present is assumed to be in thermal equilibrium with the local surroundings so $T_{H_2O,s,3} = T_3$. For this situation, the temperature at Station 3 can be written as

$$\begin{aligned}
T_3 = &\frac{\dot{m}_{air}C_{p,air}T_{air}+\dot{m}_{N_2}\left(C_{p,N_2}T_{sat,N_2}-h_{fg,N_2}\right)}{\left(\dot{m}_{air}C_{p,air}+\dot{m}_{N_2}C_{p,N_2}+\dot{m}_{H_2O}C_{H_2O}\right)}+\\
&\frac{\dot{m}_{H_2O,s}\left[C_{H_2O,l}\left(T_{H_2O,inj}-T_{freeze}\right)+h_{if,H_2O}+C_{H_2O,s}T_{freeze}\right]}{\left(\dot{m}_{air}C_{p,air}+\dot{m}_{N_2}C_{p,N_2}+\dot{m}_{H_2O}C_{H_2O}\right)}+\\
&\frac{\dot{m}_{H_2O,l}C_{H_2O,l}T_{H_2O,inj}}{\left(\dot{m}_{air}C_{p,air}+\dot{m}_{N_2}C_{p,N_2}+\dot{m}_{H_2O}C_{H_2O}\right)} \qquad (3.24)
\end{aligned}$$

where

$$\dot{m}_{air}C_{p,air}T_{air}=\left(\dot{m}_{air,e}T_{air,e}+\dot{m}_{air,inj}T_{air,inj}+\dot{m}_{air,d}T_{air,d}\right)C_{p,air} \qquad (3.25)$$

$$\dot{m}_{air}C_{p,air}=\left(\dot{m}_{air,e}+\dot{m}_{air,inj}+\dot{m}_{air,d}\right)C_{p,air} \qquad (3.26)$$

and

$$\dot{m}_{H_2O}C_{H_2O}=\dot{m}_{H_2O,s}C_{H_2O,s}+\dot{m}_{H_2O,l}C_{H_2O,l} \qquad (3.27)$$

**Case 2.** If $T_3 \geq T_{freeze}$, then we assume that all of the remaining ice will be in the process of melting so we specify $T_{H_2O,s,3} = T_{freeze}$ but we assume that the liquid water is in thermal equilibrium with the surrounding gas mixture so $T_{H_2O,l,3} = T_3$. Under these conditions, the temperature at Station 3 can be specified as

$$T_3 = \frac{\dot{m}_{air}C_{p,air}T_{air} + \dot{m}_{N_2}\left(C_{p,N_2}T_{sat,N_2} - h_{fg,N_2}\right)}{\left(\dot{m}_{air}C_{p,air} + \dot{m}_{N_2}C_{p,N_2} + \dot{m}_{H_2O,l}C_{H_2O,l}\right)} + \frac{\dot{m}_{H_2O,s}\left[C_{H_2O,l}\left(T_{H_2O,inj} - T_{freeze}\right) + h_{if,H_2O}\right]}{\left(\dot{m}_{air}C_{p,air} + \dot{m}_{N_2}C_{p,N_2} + \dot{m}_{H_2O,l}C_{H_2O,l}\right)} + \frac{\dot{m}_{H_2O,l}C_{H_2O,l}T_{H_2O,inj}}{\left(\dot{m}_{air}C_{p,air} + \dot{m}_{N_2}C_{p,N_2} + \dot{m}_{H_2O,l}C_{H_2O,l}\right)} \quad (3.28)$$

where

$$\dot{m}_{air}C_{p,air}T_{air} = \left(\dot{m}_{air,e}T_{air,e} + \dot{m}_{air,inj}T_{air,inj} + \dot{m}_{air,d}T_{air,d}\right)C_{p,air} \quad (3.29)$$

and

$$\dot{m}_{air}C_{p,air} = \left(\dot{m}_{air,e} + \dot{m}_{air,inj} + \dot{m}_{air,d}\right)C_{p,air} \quad (3.30)$$

## 3.5 Results

### 3.5.1 Conditions and thermodynamic quantities

The ambient temperature in the laboratory at USQ is taken as

$$T_{amb} = 293\,\mathrm{K}, \quad (3.31)$$

and atmospheric pressure in the laboratory is approximately

$$p_{atm} = 94\,\mathrm{kPa}. \quad (3.32)$$

The saturation temperature of the liquid nitrogen at the atmospheric pressure in the laboratory is

$$T_{sat,N_2} = 76.7\,\mathrm{K}, \quad (3.33)$$

and heat of vaporisation of the liquid nitrogen is

$$h_{fg,N_2} = 199.98 \times 10^3\,\mathrm{J/kg}. \quad (3.34)$$

The freezing temperature of the water is

$$T_{freeze} = 273.15\,\mathrm{K} \tag{3.35}$$

and the heat of fusion of water is

$$h_{if,H_2O} = 333.55 \times 10^3\,\mathrm{J/kg}. \tag{3.36}$$

The constant pressure specific heat for the air is taken as

$$C_{p,air} = 1040\,\mathrm{J/kgK} \tag{3.37}$$

and for the nitrogen (in gaseous form) the constant pressure specific heat is taken as

$$C_{p,N_2} = 1004\,\mathrm{J/kgK}. \tag{3.38}$$

The specific heats for the water in liquid and solid forms are taken as

$$C_{H_2O,l} = 4186\,\mathrm{J/kgK} \tag{3.39}$$

$$C_{H_2O,s} = 2018\,\mathrm{J/kgK} \tag{3.40}$$

### 3.5.2 Temperatures and ice concentrations

Using the above parameters and specifying the temperatures of the air and the water entering the facility as being equal to the ambient value, $T_{air,e} = T_{air,inj} = T_{H_2O,inj} = T_{air,d} = T_{amb}$, the results from the energy conservation analysis of the wind tunnel are presented in Figure 3.3, Figure 3.4, and Figure 3.5. In these figures, temperatures at Station 1, 2 and 3 are presented as functions of the mass flow rate of air and water normalised by the mass flow rate of the liquid nitrogen. This form of normalisation has been adopted because the operation of the facility hinges on the available liquid nitrogen.

Using the above parameters, the minimum mass flow rate of air for the evaporator from Equation 3.7 is

$$\frac{\dot{m}_{air,e}}{\dot{m}_{N_2}} = 0.9202, \tag{3.41}$$

and this is the minimum value on the horizontal axis in Figure 3.3. At this value for $\dot{m}_{air,e}/\dot{m}_{N_2} = 0.9202$, the temperature of the mixture at Station 1 is equal to the saturation temperature of the liquid nitrogen (76.7 K). The mixture temperature at Station 1 should be lower than approximately $-40°$C to ensure rapid freezing of the injected water droplets, and this mixture temperature can be achieved if $\dot{m}_{air,e}/\dot{m}_{N_2} \leq 6.02$. More generally, mixture temperatures at or below the freezing point can be achieved if $\dot{m}_{air,e}/\dot{m}_{N_2} \leq 20.16$, but in such cases, the production of glaciated conditions will be less certain.

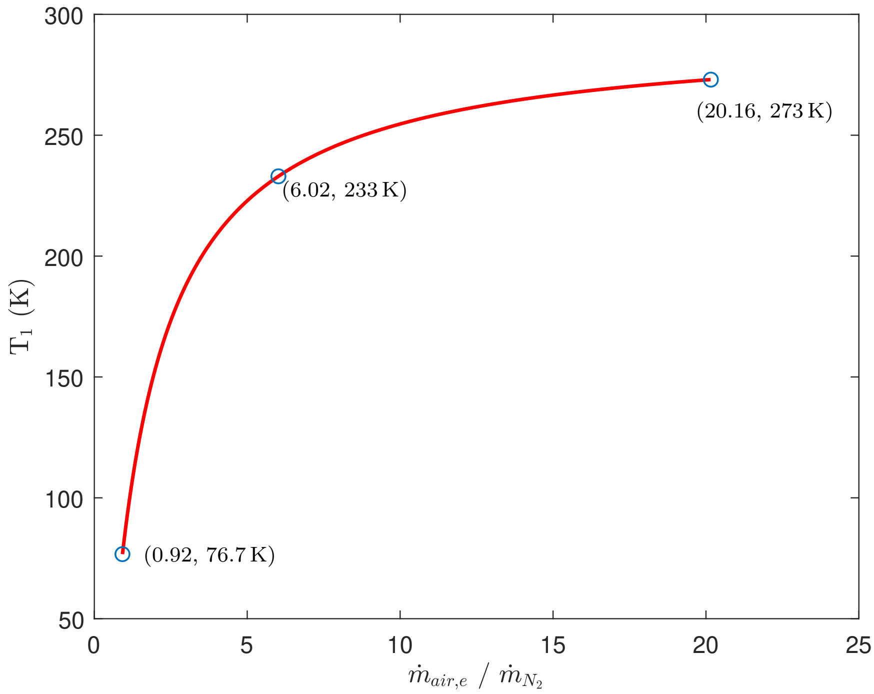


Figure 3.3: Variation of temperature of the mixture at Station 1 with the normalised mass of air entering the evaporator, based on the energy conservation analysis.

If the minimum amount of evaporator air flow is used ($\dot{m}_{air,e}/\dot{m}_{N_2} = 0.9202$), the maximum amount of water that can be injected while still achieving glaciated conditions at Station 2 is

$$\frac{\dot{m}_{H_2O}}{\dot{m}_{N_2}} = 0.9263, \tag{3.42}$$

in the case where no additional air is injected with the water, $\frac{\dot{m}_{air,inj}}{\dot{m}_{N_2}} = 0$. This operating point is illustrated in Figure 3.4. Such a facility operating condition would produce an extraordinarily high ice water content, a value in excess of 500 g/m$^3$. Therefore, more modest values of $\dot{m}_{H_2O}/\dot{m}_{N_2}$ are relevant for the practical operation of the facility, and three such values have been used ($\dot{m}_{H_2O}/\dot{m}_{N_2} = 0$, 0.2, and 0.4) in the presentation of energy conservation analysis results in Figure 3.5. Target values for the fully-mixed flow temperature at Station 3 will be within several degrees of 0°C. The results in Figure 3.5 indicate that the fully-mixed temperature at Station 3 approaches the ice melting temperature for values of $\dot{m}_{air,d}/\dot{m}_{N_2}$ between 10 and 20 for wind tunnel operating values of IWC that are relevant to the ice crystal icing problem.

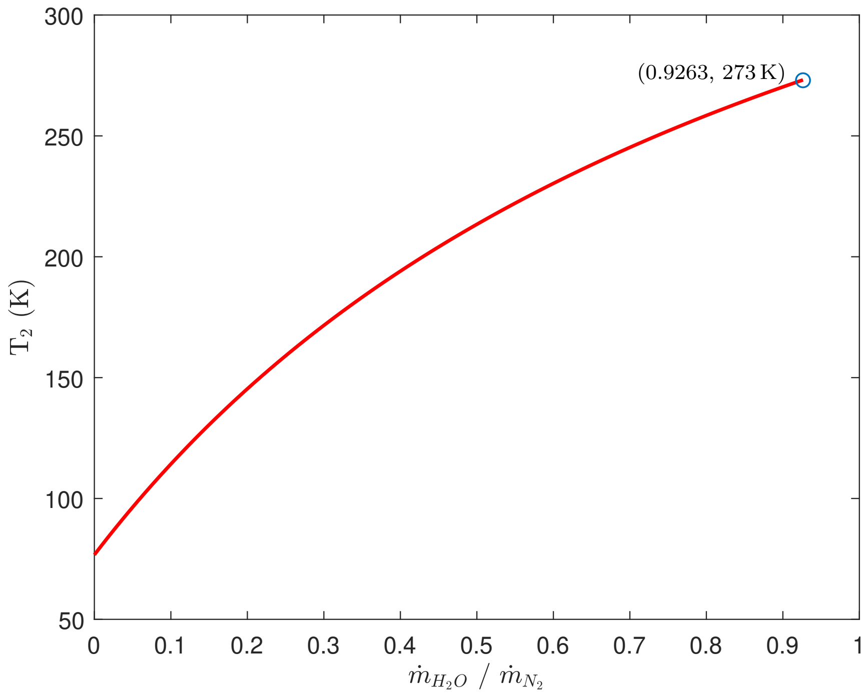


Figure 3.4: Variation of temperature of the mixture at Station 2 with the normalised mass of injected water when $\frac{\dot{m}_{air,e}}{\dot{m}_{N_2}} = 0.9202$, based on the energy conservation analysis.

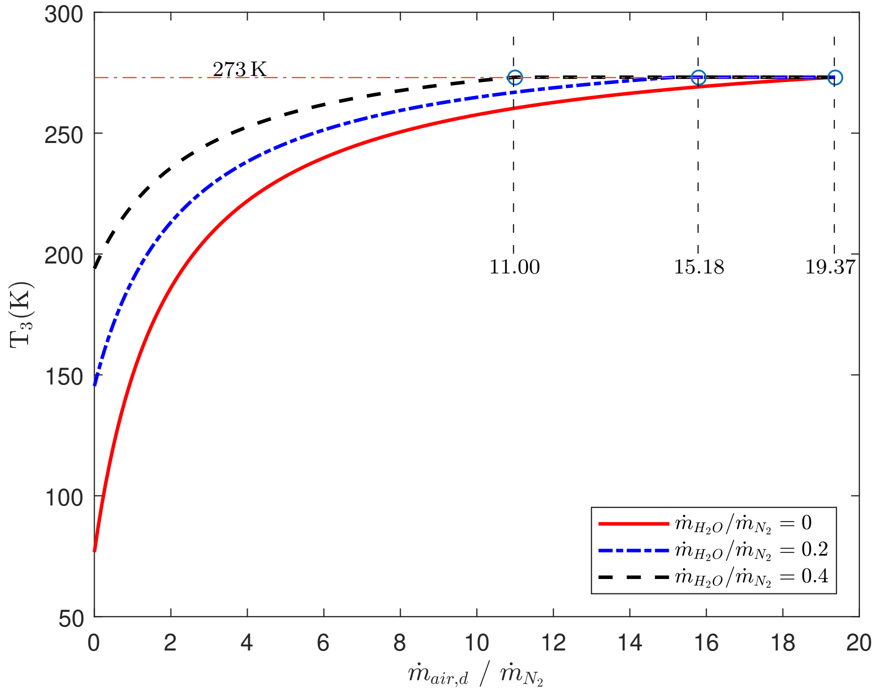


Figure 3.5: Variation of temperature at Station 3 with mass of air entering the diffuser when $\frac{\dot{m}_{air,e}}{\dot{m}_{N_2}} = 0.9202$, based on the energy conservation analysis.

Further results from the energy conservation analysis are presented in Table 3.1. In this table, the normalised evaporator mass flow rate is held constant at $\dot{m}_{air,e}/\dot{m}_{N_2} = 0.9202$, corresponding to the minimum air flow rate required for full evaporation of the liquid nitrogen, and a range of normalised water injection flow rates $\dot{m}_{H_2O}/\dot{m}_{N_2}$ are considered. The normalised diffuser mass flow rates $\dot{m}_{air,d}/\dot{m}_{N_2}$ are calculated on the basis that the fully-mixed diffuser exit temperature $T_3$ reaches the ice melting temperature according to Equation (3.21), taking $\dot{m}_{air,inj}/\dot{m}_{N_2} = 0$ for simplicity. The quantities in columns 4 and 5 of Table 3.1 are calculated according to

$$\frac{\dot{m}_{air\&N_2}}{\dot{m}_{N_2}} = \frac{\dot{m}_{air,e}}{\dot{m}_{N_2}} + \frac{\dot{m}_{air,d}}{\dot{m}_{N_2}} \tag{3.43}$$

and

$$\frac{\dot{m}_{H_2O}}{\dot{m}_{air\&N_2}} = \frac{\dot{m}_{H_2O}}{\dot{m}_{N_2}} \frac{\dot{m}_{N_2}}{\dot{m}_{air\&N_2}} \tag{3.44}$$

Column 5 of Table 3.1 specifies the IWC in the form of a mass ratio. To convert to the

Table 3.1: Selected flow rate results for fully glaciated conditions and diffuser exit temperature equal to 0°C.

| $\frac{\dot{m}_{H_2O}}{\dot{m}_{N_2}}$ | $\frac{\dot{m}_{air,e}}{\dot{m}_{N_2}}$ | $\frac{\dot{m}_{air,d}}{\dot{m}_{N_2}}$ | $\frac{\dot{m}_{air\&N_2}}{\dot{m}_{N_2}}$ | $\frac{\dot{m}_{H_2O}}{\dot{m}_{air\&N_2}}$ | $\frac{\dot{m}_{H_2O}}{\dot{V}_{air\&N_2}}$ (g/m$^3$) |
|---|---|---|---|---|---|
| 0 | 0.9202 | 19.3651 | 21.2853 | 0 | 0 |
| 0.05 | 0.9202 | 18.3198 | 20.24 | 0.002470 | 2.962 |
| 0.10 | 0.9202 | 17.2746 | 19.1948 | 0.005210 | 6.247 |
| 0.15 | 0.9202 | 16.2293 | 18.1495 | 0.008265 | 9.911 |
| 0.2 | 0.9202 | 15.1840 | 17.1043 | 0.01169 | 14.02 |
| 0.4 | 0.9202 | 11.0028 | 12.9230 | 0.03095 | 37.11 |
| 0.6 | 0.9202 | 6.8216 | 8.7418 | 0.06864 | 82.31 |
| 0.8 | 0.9202 | 2.6404 | 4.5606 | 0.1754 | 210.3 |
| 0.9263 | 0.9202 | 0 | 1.9202 | 0.4824 | 578.4 |

more traditional density-style of presentation for the IWC, the density of the air and nitrogen flow needs to be specified. Since practical flow conditions of interest in the wind tunnel will have significantly more air flow than evaporated liquid nitrogen flow, and we are considering the case of $T_3 = 0\,°\mathrm{C}$, the flow density at the diffuser exit can be calculated using

$$\rho_{air\&N_2} = \frac{p_3}{R_3 T_3} \approx \frac{94 \times 10^3}{(287)(273.15)} = 1.20\,\mathrm{kg/m^3} \tag{3.45}$$

The final column of Table 3.1 presents the values of IWC in the units of g/m$^3$ using

$$\frac{\dot{m}_{H_2O}}{\dot{V}_{air\&N_2}} = \rho_{air\&N_2} \frac{\dot{m}_{N_2}}{\dot{m}_{air\&N_2}} \tag{3.46}$$

The highlighted row in Table 3.1 indicates that the target maximum IWC of almost $10\,\mathrm{g/m^3}$ should be achieved for $\dot{m}_{H_2O}/\dot{m}_{N_2} \approx 0.15$ and $\dot{m}_{air\&N_2}/\dot{m}_{N_2} \approx 18.1$.

The thermodynamic performance of the facility is dictated largely by the availability of the liquid nitrogen and the proposed operating concept involves using a maximum of 20 litre of liquid nitrogen per run in the facility. Taking the target flow duration for the facility as 2 minutes, and the density of the liquid nitrogen as approximately $807\,\mathrm{kg/m^3}$, we have an average flow rate for the nitrogen of $\dot{m}_{N_2} = 0.135\,\mathrm{kg/s}$. Applying this nitrogen flow rate to the target maximum IWC (the conditions in the highlighted row in Table 3.1) gives $\dot{m}_{H_2O} = 0.15 \times 0.135 = 0.0203\,\mathrm{kg/s}$ and $\dot{m}_{air\&N_2} = 18.1 \times 0.135 =$

2.44 kg/s. Using the nominal density of the air-nitrogen mixture of $\rho_{air\&N_2} = 1.2\,\mathrm{kg/m^3}$, the volumetric flow rate of the air-nitrogen mixture will be $\dot{V}_{air\&N_2} = 2.44/1.2 = 2.04\,\mathrm{m^3/s}$. Taking the target maximum flow speed of the facility as 50 m/s, indicates the available cold-flow core size of the test flow will have an area of $2.04/50 = 0.0408\,\mathrm{m^2}$ or a diameter of 0.228 m.

### 3.5.3 Melting ratio

The influence of the diffuser mass flow rate on the melting ratio is illustrated in Figure 3.6 for three different flow temperatures close to the freezing temperature, and for a total water flow rate of $\dot{m}_{H_2O}/\dot{m}_{N_2} = 0.2$ which gives $TWC \approx 14\,\mathrm{g/m^3}$ (Table 3.1). According to the assumptions made in Section 3.4.4, $T_3 = 273\,\mathrm{K}$ is the only result in Figure 3.6 for which the water is in thermal equilibrium with the surrounding air flow. For $T_3 = 270\,\mathrm{K}$, the liquid water is assumed to be supercooled, and for $T_3 = 276\,\mathrm{K}$, the ice is assumed to be at the freezing temperature, and so the ice would be in the process of melting.

Figure 3.6 can be used to illustrate the relative thermal capacities of the suspended water particles and the air-nitrogen flow. For example, consider Figure 3.6 with $\dot{m}_{air,d}/\dot{m}_{N_2} \approx 18$ and the case of $T_3 = 276\,\mathrm{K}$. The melting ratio for this condition will be zero, but since the ice will be in the process of melting, over a period of time, the melting ratio will therefore increase and this will cause a decrease in the flow temperature. For a fixed diffuser mass flow rate, this melting process can be tracked along a vertical line in Figure 3.6, and thermal equilibrium will be reached at a melting ratio $MR \approx 0.9$ when $T_3 = 273.15\,\mathrm{K}$. Thus, at a fixed flow rate of warm diffuser air, a flow temperature difference of around 3°C is sufficient to cause a substantial change in the melting ratio.

Melting ratios from 0 up to approximately 0.2 are of interest in the ice crystal icing problem, and the normalised diffuser mass flow rates associated with these limiting values are presented in Table 3.2, corresponding to the conditions considered in Figure 3.6. From Table 3.2 it can be observed that at a fixed flow temperature, an increase in the diffuser mass flow rate of around 4.5 % is sufficient to cause the melting ratio to change from 0 to 0.2.

These results demonstrate that tight control of the warm air temperature and flow rate through the diffuser will be required if natural melting of the ice particles is to be produced in a repeatable manner and within reasonable limits relevant to the ice crystal icing problem.

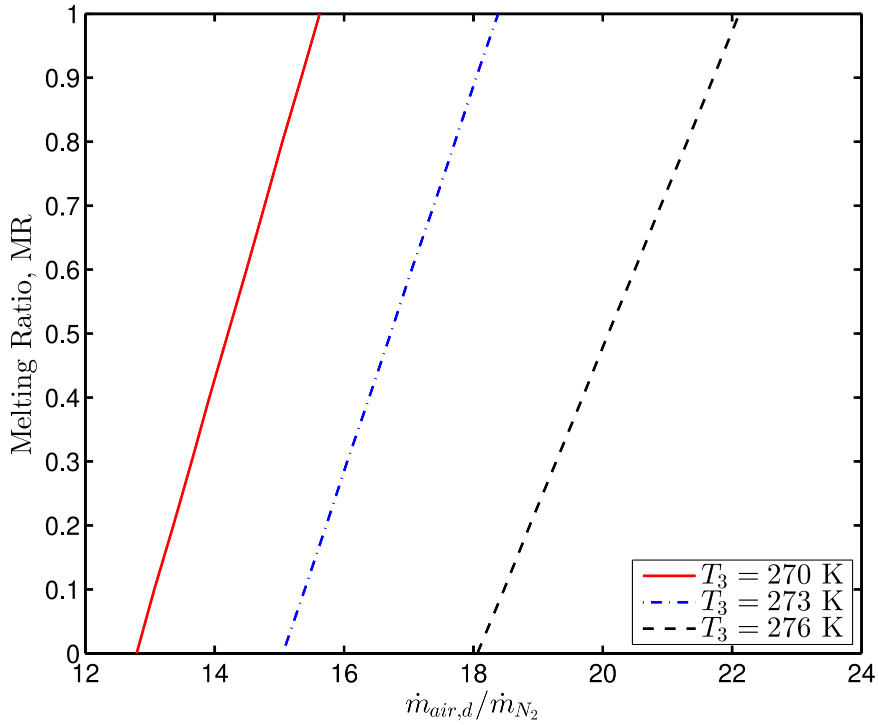


Figure 3.6: Variation of melting ratio with relative diffuser mass flow rate for $\dot{m}_{air,e}/\dot{m}_{N_2} = 0.9202$ and $\dot{m}_{H_2O}/\dot{m}_{N_2} = 0.2$.

Table 3.2: Sensitivity of melting ratio to $\dot{m}_{air,d}$.

| T$_3$ (K) | $\dot{m}_{air,d}/\dot{m}_{N_2}$ | | $\frac{\Delta \dot{m}_{air,d}}{\dot{m}_{air,d}}$ |
|---|---|---|---|
| | $MR = 0$ | $MR = 0.2$ | |
| 270 | 12.793 | 13.362 | 4.45 % |
| 273 | 15.189 | 15.858 | 4.4 % |
| 276 | 18.06 | 18.873 | 4.5 % |

## 3.6 Conclusion

A new wind tunnel facility for ice crystal icing research could provide a useful platform for fundamental experimental investigations and for development of theoretical models and simulation tools. Limitations of a small experimental facility which existed at USQ before the present investigation have been identified: it produced a relatively low flow speed and could not accommodate models with dimensions comparable to those used in other wind tunnels facilities. The concept outlined and analysed in this chapter seeks to provide a significant increase in the speed of the ice particle suspension and the cross sectional dimensions of the test section, and to simultaneously increase the concentration of ice particles and liquid water in the flow.

To assess the proposed arrangement, a conservation of energy analysis has been conducted. The conservation of energy analysis specifies that a mixture temperature equal to the liquid nitrogen saturation temperature (approximately 77 K) can be achieved when the mass flow rate of evaporator air is approximately 0.92 times the mass flow rate of liquid nitrogen. The analysis also demonstrates that using an air evaporator mass flow rate as high as 6.0 times the liquid nitrogen mass flow rate can still provide a cold environment, lower than approximately $-40°$C, to ensure freezing of the injected water droplets. Results indicate that the fully-mixed temperature in the test section achieves the ice melting temperature for total air mass flow rates (including the additional air introduced through the diffuser) of between 10 and 20 times the liquid nitrogen flow rates for wind tunnel operating values of IWC that are relevant to the ice crystal icing problem. However, if natural melting of the ice particles is to be achieved, then the mass flow rate of warm laboratory air introduced through the diffuser should be tightly controlled because the melting ratio increases from zero to 0.2 for diffuser air mass flow rate changes of approximately 4.5 %.

The thermodynamic performance of the facility is dictated largely by the availability of the liquid nitrogen and the proposed operating concept involves using a maximum of 20 litre of liquid nitrogen per run in the facility within 2 minutes. The analysis highlights that by controlling the mass flow rates in the evaporator, air introduced via the diffuser, and injected water content with respect to the mass flow rate of liquid nitrogen, a range of operating conditions relevant to the ice crystal icing problem can be generated. The results of the analysis indicate that the new icing wind tunnel concept is viable.

# Chapter 4

# Facility Design and Arrangement

## 4.1 Introduction

An icing wind tunnel has been established to simulate elements of the thermal and flow conditions associated with the ice accretion problem. The icing wind tunnel facility consists of two main parts. The first part is the icing jet generator which produces an artificial cloud consisting of ice particles suspended in a cold air flow. The second part is an open circuit, low speed wind tunnel which is used to provide a co-flowing stream in the test section. This tunnel has been designed to produce approximately spherical ice particles suspended in a cold air flow. These particles are generated by the freezing of approximately spherical liquid droplets at a temperature less than $-40\,^{\circ}$C. A probe traversing system has also been established to allow measurement of the distribution of the velocity, temperature and total water content in the test section. This chapter describes the elements of the new icing wind tunnel facility and its associated instrumentation.

## 4.2 Icing jet generator

### 4.2.1 Overview

To produce an artificial cloud that contains ice particles similar to those that exist in a natural cloud, it would be necessary to replicate the features of the ice crystals such as irregular crystal shapes and low density structures as well. Cloud particle morphology is not replicated generally for icing wind tunnel work. For icing wind tunnel tests, there are three common methods that have been used to generate the glaciated and mixed phase conditions: Rasp technology (an ice shaver method), snow gun methods, and cloud chamber technology (Al-Khalil, 2003; Baumert et al., 2015; Riley, 1999). Ice particle production is considered one of the most important aspects for any icing test and it can also be expensive, especially for high speed wind tunnels (Bansmer et al., 2018).

In the current application, ice production involves the use of spray nozzles to produce approximately spherical liquid droplets within a cold flow. Cold air at temperatures below $-40\,^{\circ}\mathrm{C}$ is provided to ensure liquid water droplets freeze. This can be achieved without the need for a dedicated refrigeration system if a source of liquid nitrogen is available. The cold stream is achieved by mixing between the air at room temperature and the evaporating liquid nitrogen. Water droplets are injected into the mixture of evaporated nitrogen and air in a manner that is intended to keep the droplets away from the walls of the pipe, at least until they are frozen. The flow temperatures and particles residence times are such that there is virtually no possibility of the liquid phase remaining. In the second stage, the multiphase flow of ice and cold air is diluted in a perforated diffuser which introduces air at approximately room temperature.

As shown from Figure 4.1, the icing jet generator consists of a diffuser, shell, nozzle contraction, spray guide pipe, ultrasonic atomiser nozzles, liquid nitrogen tank, liquid nitrogen dewar, pressurised water tank, and compressed air vessel.

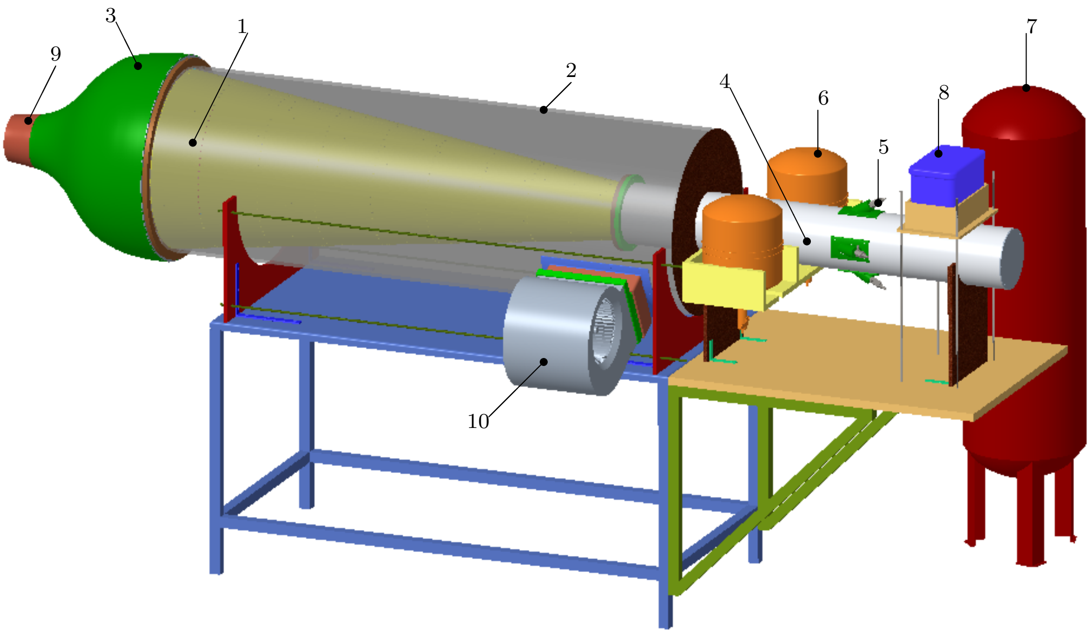


Figure 4.1: Icing jet hardware consisting of: (1) Diffuser; (2) Shell; (3) Nozzle Contraction; (4) Spray guide pipe; (5) Ultrasonic atomiser nozzle; (6) Pressurised water tank; (7) Compressed air vessel; (8) liquid nitrogen tank; (9) Contraction nozzle lip; and (10) Fan.

### 4.2.2 Conical Diffuser

The conical diffuser mixes air at approximately room temperature with the cold flow of evaporated nitrogen to provide a relatively cold stream to the wind tunnel. The ice particles are kept away from the walls of the chamber by injection of the air. The diffuser has been configured in the manner illustrated in Figure 4.2. Its performance was assessed through CFD (see Chapter 6, Section 6.3.2) and experimentally in a small prototype (see Appendix A) prior to fabrication of the full scale device.

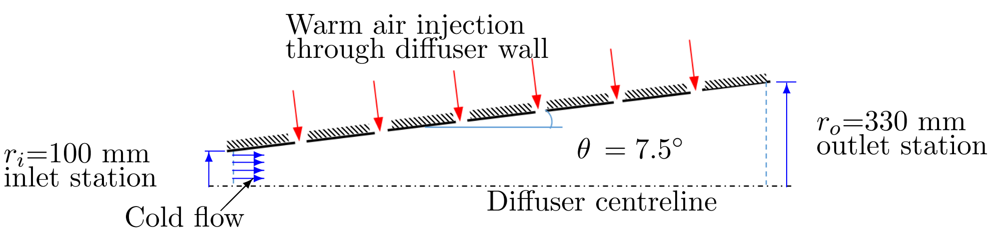


Figure 4.2: Schematic diagram of diffuser and the injection ports.

The diffuser is made from sheet metal, 0.7 mm thick. It includes two longitudinal halves which have been assembled together with rings to make a conical diffuser with two open ends as shown in Figure 4.3. The small end diameter is 200 mm, and the large end diameter is 660 mm. The length of the diffuser is 1747 mm and its divergence half angle is 7.5°. The assembled conical diffuser has 400 holes of 6 mm diameter distributed on its wall. The design of the diffuser is further discussed in Appendix B. The conical

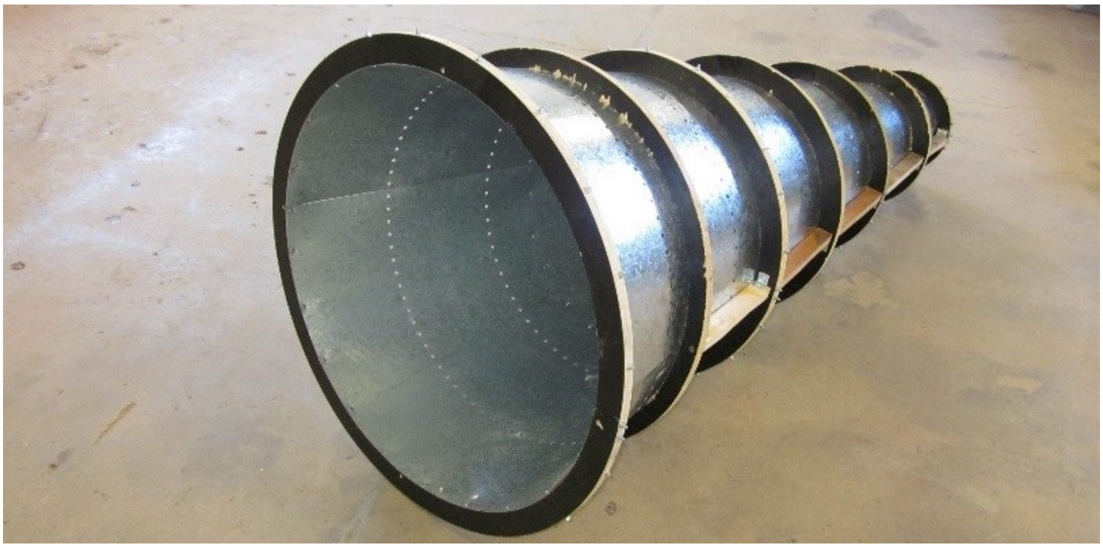

Figure 4.3: Photograph of conical diffuser assembly.

diffuser is held and sealed inside a Polyethylene shell with inner diameter of 663 mm, and length of 2060 mm. The shell receives air from a fan and distributes this air to the injection ports on the conical diffuser.

### 4.2.3 Nozzle contraction

The nozzle contraction is used to increase the flow velocity and to decrease the non-uniformity of the flow velocity at the exit of the jet. The features which are taken into account in contraction design are: the Contraction Ratio (CR), the contour shape, and contraction length. Also, the important criteria in the contraction design are: flow uniformity at the nozzle exit, available space and cost. The nozzle exit flow uniformity will be adversely affected if the nozzle boundary layer separates or the boundary layer thickness is large, so these are important considerations for the contraction design as well. For the current application, to achieve a short, non-separated nozzle contraction, two reverse cubic arcs connecting together have been chosen. According to Morel (1975), the cubic profile is very efficient.

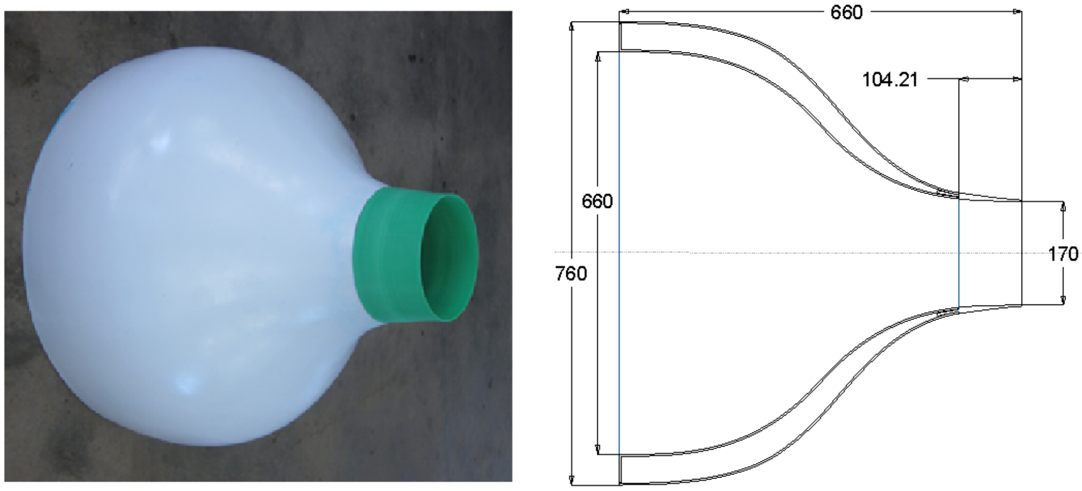


a b

Figure 4.4: Nozzle contraction. (a) Photograph; (b) sketch showing primary dimensions.

The contraction was made in fibre glass and it consists of two layers: an inner and outer layer and between them, a gap exists as shown in Figure 4.4. Two layers were used to achieve a smooth surface both on the inside and on the outside of the contraction. The nozzle contraction inlet has a diameter of 660 mm, and the exit has a diameter of 170 mm. The length of the contraction is equal to the inlet diameter of 660 mm. For details on the design, fabrication and assembly of the nozzle contraction, see Appendix C.

### 4.2.4 Fan

A centrifugal fan (Figure 4.5) is used to blow air from the laboratory into the shell of the icing jet generator. This fan is classified as a blower unit (DDG-270-360) which is a direct driven fan with forward-curved blades installed on the motor shaft. The airflow enters the fan via two inlets, drawing air from both sides of the fan, and this air flow also cools the motor. The fan selection proceeded based on the CFD results and preliminary tests of the icing jet generator. The maximum power consumption of the fan is about 750 W, and the maximum flow rate is around 1100 litre/s for atmospheric pressure output. The fan data sheet is provided in Appendix D. To attach the fan to the icing jet generator shell, a flexible duct adaptor was used. The adaptor duct shown in Figure 4.6, was produced using a 3D printer. The duct includes two parts joined together using a rubber layer which accommodated misalignment and acted to reduce

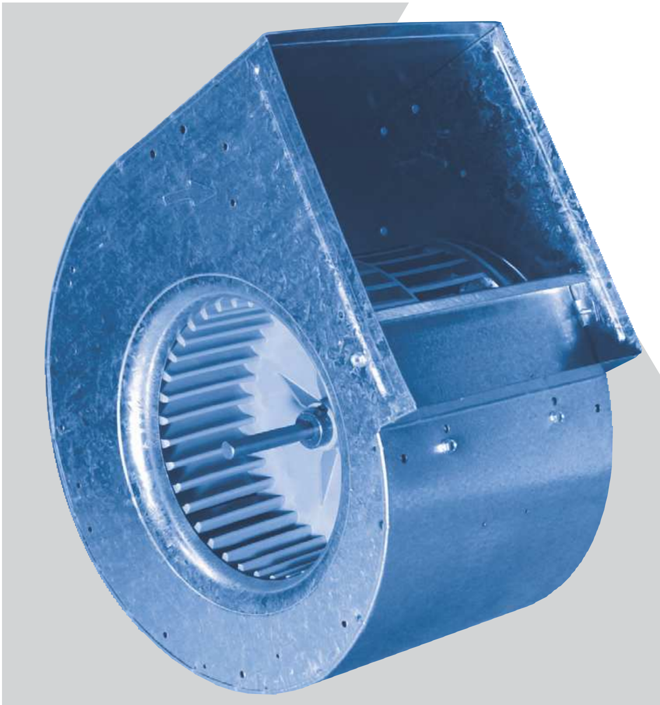

Figure 4.5: Photograph showing the centrifugal fan which is used to supply air to the shell of the generator (Torin Industries, www.torin.com.au).

the transmission of vibration. An assessment of the installed performance of the fan operating in conjunction with the perforated diffuser is presented in Appendix D. Results indicate that the mass flow rate generated by the fan in the installed configuration is approximately 0.6 kg/s, through based on assessment of the discharge coefficient for the perforated diffuser, a value of 0.49 kg/s is estimated.

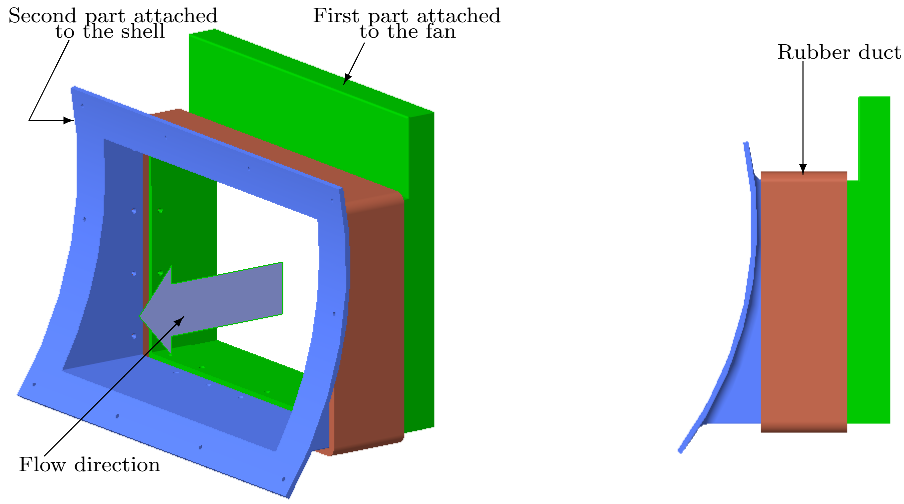


(a) (b)

Figure 4.6: Illustration of the flexible duct adaptor showing primary parts and flow direction. (a) Isometric view; (b) side view.

### 4.2.5 Spray guide pipe

The spray guide pipe was attached to the inlet of the conical diffuser via a flange and the other end was partially opened to allow the evaporator air to enter. PVC with an internal diameter of 203 mm and a length of 1500 mm and a wall thickness of 11 mm was used. The spray guide pipe has a hole with a diameter of 20 mm on the upper side for connection with the nitrogen receiver. Opposite this hole on the lower side and at the same axial location, a hole with a diameter of 18 mm was drilled to attach the stepper motor and its tethered shaft which is used to actuate the liquid nitrogen valve, as discussed in Section 4.2.6. Inside the spray guide pipe, evaporation of the liquid nitrogen first occurs, then water is injected through the atomising nozzles. The flow mixture drawn through this spray guide pipe is delivered into the conical diffuser.

### 4.2.6 Liquid nitrogen receiver and valve

The liquid nitrogen receiver and valve system is illustrated in Figure 4.7. The liquid nitrogen is supplied from a 20 litre insulated tank which is attached to the spray guide pipe. A valve has been added to the bottom of the tank in order to control the liquid nitrogen flow. During charging of the liquid nitrogen receiver, the valve is closed via two springs on the top of a plastic piston inside the plug holder. On the other face of the piston there is a rubber washer to prevent the leakage of liquid nitrogen from the receiver. The valve is opened by pushing the piston with a threaded shaft which moves in the upward direction. The liquid nitrogen flow rate can be controlled by using a stepper motor which is attached underneath the guide pipe and controls the threaded shaft movement in both the upward and downward directions. The stepper motor is driven by a micro-controller circuit (Arduino) to enable the opening and closing the plug to generate the desired flow rate.

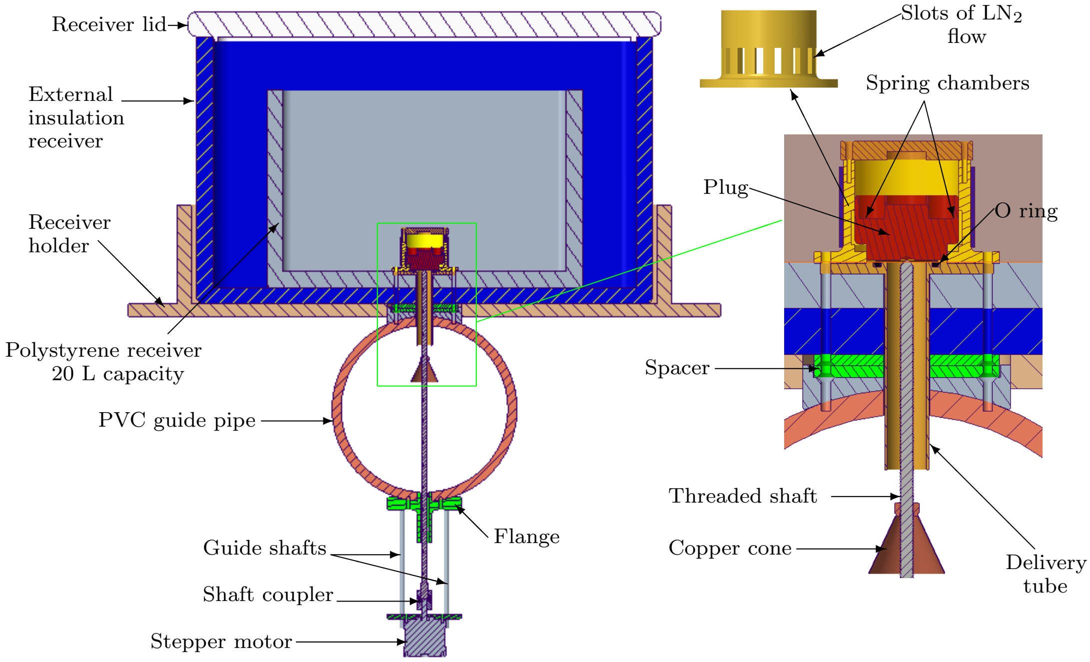


Figure 4.7: Liquid nitrogen receiver and valve.

Figure 4.8 illustrates a liquid flowing from the tank through one exit hole at the bottom. The outlet velocity of the liquid during drainage from the tank can be calculated as

$$u_e = \sqrt{2gy_l} \tag{4.1}$$

where $u_e$ is the instantaneous outlet velocity (m/s), $y_l$ is the instantaneous height of the liquid in the tank (m), and $g$ is the acceleration of gravity taken as $9.81\,\mathrm{m/s^2}$. The velocity of the liquid flowing out of the tank is dependent on the height of the liquid in the tank.

The instantaneous liquid volume flow rate $\dot{v}_e$ ($\mathrm{m^3/s}$) from tank exit is calculated as

$$\dot{v}_e = C_d A_e \sqrt{2gy_l} \tag{4.2}$$

where $C_d$ is the discharge coefficient for the orifice exit, and $A_e$ is the cross sectional area at the tank exit.

In the current study, the cross sectional area of the tank exit depends on the valve position which is controlled by a threaded shaft attached to the stepper motor. Figure 4.8 illustrates the valve opening area at the tank exit. The open area is the perimeter of the exit hole multiplied by the gap between the piston and the lower seal and can be calculated as

$$A_e = \pi d_e y_{sh} \tag{4.3}$$

where $d_e$ represents the exit hole diameter, and $y_{sh}$ is the gap height between the piston and the hole surface. The valve of $y_{sh}$ was controlled by the threaded shaft's upward displacement. The value of $A_e$ becomes independent of the shaft movement when the shaft axial displacement is such that $A_e$ reaches the maximum limit corresponding to the annular area between the hole and shaft cross sectional area which is given by

$$A_{e,max} = \frac{\pi}{4}\left(d_e^2 - d_{sh}^2\right) \tag{4.4}$$

where $d_{sh}$ is the threaded shaft diameter.

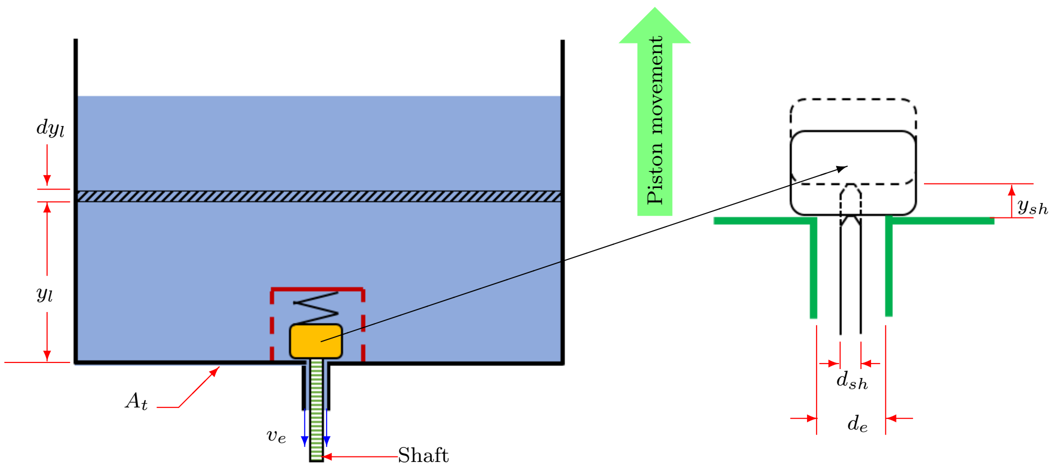


Figure 4.8: Schematic diagram of liquid flowing from receiver through the valve.

The liquid volume flow rate is also equal to the rate of decrease in the tank liquid volume with time and can be expressed as

$$\dot{v_e} = -A_t \frac{dy_l}{dt} \tag{4.5}$$

where $A_t$ is the tank base area. The drainage time between any particular state 1 and state 2 can be obtained by equating Equation 4.5 and Equation 4.2 and integrating

$$t_2 - t_1 = \sqrt{\frac{2}{g}}\frac{A_t}{C_d A_e}\left(\sqrt{y_{l,1}} - \sqrt{y_{l,2}}\right) \tag{4.6}$$

Taking an instantaneous valve opening at $t_1 = 0$ and the initial height of the liquid in the tank to be $y_{l,1} = h_l$, the instantaneous height of the liquid in the tank $y_l$ at time $t$ after valve opening can be written as

$$y_l = \left(\sqrt{h_l} - C_d\frac{A_e}{A_t}t\sqrt{\frac{g}{2}}\right)^2 \tag{4.7}$$

For an initial liquid height of $h_l = 0.216\,\mathrm{m}$ corresponding to 18 litres of liquid nitrogen initially in the tank, $d_e = 15.4\,\mathrm{mm}$, $d_{sh} = 5.6\,\mathrm{mm}$, $A_t = 0.08334\,\mathrm{m}^2$ (corresponding to the physical values of the apparatus), and $C_d = 0.81$ corresponding to the discharge coefficient for a short tube orifice (Dally et al., 1993), the liquid volume flow rate variation for different valve openings is illustrated in Figure 4.9, and the liquid volume variation with time is illustrated in Figure 4.10.

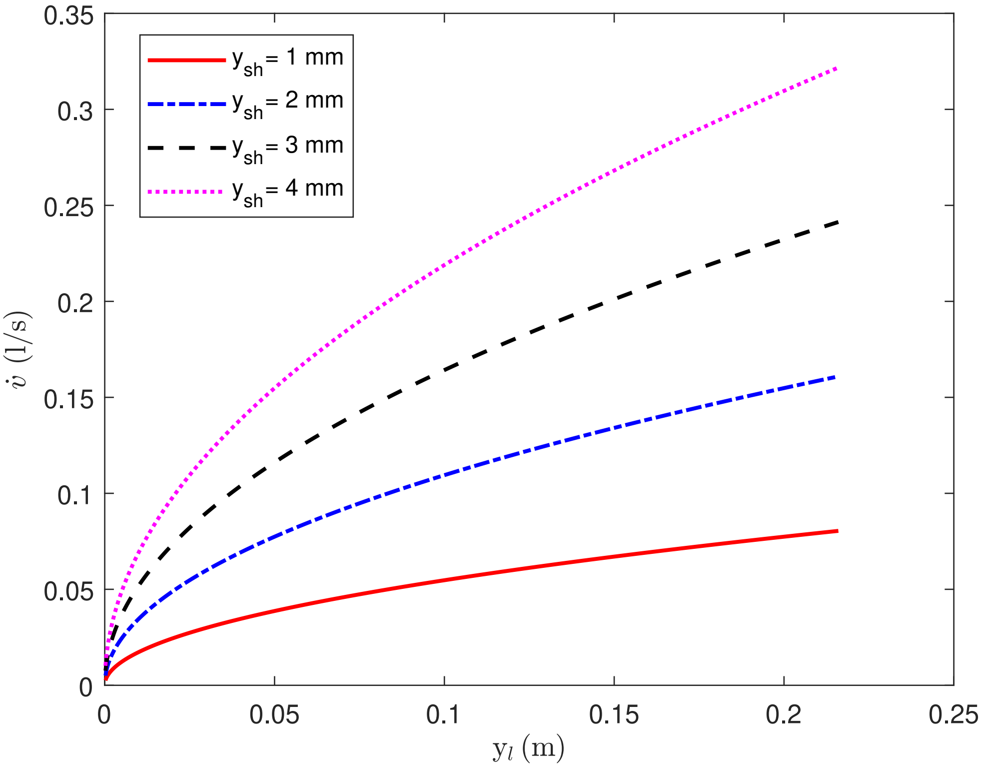


Figure 4.9: Variation of liquid volume flow rate with the liquid level in the tank at different valve openings.

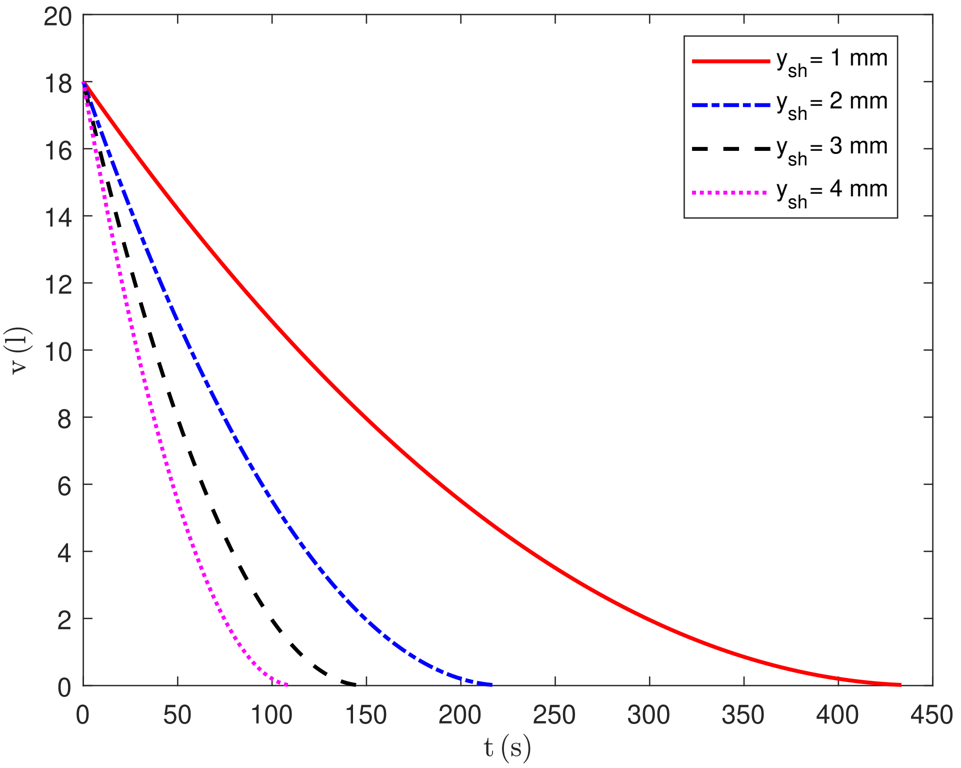


Figure 4.10: Variation of liquid volume with time at different valve area openings.

The opening area of the valve for different values of the shaft movement (the gap between the piston and the hole face) is presented in Table 4.1.

Table 4.1: Valve opening area corresponding to the shaft displacement.

| $y_{sh}$ (mm) | $A_e$ (mm$^2$) |
|---|---|
| 0 | 0 |
| 1 | 48.4 |
| 2 | 96.8 |
| 3 | 145 |
| 4 | 193.5 ($A_{e,max}$) |

The liquid nitrogen receiver and its valve were tested experimentally, initially using 15 litre of water having a height of 0.18 m. Experimental volume flow rates were obtained from

$$\dot{v}_{exp} = \frac{v_{flow}}{t} \tag{4.8}$$

where $v_{flow}$ is the water volume delivered from the receiver, and $t$ is the measured time period over which this volume was delivered. The experimental results are presented in Table 4.2.

Table 4.2: Experimental data of liquid volume flow rate flowing from the liquid nitrogen receiver operating with water and comparison with theoretical results for $v = 15$ litre.

| $y$ (mm) | $v_{flow}$ (l) | $t$ (s) | $\dot{v}_{exp}$ (l/s) | $\dot{v}_{th}$ (l/s) | error (%) |
|---|---|---|---|---|---|
| 1 | 1.75 | 23.88 | 0.0733 | 0.0734 | 0.14 |
| 2 | 1.9 | 14 | 0.1357 | 0.1469 | 7.62 |
| 3 | 3 | 14 | 0.214 | 0.2203 | 2.86 |
| 4 | 3.1 | 11.5 | 0.269 | 0.2937 | 8.41 |

Theoretical results from the above analysis are also presented in Table 4.2 and it is observed that there is generally a very good agreement between the experimental data and the analysis, with errors less than 10 %.

Flow rate experiments were also performed using liquid nitrogen. Figure 4.11 presents

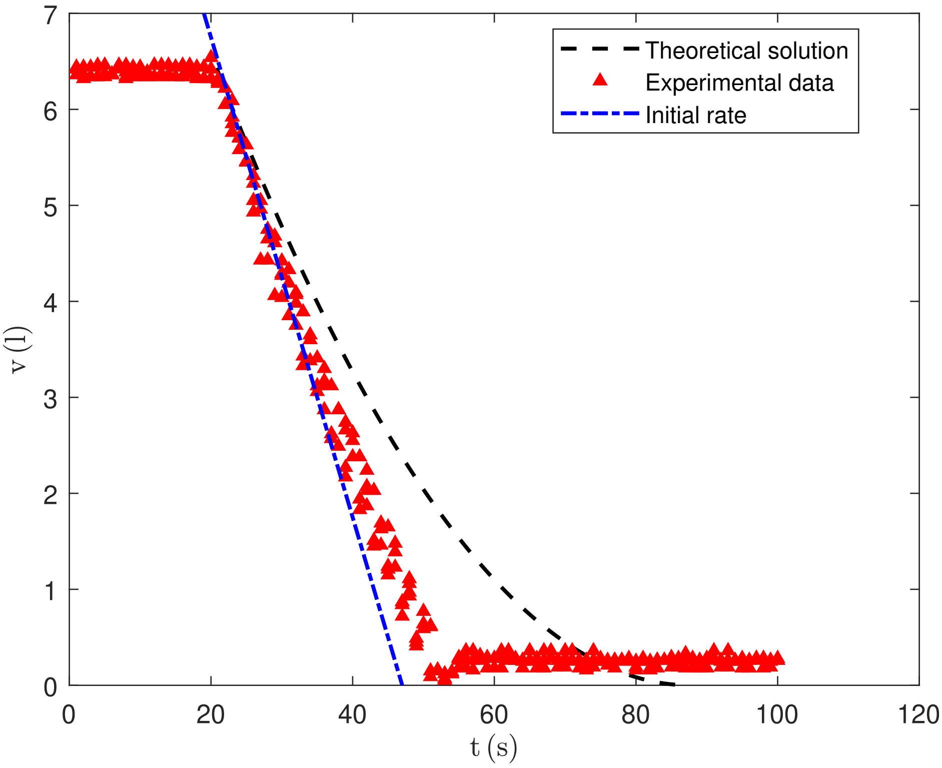


Figure 4.11: Experimental data of liquid nitrogen consumption for an experiment with an initial volume of 6.6 litre of nitrogen and at fully-opened valve area.

the experimental data of liquid nitrogen delivery during a test in which the liquid level was recorded using an ultrasonic distance sensor. The initial amount of liquid nitrogen in the tank was approximately 6.6 litre before opening the valve. The valve was then opened fully so that the open area was specified by $A_{e,max}$. As shown in Figure 4.11, the initial volume flow rate in this case is approximately 0.191 litre/s. This compares favourably with the theoretical value of 0.195 litre/s for a level of 0.079 m corresponding to an initial volume of 6.6 litre. However from Figure 4.11 it is noted that the experimentally measured flow rate remains more constant than the theoretical results. The accuracy of the ultrasonic sensor measurement reduces when using a larger volume of liquid nitrogen, so reliable ultrasonic sensor results are not currently available for initial volumes approaching 18 litre.

Results in Table 4.2 show the theory over-predicts flow rate by up to 10% for volumes of 15 litres, but Figure 4.11 shows the theory increasingly under-predicts the flow rate as the remaining volume become smaller than 6 litres. These errors are attributed to the following sources. (1) The discharge coefficient in the theoretical analysis has been chosen from a textbook for a related configuration which may not be entirely appropriate for the current configuration and could comfortably account for the over-prediction of flow rate for the higher volumes. (2) The suction due to the wind tunnel fan causes a sub-atmospheric pressure in the evaporator region, and this effect has not been accommodated in the theoretical analysis. This effect tends to increase the volume flow rate, and has a larger relative significance for smaller liquid volumes which have a smaller gravity head.

### 4.2.7 Liquid nitrogen evaporator

To evaporate the liquid nitrogen delivered from the receiver into the spray guide pipe, a thin sheet copper heat exchanger was placed inside the guide pipe immediately below the liquid nitrogen tank orifice. The evaporator contains trays, sheet fins and a cone head (to deflect the falling liquid nitrogen onto the first tray) as shown in Figure 4.12. Copper has been used in the construction to maximise the heat transfer from the air to the liquid nitrogen, and 0.1 mm thick foil has been used to minimise thermal inertia. Once the valve opens and the liquid nitrogen flows from the liquid nitrogen receiver tank, the liquid nitrogen cascades to separate trays of the heat exchanger. Experimental assessment of this configuration indicated that modifications were required to eliminate pooling of the liquid nitrogen at the bottom of the PVC pipe (the spray guide pipe) and to improve temperature uniformity at the exit of the diffuser contraction. Therefore, an additional upper tray was fabricated from the copper sheet and added to the heat exchanger as shown in Figure 4.12 (b). The surface of the upper tray was perforated to allow the liquid nitrogen to cascade to the other copper trays in a more controlled manner. By this method, the liquid nitrogen was detained in the upper layer and liquid accumulation at the bottom of the PVC pipe was eliminated. Figure 4.12 (c) shows the heat exchanger installed in the PVC pipe.

The entrance of the spray guide pipe is partially closed by a circular acrylic cap as shown in Figure 4.13 to enable viewing of the liquid nitrogen evaporation and water injection process. The cap has 44 holes each with a diameter of 12 mm distributed across the cap to allow the evaporator air to enter the system. To estimate the evaporator air flow rate

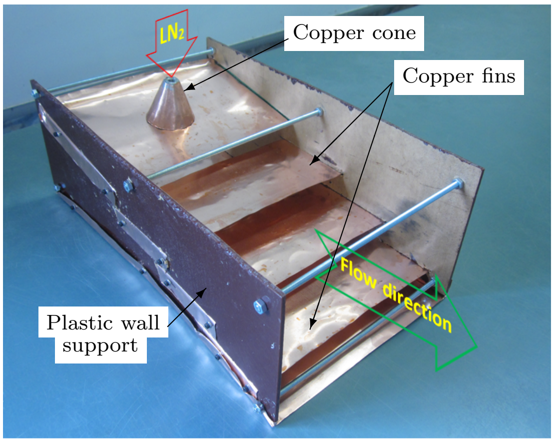


(a)

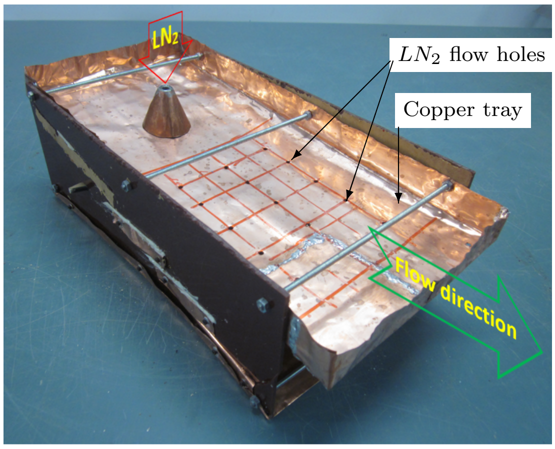


(b)

(c)

Figure 4.12: Photographs showing the heat exchanger which is placed inside the guide pipe and is used to evaporate the liquid nitrogen. (a) Before enhancement with upper tray; (b) after enhancement with upper tray; and (c) heat exchanger installed in the PVC pipe.

through the perforated entrance plate, the pressure drop across the perforated entrance plate was measured and a correlation for the perforated plate discharge coefficient was applied, as presented in Appendix E. The resulting mass flow rate of air was found to be $\dot{m}_{air,e} = 0.177\,\mathrm{kg/s}$.

Figure 4.13: Evaporator entrance showing 44 holes distributed on the acrylic cap through which laboratory air enters.

The minimum evaporator air flow rate required for complete evaporation of the liquid nitrogen is given by $\dot{m}_{air,e}/\dot{m}_{N_2} = 0.92$, according to the conservation of energy analysis presented in Chapter 3, Equation 3.7. The maximum anticipated liquid nitrogen consumption for the facility is 0.135 kg/s, corresponding to 20 litres of liquid nitrogen being consumed in 2 minutes. For such a flow rate of nitrogen, the minimum air flow rate is therefore 0.124 kg/s whereas, for the present perforated plate on the evaporator inlet we have $\dot{m}_{air,e} = 0.177$ kg/s, which provides a significant margin for the evaporator not fully-utilising the inlet air flow in the evaporation process. At the present operating condition, we have an excess air flow of approximately 30 % above the minimum (thermodynamic) value required for the target nitrogen mass flow rate of 0.135 kg/s.

### 4.2.8 Water injection

The injected water droplets are produced using atomiser nozzles (PNR Nozzles model MAD 0301 B1), one of which is illustrated in operation in Figure 4.14. Three ultrasonic atomiser nozzles are attached to the spray guide pipe to supply the water droplets. Each nozzle is set separately in a holder which is 3D printed. The atomised water is injected at an angle of 30° to the axis of the spray guide pipe as shown in Figure 4.15. Each nozzle is fed with compressed air and pressurised water. To control the droplet size and water content delivered into the spray guide pipe, adjustment of the air and water pressure in each nozzle is required. The pressurised air is supplied from the compressed air vessel which has a 2.2 $m^3$ capacity with maximum operating pressure of 12 bar. The distilled water is supplied from the pressurised water tank of 18 litre capacity with a maximum operating pressure of 10 bar. The droplets generated by the nozzles change phase when those liquid droplets deliver heat to the evaporated mixture of nitrogen and air. For more details of the atomiser nozzle, the data sheet is provided in Appendix F.

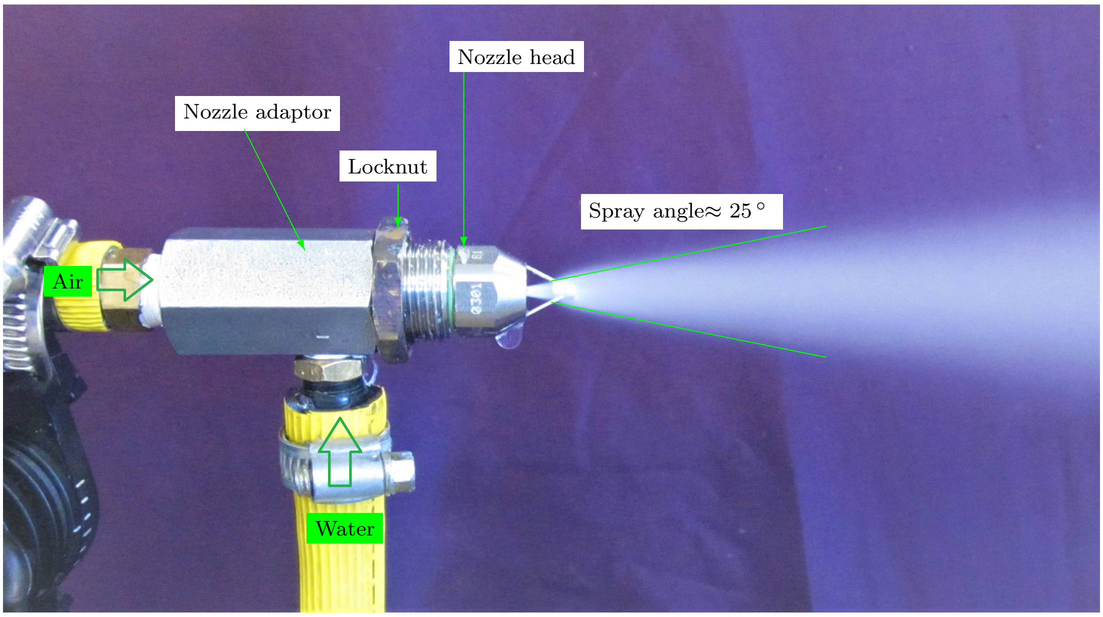


Figure 4.14: Photograph showing ultrasonic atomiser nozzle parts and the spray angle.

The atomiser nozzles were tested with different inlet pressures for both the air and the water supply lines. The supplied air pressure ranged between 3 and 6 bar pressure, and the water pressure ranged between 1 and 5 bar. Table 4.3 presents the variation of air and water flow rates with both air and water pressures. The air volume flow rates which

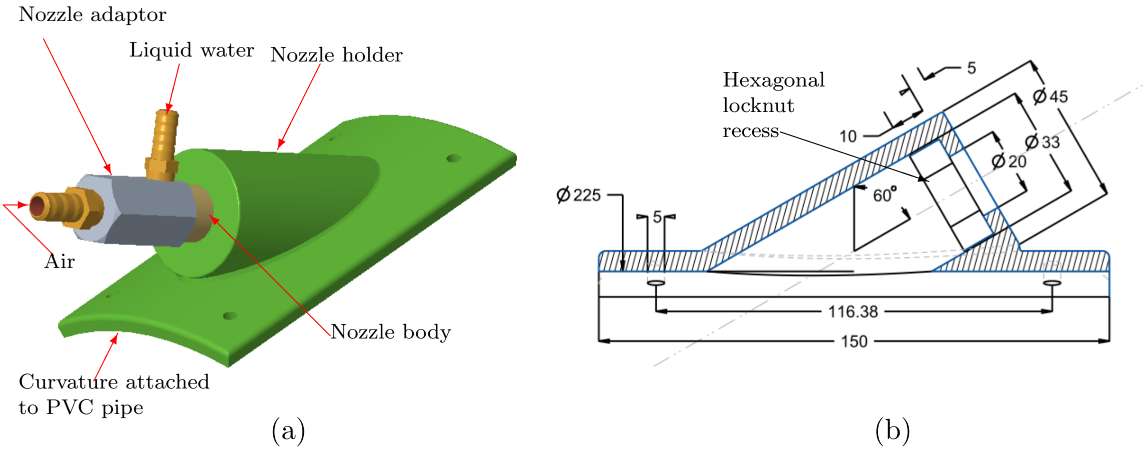


Figure 4.15: Ultrasonic atomiser nozzle holder. (a) Assembly showing atomiser nozzle and 3D printed holder; (b) Sketch showing nozzle holder dimensions.

are presented in Table 4.3 were measured at the elevated pressure and represents the air volume flow rate entering the ultrasonic nozzle, before expansion to the guide pipe pressure. As shown in Table 4.3, at a given air pressure, the water flow rate increases with increasing water pressure, but the air flow rate decreases.

Table 4.3: Experimental data on the total water and air flow rate through three atomiser nozzles for different supply pressures.

| | Air pressure (bar) | | | | | | | |
|---|---|---|---|---|---|---|---|---|
| Water pressure (bar) | 3 | | 4 | | 5 | | 6 | |
| | Air (LPM) | Water (LPM) | Air (LPM) | Water (LPM) | Air (LPM) | Water (LPM) | Air (LPM) | Water (LPM) |
| 2 | 21 | 0.84 | 25.3 | 0.72 | 26.6 | 0.64 | 26.5 | 0.62 |
| 3 | 13.6 | 0.91 | 19.6 | 0.73 | 25 | 0.66 | 25.7 | 0.64 |
| 4 | 5.6 | 1.81 | 13.8 | 1.08 | 21.3 | 0.76 | 24 | 0.7 |
| 5 | N/A | N/A | 7 | 1.73 | 19.5 | 0.86 | 20.5 | 0.8 |

With regard to the target operating conditions of the facility as described in Chapter 3 and Table 3.1, if $\dot{m}_{N_2} = 0.135\,\mathrm{kg/s}$ and for $\dot{m}_{H_2O}/\dot{m}_{N_2} = 0.15$ (giving a water concentration of approximately $10\,\mathrm{g/m^3}$), then the mass flow rate of water should be $\dot{m}_{H_2O} = 0.02\,\mathrm{kg/s}$ or 1.2 LPM. In Table 4.3, the maximum volume flow rate was measured to be 1.81 LPM when using pressurised air at 3 bar and pressurised water at 4 bar.

Thus the target water mass flow rate is within the capabilities of apparatus when using three atomiser nozzles.

In the study by Saleh (2013), the same type of atomiser nozzle was used, and samples slides of the droplets generated by the atomiser nozzle were analysed using image analysis software to characterise the particle size and distribution. The total number of the particles was more than 100 particles for most samples and the total number of particles was between 4000 and 5000. In future work, a larger sample size should ideally be obtained for improved statistical reliability. The samples were collected at different operating conditions of the nozzle: air pressure between 3.5 and 5.5 bar, and water pressure between 2.8 and 4.2 bar. The tests were conducted at 23 °C, the ambient temperature. Figure 4.16 shows the droplet size distribution histograms from the Saleh (2013) study and Table 4.4 presents statistical results for the average droplet diameter (MVD) and standard deviation for different air and water supply pressures. As shown in Figure 4.16 and reflected in Table 4.4, the size of droplets typically varied between 20 $\mu$m and 260 $\mu$m and smaller droplet sizes tend to be produced at the higher operating pressures.

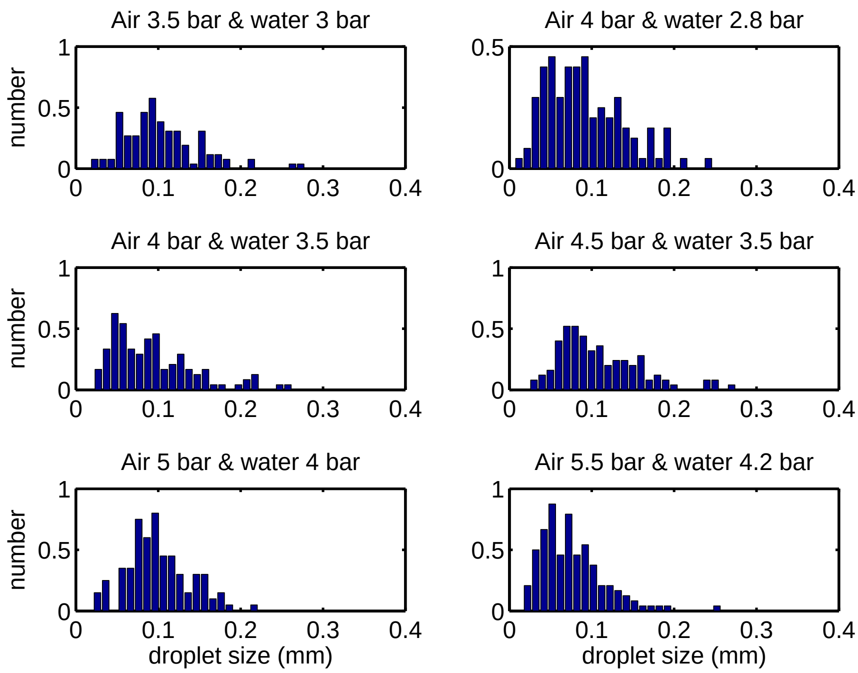


Figure 4.16: Droplets size distribution histograms for different nozzle operating pressures (Saleh, 2013).

Table 4.4: Statistical data for average water droplet diameters generated by the atomiser nozzle for different supply pressures.

| Air pressure (bar) | Water pressure (bar) | MVD ($\mu$m) | STD ($\mu$m) |
|---|---|---|---|
| 4 | 2.8 | 92 | 47.5 |
| 3.5 | 3 | 104 | 46 |
| 4 | 3.5 | 94 | 51 |
| 4.5 | 3.5 | 108 | 49.7 |
| 5 | 4 | 100 | 37.7 |
| 5.5 | 4.2 | 76 | 38.8 |

## 4.3 Wind tunnel

A low speed, open circuit wind tunnel that was used for undergraduate teaching at USQ became available for research during the current project. In its original configuration as shown in Figure 4.17, the wind tunnel consisted of several distinct sections: entrance (bell mouth and contraction duct), test section, settling chamber, diffuser, fan, and silencer. The area ratio of the contraction is 6.4. The test section is square with dimensions of $0.3025 \times 0.3025$ m and a length of 0.61 m. The entrance to the diffuser has a square cross section with dimensions of $0.32 \times 0.32$ m and it is attached to the connecting part between the diffuser and the test section. The diffuser exit has a circular cross section with diameter of 0.508 m. In its original configuration the wind tunnel also has two honeycomb sections (one in the entrance section and the second before the fan) and three screen meshes located before the contraction duct. The fan is a centrifugal type driven by a 10 hp, 3 phase motor. Further features of the wind tunnel are shown in Table 4.5.

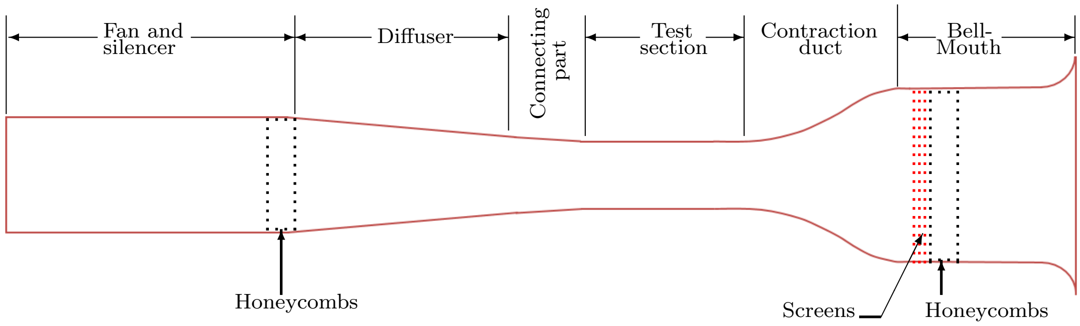


(a)

(b)

Figure 4.17: Wind tunnel in its original configuration. (a) Illustration of components; (b) photograph of arrangement.

Table 4.5: Dimensions and features of wind tunnel sections.

| **Sections** | **Shape** | **Dimensions / Specifications / notes** |
|---|---|---|
| Conventional bell-mouth inlet | 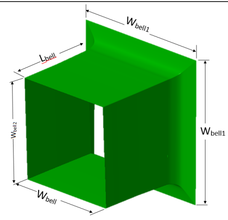 | $W_{bell1}$=1.08 m<br>$W_{bell2}$=0.75 m<br>$L_{bell2}$=0.55 m<br>Not used in icing Exp. |
| Conventional contraction duct | 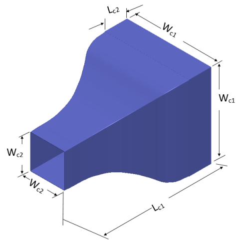 | $W_{c1}$=0.75 m<br>$W_{c2}$=0.3025 m<br>$L_{c1}$=1.11 m, $L_{c2}$=0.2 m<br>Not used in icing Exp. |
| Icing bell-mouth inlet | 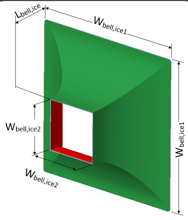 | $W_{bell,ice1}$=0.9 m<br>$W_{bell,ice2}$=0.3025 m<br>$L_{bell,ice}$=0.311 m<br>Used in icing Exp. |
| Test section | 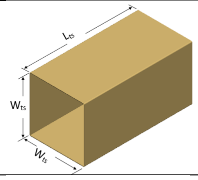 | $W_{ts}$=0.3025 m<br>$L_{ts}$=0.61 m |
| Connecting part between the test section and the diffuser | 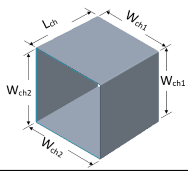 | $W_{ch1}$=0.3025 m<br>$W_{ch2}$=0.32 m<br>$L_{ch}$=0.3 m |
| Diffuser | 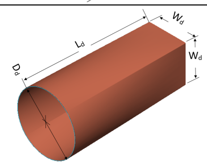 | $W_d$=0.32 m<br>$D_d$=0.508 m<br>$L_d$=1.07 m |
| Fan and motor |  | Centrifugal fan 10 hp motor 3 phase. |
| Honeycombs | 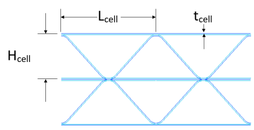 | 2 layers, thickness of 0.1 m<br>$H_{cell}$=14 mm , $L_{cell}$=25 mm<br>$t_{cell}$=0.75 mm |
| Screens | 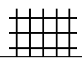 | 3 layers, thickness of 1 mm |

Two options were considered for integration of the cloud generator with the wind tunnel duct, as illustrated in Figure 4.18. In Option 1, the cloud generator delivers either a relatively low speed cold flow into the inlet of the existing contraction without the screens installed, or a relativity long contraction nozzle is designed for the cloud chamber to deliver the cold flow into the test section of the existing, conventional inlet. In Option 2, a short contraction nozzle is used on the cloud generator and a higher speed cold flow is delivered directly into the test section.

Changing the cold-flow path length between the ice flow injection exit and the test section could be used to control the melting of ice particles, and the the NRC RATFac (described in Section 2.4.5) uses such an approach. However, in this work the control of particle melting is intended to be performed by the perforated diffuser. Further mixing with the air at room temperature in the laboratory should not be needed. In either version of Option 1, a significant fraction of the cold flow will be lost through mixing layer or boundary layer entrainment, resulting in an inefficient use of the available cooling capacity. Therefore, Option 2 has been adopted for the present work, but this has required the fabrication of a new bell mouth inlet for the wind tunnel.

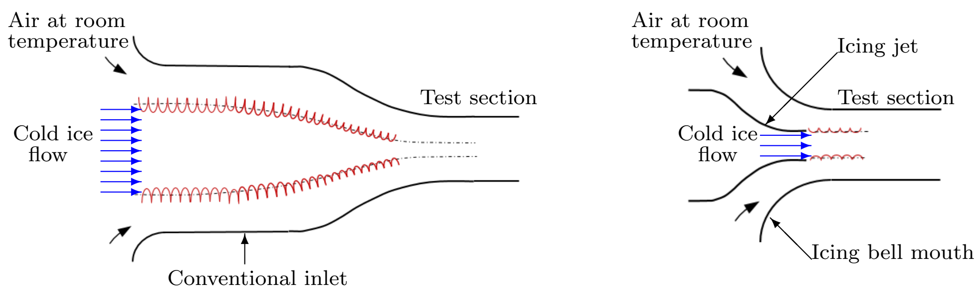


(a) Option 1. (b) Option 2.

Figure 4.18: Schematic diagram showing two possible arrangements for providing cold flow to the wind tunnel.

The new bell mouth was designed to be compatible with the ice generator contraction. The downstream end of bell mouth must attach to the test section which has dimensions of 302.5×302.5 mm and the intake size is also limited by the base frame of the wind tunnel. The profile of the bell mouth in cross section view was chosen based on the outer layer profile of the ice generator contraction nozzle such that the available cross sectional flow area continuously decreased as the flow progressed in the downstream direction.

To assess the performance of the proposed new bell mouth prior to fabrication, a CFD study of the proposed configuration was performed as described in Chapter 6, Section 6.5.3. The profile of the new bell mouth is illustrated in Figure 4.19. The bell mouth has a contraction ratio of 8.85. After confirming the validity of the new configuration through CFD, the new bell mouth was fabricated from fibreglass having a finished thickness of approximately 5 mm. The new bell mouth was attached to the wind tunnel test section to complete the full facility as shown in Figure 4.20.

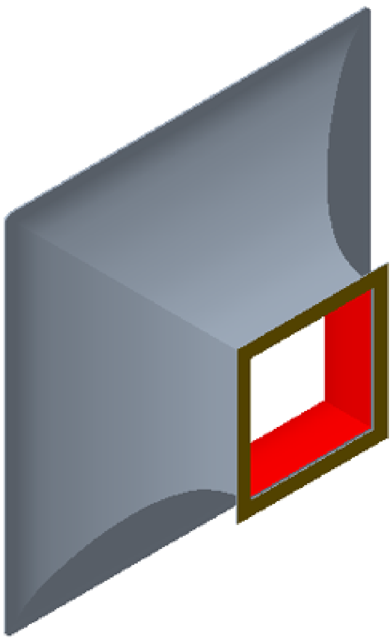

(a)

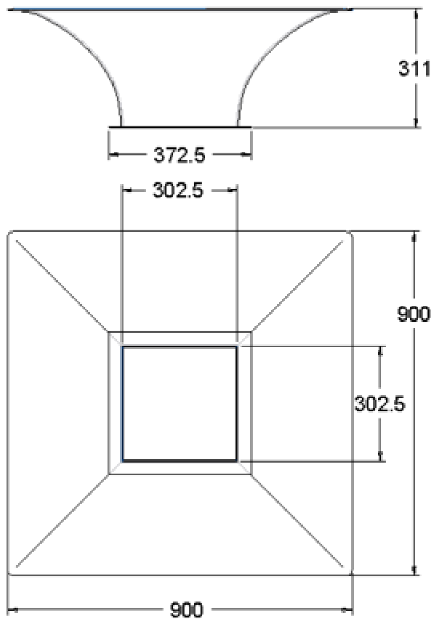


(b)

Figure 4.19: Icing bell mouth configuration. (a) View of solid model; (b) sketch showing primary internal dimensions.

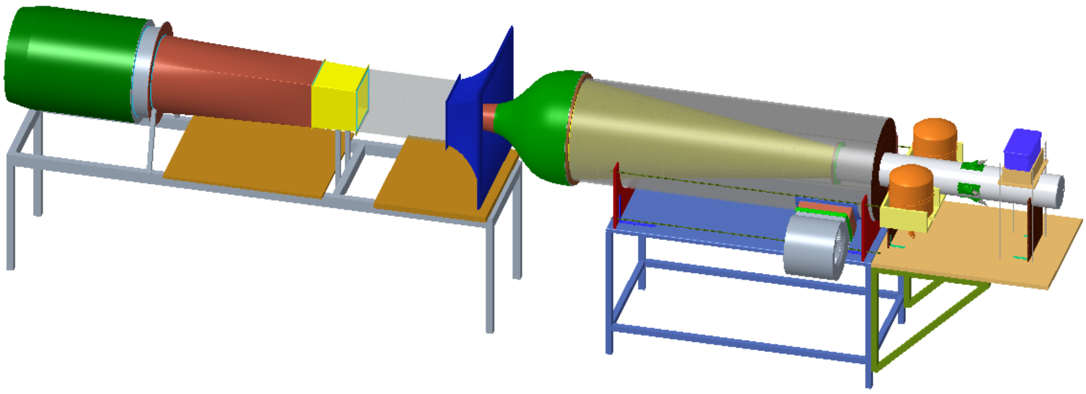

Figure 4.20: Solid model illustrating the full facility.

## 4.4 Instrumentation

### 4.4.1 Pitot probe

A pitot probe was used to measure the local flow speed in the wind tunnel test section. The pitot probe consists of pitot and static pressure ports, a differential pressure sensor, connecting silicon tubes, brass tubes and either an Arduino Uno board or an amplifier board, depending on the type of pressure sensor that was used. The pitot-static pressure tube which is used in the current experimental work is very similar to the modified pitot static tube used in the study of Salter et al. (1962). Salter et al. (1962) suggested the selection of either a long distance of the static pressure holes from the upstream end in the case of a probe nose of arbitary shape, or a suitably designed nose for a somewhat shorter length from the nose to the static ports. In the current study, the Ardupilot Arduplane Pitot static tube (APM−2.5/2.6) with ellipsoid nose has been used, see Appendix G for further information.

Initial differential pressure measurements were performed using a differential sensor type MPXV-7002DP which was attached to the pitot-static tube. For the initial measurements, an Arduino Uno board was used and Appendix G provides further information on this arrangement. To improve the response of the measurement system, a Honeywell SDX series differential pressure sensor was used in subsequent testing. The response time of the SDX series is specified as around 100 $\mu$s (see the data sheet in Appendix G) but in the present implementation, measurement system response time will be dictated by the filling and discharge times of the pressure tubing. Calibration of the pressure sensors used in this work is also described in Appendix G.

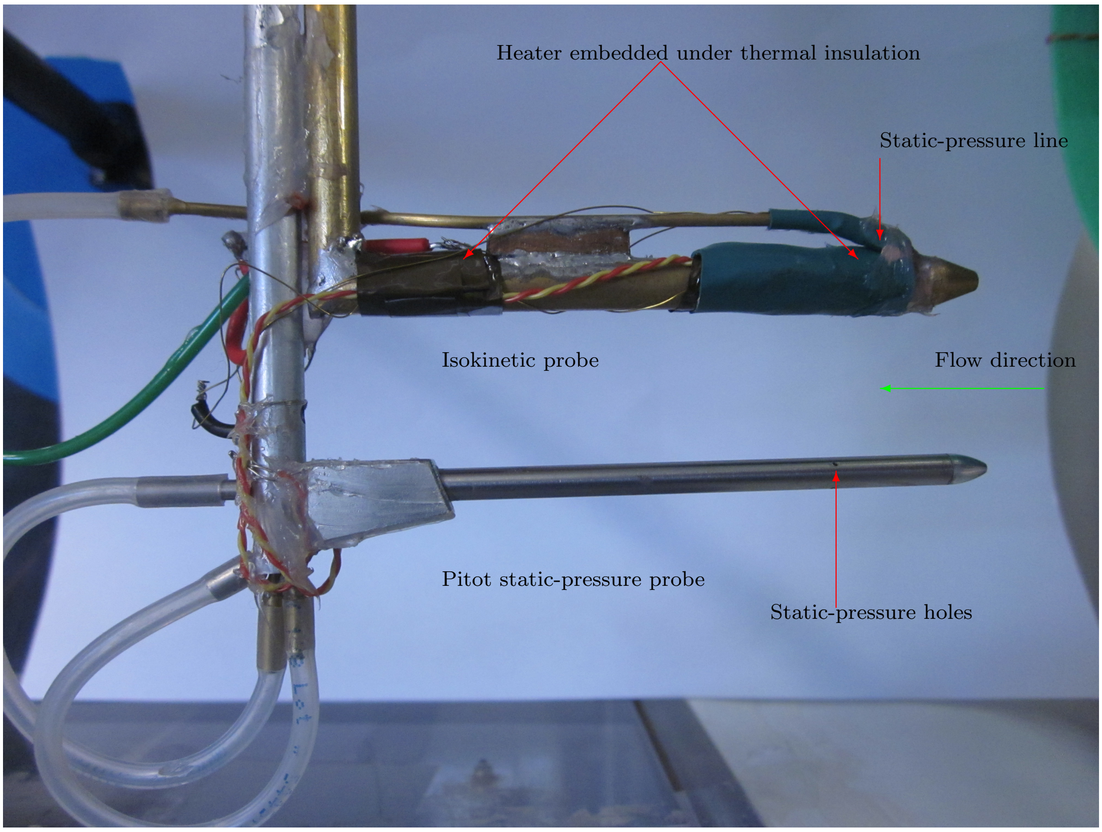


Figure 4.21: Photograph of isokinetic probe and pitot probe installed in the test section.

### 4.4.2 Isokinetic total water content probe

#### 4.4.2.1 Arrangement

One of the the most important measurements relating to icing problems and icing wind tunnels is the Total Water Content (TWC), which is the sum of the Ice Water Content (IWC), the Liquid Water Content (LWC), and the water vapour content associated with the air humidity. The water content, be it the vapour, liquid, or solid forms, expresses the mass concentration of water, typically in grams per cubic meter of air.

A range of different instruments have been used for measuring liquid and total water content in clouds, but not all of these are suitable for use in icing wind tunnels, because of their size as well as accuracy in some cases. Water content instruments include hot wire LWC instruments (Johnson-Williams, CSIRO-King, and Nevzorov instruments), optical probes, icing blade, rotating cylinder, and droplet sizing probes (Abel et al., 2014; Ide, 1999). These devices typically have a low and/or uncertain capture efficiency (Davison et al., 2009), and this might cause the IWC to be under-estimated by a factor of around 3 in some circumstances (Korolev et al., 2013). In the optical probe case, the device was developed to measure LWC only (Rudoff et al., 1993; Gerber et al., 1998). Over last decade, The National Research Council of Canada has developed an isokinetic total water content probe in an effort to improve the accuracy of TWC measurement (Davison et al., 2008, 2009, 2017).

The Iso-Kinetic Probe (IKP) design which was developed for this study is similar to that used in the study of Davison et al. (2009). As shown in Figure 4.22, the main parts of the IKP are: the probe intake, brass delivery tube, heater, insulation layer, intake static pressure tube, air flow-meter, differential pressure sensor, hygrometer with probe, and a vacuum device. The probe intake arrangement which is presented in Figure 4.23, includes a diffuser for flow dynamic pressure recovery. A trace heating wire is wrapped around the tube near the inlet region of the probe and in the 90 degree junction to heat the intake of the probe and prevent ice built up near the intake and to evaporate liquid and solid forms of water entering the intake. To measure the temperature of the IKP when operating, a K-type thermocouple was embedded under the trace heater.

The flow into the probe is drawn through the brass tube and then through the hygrometer probe (Tinytag Thermohygrometer, $\pm 1°$C, and $\pm 3\%$ RH) to measure the psychrometric properties of the flow. A choke on the suction device is adjusted so that probe draws a flow rate such that the flow speed entering the probe is the same as that in the undisturbed free stream flow in the test section. In this manner, the so-called iso-kinetic inlet flow conditions can be achieved. The required volume flow rate can be calculated based on the intake probe cross section area, and the flow rate can then be adjusted depending on the reading from air flow-meter which is installed in the tubing after the hygrometer. As an independent check on whether iso-kinetic conditions have been achieved, the static pressure measured on the IKP inlet is compared with static pressure of pitot tube using a differential pressure sensor.

Measurements performed with the hygrometer under the typical operating conditions

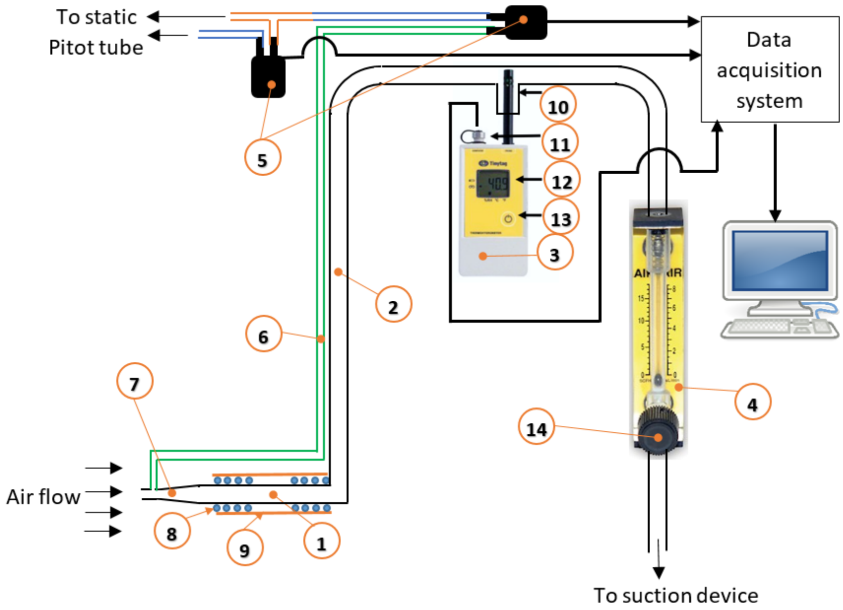


Figure 4.22: Schematic diagram of isokinetic probe (IKP) and its components. (1) IKP body; (2) Brass delivery tube; (3) Hygrometer; (4) Air flow-meter; (5) Differential pressure sensors; (6) Intake static pressure tube; (7) IKP intake; (8) Heater; (9) Insulation layer; (10) Temperature/Humidity probe and its holder; (11) Computer socket for data connection; (12) LCD display; (13) Display on/off button; (14) Flow rate adjustment valve.

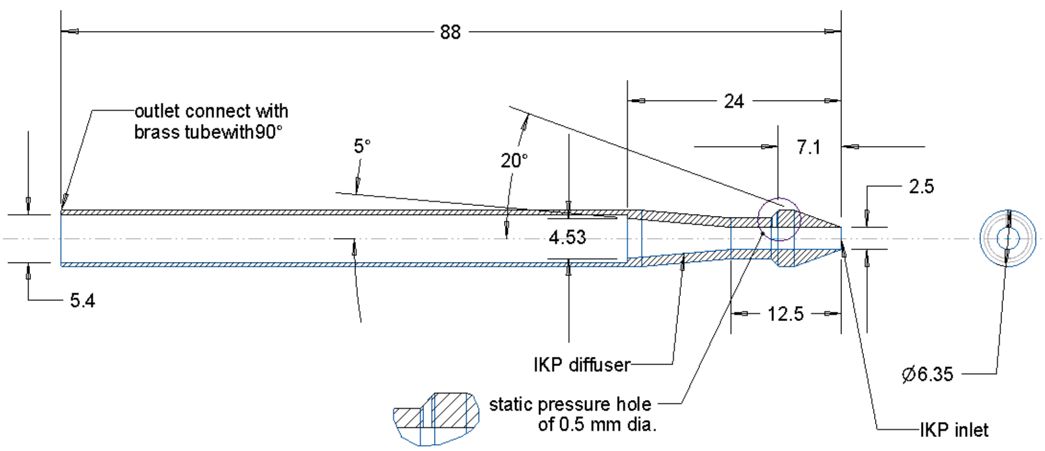


Figure 4.23: Sketch showing isokinetic probe intake layout and dimensions.

of the IKP during experiments performed in this work gave temperature and relative humidity values of around 60 % and 20°C respectively. Based on the specified measurement uncertainties of the Tinytag Thermohygrometer used in the IKP of ±1°C and ±3 % in relative humidity, the net uncertainty in the measurement of specific humidity and thus the total water content is around ±8 %, at the typical operating conditions specified above. Clearly there are opportunities to aim for reduced uncertainties in both the temperature and relative humidity measurements. Such reductions, if they can be achieved, will have a direct impact on reducing the uncertainty in the total water content measurement.

#### 4.4.2.2 Thermal performance

The performance of the iso-kinetic probe was initially investigated by operating it in the wind tunnel environment without water injection at approximately ambient temperature flow conditions with a speed of $u_\infty = 28\,\mathrm{m/s}$. Temperature and electrical heater measurements from these experiments are presented in Table 4.6 which shows the free stream flow temperature $T_\infty$, the probe surface temperature measured with the thermocouple bonded to the outer diameter $T_w$, the flow temperature within the probe after the heating length $T_L$, and the heater current $I$ and voltage $V$. Results from the measurements of IKP performance are also presented in Figure 4.24 in the form of heat transfer to the flow calculated according to

$$Q_{exp} = \dot{m}C_p(T_L - T_\infty). \tag{4.9}$$

In Figure 4.24, a calculation from a pipe flow heat transfer correlation is also presented. For this calculation, the heat transfer was obtained from

$$Q_{corr} = hA(T_w - T_\infty), \tag{4.10}$$

where $h$ is the heat transfer coefficient, and $A$ is the internal surface area of the probe over which the heat transfer takes place. The temperature difference at flow entrance to the probe $T_w - T_\infty$ is used in this calculation because the probe surface temperature is measured near the probe tip and the trace heating wire was coiled around the probe in a uniform manner that should have provided an approximately constant heat flux. The Reynolds number of the pipe flow within the probe was around 2000, so fully-developed turbulent pipe flow conditions were unlikely to exist within the aspirating tube. To obtain an estimate of the heat transfer coefficient under such conditions, the pipe flow friction factor was first calculated according to

$$f_{lam} = \frac{64}{Re_D} \quad \text{for} \quad Re_D \leq 2000, \tag{4.11}$$

Table 4.6: Iso-kinetic probe results in wind tunnel with $u_\infty = 28\,\text{m/s}$.

| $T_\infty$ (°C) | $T_w$ (°C) | $T_L$ (°C) | $I$ (A) | $V$ (V) | $P_{elec}$ (W) |
|---|---|---|---|---|---|
| 22.0 | 31.5 | 24.5 | 0.57 | 8.7 | 5.0 |
| 22.5 | 38.5 | 27.0 | 0.75 | 11.5 | 8.6 |
| 23.5 | 43.5 | 29.0 | 0.83 | 12.7 | 10.5 |
| 24.0 | 47.0 | 30.5 | 0.87 | 13.3 | 11.6 |

$$\frac{1}{\sqrt{f_{turb}}} = -1.8 \log\left[\left(\frac{\epsilon/D}{3.7}\right)^{1.11} + \frac{6.9}{Re_D}\right] \quad \text{for} \quad 4000 \leq Re_D, \tag{4.12}$$

and

$$f_{trans} = f_{lam} + \frac{Re_D - 2000}{4000 - 2000}\left(f_{turb} - f_{lam}\right) \quad \text{for} \quad 2000 < Re_D < 4000 \tag{4.13}$$

where $\varepsilon$ is the pipe roughness, taken as $\varepsilon = 0.0025\,\text{mm}$, $D$ is the pipe internal diameter, and $Re_D$ is

$$Re_D = \frac{\rho_\infty u_\infty D}{\mu_\infty} \tag{4.14}$$

The heat transfer coefficient was then calculated from

$$Nu_D = \frac{hD}{k} = \frac{f}{8} Re_D Pr. \tag{4.15}$$

Results in Figure 4.24 indicate that the pipe flow heat transfer correlation provides a good match to the experimental results, so it is expected that the correlation can also be used to estimate the power required for the IKP to maintain aspiration of the flow into the hygrometer at other conditions, although when multi-phase flow effects are also present, the reliability of the heat transfer correlation is more uncertain.

Comparing the electrical power figures in Table 4.6 with the heat transfer results in Figure 4.24 indicates that only about 10 % of electric power goes into heating the flow in the probe. This poor value of efficiency arises because the probe is poorly insulated, so a significant fraction of the heating will be convected into the flow external to the probe. A significant fraction of the heat is also expected to be conducted along the leg of the brass pipe away from the initial heating length.

Improvements to the IKP arrangements are required for the target flow speed of 50 m/s and TWC of 10 g/m$^3$. In particular, an improved insulation arrangement for the probe is required to minimise the parasitic losses and achieve the heat transfer into the flow within the probe that is needed to fully evaporate the water. Improved insulation can be readily applied, but as this will also increase the surface temperature of the probe, it is advisable to re-design the heat transfer arrangement for the probe so that additional convective heating power can be delivered to the internal flow with only modest increases in the surface temperature. A revised version of the IKP with an improved convective heat transfer arrangement and improved external insulation should be designed to access the higher flow rate wind tunnel conditions.

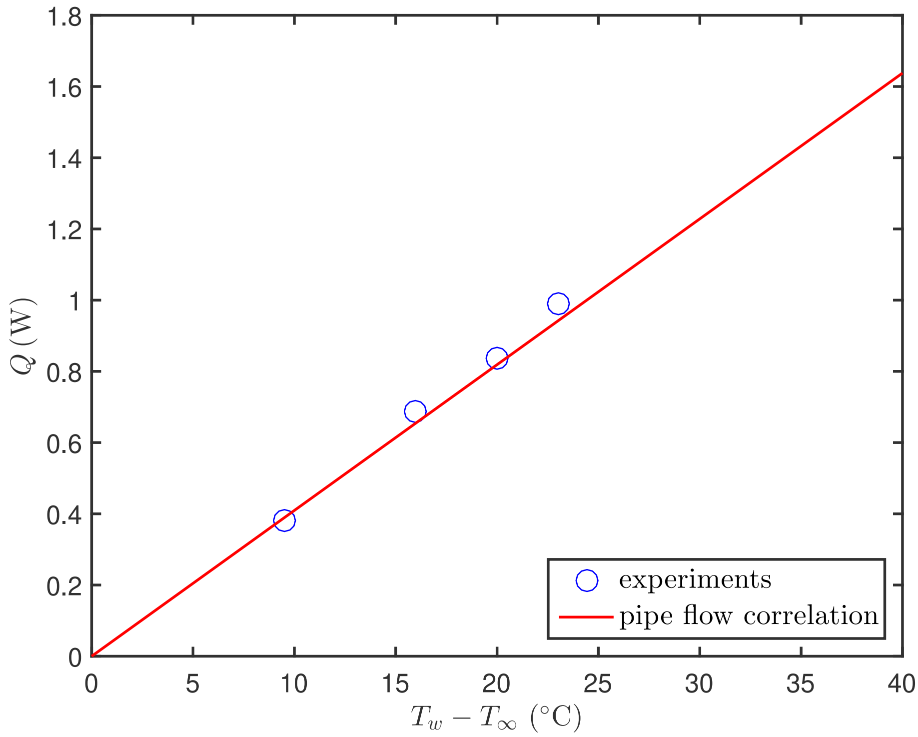


Figure 4.24: IKP heat transfer variation with surface-to-free-stream temperature difference for ambient temperature flow in the wind tunnel with $u_\infty = 28$ m/s.

#### 4.4.2.3 Response time

To assess the time response of the hygrometer, an experiment was conducted without the pipe connecting the probe with the hygrometer. The experiment involved supplying the hygrometer with a constant volume flow rate of air at a low relative humidity from an air compressor. At the outlet of the hygrometer, the suction device was connected. The air line supply from the compressor was then suddenly disconnected to allow air from the atmosphere to be drawn into the hygrometer. The signal from the hygrometer was recorded as a function of time. Three volumetric air flow rates were used in this experiment 5, 7, and 12 LPM.

Figure 4.25 shows the variation of RH with time for the hygrometer. The time constant in each case was identified for each flow rate based on the time for the change in RH to reach 63 % of its final value which was specified as the value recorded one minute after the first change in RH (at 40 s on the scale in Figure 4.25). Results from this analysis are presented in Table 4.7. The results show the time constant ($\tau$) for these experiments range from 4.8 to 5.9 s.

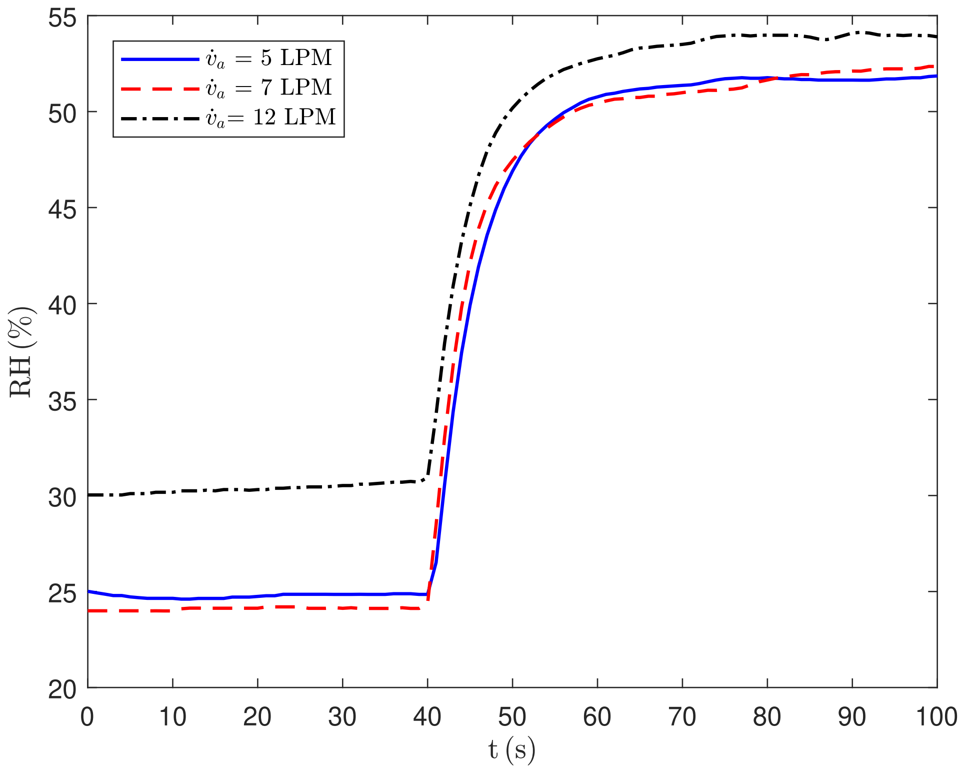


Figure 4.25: Variation of relative humidity with time for the hygrometer.

The experiment was then conducted with the isokinetic probe and the connecting pipe length of approximately 2 m included. Figure 4.26 shows the variation of RH with

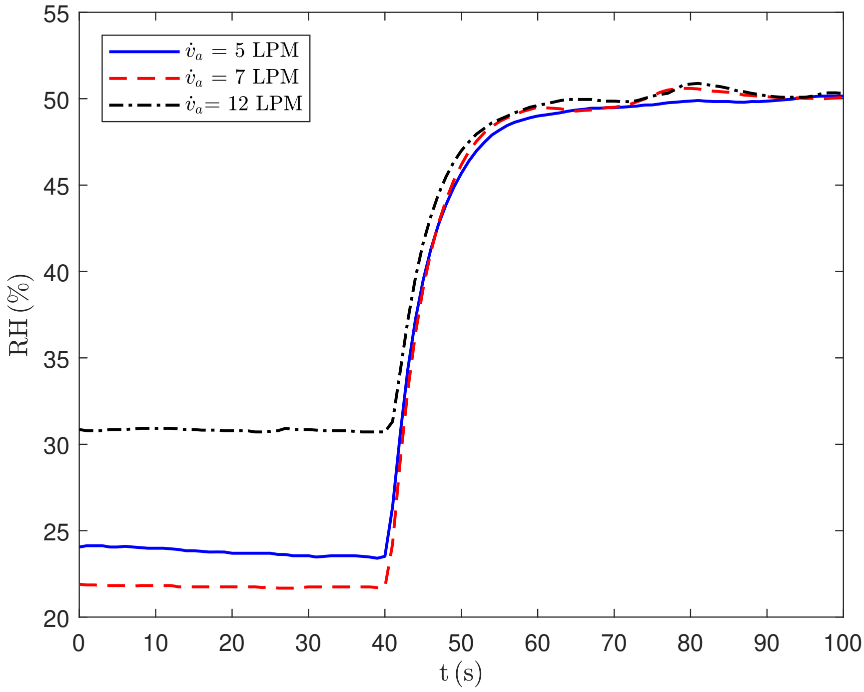


Figure 4.26: Variation of relative humidity with time in the case of the IKP connected with the hygrometer.

time for this experiment and demonstrates a very similar response to the case of the hygrometer operating alone (Figure 4.25). Time constant results for the IKP and connecting pipe included in the system are also presented in Table 4.7. It is evident that the response of the system was not greatly affected by the addition of the probe and its pipe connection. Assuming the measurement system can be treated as a first order system, the settling time of this system is approximately $4\tau$, and is therefore estimated to be up to 24 s. This settling time is too long for reliable IKP probe traversing in a single experiment that has a flow duration of around 2 minutes. Therefore the IKP was not used in an automated probe traversing manner for this reason. The IKP was moved into position prior to initiation of wind tunnel flow and was held in that position until a sufficient duration had elapsed to ensure a reliable measurement had been achieved. When the surveys of the LWC distribution were performed, the IKP was moved manually to the different positions. Pitot probe and temperature probe measurements made using the automated probe traversing features were obtained separately from the IKP measurements.

Table 4.7: Time constant results for the IKP.

| LPM | $RH_{init}$ (%) | $RH_{final}$ (%) | $0.63\Delta RH$ (%) | $\tau$ (s) | configuration |
|---|---|---|---|---|---|
| 5 | 24.781 | 51.712 | 16.97 | 5.9 | hygrometer |
| 7 | 24.107 | 51.82 | 17.46 | 4.8 | |
| 12 | 30.36 | 53.908 | 14.835 | 5.1 | |
| 5 | 23.768 | 50.039 | 16.55 | 5.5 | probe and hygrometer |
| 7 | 21.766 | 50.267 | 17.8 | 5.3 | |
| 12 | 30.817 | 50.295 | 12.27 | 5.9 | |

### 4.4.3 Traversing system

The traversing device moves the pitot probe and the IKP across the test section. As shown in Figure 4.27, the traverse is comprised of an aluminium frame, two support angles, four linear guide rails, four support brackets, four bearings, two timing belts, four timing belt pulleys, two potentiometers, two stepper motors (Nema 17 type 42BYGH47-401A), two Arduino board Uno, and two Easy Driver boards (v4.5).

The system was assembled, wired, and coded a manner that enabled the two stepper motors to move the probes in the two directions independently. The programmed scanning motion of the traverse provides the ability to move the probe in two linear direction (vertically and horizontally) with different speeds. It gives the coordinate position of the probe with respect to the test section walls. The total stroke of probe motion in the x-direction is approximately 215 mm, and in the y-direction is approximately 222 mm. Two potentiometers indicate the coordinates by sending signal voltages to the either an Arduino board or the LabView data acquisition system.

The traversing device is supported at the test section of the wind tunnel by another frame support with a rectangular base as shown in Figure 4.28. A slot of 240 mm$\times$18 mm has been made in the roof of the test section to allow the probe arm to move vertically and horizontally in the test section, while sealing is achieved by a cover of clear plastic sheet.

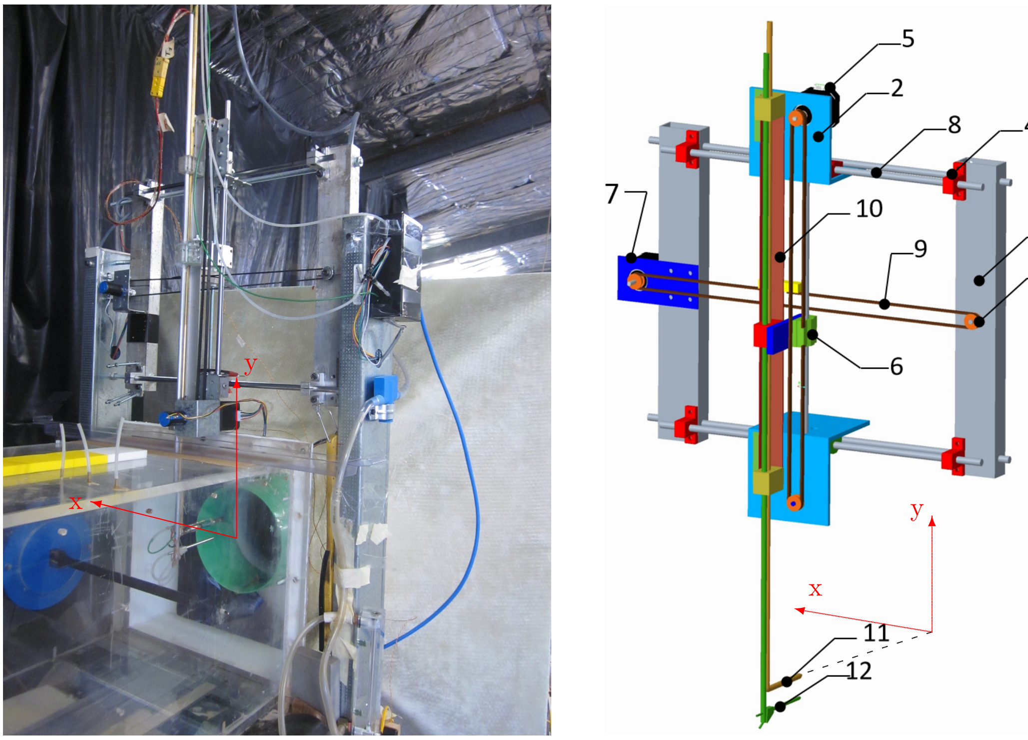


(a) (b)

Figure 4.27: Traversing device for the IKP and the pitot-static tube. (a) Photograph; (b) Solid modeling projection showing main parts: (1) Frame; (2) Support angles; (3) Pulley; (4) Support bracket; (5) Stepper motors; (6) Bearing; (7) Motor holder; (8) Linear guide rails; (9) Timing belt; (10) Sliding probes holder; (11) IKP; (12) Pitot probe.

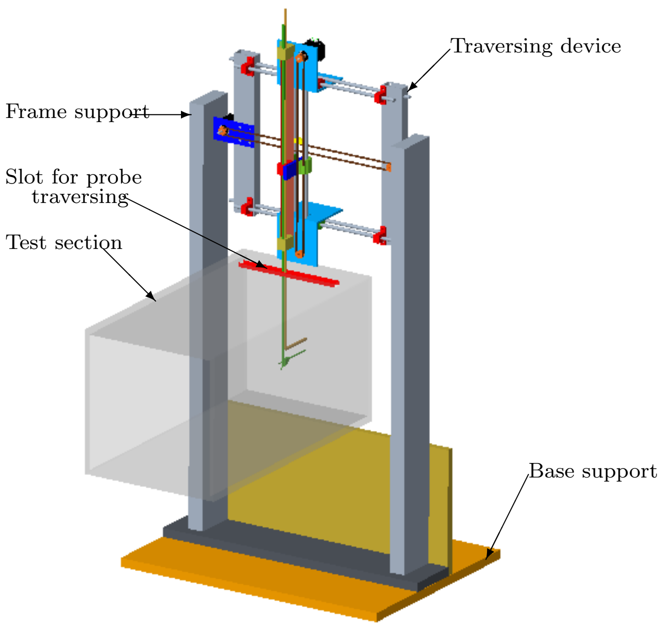


Figure 4.28: Solid model representation of the traversing device in the test section.

### 4.4.4 Temperature measurement and thermocouples distribution

Temperatures are measured using type K thermocouples having a manufacturer-specified uncertainty of ±2.2 °C. Each thermocouple has been directly attached to the LabView acquisition unit. Eight different positions have been chosen in different parts of the apparatus to specify the temperature distribution within the facility. Figure 4.29 shows the thermocouples locations. $T_1$ measures the temperature of the air-nitrogen-water droplet mixture that enters the perforated diffuser. $T_2$ measures the ambient temperature in the shell. To investigate of temperature uniformity of the stream at the nozzle exit, three thermocouples have been positioned just upstream of the nozzle exit: one near the top ($T_3$), one near the bottom ($T_4$), and one on the side ($T_8$) of the nozzle exit.

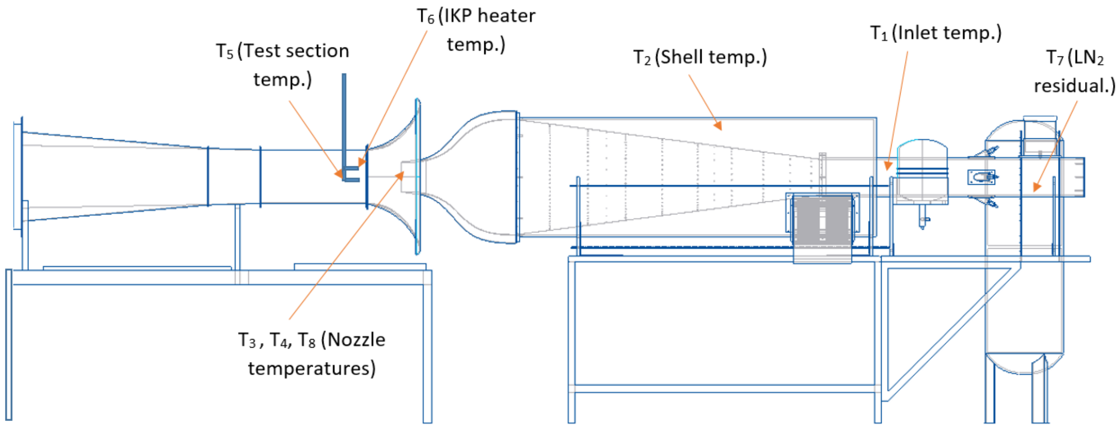


Figure 4.29: Thermocouple locations.

To achieve a fast response temperature measurement of the icing jet nozzle exit flow ($T_5$), a precision fine wire type K thermocouple with a welded-bead diameter of $0.003''$ was attached on a small probe located between the IKP and the pitot probe on the movable arm of the traversing device. The welded bead junction was exposed directly to the flow, and was used for measurements of air temperature in the flow when the facility was operated without water present in any form, apart from the ambient humidity in the air. The National Instruments type cDac-9174 NI compact DAQ has been used for both pressure and temperature data acquisition. A Cold Junction Compensation (CJC) channel built in the terminal block was used. To measure the IKP temperature during operation, $T_6$ is attached to the IKP intake. The last thermocouple, a foil thermocouple (Alumel-Chromel thickness 0.0005″) has been attached to the cylindrical specimen surface (cylindrical test article of diameter of 13 mm), as it is described in Chapter 7.

## 4.5 Conclusion

The icing wind tunnel concept proposed in Chapter 3 has been developed into physical hardware that forms the new icing wind tunnel facility, and this new hardware is described in the present chapter. The hardware includes an icing jet generator to produce an artificial cloud of partially melted ice particles suspended in a cold air flow and an open circuit wind tunnel that provides a co-flowing stream in the test section of the wind tunnel. The icing jet generator consists of a perforated diffuser, shell, nozzle contraction, spray guide tube, ultrasonic atomiser nozzles, liquid nitrogen receiver, pressurised water tank, and compressed air vessel. The open circuit wind tunnel is largely of a conventional design, but a new bell-mouth inlet was developed to enable effective operation with the icing jet generator.

A liquid nitrogen receiver and valve system was designed to supply the liquid nitrogen into the evaporator at the upstream end of the spray guide tube at a metered and controllable rate. The ice production technique involves the use of spray nozzles to produce approximately spherical liquid droplets within a cold flow. Flows of cold air and nitrogen mixtures at temperatures below $-40\,^{\circ}\mathrm{C}$ are provided to ensure liquid water droplets freeze. The perforated conical diffuser which receives the cold flow of suspended ice particles was designed to dilute the cold flow stream with warm air. A centrifugal fan is connected to the shell of the perforated conical diffuser to supply the warm air for the dilution method. The icing jet nozzle contraction which is attached to the downstream end of diffuser chamber was designed to increase the flow velocity and to decrease the non-uniformity of the flow velocity at the exit of the jet. A new bell-mouth intake was fabricated and connected to the conventional wind tunnel test section to match the requirements of the current study. A pitot-static probe, a welded-bead thermocouple probe, and an isokinetic total water content probe are also described. A traversing system was also established to enable automated surveys of the test flow to be performed so that quantification for flow uniformity could proceed.

The liquid nitrogen mass flow rate was controlled by setting valve-lift heights (valve is opened by threaded shaft attached with a stepper motor) and provided a range of flow rates between 0.06 and 0.217 kg/s. The mass flow rate of air introduced through the perforated diffuser was estimated to be between 0.49 and 0.61 kg/s. The water droplet size and the volume of water injected were controlled by adjusting the air and water pressures delivered to the atomiser nozzles. The target water mass concentration of $10\,\mathrm{g/m^3}$ is within capabilities of the facility when using three atomiser nozzles, and based on data taken from a previous study for the water droplets generated by the same type of atomiser nozzle used in this work, the size of droplets will be between $20\,\mu$m and $260\,\mu$m.

The IKP performance was assessed to estimate the electrical power required, and experiments were conducted initially without water injection and with 28 m/s flow speed. The results indicated that only about 10 % of the electrical power goes into heating the flow in the initial length of probe; the losses are attributed to the significant fraction of the heating that will be convected to the flow external to the probe and conducted along the leg of probe.

# Chapter 5

# Performance of Facility

## 5.1 Introduction

The facility components have been described in Chapter 4. The performance of the individual components is also described in Chapter 4. In this chapter, the performance of the facility as an integrated unit is described. Pressures and temperatures during the tests at representative operating conditions were logged using the data acquisition system. Probe traverses at the icing jet nozzle exit have been performed to assess the flow uniformity. The TWC distribution in test section has also been measured.

## 5.2 Thermodynamic performance

### 5.2.1 Steady state

The icing jet nozzle exit temperature was measured for several different liquid nitrogen mass flow rates which were achieved by setting different valve-lift heights: shaft displacements of $y_{sh}$ = 0.5, 1.0, and 2.0 mm were used to achieve the different liquid nitrogen flow rates. Experimental data is represented in Figure 5.1 using the symbols and error bars. No water injection was used in these experiments. Figure 5.1 also shows the theoretical variations based on the conservation of energy analysis presented in Chapter 3, Equation 3.16 and taking the value of temperature at the icing jet nozzle exit as $T_4 = T_3$.

Two different theoretical lines are presented in Figure 5.1: the first with $\dot{m}_{air,d} = 0.6\,\mathrm{kg/s}$ and the second with $\dot{m}_{air,d} = 0.4\,\mathrm{kg/s}$. In both cases, the theoretical results were calculated with $\dot{m}_{air,e} = 0.18\,\mathrm{kg/s}$, which is the estimated value as described in Chapter 4, Section 4.2.7. The value $\dot{m}_{air,d} = 0.6\,\mathrm{kg/s}$ corresponds to the nominal fan mass flow rate presented in Section 4.2.4. The theoretical, conservation of energy approach does not account for heat transfer from the warm wind tunnel duct surfaces to the cold flow which would tend to increase the nozzle exit temperature for any given mass flow rate of liquid nitrogen. Therefore, achieving lower-than-theoretical-temperatures in the experiments for the two lower liquid nitrogen mass flow rates appears unreasonable. One possible reason for the lower-than-theoretical-temperatures might be an over-estimation of the diffuser mass flow rate of the air, $\dot{m}_{air,d}$, and this is the reason that another theoretical result at $\dot{m}_{air,d} = 0.4\,\mathrm{kg/s}$ is presented in Figure 5.1.

The extent of the vertical error bars in Figure 5.1 is indicative of the measured temporal and spatial variation at the icing jet nozzle exit. The location of the right-hand end of the horizontal error bars indicates the liquid nitrogen mass flow rate deduced from the nominal valve-lift height and the initial volume of liquid nitrogen in the receiver using the valve discharge theory presented in Section 4.2.6. The location of the left-hand end of the horizontal error bars indicates the liquid nitrogen mass flow rate based on the same nominal valve-lift height in each case, but with the volume of the liquid nitrogen in the receiver being half of the initial value. Based on the assessment of the valve discharge theory presented in Section 4.2.6, it is concluded that the theory may either over-estimate or under-estimate the actual discharge rate by a substantial margin, depending on the liquid nitrogen volume remaining in the receiver. If a correction was applied for over-estimation in liquid nitrogen mass flow rate, then the experimental data points on Figure 5.1 would be pushed further to the left, which would only improve the agreement of the highest liquid nitrogen flow rate data point with the theoretical results. However, if a correction was applied for under-estimation of the liquid nitrogen mass flow rate, then only the lower two liquid nitrogen flow rate data points would have improved agreement with the theoretical results.

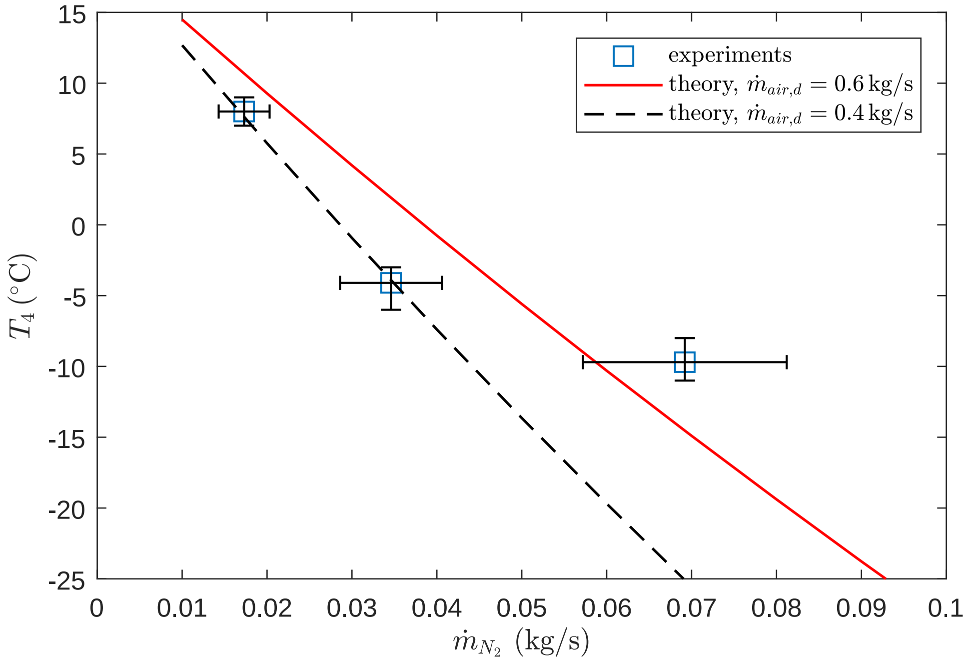


Figure 5.1: Variation of icing jet nozzle exit temperature $T_4$ with mass flow rate of liquid nitrogen $\dot{m}_{N_2}$ for $\dot{m}_{air,e} = 0.18\,\mathrm{kg/s}$ but no injection of water and associated air, $\dot{m}_{air,inj} = \dot{m}_{H_2O} = 0$.

### 5.2.2 Transient response

Figure 5.2 shows the temporal variation of the measured temperature at the icing jet nozzle exit for different mass flow rates of liquid nitrogen, as governed by the nitrogen receiver valve-lift height, $y_{sh}$. Results for two case are presented: $y_{sh} = 0.5\,\mathrm{mm}$ and $y_{sh} = 1.0\,\mathrm{mm}$. The time of 0 seconds on the horizontal axis corresponds to the time when the valve in the nitrogen receiver started to open, allowing the initiation of the liquid nitrogen flow into the evaporator. Figure 5.2 indicates that for the larger mass flow rate of nitrogen (for $y_{sh} = 1.0\,\mathrm{mm}$), the temperature at the icing jet nozzle exit dropped rapidly, reaching the minimum temperature of approximately $-5.5$°C over a period of about 20 s and in the lower nitrogen flow rate case (for $y_{sh} = 0.5\,\mathrm{mm}$), the corresponding period of time to reach the minimum of approximately 7.6°C was about

50 s. In both of the nitrogen flow rate cases, the stepper motor opened the valve to its designated lift-height within approximately 1 second of the open-command being issued. Therefore, the period taken to reach the minimum temperature in each case is primarily associated the establishment of quasi-steady heat and mass transfer processes in the evaporator and/or the downstream wind tunnel hardware.

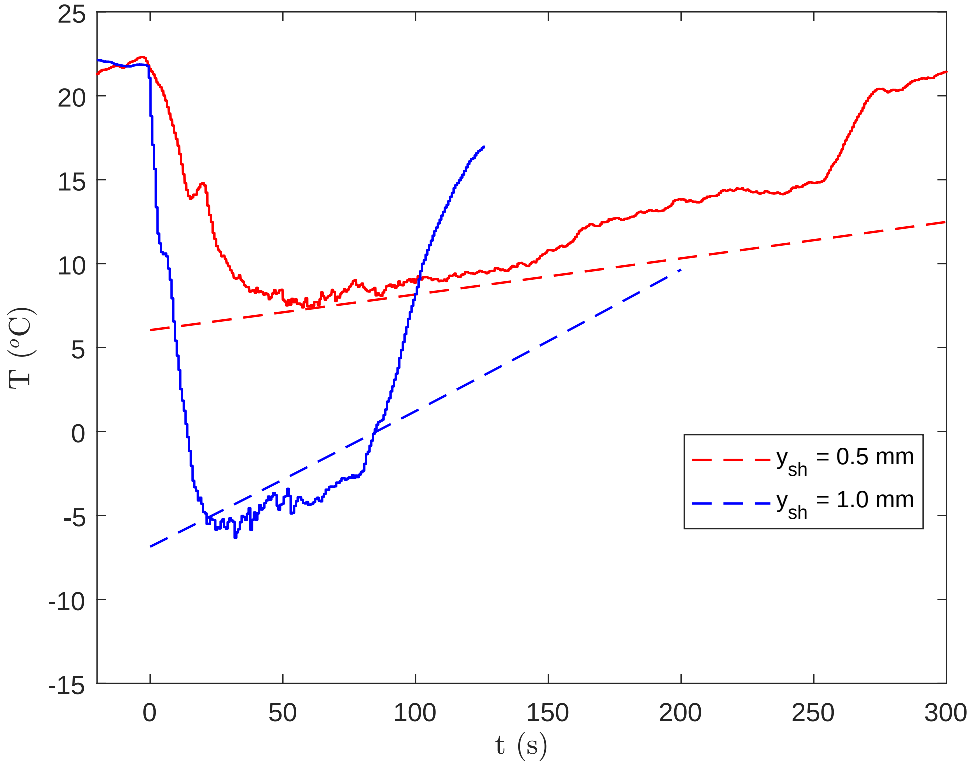


Figure 5.2: Variation of icing jet nozzle exit temperature with time for different liquid nitrogen mass flow rates and no injection of water and associated air, $\dot{m}_{air,inj} = \dot{m}_{H_2O} = 0$.

The two broken lines shown in Figure 5.2 indicate the variation in the icing jet nozzle exit flow temperature based on the steady flow energy equation analysis as presented in Chapter 3. To achieve the temporal variation in the nozzle exit temperature illustrated, the energy equation analysis used as an input, the liquid nitrogen mass flow rate which, for a fixed valve-lift, varied with time according to the model presented in Section 4.2.6. For both $y_{sh} = 0.5\,\text{mm}$ and $y_{sh} = 1.0\,\text{mm}$, the specified initial volume of liquid nitrogen was 9 litres, corresponding approximately to the quantity used in the experiments. The other parameters used in the energy equation analysis were $\dot{m}_{air,e} = 0.18\,\text{kg/s}$

and $\dot{m}_{air,d} = 0.5\,\mathrm{kg/s}$. Although the analysis comprised of the nitrogen receiver valve discharge theory coupled with the energy equation does not offer a complete explanation of the temperature variations measured at the nozzle exit (Figure 5.2), the gradual increase in temperature for each case is modelled reasonably well with this approach. There appears to be good prospects for adjusting the valve-lift during the facility run time so as to obtain a more constant flow temperature through either either a pre-programmed increase in valve-lift with time, or a closed-loop control system based on the measured nozzle exit temperature.

## 5.3 Flow speed uniformity

### 5.3.1 Icing bell mouth alone

To investigate the flow uniformity, the flow speed data is deduced from the pitot tube traversed across the test section. Figure 5.3 shows the arrangement of the probe with respect to the test section in the wind tunnel. The origin of the x-y coordinate system is taken to be on the geometric centre-line of the wind tunnel and the x-y plane is aligned with the start of the test section. The fast-response pressure sensor (Honeywell sensor) was used and the experiment was performed with an ambient temperature of 19 °C and local atmospheric pressure of 94.6 kPa. For this experiment, the icing jet nozzle was removed, the wind tunnel was operated with the icing bell mouth alone. The experimental data have been drawn as a contour graphic to show the velocity distribution in the test section entrance plane, as shown in Figure 5.4. The pitot pressure data covers an area from -105 to +103 mm in x-direction and from -90 to +101 mm in y-direction. The presence of the isokinetic probe positioned above pitot tube with a 25 mm separation restricted the pitot tube travel in the positive y-direction. The contours show a good uniformity near the centre of the test section. The velocity increases near the corners of the test section and the maximum velocity recorded during the probe traversing was approximately 45.6 m/s. Figure 5.5 shows selected velocity distribution at different locations for the same experimental results in Figure 5.4. Over the region of flow within a radius of 85 mm of the axis of the test section, which corresponds to the radius of the icing jet nozzle, the average flow speed was $43.81 \pm 1.4\,\mathrm{m/s}$, with the limits encompassing the actual maximum and minimum in this region.

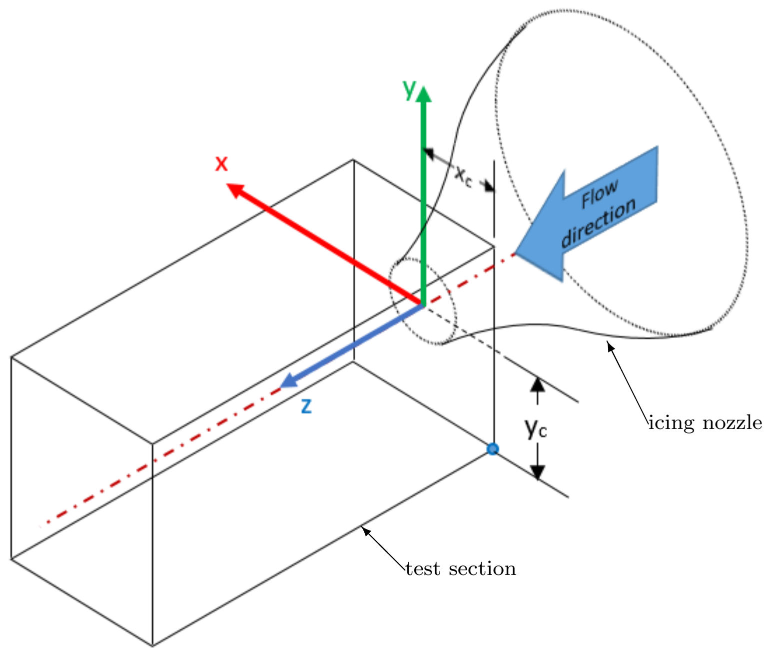


Figure 5.3: Diagram showing coordinate system location of the probe relative to the wind tunnel and icing jet.

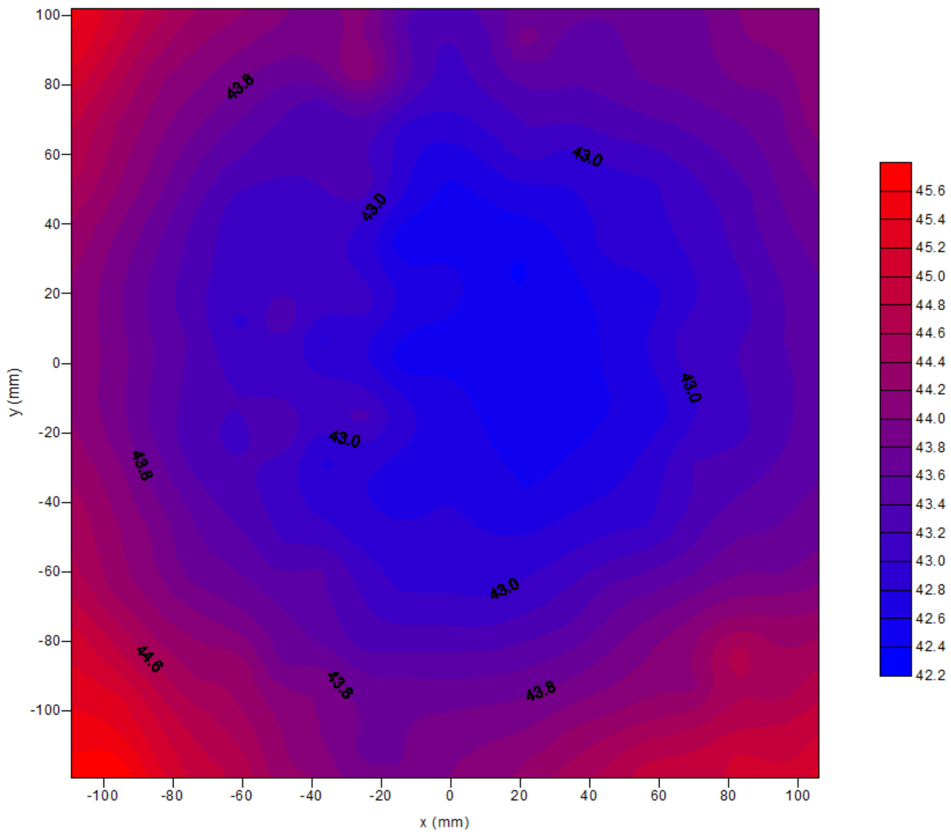


Figure 5.4: Velocity distribution at in the test section entrance plane when the wind tunnel was operated without the icing jet nozzle present.

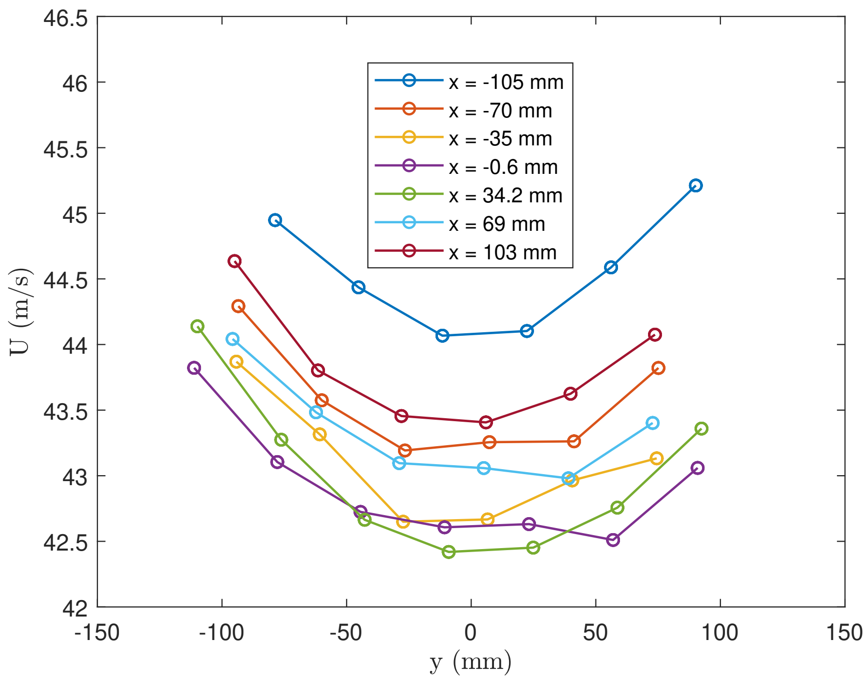


Figure 5.5: Velocity distribution for several x locations in the test section entrance plane when the wind tunnel was operated without the icing jet nozzle present.

### 5.3.2 Icing bell mouth plus icing jet nozzle

Figure 5.6 shows the velocity contour at the test section entrance but when the whole system – the wind tunnel and the icing jet generator – was operated together. The experiment was performed with only air flow drawn by main tunnel fan and the ice generator fan operating: no nitrogen or water injection was used in this case. Figure 5.6 demonstrates that the uniformity of air velocity is still good, and the speed is higher towards in the corners of the test section. The co-flowing stream is intended to provide flow conditions that approximately match the static and dynamic pressure in the icing jet nozzle so that models having a size approaching that of the icing jet diameter can be tested without the results being compromised by aerodynamic blockage effects. The experiment was performed at ambient laboratory conditions of 94.6 kPa and 15.8 °C. Figure 5.7 shows selected velocity distributions at different locations. The velocity in

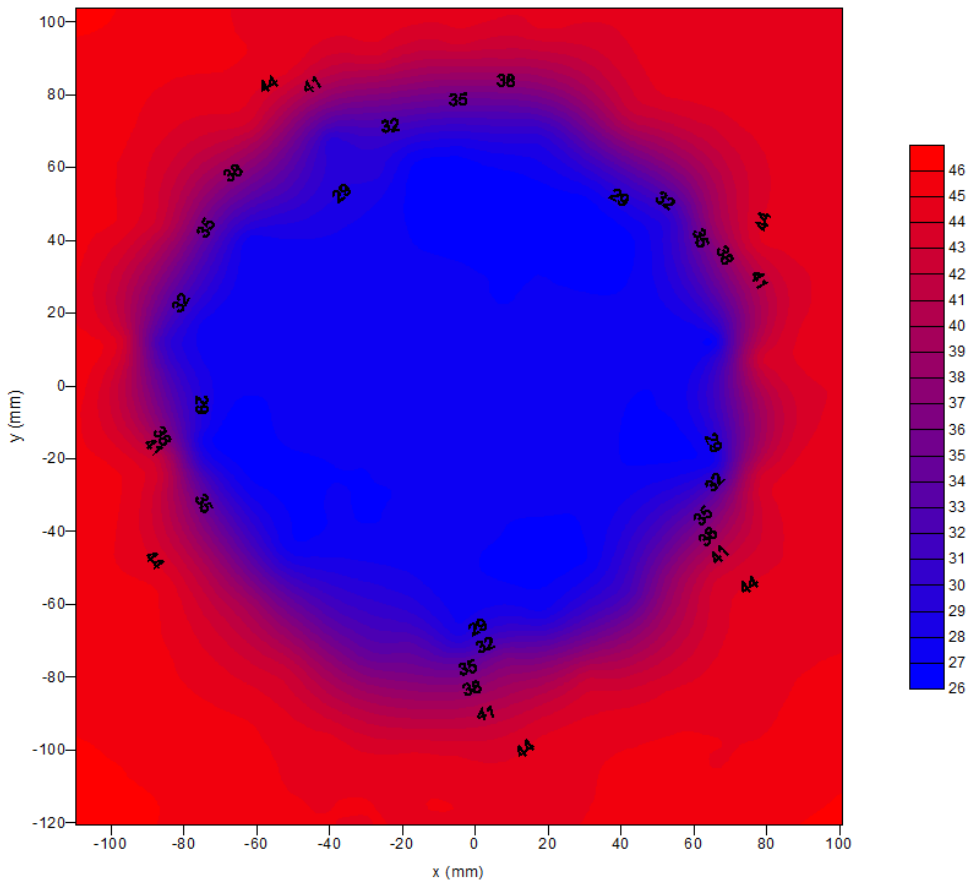


Figure 5.6: Velocity distribution in the test section entrance plane when the wind tunnel was operated with the icing jet nozzle but at ambient temperature.

the icing jet is around 28 m/s, depending on the ambient conditions and the air density of the test operation conditions.

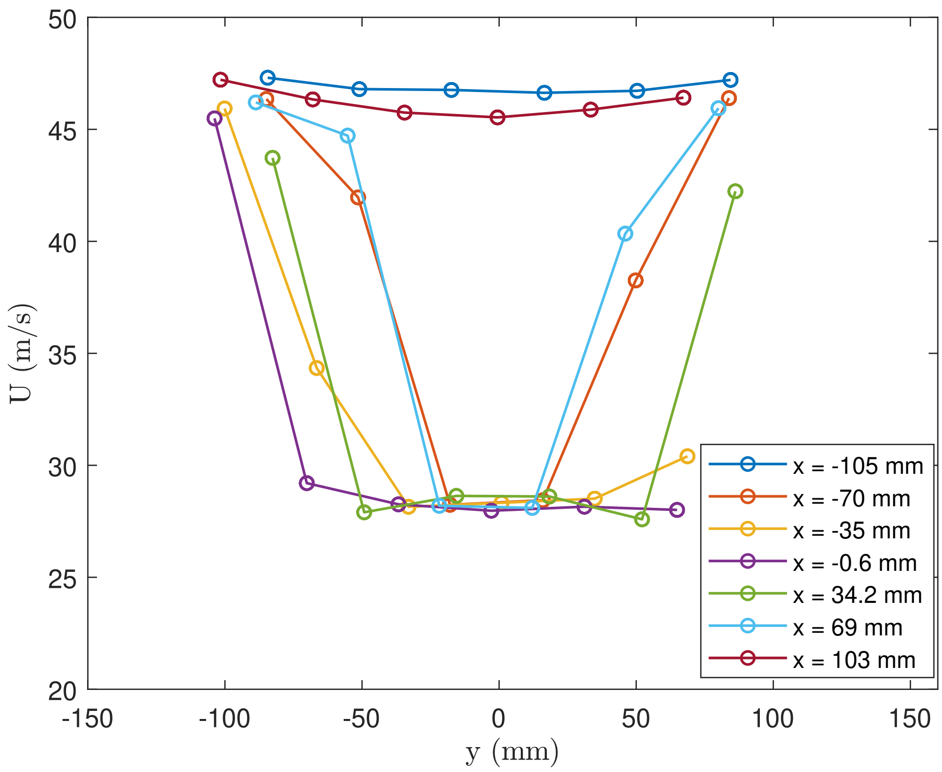


Figure 5.7: Velocity distribution for several x locations in the test section entrance plane when the wind tunnel was operated with the icing jet nozzle but at ambient temperature.

To improve quantification of icing jet flow uniformity, more detailed measurements were performed with a survey along the lines of $x = 0$, and $y = 0$. Figure 5.8 shows the comparison between the experimental velocity along the horizontal line at $y = 0$ and the experimental velocity along the vertical line $x = 0$, and both surveys lines were at test section entrance plane ($z = 0$). The motion of the traversing system probe was specified to provide spatial increments of 2 mm. The experiment was performed when the laboratory ambient temperature was 20.5 °C. As shown in Figure 5.8, the flow speed from the icing jet nozzle appears quite uniform and symmetric. Over the core flow region within a radius of 70 mm the average flow speed was $28.1 \pm 1.1$ m/s, with the limits encompassing the actual maximum and minimum in this region.

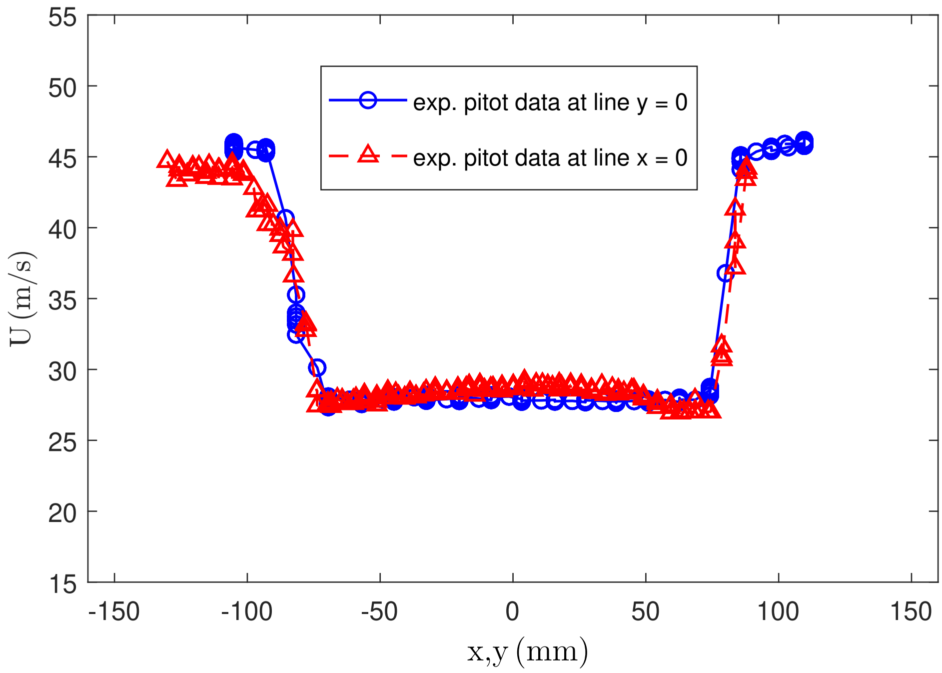


Figure 5.8: Detailed measurements of velocity along the horizontal line y = 0 and the vertical line x = 0 at the test section entrance plane when the wind tunnel was used with the icing jet nozzle but at ambient temperature.

## 5.4 Temperature uniformity

The temperature distribution within the flow delivered to the test section depend primarily on the mass flow rate of liquid nitrogen. The presence of the evaporated liquid nitrogen has only a small impact on the evaporator and air diffuser mass flow rates. Variation in the ambient temperature also has only a small influence on the heat transfer and thus the evaporation rate of the liquid nitrogen. To assess the temperature uniformity in the jet flow at the test section plane, a set of tests was conducted first without using either liquid nitrogen or water injection. In this case, the air temperature of the jet region is slightly higher than the air temperature of the co-flow because of the compression effect due to the fan that delivers air into the shell of the diffuser (see Section 4.2.4). Figure 5.9 shows the temperature distribution measured by three traverses of the probe along the y-direction at x = 0 at the test section entrance plane. The results demonstrate the temperature uniformity in the jet region and also demonstrate a clear distinction between the jet flow and the co-flow. Data was also collected along the x-direction at y = 0 as shown in Figure 5.10 to assess the temperature uniformity in the horizontal direction. Over the core flow region within a radius of 70 mm the average temperatures in the y-direction were $21.2 \pm 0.3\,^{\circ}\mathrm{C}$ for traverse 1, $21.1 \pm 0.1\,^{\circ}\mathrm{C}$ for traverse 2, and $21 \pm 0.3\,^{\circ}\mathrm{C}$ for traverse 3, and the average temperature in the x-direction was $20.7 \pm 0.3\,^{\circ}\mathrm{C}$, with the limits encompassing the actual maximum and minimum in this region.

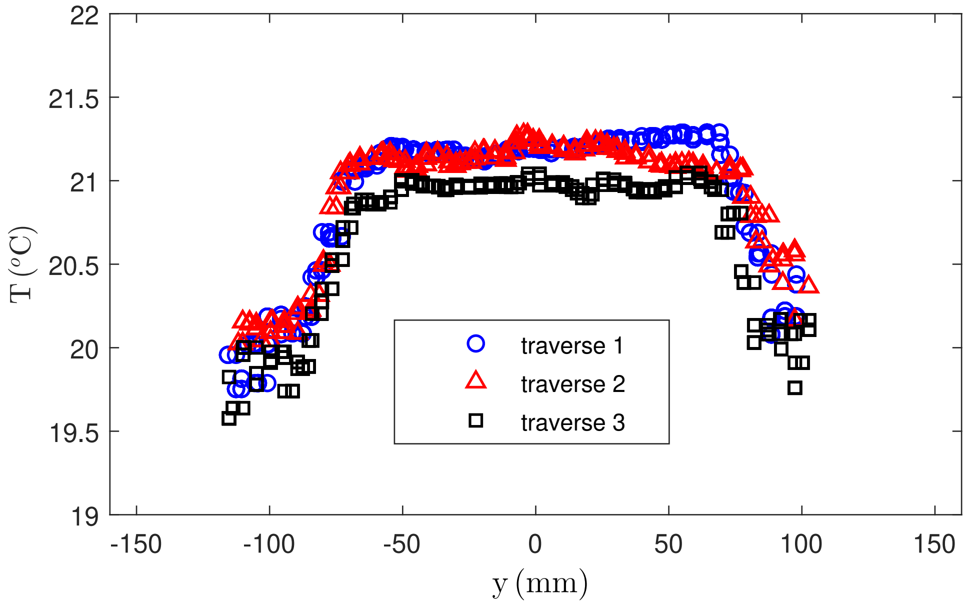


Figure 5.9: Temperature distribution along the vertical line x = 0 at the test section entrance plane when the facility was operated without either nitrogen evaporation or water injection.

Experiments were also performed in the cold icing jet environment using different mass flow rates of liquid nitrogen but again, without any water injection. The different flow rates were archived by adjusting the valve-lift height of the valve in the liquid nitrogen receiver. Figure 5.11 shows the temperature distribution along y-direction for the different valve-lift heights. As shown in Figure 5.11 the temperatures in the jet region are sensitive to amount of the nitrogen consumption. For these experiments the probe was traversed at a speed of approximately 0.038 m/s without stopping at points along its displacement because the duration of the test was limited. The average temperatures in the jet flow region were $8.0 \pm 0.6\,^{\circ}\mathrm{C}$ for $y_{sh} = 0.5\,\mathrm{mm}$, $-4.0 \pm 2.0\,^{\circ}\mathrm{C}$ for $y_{sh} = 1\,\mathrm{mm}$, and $-9.1 \pm 1.9\,^{\circ}\mathrm{C}$ for $y_{sh} = 2\,\mathrm{mm}$, with the limits encompassing actual maximum and minimum values within the jet core flow (over a diameter of 140 mm).

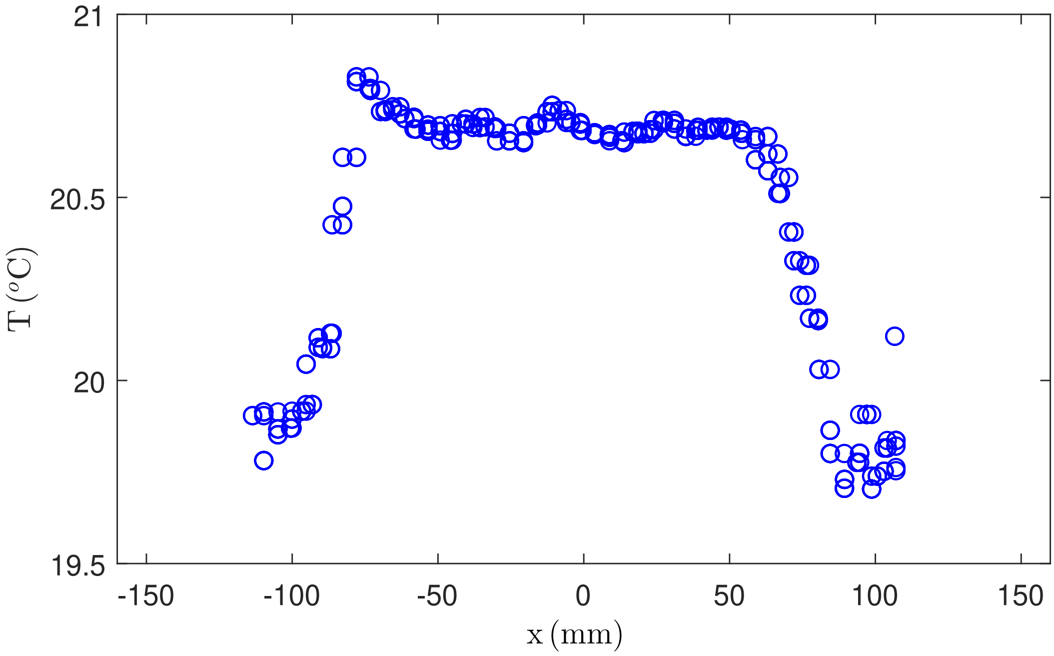


Figure 5.10: Temperature distribution along the horizontal line y = 0 at the test section entrance plane when the facility was operated without either nitrogen evaporation or water injection.

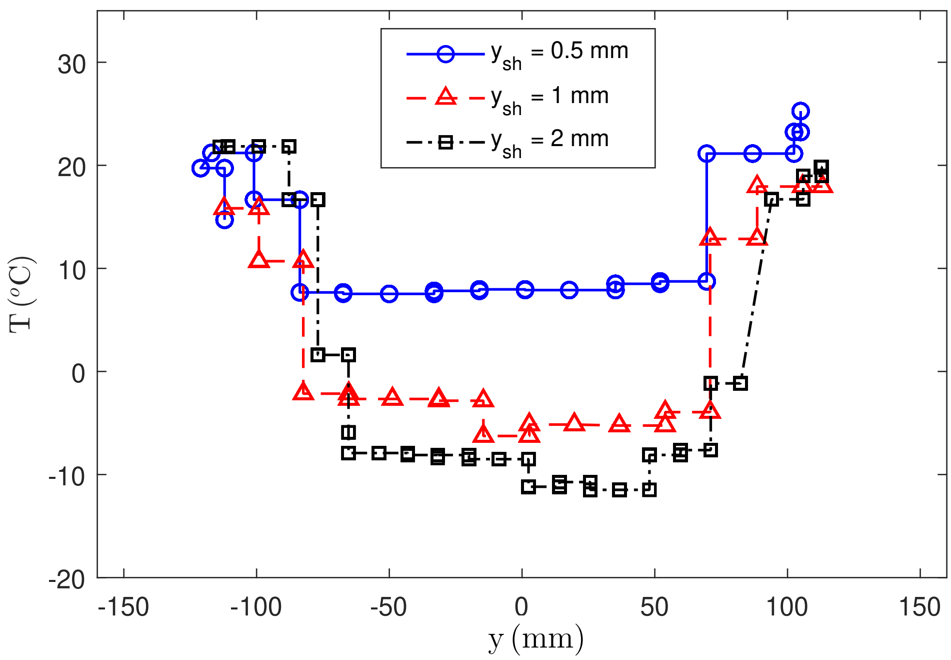


Figure 5.11: Temperature distribution along the vertical line x = 0 at the test section entrance plane when the facility was operated with different valve-lift heights giving different liquid nitrogen mass flow rates.

## 5.5 Total water content uniformity

The total water content (TWC) distribution within the icing jet nozzle exit flow has been obtained using the IKP and hygrometer device when the three atomiser nozzles were operating. The nozzles were operated at a water delivery pressure of 4 bar, and an air delivery pressure of 5 bar. The speed of the flow leaving the icing jet nozzle was 28 m/s and if this speed was uniform across the entire nozzle exit (170 mm diameter) the volumetric flow rate would have been 0.64 $m^3$/s. At this operating condition, the total injected water mass flow rate was 12.7 g/s (Chapter 4, Section 4.2.8) therefore, if all of the water was suspended in the air flow, the concentration would have been approximately 20 g/$m^3$. For these experiments, the facility was operated at ambient temperature so there was no freezing of the liquid droplets.

For the present experiments, the water was injected from a reservoir at close to the laboratory ambient temperature. Although the temperature of the water supply to the spray nozzles has an effect on evaporation, controlling the temperature of the water supply was not include as an objective in the present project.

The TWC has been derived from the relative humidity and temperature measurements of the flow samples entering to the IKP. The water vapour pressure $P_w$ at the hygrometer can be determined from the measured relative humidity using

$$\phi = \frac{P_w}{P_s} \tag{5.1}$$

where $\phi$ is the relative humidity measured in the flow sample, and $P_s$ is the saturation pressure at the temperature $T_s$ of flow sample as also measured at the hygrometer.

The specific humidity ($\omega$) which is defined as mass of water vapour per unit mass of dry air has been calculated from

$$\omega = 621.97 \frac{P_w}{P - P_w} \tag{5.2}$$

where $P_w$ is water vapour pressure, and $P$ is ambient pressure of flow sample. The form of Equation 5.2 gives the result in grams per kilogram of dry air.

The $TWC$ is then calculated from

$$TWC = \rho_{air}\omega \tag{5.3}$$

where $\rho_{air}$ is the air density at the wind tunnel flow conditions.

The water content due to injection ($\Delta TWC$) is then calculated from

$$\Delta TWC = \rho_{air} \Delta \omega \tag{5.4}$$

where $\Delta \omega$ is the specific humidity due to water injection, which is calculated as the difference between the measured specific humidity with water injection and that without water injection.

Table 5.1 presents the $\Delta TWC$ results for a vertical traverse through the nozzle exit flow, and Figure 5.12 presents the $\Delta TWC$ variation with vertical position in the left half of the test section. The probe was moved manually into each position and held in that position until the hygrometer output stabilised.

The magnitude of added $\Delta TWC$ measured by the IKP as presented in Table 5.1 and illustrated in Figure 5.12 is much lower than anticipated based on the water delivery and the volumetric air flow rate ($20\,\mathrm{g/m^3}$). During these experiments, large volumes of liquid water accumulated in the spray guide pipe and in the shell of the diffuser. Thus only a small fraction of the water delivered to the injectors is actually being delivered through the icing jet nozzle in the case of the liquid water experiments performed in this work.

Future work should explore the possibility of minimizing the pooling of liquid water pooling effects which might be achieved through repositioning of the water spray nozzles. Improvements in the operation and calibration of the IKP are also a priority for future work, and calibration is probably best performed through experiments that are separate from the wind tunnel characterisation experiments. However, if the minimization of liquid water accumulation within the facility can be achieved, it may be possible in future experiments to further verify the IKP measurements by comparing the integrated results from detailed nozzle exit surveys against the flow rates of the liquid water and air delivered into the wind tunnel.

Although a small fraction of water was observed to accumulate in the shell of the diffuser in the experiments when the facility operated at glaciated conditions, a larger volume of water accumulated and froze within the spray guide pipe. Improving the

Table 5.1: $TWC$ measurement and analysis for the traverse at x = 0.

| y mm | $\phi_{amb.}$ % | $\phi_{inj.}$ % | $T_{amb.}$ °C | $T_{inj.}$ °C | $\omega_{amb.}$ g/kg | $\omega_{inj.}$ g/kg | $\Delta\omega$ g/kg | $\rho_{air}$ kg/$m^3$ | $TWC$ g/$m^3$ | $\Delta TWC$ g/$m^3$ |
|---|---|---|---|---|---|---|---|---|---|---|
| -85 | 53.4 | 52.6 | 20.38 | 20.74 | 8.563 | 8.625 | 0.062 | 1.118 | 9.646 | 0.07 |
| -65 | 55.3 | 63.37 | 20.14 | 20.3 | 8.73 | 10.093 | 1.363 | 1.119 | 11.297 | 1.53 |
| -45 | 54.4 | 65.3 | 20.46 | 20.5 | 8.797 | 10.552 | 1.755 | 1.118 | 11.798 | 1.96 |
| -25 | 54.4 | 64.13 | 20.6 | 21.31 | 9.172 | 10.946 | 1.774 | 1.118 | 12.233 | 1.98 |
| -5 | 51.505 | 62.875 | 21.23 | 21.63 | 8.86 | 10.74 | 1.88 | 1.115 | 11.977 | 2.1 |
| 15 | 51.85 | 62.325 | 20.91 | 21.63 | 8.905 | 10.831 | 1.88 | 1.116 | 12.091 | 2.1 |
| 35 | 52.235 | 64.62 | 20.83 | 20.74 | 8.931 | 10.625 | 1.694 | 1.117 | 11.865 | 1.89 |
| 55 | 53.035 | 62.745 | 21.03 | 21.23 | 8.894 | 10.641 | 1.747 | 1.116 | 11.874 | 1.95 |
| 75 | 68.1 | 73.41 | 18.86 | 19.3 | 10.057 | 11.53 | 1.473 | 1.124 | 11.962 | 1.66 |
| 95 | 67.78 | 69.355 | 18.82 | 19.14 | 9.885 | 10.353 | 0.468 | 1.124 | 10.64 | 0.53 |

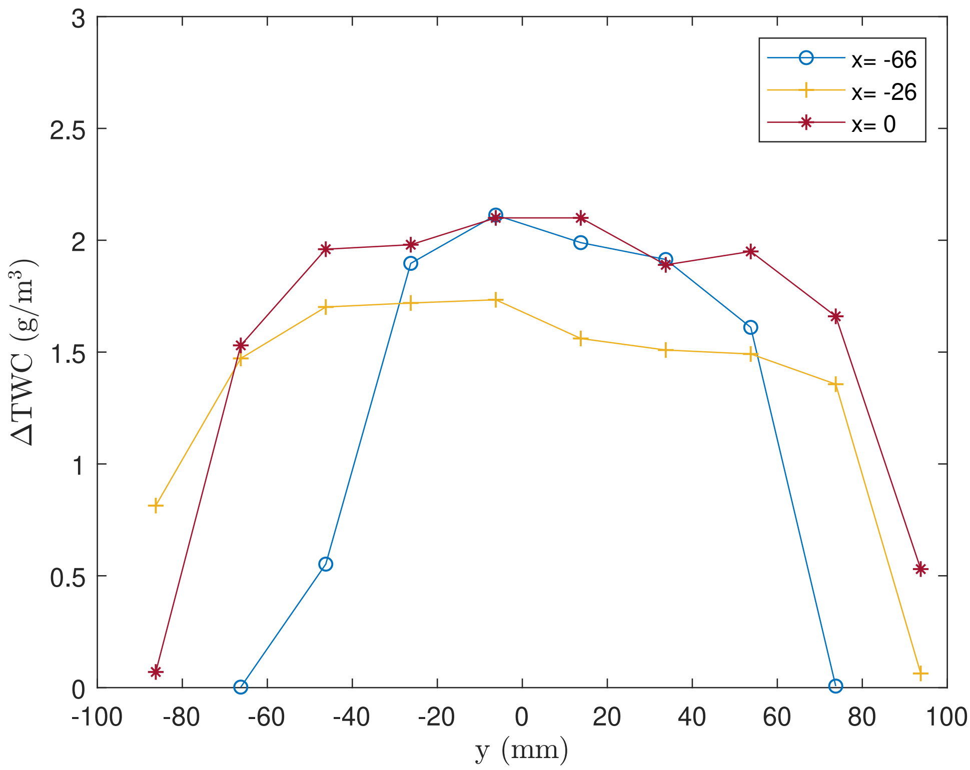


Figure 5.12: Distribution of $\Delta TWC$ with y-position for three different x-locations.

orientation of spray nozzles within the spray guide pipe should also have a positive impact on the facility performance under glaciated conditions. Unfortunately it was not possible to perform nozzle exit surveys with the IKP under glaciated conditions due to the relatively short run time of the facility under such conditions combined with the slow response time of the hygrometer being used in the IKP. Therefore, it is not certain how the present results obtained with the IKP for the facility operating under liquid water conditions will translate to operation under glaciated conditions. Improving the performance and calibration of the IKP remains a priority for future work.

## 5.6 Conclusion

The performance of the facility as an integrated unit has been assessed, first in terms of the temperature achieved at the icing jet nozzle exit. These temperatures were measured for several different liquid nitrogen mass flow rates and results were compared with the theoretical analysis based on the conservation of energy analysis from Chapter 3. The conservation of energy analysis does not currently account for heat transfer from the warm wind tunnel duct surfaces to the cold flow which would tend to increase the nozzle exit temperature for any given mass flow rate of liquid nitrogen. However, the measured temperatures were lower than theoretical temperatures at the two lower liquid nitrogen mass flow rates. One possible reason for the lower-than-theoretical-temperatures might be an over-estimation of the diffuser mass flow rate of the air that was used in the theoretical analysis.

A set of experiments has also been performed to assess the velocity uniformity at the test section entrance plane. In the case when the wind tunnel was used with the new icing bell-mouth, the velocity distribution shows a good uniformity near the centre of the test section and the velocity increases near the corners of the test section. Over the region of flow within a radius of 85 mm of the axis of the test section, which corresponds to the radius of the icing jet nozzle, the average flow speed was $43.8 \pm 1.4\,\mathrm{m/s}$. In the case when the wind tunnel and icing bell-mouth were operated with the icing jet nozzle at ambient temperatures, the results demonstrate that within the nozzle core flow region having a radius of 70 mm, the average flow speed was $28.1 \pm 1.1\,\mathrm{m/s}$. A comparison between the experimental velocity profiles along the horizontal and vertical lines through the axis of the icing jet nozzle exit flow indicate a high degree of uniformity. When the icing jet is operating, the co-flowing stream that enters the test section through the icing bell-mouth has a speed of approximately 47 m/s.

The temperature uniformity of the icing jet nozzle exit flow within the test section has also been investigated when the facility was operated with- and without using liquid nitrogen cooling. When the facility was operated at ambient temperatures, a clear distinction between the jet flow and the co-flow temperatures was observed. Within the jet core flow region, defined as the region within a radius of 70 mm of the nozzle axis, the jet temperature was higher than the ambient temperature by approximately 1 °C and was uniform to within $\pm 0.3\,^{\circ}$C. When the facility was operated with liquid nitrogen, good temperature uniformity was also observed. For example, when the liquid nitrogen receiver valve-lift height was approximately 2 mm, the average temperature measured in the jet core flow region was $-9.1 \pm 1.9\,^{\circ}$C.

The total water content (TWC) distribution within the icing jet nozzle exit flow within the test section has also been measured using the isokinetic probe and hygrometer device when the facility was operated at ambient temperature with the three atomiser nozzles injecting liquid water into the air stream. The nozzles were operated at a water delivery pressure of 4 bar, and an air delivery pressure of 5 bar. Although the distribution of TWC along a vertical line passing through the axis of the nozzle indicates a good degree of uniformity across the entire core flow region, the vertical traverse performed at x = $-66$ mm indicates a lower water concentration, suggesting substantial non-uniformity in the distribution of TWC within the core flow radius of 70 mm.

# Chapter 6

# Computational Fluid Dynamics Simulations

## 6.1 Introduction

In this chapter, Computational Fluid Dynamics (CFD) simulations of the wind tunnel, icing jet generator, and the combination of the wind tunnel with the icing jet generator are presented. These computational simulations were performed to aid in the facility design process and were largely completed prior to the development of the majority of the hardware presented in Chapter 4. However, presentation of the CFD work has been delayed until this point in the dissertation because the arrangement and geometry of the facility have now been detailed in Chapter 4, so a repeated coverage of this material can be avoided. Two cases for the wind tunnel – with and without screens and honeycomb – have been simulated. The screens are removed and a different bell-mouth inlet is used when icing work is performed, but the reason for simulating the wind tunnel cases with screens and honeycomb was to establish the reliability of the CFD simulations through comparison with experimental data prior using the CFD in the assessment of proposed design modifications.

Mesh refinement of the simulations for both the wind tunnel and the icing jet generator has been assessed. Simulation of the velocity and temperature distribution in the test section of the wind tunnel and at the icing nozzle exit, as well as the static pressure distribution along the wind tunnel will be discussed. For the combination of the icing jet with the icing wind tunnel case, comparison between CFD results and experimental data will be presented. The effect of the ratio between the warm air mass flow rate introduced through the perforated diffuser to the cold air mixture mass flow rate entering the core of the diffuser will also be discussed.

## 6.2 Overview of CFD approach

ANSYS Fluent 18.2 was used to simulate the flow characteristics inside both the wind tunnel and the icing jet generator. A full-scale CFD model for both components has been simulated. The flow field has been assumed to be 3-dimensional, steady, incompressible, and fully turbulent. The working fluid is air and is treated as an ideal gas. The Fluent model employs a finite volume technique to solve the Reynolds averaged Navier-Stokes equations. The standard k-$\varepsilon$ epsilon turbulence model with double precision was selected to define the turbulent energy and dissipation rate. Standard wall functions were used for the treatment of the boundary layers in this study.

The adopted solution method which is used in the CFD simulation includes an implicit method for pressure-linked equations, the simple algorithm for the velocity-pressure coupling, and the second order upwind approach for all transports equations except the turbulence dissipation rate, which was first order. The target residuals for continuity, momentum energy, and turbulence equations were less than $1\times10^{-5}$.

## 6.3 Geometry

### 6.3.1 Wind tunnel

A quarter of the wind tunnel geometry was generated using Design Modeller in ANSYS software. The dimensions were taken from the low speed wind tunnel as described in Section 4.3. The geometry includes all features from the bell mouth intake to the exhaust fan, however the silencer of the wind tunnel which is downstream from the fan has not been included. To position the upstream boundary condition away from the physical wind tunnel inlet, a bicylinder geometry generated by the intersection of two right angle cylinders was generated as shown in Figure 6.1.

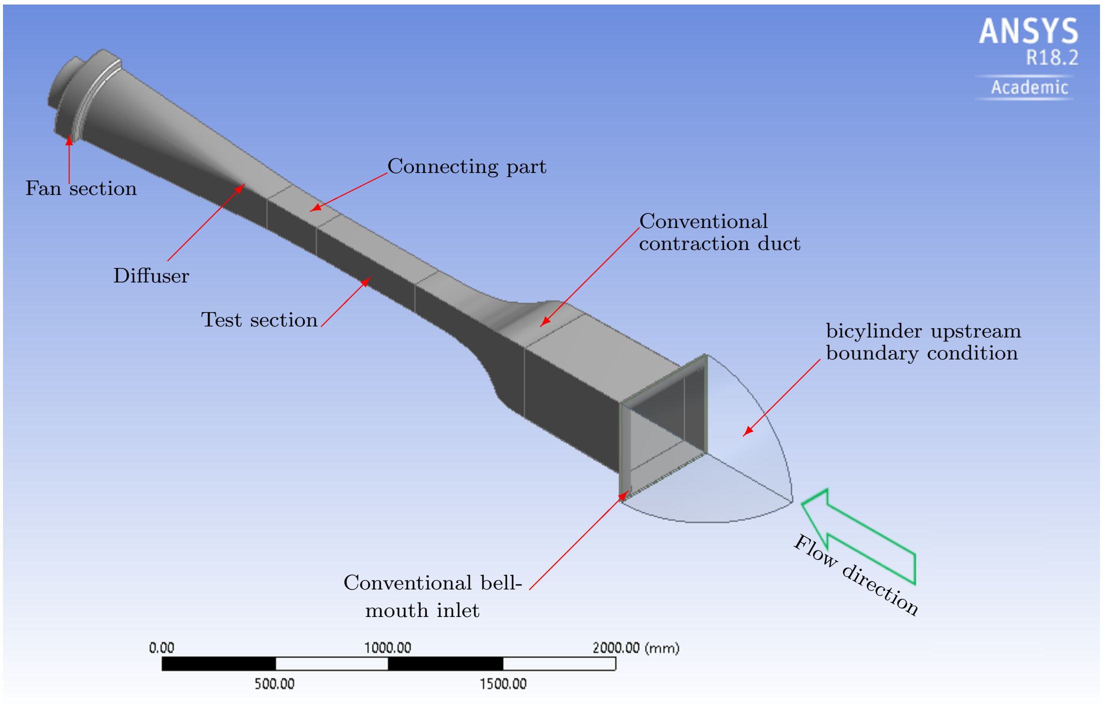


Figure 6.1: Wind tunnel geometry model showing the primary components of the tunnel without screens. A quarter of the wind tunnel cross section has been modelled.

Two cases were investigated for the wind tunnel geometry: with and without screens and honeycombs layers as shown in Figure 6.1 and Figure 6.2. Three screen layers and one honeycomb section were simulated in the case illustrated in Figure 6.2.

### 6.3.2 Icing jet generator

The geometry of the icing jet generator consists of a conical diffuser with injection orifices of 6 mm diameter distributed along the diffuser wall, the diffuser shell, and the nozzle contraction. The total number of the injection orifices in the diffuser was 400 for the whole icing jet geometry. A quarter of the geometry (a 90° segment), was modelled as shown in Figure 6.3.

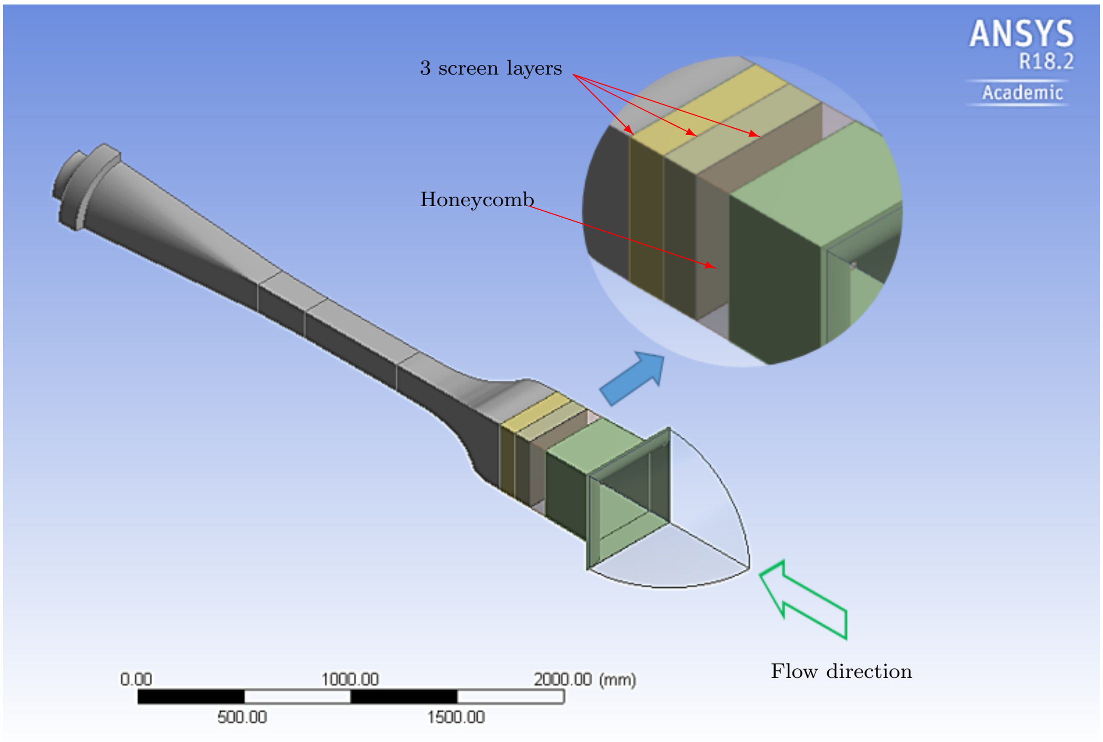


Figure 6.2: Wind tunnel geometry model with screen layers and honeycomb.

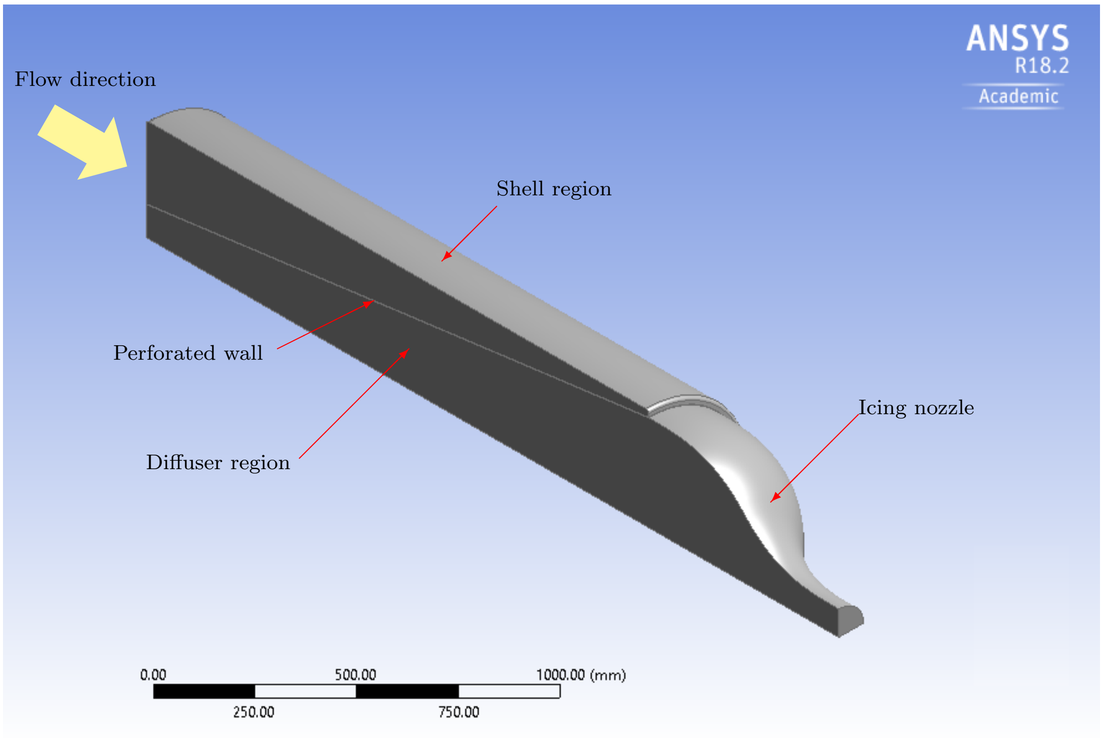


Figure 6.3: Geometry of icing jet generator.

## 6.4 Boundary conditions

### 6.4.1 Wind tunnel

In the case of the wind tunnel simulations including the screens and honeycomb, the screen layers were treated as a porous jump zone (pressure jump) and the honeycomb was treated as a porous zone with a porosity of 90 %, a triangular cross section, with each cell having a height of 14 mm and a side length of 25 mm (similar to the real honeycomb which is used in the wind tunnel). The energy equation was not included in the solution strategy since isothermal conditions prevailed in this case. The boundary

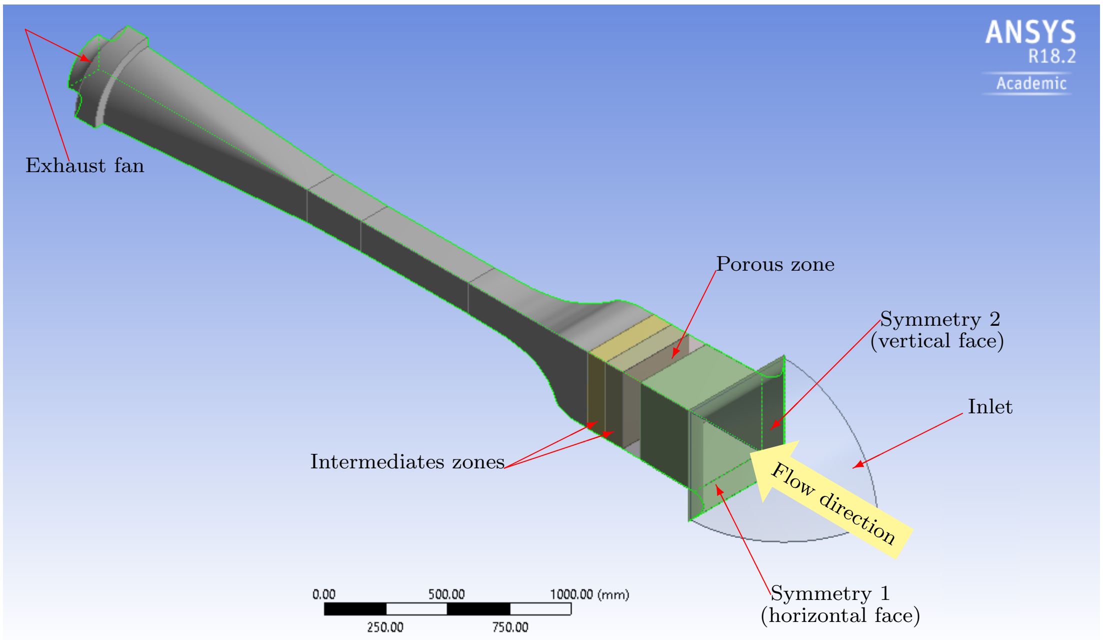


Figure 6.4: Wind tunnel boundary conditions.

conditions for the wind tunnel for cases with and without the screens and honeycomb both used atmospheric pressure of 94 kPa at the inlet and the exhaust fan at the outlet was set with a pressure of 92.8 kPa. The two faces of the quarter geometry were set as symmetry planes are shown in Figure 6.4.

### 6.4.2 Icing jet generator

In the icing jet generator simulation, two inlets and one outlet were specified. As shown in Figure 6.5, Inlet 1 delivers the cold air to the core of the diffuser. In the physical arrangement, this cold core flow is composed of the mixture of the evaporated liquid nitrogen, air, and injected water droplets. To simplify the simulations, the mixture was treated simply as cold air in the CFD simulations. Inlet 2 delivers the nominally room temperature air into the shell of the diffuser which mixes with cold air in the core of diffuser. The difference in temperatures in this case requires the energy equation to be included in the solution strategy.

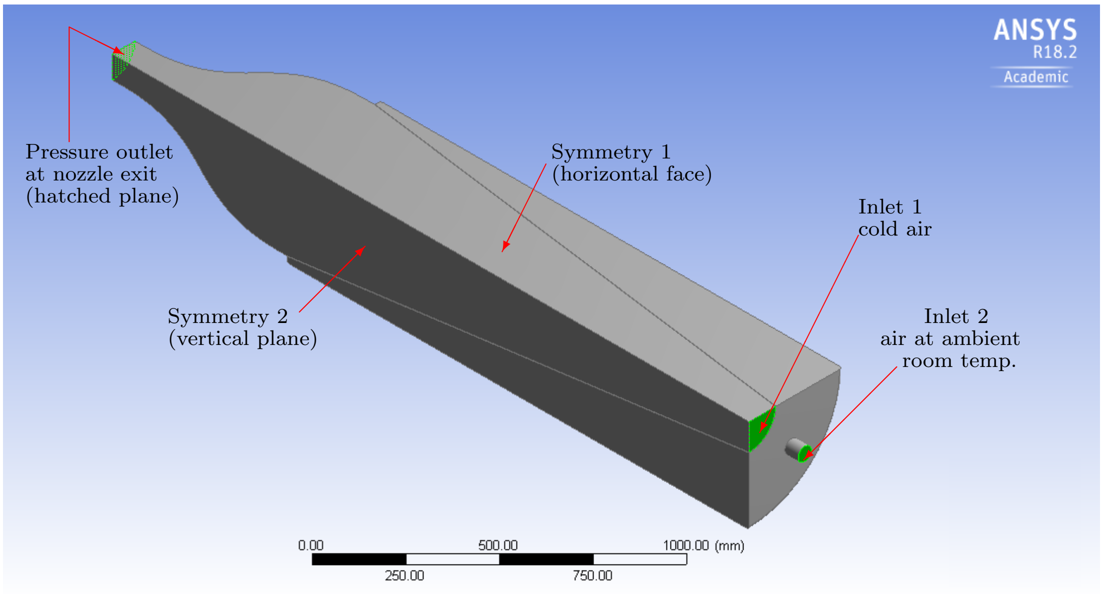


Figure 6.5: Icing jet generator boundary conditions.

A mass flow rate boundary condition for Inlet 1 was specified as 0.02525 kg/s (corresponding to a quarter of the total mass flow rate) with the total temperature of 113 K ($-160\,^{\circ}$C). At Inlet 2, a mass flow rate boundary condition was also specified, this time with a value of 0.113625 kg/s (again, a quarter of total mass flow) with the total temperature of 298 K (25 °C). The present chapter uses the term Mixing Ratio (MR) to specify the ratio of the mass flow rate of warm air introduced through the perforated diffuser to the mass flow rate of the cold air mixture entering the core of the diffuser. Unless otherwise specified, the mixing ratio is approximately MR = 4.5. The boundary condition at the outlet was set as a pressure outlet with a value of -1000 Pa, corresponding to the static gauge pressure value when the nozzle exit of the icing jet is positioned near the start of the test section of the wind tunnel as occurs during the physical experiment. Adiabatic wall boundary conditions were also applied in the icing jet generator simulations.

### 6.4.3 Mesh refinement

The mesh quality plays an important role in the convergence and accuracy of the CFD solution. Prismatic mesh elements were generally used in the computational models. The options of fine mesh with high smoothing and fine span angle centre were selected to improve the results. The inflation parameter was set for all solid walls of the fluid computational domain using seven layers, with a total thickness inflation option set to 9 mm to resolve the boundary layers. A grid sensitivity analysis was conducted for the quarter wind tunnel model and the quarter icing jet model to assess the numerical results. The element size was used to increase the number of elements in both the wind tunnel and the icing jet simulations. Also, the mesh was modified and refined within the regions of particular interest: the test section in the wind tunnel, and the nozzle exit region for the icing jet as shown in Figure 6.6 and 6.7 respectively. The number of cells across each orifice in the perforated diffuser was 32 and this number of cells was obtained after solution adaption which had a 4 times refinement compared with original mesh. The $Y^+$ for all cases after refinement mesh was less than 60.

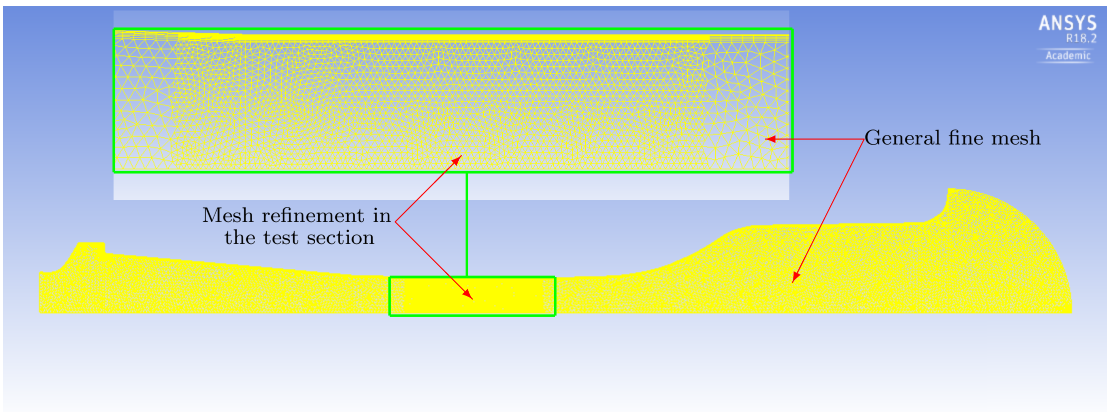


Figure 6.6: Illustration showing mesh refinement within one of the planes of symmetry in the wind tunnel model.

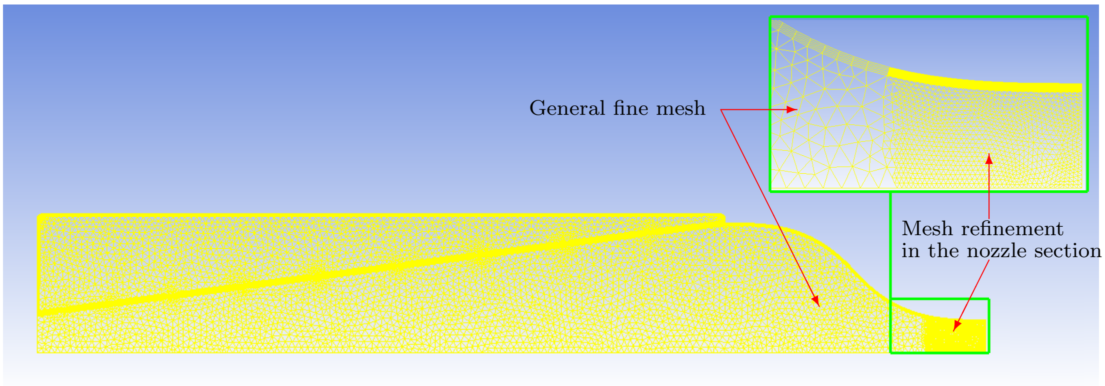


Figure 6.7: Illustration showing mesh refinement within one of the planes of symmetry in the 90° segment icing jet generator model.

Figures 6.8 and 6.9 show the effect of element numbers on the velocity distributions in the wind tunnel (for the case of without screens and honeycomb) and at the exit of the icing nozzle, respectively. Figure 6.10 illustrates the effect of the mesh refinement on the temperature distribution at the exit of the icing nozzle. In these figures the zero position of the x-axis represents the centre line of the test section and the icing jet flows. In the wind tunnel case, the number of mesh elements ranged between 834579 and 1395108 for the mesh refinement analysis. In the icing jet case, the range was between 1225499 and 1897542. The mesh arrangement used for the majority of the simulations was the 930880 element mesh for the wind tunnel and the 1897542 element mesh for the icing jet generator. Table 6.1 presents the grid details used in simulation of the wind tunnel and the icing jet generator.

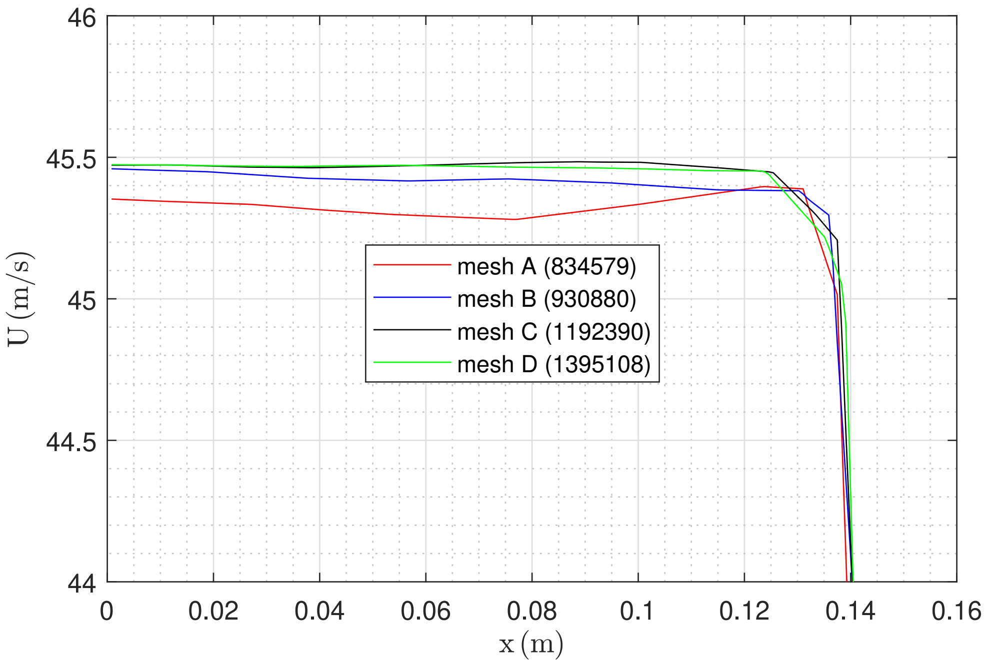


Figure 6.8: Simulated velocity distribution along the horizontal line from the axis of the test section at the test section entrance plane for simulations with different numbers of elements.

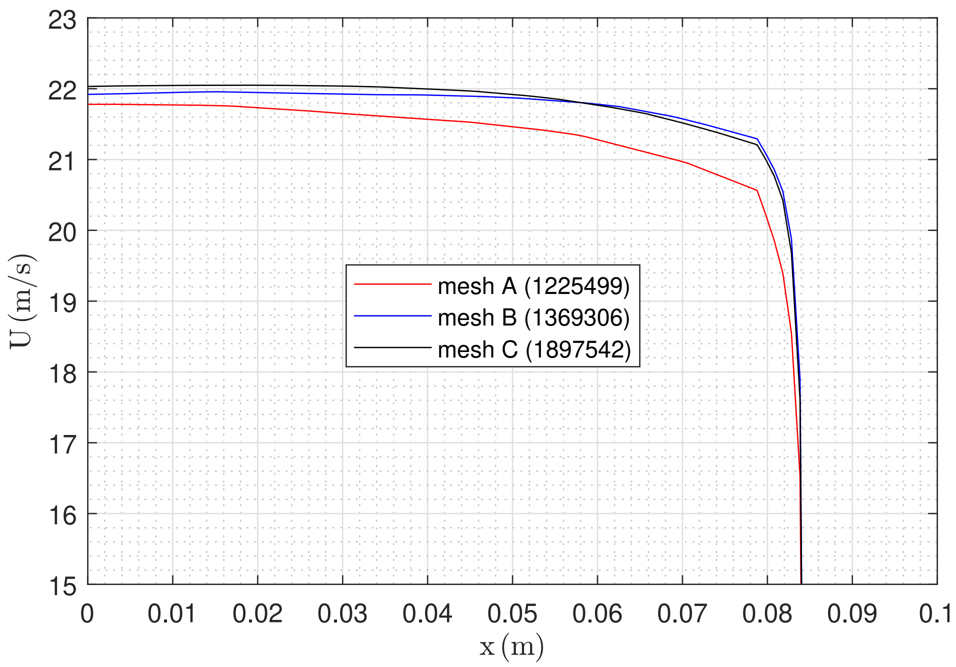


Figure 6.9: Simulated velocity distribution along the horizontal line from the axis of the test section at the icing jet nozzle exit plane for simulations with different numbers of mesh elements.

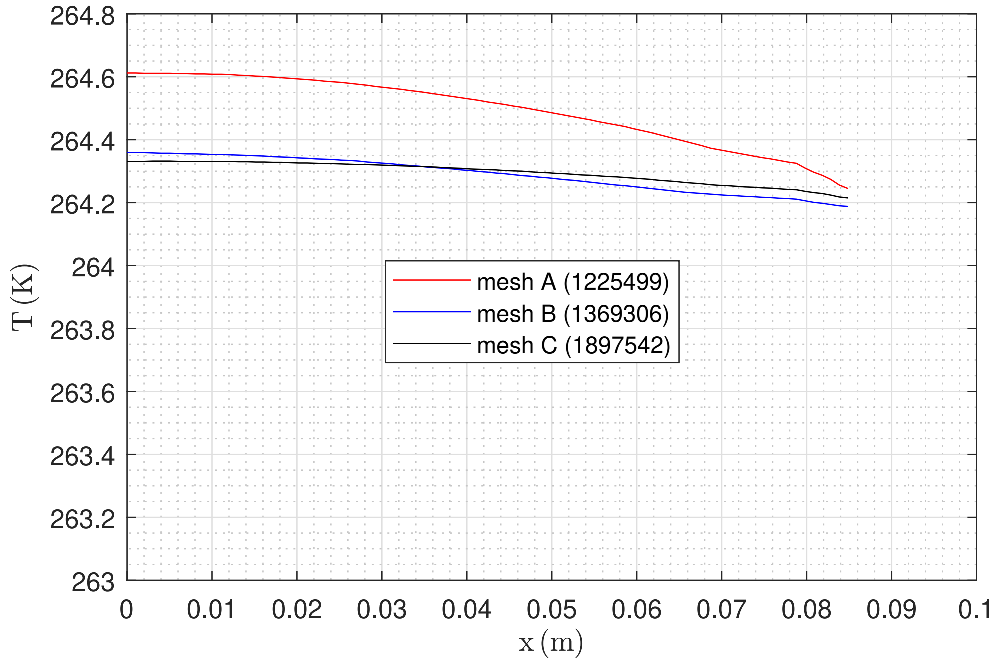


Figure 6.10: Simulated temperature distribution along the horizontal line from the axis of the test section at the icing jet nozzle exit plane for simulations with different numbers of mesh elements.

Table 6.1: Mesh number and size for both cases: wind tunnel and icing jet generator

| | Wind tunnel | | Icing jet generator | |
|---|---|---|---|---|
| Grid details | Original mesh | Adapted mesh | Original mesh | Adapted mesh |
| Cell no. | 1,395,108 | 1,618,653 | 1,897,542 | 1,970,930 |
| Face no. | 3,022,977 | 3,507,143 | 4,031,182 | 4,189,623 |
| Node no. | 378,215 | 439,571 | 463,961 | 483,807 |
| Max face size | 12 mm | 4 mm | 11 mm | 2.75 mm |

To demonstrate the level of symmetry in the results for both wind tunnel and icing jet generator in the horizontal and vertical directions, a comparison between the axial velocity along the horizontal symmetry plane and the vertical symmetry plane is presented in Figure 6.11. The velocity results in both cases are very similar. For the wind tunnel case, the maximum velocity difference between values along the horizontal and vertical lines is approximately 0.203 m/s and the maximum relative error is approximately 0.54 %. For the icing jet case, the maximum difference between values along the horizontal and vertical lines is approximately 0.633 m/s and the maximum relative error is approximately 4.4 %, indicating that a reasonable degree of symmetry has been achieved.

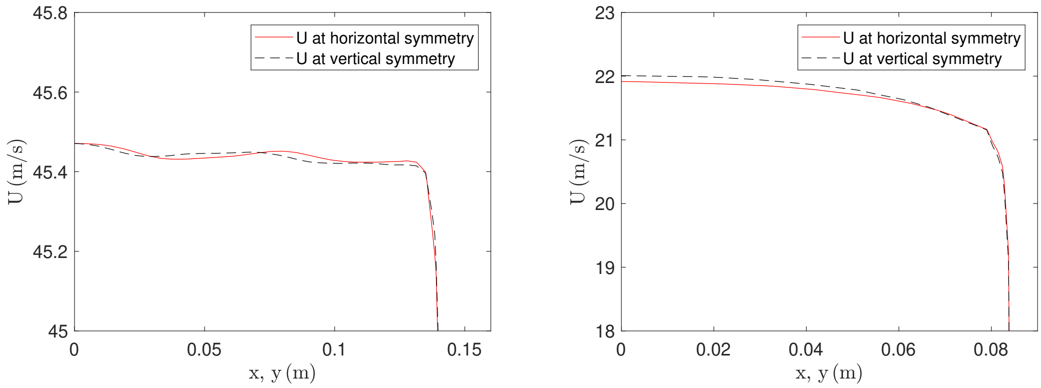


(a) (b)

Figure 6.11: Comparison of simulated velocity along horizontal and vertical symmetry lines. (a) Test section of wind tunnel (without screens and honeycomb, and for mesh of 1192390); and (b) Nozzle exit of icing jet generator (90° segment, and for number of mesh elements of 1897542).

## 6.5 Results

### 6.5.1 Wind tunnel

A comparison between the CFD results and experimental data for the static pressure distribution along the tunnel and the velocity in the test section was made to determine if the present implementation of the CFD model provides reliable results.

Figure 6.12 shows the static pressure along the wind tunnel with the three screen layers and honeycomb. Static pressure measurements were made along the wind tunnel wall at 24 points. The zero position of the z-axis represents the wind tunnel inlet plane, and 3.6 m corresponds to the downstream end of the conical diffuser. A generally good agreement between the CFD results and the experimental data has been achieved. Of particular note is the fact that the CFD simulates a slightly lower static pressure in the test section – the difference is about 100 Pa – with respect to the physical experimental data. The experimental velocity profile derived from the pitot pressure measurements

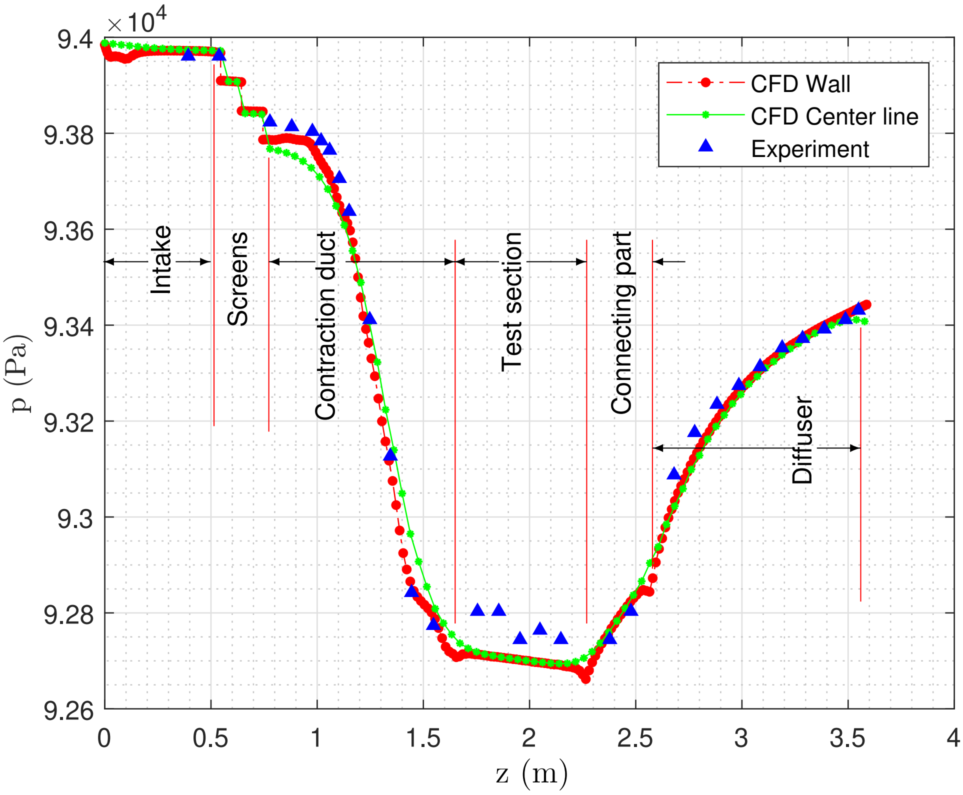


Figure 6.12: Static pressure along the wind tunnel with screens and honeycomb. Comparison between CFD simulation and experimental data.

agreed well with the CFD results across the wind tunnel test section as illustrated in Figure 6.13. Over the core flow region ($-0.13 \leq x \leq 0.13\,\mathrm{m}$), the average value of flow speed from the experiments is $42.4\,\mathrm{m/s}$ and the simulations over estimate the flow speed and the mean difference between the experiments and the simulation is $0.2\,\mathrm{m/s}$.

Experiments and simulations were also performed to assess the effect of removing the honeycomb and the three screen layers and results are presented in Figure 6.14. The results indicate relatively small changes in the static pressure values within the test section relative to the case illustrated in Figure 6.12. The average static pressure difference between the CFD and the experimental data in the no screens and honeycomb case is approximately 70 Pa in the test section region.

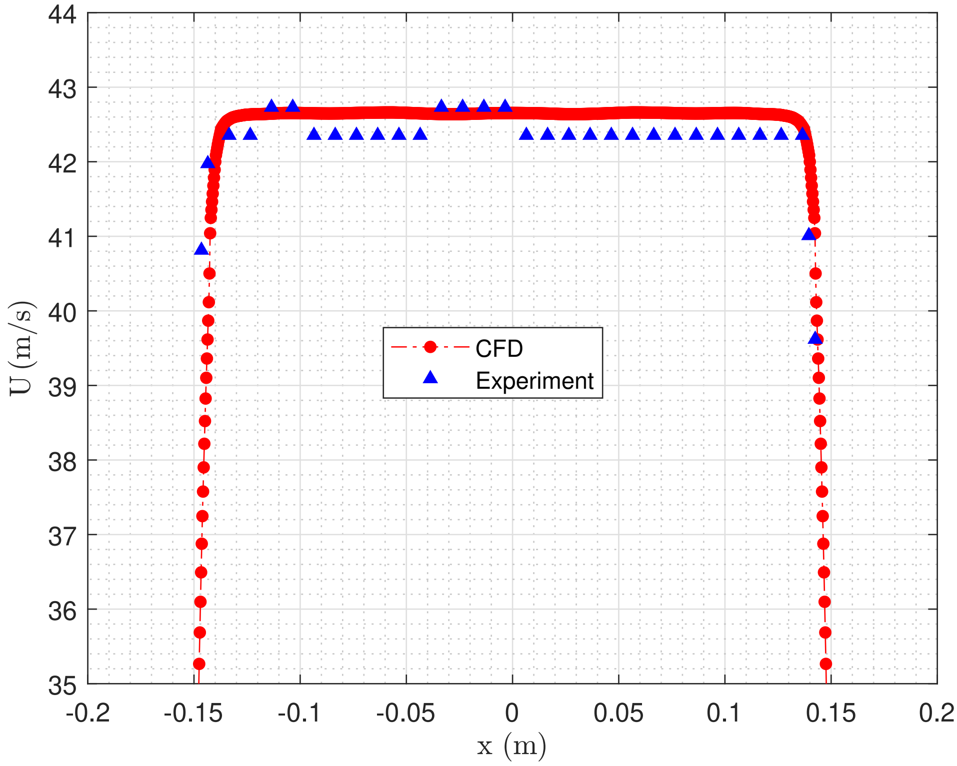


Figure 6.13: Velocity distribution across the test section in the case of the wind tunnel operating with screens and honeycomb. Comparison between CFD simulation and experimental data on the vertical centre plane of the test section.

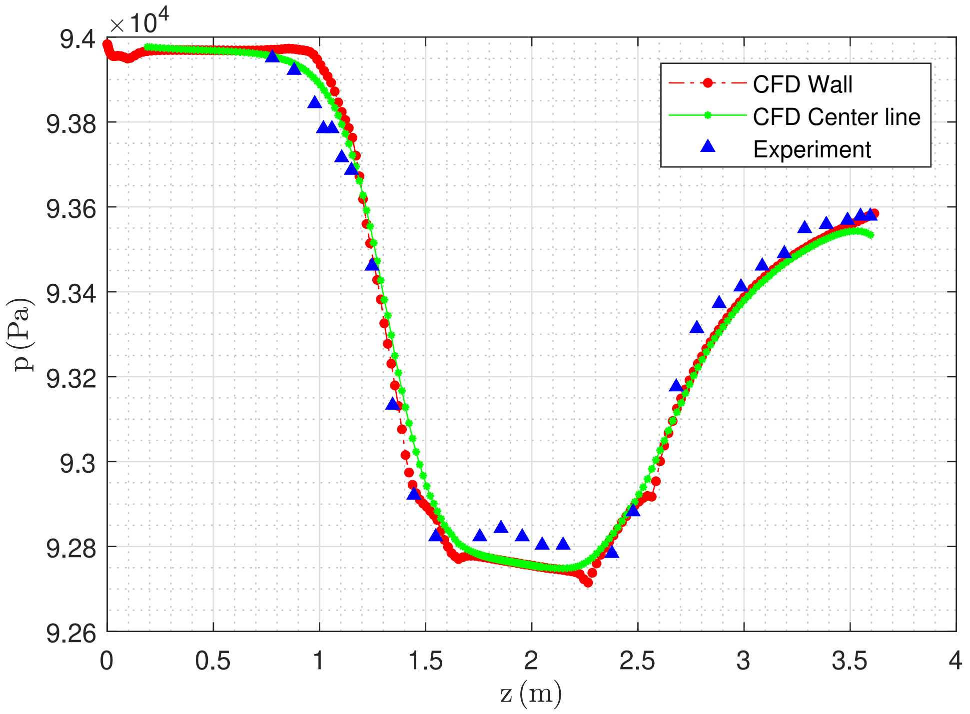


Figure 6.14: Static pressure along the wind tunnel operating without screens and honeycomb.

The main difference between the two cases, with and without screens and honeycomb, is observed in the static pressure values in the diffuser: the pressure in the screens and honeycomb case is lower than without these devices for the same boundary conditions as shown in Figure 6.12 and Figure 6.14. The velocity in the test section is higher when the screens and honeycomb are removed as illustrated in Figure 6.15. The loss of dynamic pressure through the screens and honeycomb directly affects the flow speed in the test section and the recovery of static pressure in the diffuser, but the test section static pressure is largely unaffected. From Figure 6.15 it is noted that in the case without the screens and honeycomb, the simulations also over estemate the flow speed in the test section. Over the core flow region, the mean of the experimental velocity data is 44.5 m/s. The difference between the experiments and simulated flow speed in the test section for the case without the screens and honeycomb is approximately 1.6 m/s across the core flow region ($-0.13 \leq x \leq 0.13$ m).

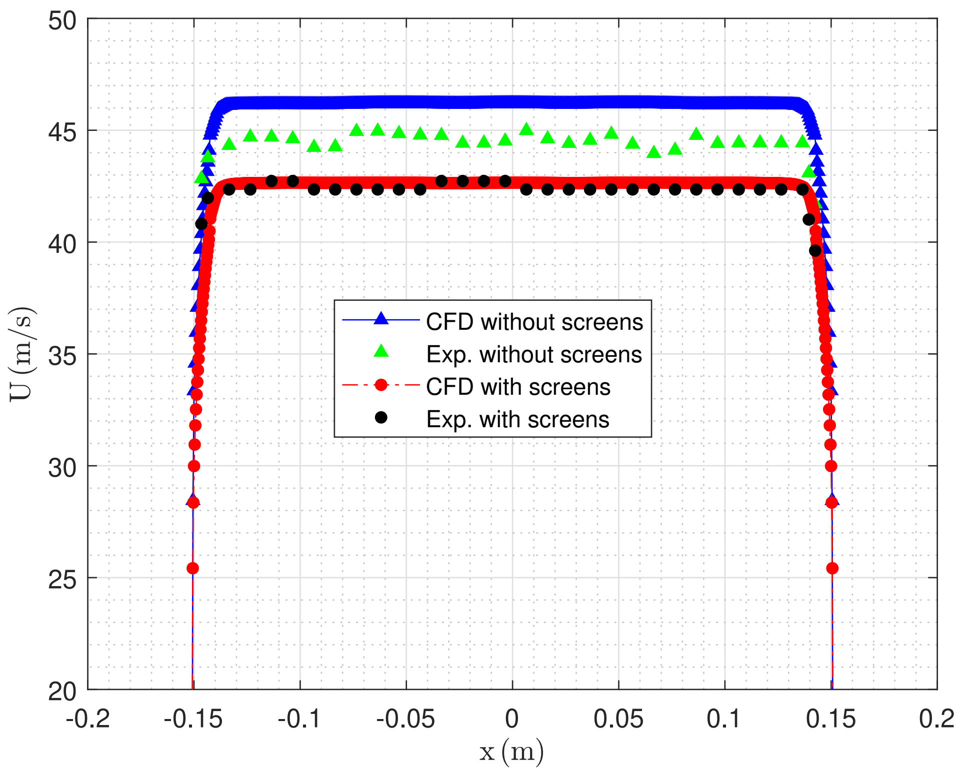


Figure 6.15: Velocity distribution across the test section in the wind tunnel. Comparison between the CFD simulations and experimental data with and without screens and honeycomb on the vertical centre plane of the test section.

### 6.5.2 Icing jet generator

Figure 6.16 shows a three dimensional colour rendering of the velocity distribution inside the icing jet generator. As shown in Figure 6.16, the warm air injection occurs via small orifices in the diffuser which enables the warm air from the shell to mix with the cold air mixture inside the core. The flow speed through all orifices within the conical diffuser wall is initially high, and then decreases gradually when the air mixes with the core. The velocity at the nozzle exit is approximately of 22 m/s. Figure 6.17 displays a two dimensional rendering of the velocity in the vertical symmetry plane. A uniformity of the flow speed at the nozzle exit has been achieved.

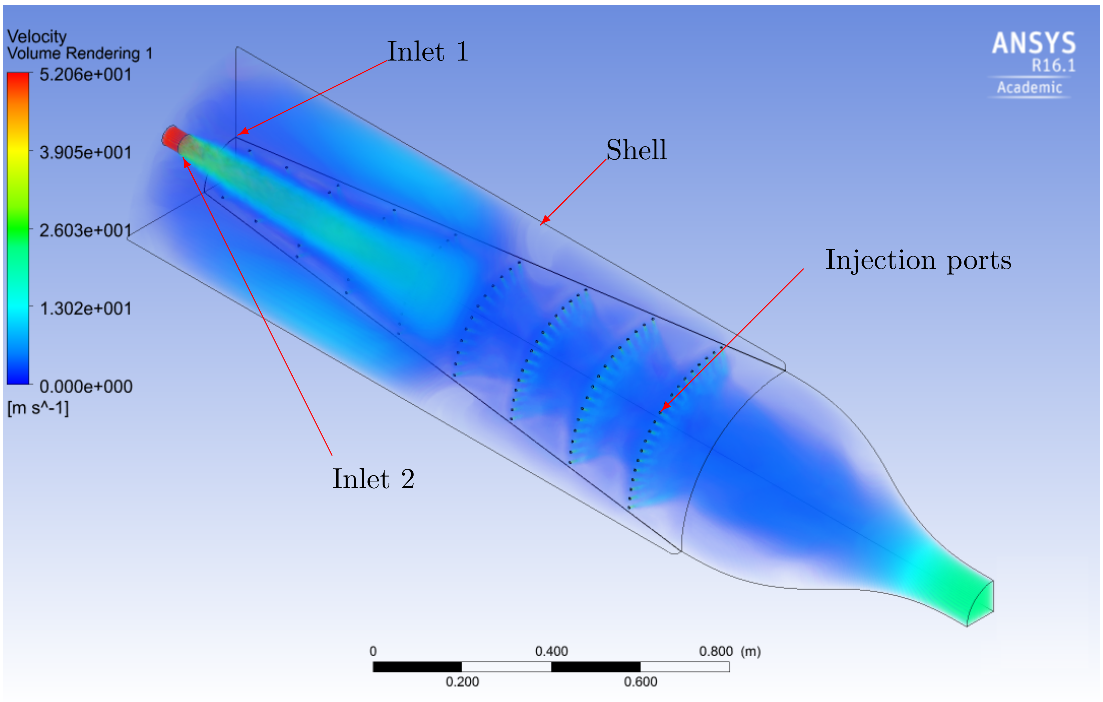


Figure 6.16: Three dimensional colour rendering of velocity in the icing jet generator(quarter segment).

Figure 6.18 illustrates the temperature distribution on the vertical symmetry plane of the icing jet generator. A good uniformity of flow temperature has been achieved at the exit of the nozzle. Based on the cold core flow temperature at Inlet 1 of $-160\,^{\circ}$C and the warm air temperature of $25\,^{\circ}$C at the Inlet 2, and the mixing ratio of $\mathrm{MR} = 4.5$, the expected fully-mixed temperature is approximately $-8.6\,^{\circ}$C, for adiabatic mixing. This full-mixed temperature value agrees closed with the CFD result observed in Figure 6.18.

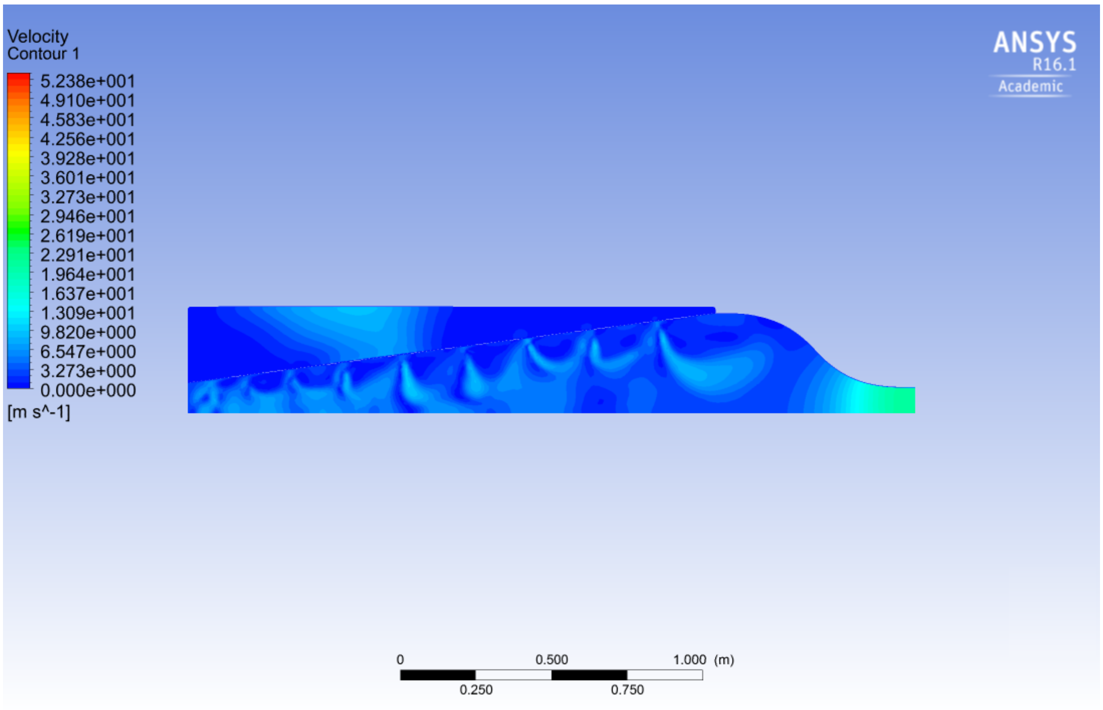


Figure 6.17: Two dimensional rendering of velocity magnitude in the Symmetry 1 plane of the icing jet generator.

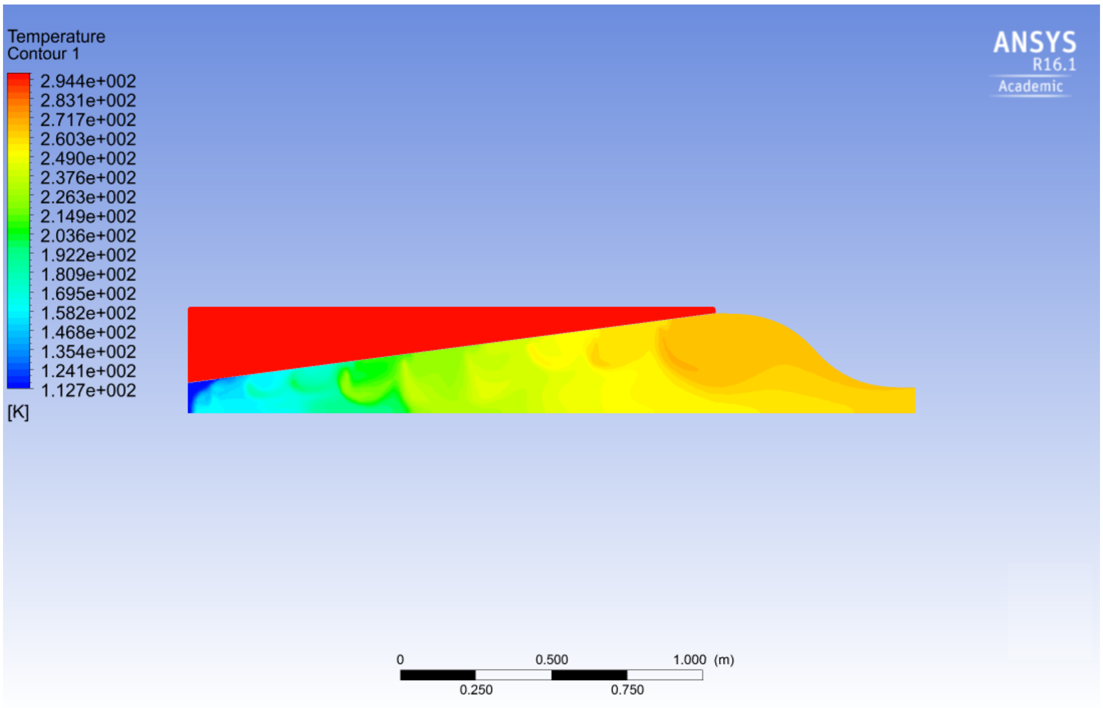


Figure 6.18: Two dimensional rendering of temperature in the Symmetry 1 plane of the icing jet generator.

### 6.5.3 Wind tunnel with icing bell mouth

To assess the icing bell mouth performance prior to fabrication, a CFD study with the proposed new configuration for the wind tunnel was performed. The new configuration of wind tunnel with the icing bell mouth as shown in Figure 6.19 was meshed and the boundary conditions and the CFD solution strategies outlined in Section 6.4.3 were applied.

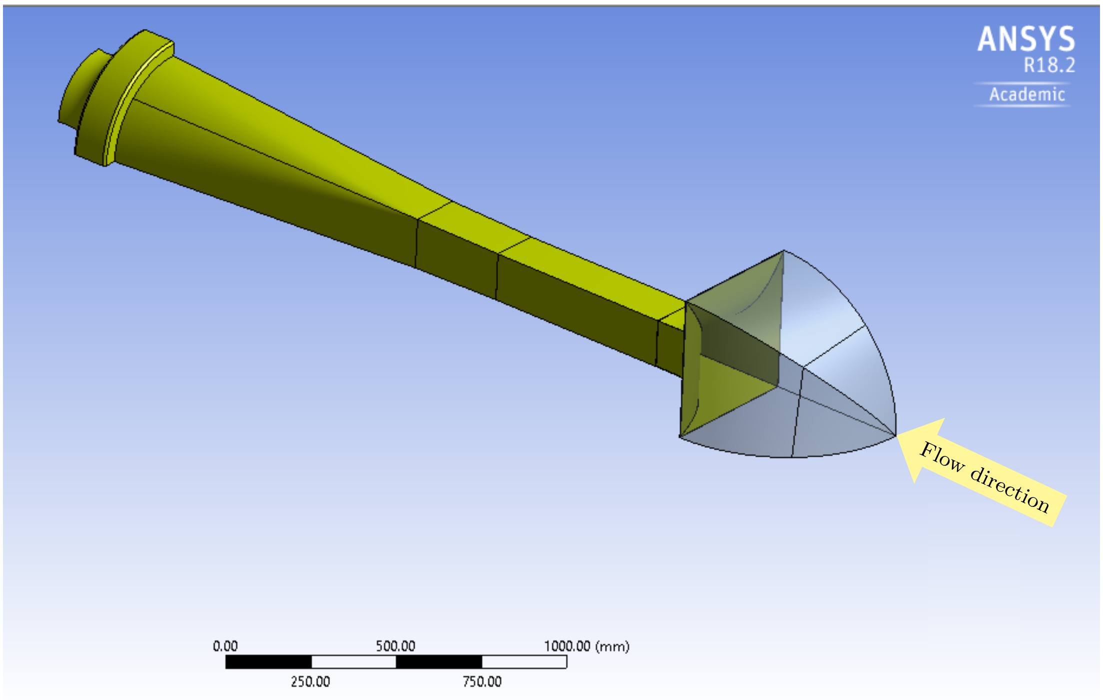


Figure 6.19: Geometry of wind tunnel with new bell mouth intake configuration (axisymmetric).

The simulation results for the test section flow velocity are presented in Figure 6.20 for two transverse horizontal lines: one in the middle, and the other at the entrance of the test section. The simulated velocity profiles indicated reasonable uniformity of the flow, so fabrication of the new bell-mouth proceeded. Experimental data for the new bell-mouth which have been obtained from the pitot static probe at the test section entrance are also presented in the Figure 6.20. The CFD results indicate that in the middle of the test section, the velocity uniformity should be very good while at the entrance, the velocity profile has a slight variation amounting to a deviation of about 1 m/s close to the centre of the test section. The experimental data for the velocity at the entrance to the test section are in good agreement with CFD results in terms of both the magnitude and distribution of the velocity. In this case, the computational simulations underestimate the magnitude of the measured velocity at the entrance to the test section, and the mean difference between the simulations and the experiments is 0.4 m/s. While the air flow is accelerated over a somewhat shortened intake path length compared with the original wind tunnel configuration, a good uniformity of flow velocity can still achieved within the test section.

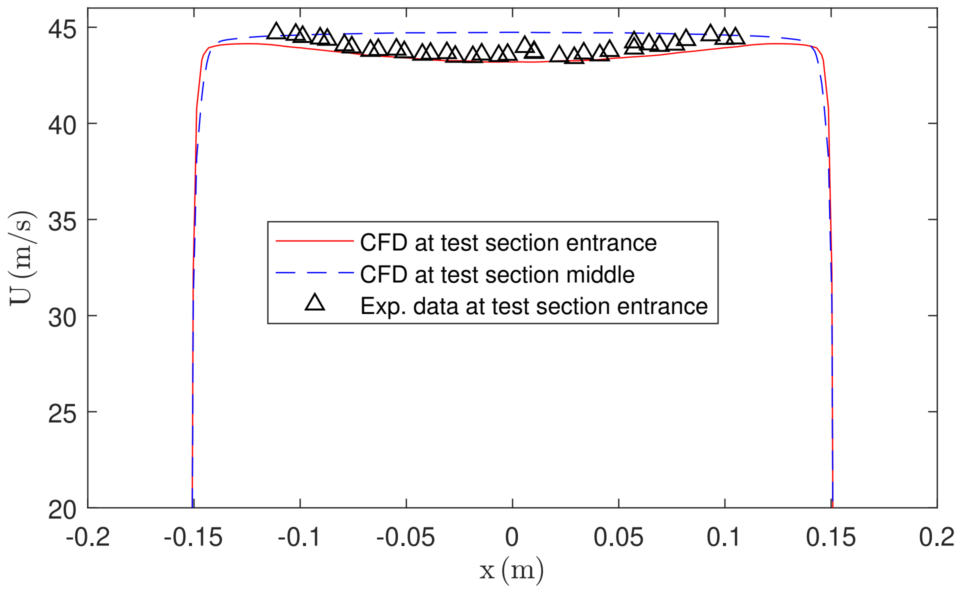


Figure 6.20: Velocity distribution within the test section for the wind tunnel operated with the icing bell mouth: comparison of experimental data and CFD simulations.

### 6.5.4 Icing jet generator combined with icing wind tunnel

The combined system consisting of the icing jet generator and the icing wind tunnel are treated as one unit and simulated in CFD. Like each part simulated before, a quarter geometry of combined system was simulated as shown in Figure 6.21. The icing jet nozzle exit was positioned at the test section entrance plane. Experimentally-derived flow conditions were applied as boundary conditions in the CFD model. The boundary conditions for the model are presented in Table 6.2.

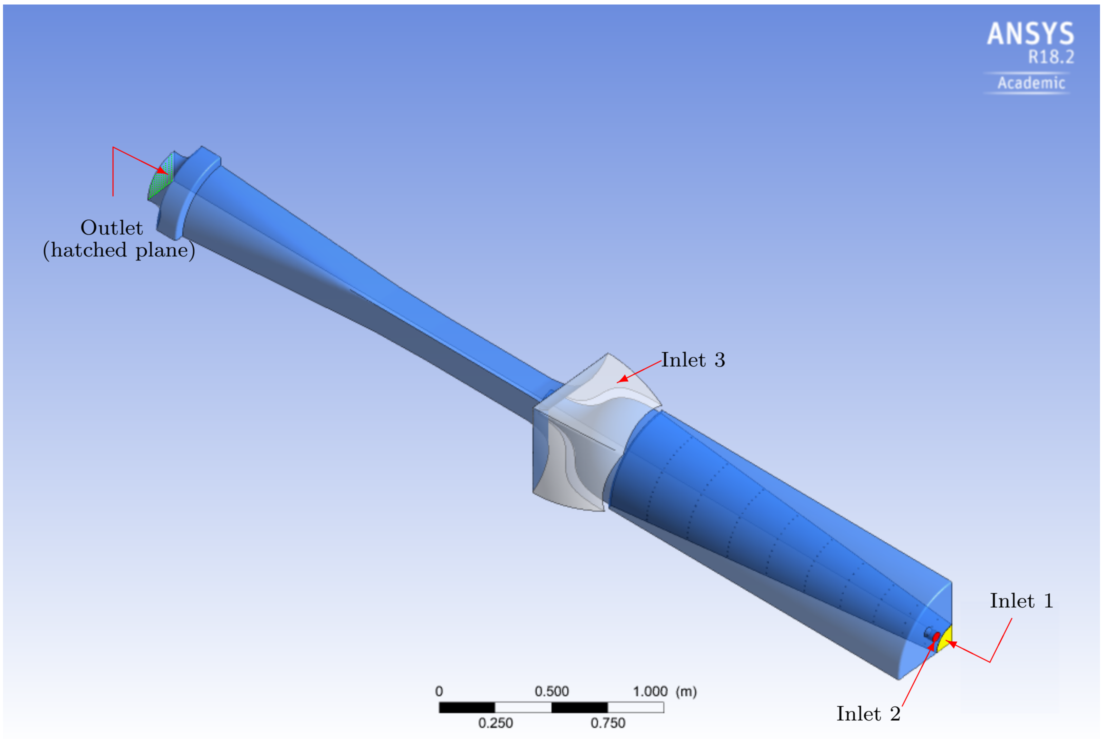


Figure 6.21: Geometry of the combined arrangement with icing jet generator and icing wind tunnel. A quarter of the combined system cross section has been modelled.

Table 6.2: Boundary conditions for simulation of the combined icing jet generator and icing wind tunnel system.

| Boundary | Description | Type | Units | Value | Temperature (K) |
|---|---|---|---|---|---|
| Inlet 1 | cold air mixture from spray guide pipe | mass flow inlet | kg/s | 0.05085 | 166 |
| Inlet 2 | warm air delivery to shell | mass flow inlet | kg/s | 0.1225 | 293 |
| Inlet 3 | warm air entering icing bell-mouth | pressure inlet | Pa | 0 | 293 |
| Outlet | exhaust | exhaust fan | Pa | -1200 | outcome |

Figure 6.22 illustrates the coordinate system adopted for presentation of results. Figure 6.23 shows the simulated velocity distribution at three positions on the horizontal symmetry plane for different $z$ locations. The mixing ratio in this case is $\mathrm{MR} = 2.41$. A uniform flow speed of approximately 30 m/s is simulated in the nozzle exit core flow

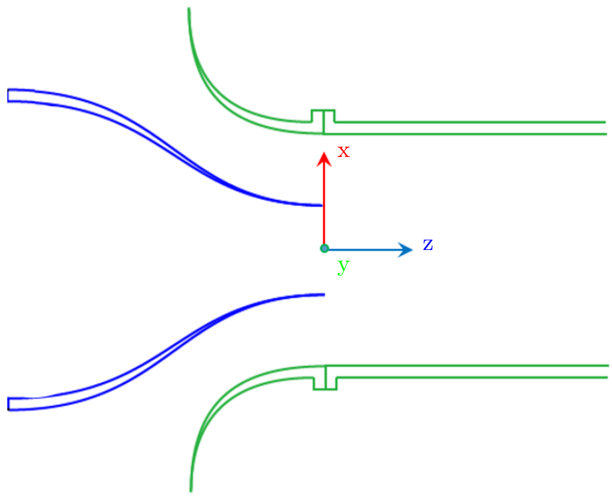


Figure 6.22: Illustration showing the arrangement and coordinate system for the icing jet nozzle and the test section of the wind tunnel.

as shown by the broken green line in the region ($-0.075 \leq y \leq 0.075\,\text{m}$) in Figure 6.23. In the vicinity of the nozzle lip ($y \approx -0.085$ and $y \approx 0.085\,\text{m}$) the velocity decreases to almost zero because this is in the wake region of the finite thickness nozzle lip. In the region $y < -0.09\,\text{m}$, the flow velocity is approximately $47\,\text{m/s}$ and this region corresponds to the warm air flow admitted by the icing bell-mouth. To validate the CFD simulations, experimental data of the velocity derived from the pitot probe traversed along the horizontal plane at the test section entrance were compared with the CFD results. The experimental data are in good agreement with simulated velocity as shown in Figure 6.23.

Results for the simulated flow speeds a several distances downstream of the icing jet nozzle exit were plotted to assess the development of the flow velocity in the jet core flow. The simulated velocity at $z = 305\,\text{mm}$ (corresponding to the middle of the test section) is slightly higher than the velocity at test section entrance ($z = 0\,\text{mm}$). The magnitude of the simulated velocity at $z = 50\,\text{mm}$ falls between the values at $0\,\text{mm}$ and $305\,\text{mm}$, but the velocity profile is less uniform than either of the other cases.

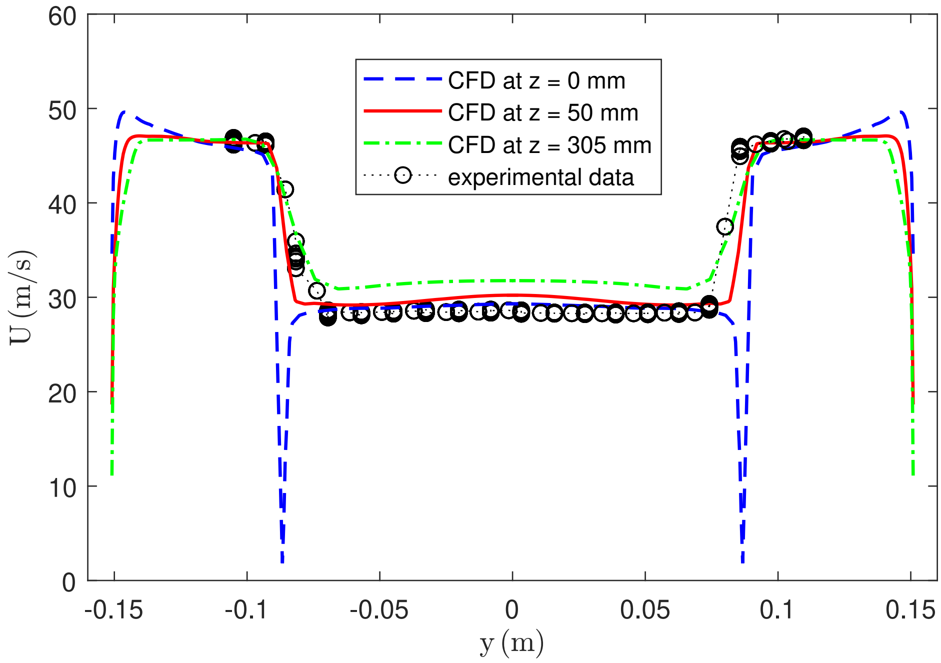


Figure 6.23: Velocity distribution across the test section in the combined facility at different positions. The simulation results have been mirrored around the $y = 0$ location.

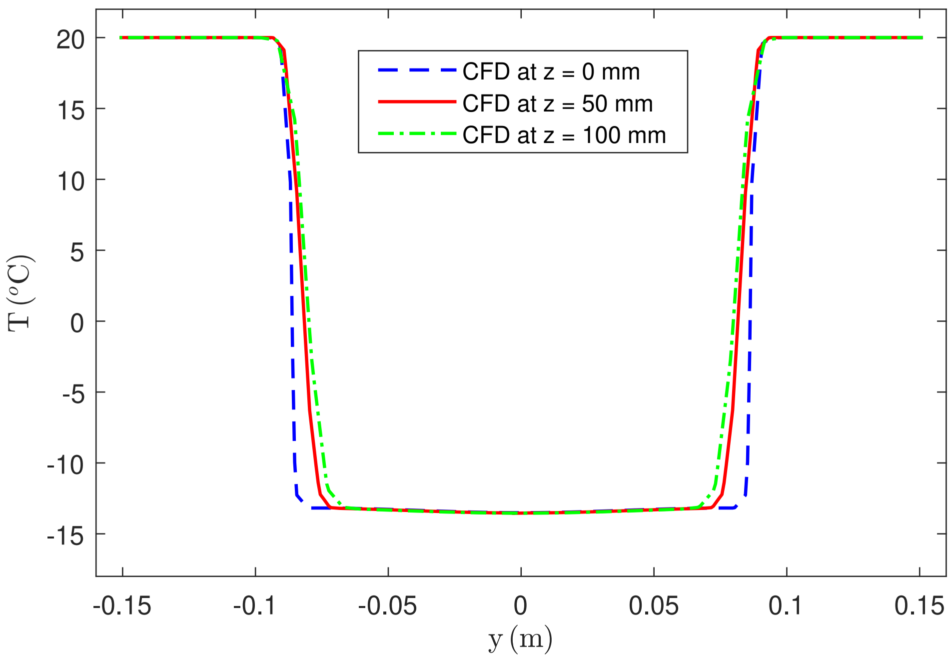


Figure 6.24: Illustration showing the development of the mixing layer between the cold core flow and the warm co-flowing stream at different positions in the test section. The simulation results have been mirrored around the $y = 0$ location.

Figure 6.24 shows the simulated temperature distribution at $z = 0$, 50, and 100 mm. As shown in the figure, the simulated temperature in the core region of the facility is reasonably uniform and is approximately $-13\,°C$ at the specified operating condition. Outside of the cold core flow, the temperature is also uniform and is approximately equal to room temperature, $20\,°C$. The mixing layer that develops from the trailing edge of the nozzle lip increases its thickness with downstream distance from the nozzle and this increasing thickness effect is reflected in the temperature distributions in the vicinity of $y = \pm 0.08$ m.

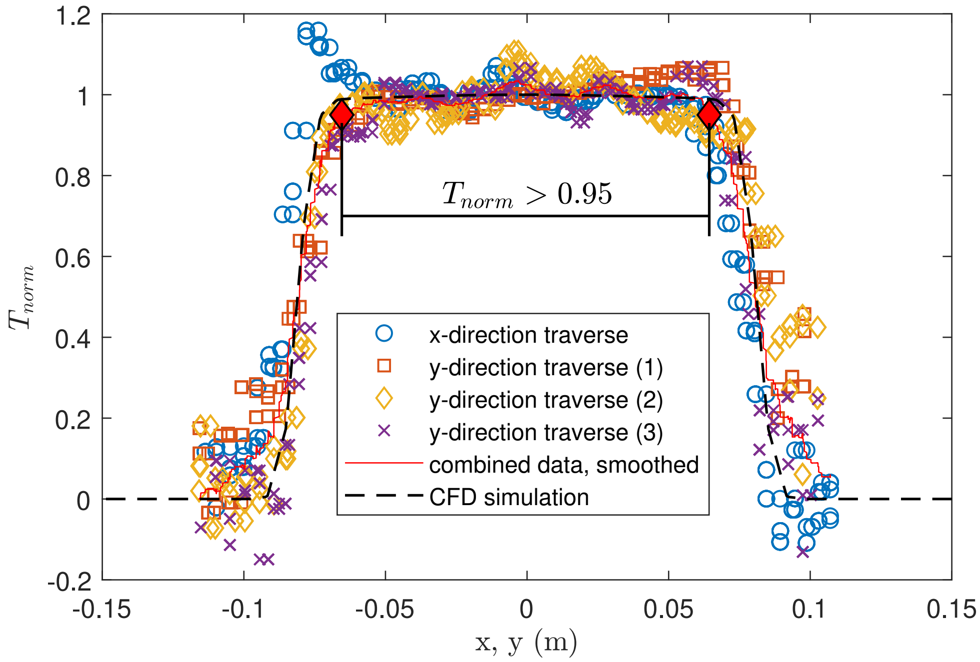


Figure 6.25: Temperature distribution across the test section in the combined facility showing a comparison of CFD simulations results at $z = 100$ mm and experimental measurements in normalised form.

Figure 6.25 shows the comparison between the CFD simulations and the experimental data for the temperature distribution in normalised form at $z = 100$ mm. The form of normalisation applied to both the CFD simulations and the experimental data is

$$T_{norm} = \frac{T - T_{cf}}{T_{core} - T_{cf}} \tag{6.1}$$

where $T$ is the local temperature in the stream, $T_{core}$ is the in the jet core near axis of the jet, and $T_{cf}$ is the temperature in the co-flowing stream external to the mixing layer. The results from the CFD were obtained at MR = 2.41 which simulates the operating conditions presented in Table 6.2. The experimental temperature measurements in Figure 6.25 were described in Chapter 5, Section 5.4 and were obtained from probe traverses in both $x$, and $y$. The simulated temperature distribution is very similar to the experimental data: the temperature is uniform in the core of the jet in both the simulation and the experiments, and the jet width is also similar in both the simulation and the experiments. The region in which the combined and smoothed data has values of $T_{norm} > 0.95$ extends from $-65.4$ mm to $+64.3$ mm whereas the CFD simulations gives this same zone as $\pm 72.4$ mm.

### 6.5.5 Effect of mixing ratio

To study the effect of different values of air mass flow rates introduced through the perforated diffuser on the velocity and temperature magnitude and uniformity, an additional five cases with different mixing ratios were simulated. The mixing ratio in the present context is the mass flow rate ratio of the warm air introduced through the perforated diffuser to the cold air mixture in the diffuser core flow. For these simulations, the mass flow rate boundary condition at Inlet 1 was held constant and equal to the experimental value of 0.05085 kg/s (corresponding to a quarter of the total mass flow rate) with total temperature of 166 K ($-107$ °C). The air mass flow rate introduced through the perforated diffuser wall (Inlet 2) was varied to produce the five mixing ratios: MR = 3, 3.5, 4, and 5 and the air temperature for Inlet 2 was specified as a temperature of 20 °C.

Figure 6.26 shows the velocity distribution at $z = 0$, the zero on x-axis representing the axis of the test section and the value of 0.15125 m representing the side wall of the test section. The velocity in the icing jet core region of the test section increases with increasing mixing ratio, caused by increasing the mass flow rate entering through the perforated diffuser. The icing jet core flow speed approximately matches that of the co-flow at MR between 4 and 5. Figure 6.27 shows the velocity distribution at $z =$ 100 mm. With the flow progression from the nozzle exit to 100 mm downstream from the nozzle exit, the velocity uniformity is improved in both jet and co-flow region in the test section. The thickness of the velocity shear layer between the jet and the co-flow seems to be independent of the mixing ratios and is equal to approximately 25 mm at

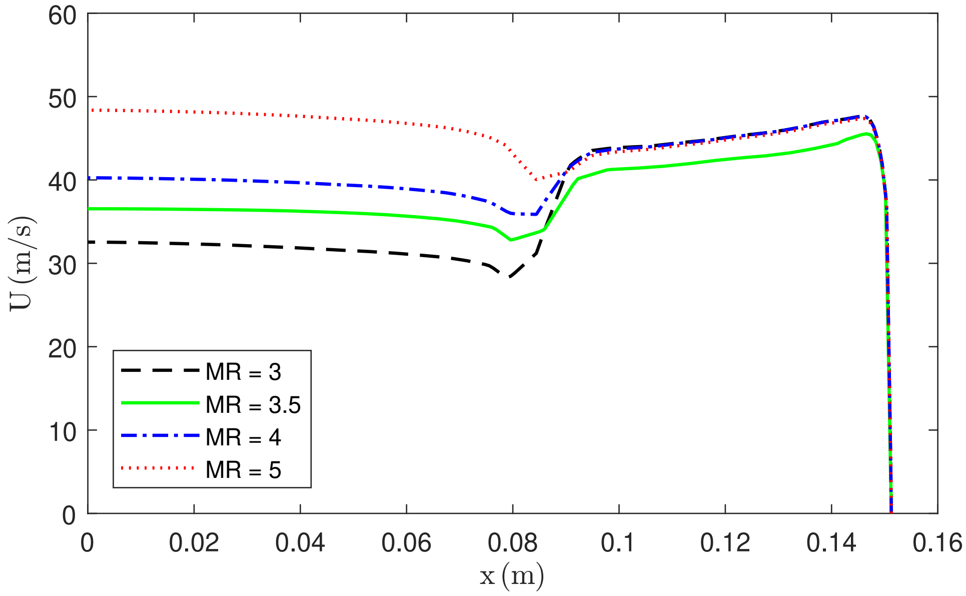


Figure 6.26: Simulated velocity distribution across the test section at $z = 0$ for different mixing ratios.

100 mm downstream.

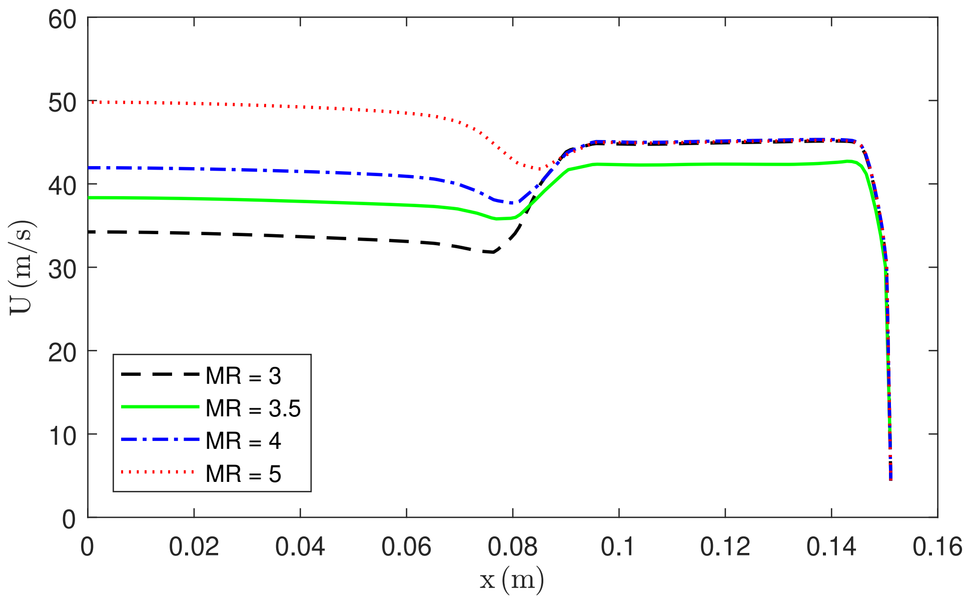


Figure 6.27: Simulated velocity distribution across the test section at $z = 100$ mm for different mixing ratios.

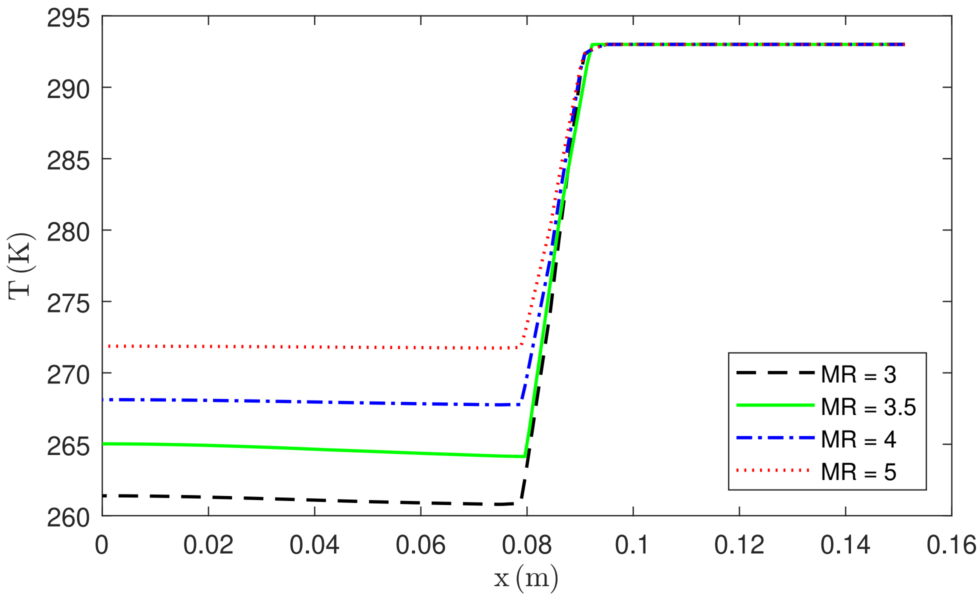


Figure 6.28: Simulated temperature distribution across the test section at $z = 0$ for different mixing ratios.

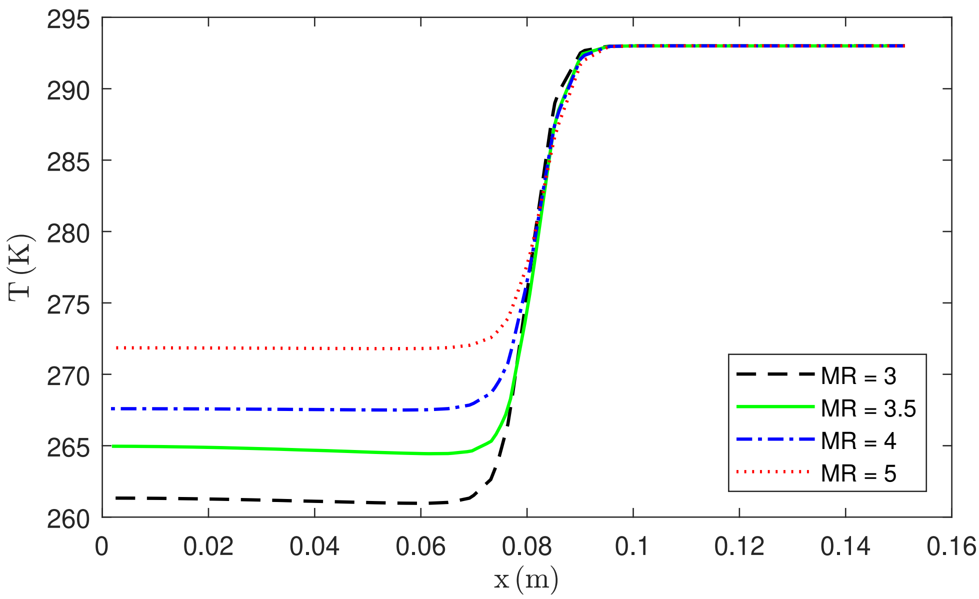


Figure 6.29: Simulated temperature distribution across the test section at $z = 100\,\mathrm{mm}$ for different mixing ratios.

Figure 6.28 shows the temperature distribution at $z = 0$. A good uniformity of temperature is simulated at all of the different mixing ratios. The temperature at the test section inlet ranges between $-11.6\,^{\circ}\mathrm{C}$ for $\mathrm{MR} = 3$ to $-1\,^{\circ}\mathrm{C}$ for $\mathrm{MR} = 5$. Figure 6.29

shows the temperature distribution at $z = 100\,\mathrm{mm}$. The low temperature region of the jet spans up to a maximum radius of about 0.07 m, which indicates to a core flow diameter of around 0.14 m.

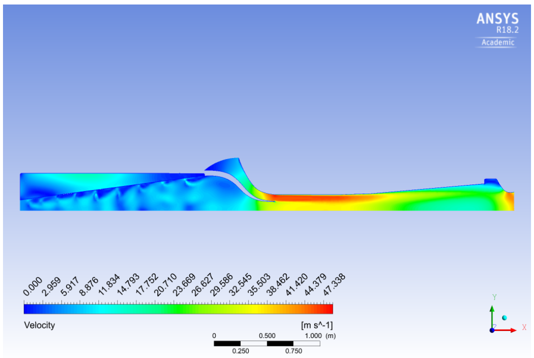


(a) Velocity for MR = 3.

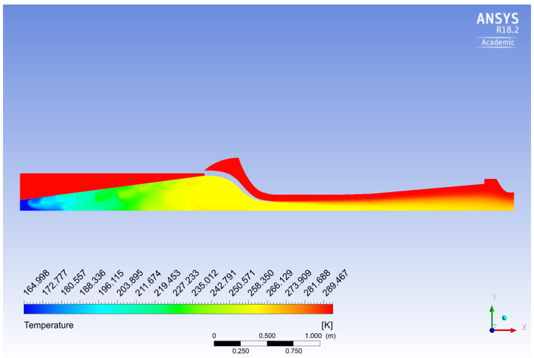


(b) Temperature for MR = 3.

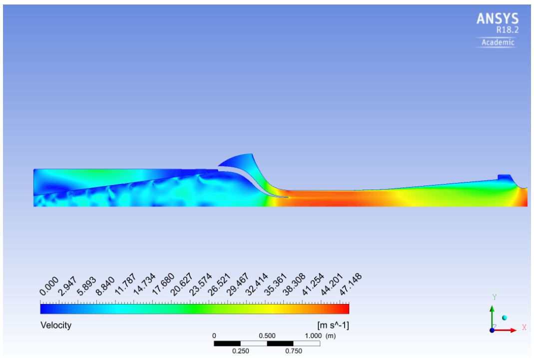


(c) Velocity for MR = 4.1.

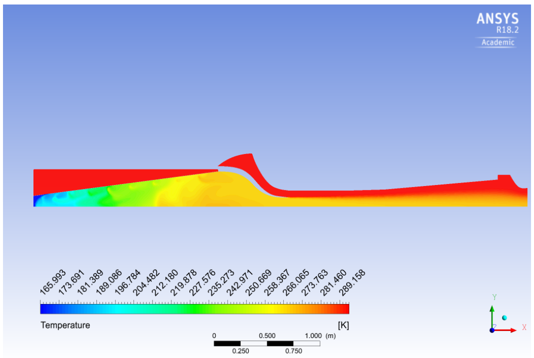


(d) Temperature for MR = 4.1.

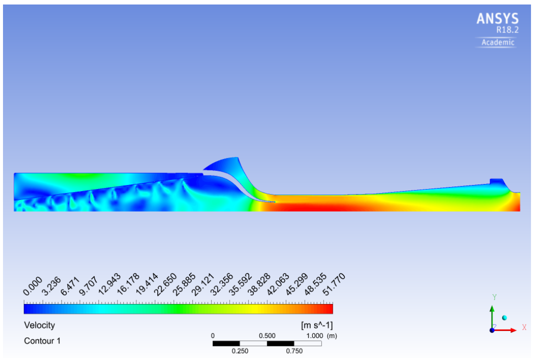


(e) Velocity for MR = 5.

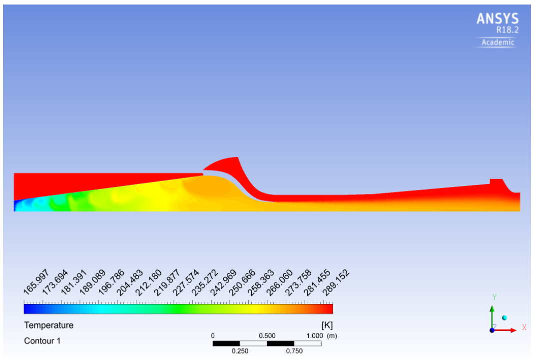


(f) Temperature for MR = 5.

Figure 6.30: Two dimensional contours in the horizontal symmetry plane of the combined icing jet and wind tunnel facility for operation at different mixing ratios. Local velocity distributions shown in the left hand column; temperature distributions shown in the right hand side.

Figure 6.30 shows the local velocity and temperature contours in the vertical symmetry plane for three mixing ratios. The local velocity difference between the nozzle exit velocity and the free stream velocity in the test section region is almost zero in the case of MR = 4.1, but is approximately $-10\,\mathrm{m/s}$ at MR = 3 and is approximately $+6.7\,\mathrm{m/s}$ at MR = 5. The temperature distribution for all three cases seems to be uniform within both the jet and the co-flow, but the temperature value in the jet is obviously a function of MR.

Figure 6.31 shows a comparison between the CFD simulations and the energy equation analysis results for the temperature at the icing jet nozzle exit for the different MR. The CFD results shown in this figure are values from the centreline of the jet whereas the energy equation analysis treats the flow as being fully mixed. Figure 6.31 demonstrates a good agreement was achieved between the CFD and the energy equation analysis for different mixing ratios, and this offers further confirmation that fully-mixed conditions are simulated in the CFD modelling.

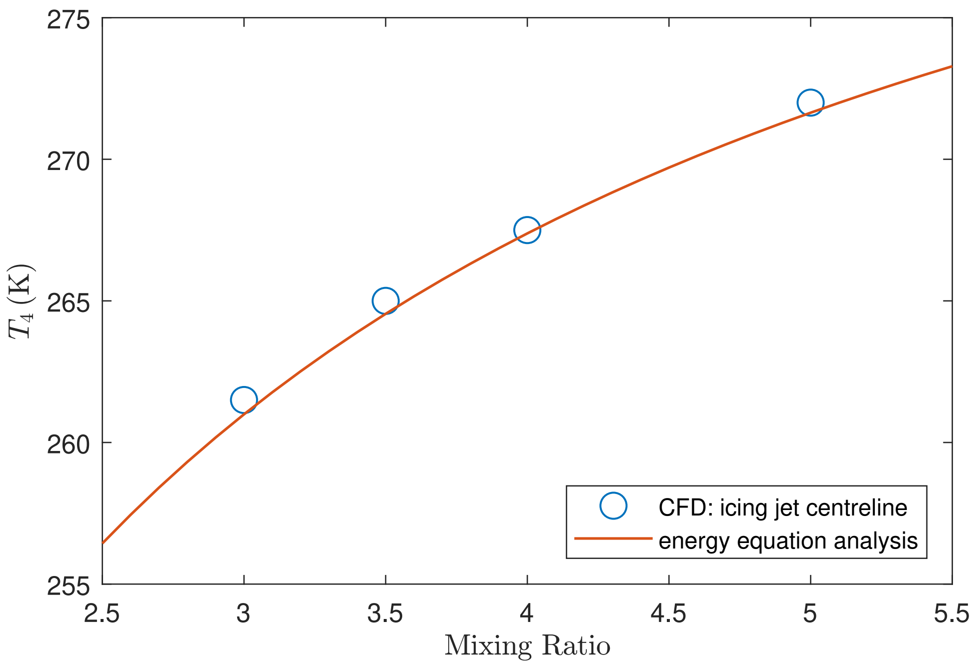


Figure 6.31: Comparison between CFD and energy equation analysis for the temperature of the icing jet exit for different mixing ratios.

## 6.6 Particle trajectory study

To study the effects of the ice particle size on the particle distribution at the icing jet nozzle exit, CFD simulations of the particle trajectory were performed. The study focused on the two main parts of the facility: (1) the icing jet nozzle plus wind tunnel; and (2) the perforated diffuser. A study was performed for each part separately to investigate particle accumulation in each part and how such accumulation may impact the overall facility performance.

The CFD simulations proceeded using the discrete phase model in Fluent to study the particle trajectories. For the icing jet nozzle plus wind tunnel simulations, spherical particles were injected normal to the inlet surface of the icing jet nozzle. Uniform particle diameters were simulated for six different cases in this study: 25, 50, 75, 100, 150, 200 $\mu$m. The particles were treated as solid ice particles in thermal equilibrium with the surrounding air stream. For these simulations, solution convergence was first achieved for representative experimental flow conditions, and the initial velocity of the injected particles was specified as 2 m/s to match the air velocity at the inlet section of the icing jet nozzle which varied between 1.86 and 2 m/s across the inlet radius. The overall mass flow rate of the particles was 3.5 g/s. Two types of Direct Phase Model (DPM) boundary condition for the walls were applied: reflected and trapped boundary conditions. Particles are not likely to bounce off the surface in a perfect manner as implied by the reflecting boundary condition, and nor are the particles likely to be fully trapped at the surface of the contraction. However, simulations from these two cases are presented because each produces different particle size distributions; the physical reality may lie somewhere between these two extremes.

Figure 6.32 shows the particle trajectories results on a symmetry plane of the icing jet nozzle and test section for particle diameters of 25, 75, and 150 $\mu$m for the case of the reflected boundary. Ice particles with the larger diameters are seen to impact on the contraction more than ice particles of small diameters. The zone over which the impacts occur is increased when the particle diameter increases and this zone indicates the region over which accumulation is likely to occur. Furthermore, because of the reflected boundary condition, there is a concentration of particles towards the centreline of the test section which is particularly pronounced for large particles, whereas a reasonable particle uniformity appears to be achieved for the smaller particles.

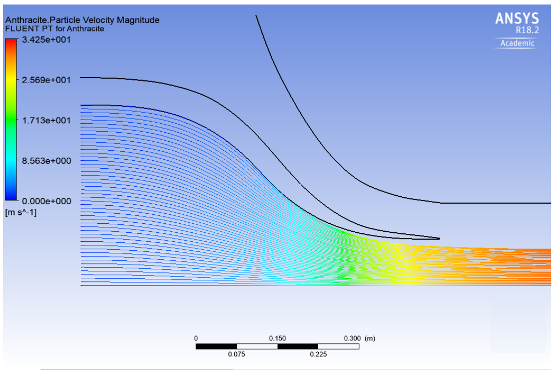


(a) PD=25 $\mu$m

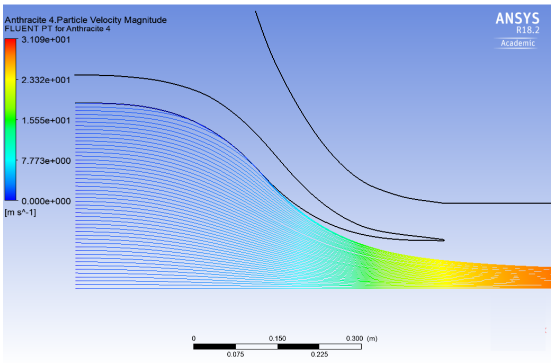


(b) PD=75 $\mu$m

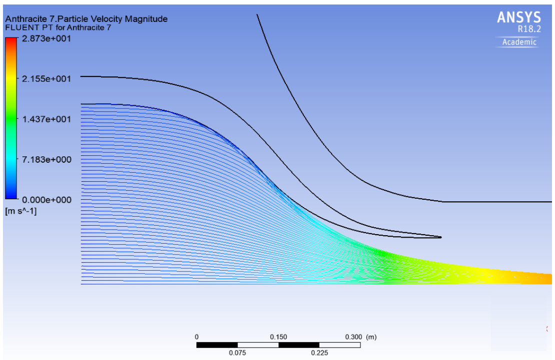


(c) PD=150 $\mu$m

Figure 6.32: Ice particles trajectories (coloured according to particle speed) in the icing jet nozzle and wind tunnel test section for reflected wall boundary condition on the contraction and particle diameters of 25, 50 and 150 $\mu$m.

Figure 6.33 compares the air flow path-lines and the ice particles trajectories for the 25 $\mu$m and the 200 $\mu$m diameter ice particle simulations. The smaller particles follow the air flow path-lines reasonably well, whereas larger particles have a ballistic component.

Figure 6.34 shows the variation of the relative concentration of the ice particles across the icing jet nozzle radius for various particle diameters for the case of the reflected boundary. For this analysis, the relative concentration is defined as the number of ice particles per unit annular area at any given radius on the icing jet nozzle exit plane ($n_p$) divided by the total number of particles at the same plane ($n_T$). As shown in Figure 6.34, a reasonably uniform distribution of ice particles is achieved for diameters of 25 and 50 $\mu$m. For example, within a radius of 67 mm on the icing jet nozzle plane,

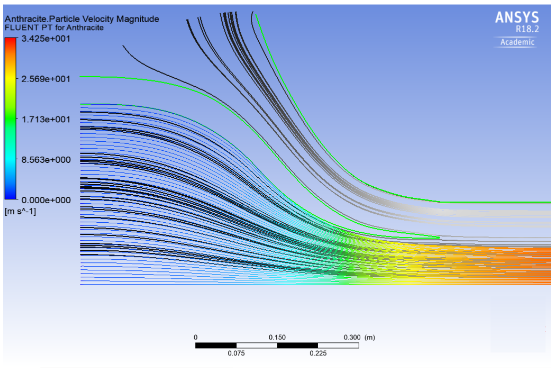


(a) PD=25 $\mu$m

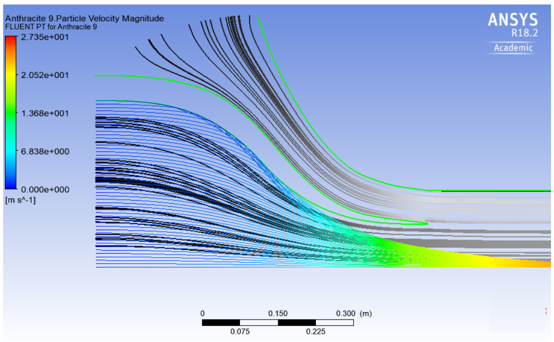


(b) PD=200 $\mu$m

Figure 6.33: Ice particles trajectories (coloured according to particle speed) and air flow path lines (grey scale) in the icing jet nozzle and wind tunnel test section for reflected wall boundary condition on the contraction and particle diameters of 25 and 200 $\mu$m.

the average concentration was $2.2\times10^{-4}\pm0.45\times10^{-4}$ per mm$^2$ for 25 $\mu$m particles, and within a radius of 56 mm on the icing jet nozzle plane, the average concentration was $3.02\times10^{-4}\pm0.6\times10^{-4}$ per mm$^2$ for 50 $\mu$m particles. The large particles tend to be concentrated near to the centre of the icing jet nozzle exit. The peak values of relative concentration for each particle diameter are located toward the outer regions of distribution. The reflected boundary on the wall of the contraction contributes to this peak in concentration. The non-uniformity in particle concentration becomes particularly pronounced in the region between radii of 20 and 40 mm for particles larger than 75 $\mu$m.

Figure 6.35 shows the variation of the relative concentration of the ice particles across the icing jet nozzle radius for various particle diameters for the case of the trapped boundary. In this case, the total number of particles which exit from the icing jet nozzle is different for each particle size because more of the larger particles impact the wall of the nozzle contraction because of their larger inertia. Figure 6.35 indicates the difference between the peak and the average concentration for each particle diameter is lower relative to the reflected boundary simulations.

Table 6.3 presents the total number of particles injected on the inlet plane of the icing jet nozzle, the number of particles trapped on the contraction wall, and the percentage loss of particles which represents the simulated percentage loss of TWC by the contraction

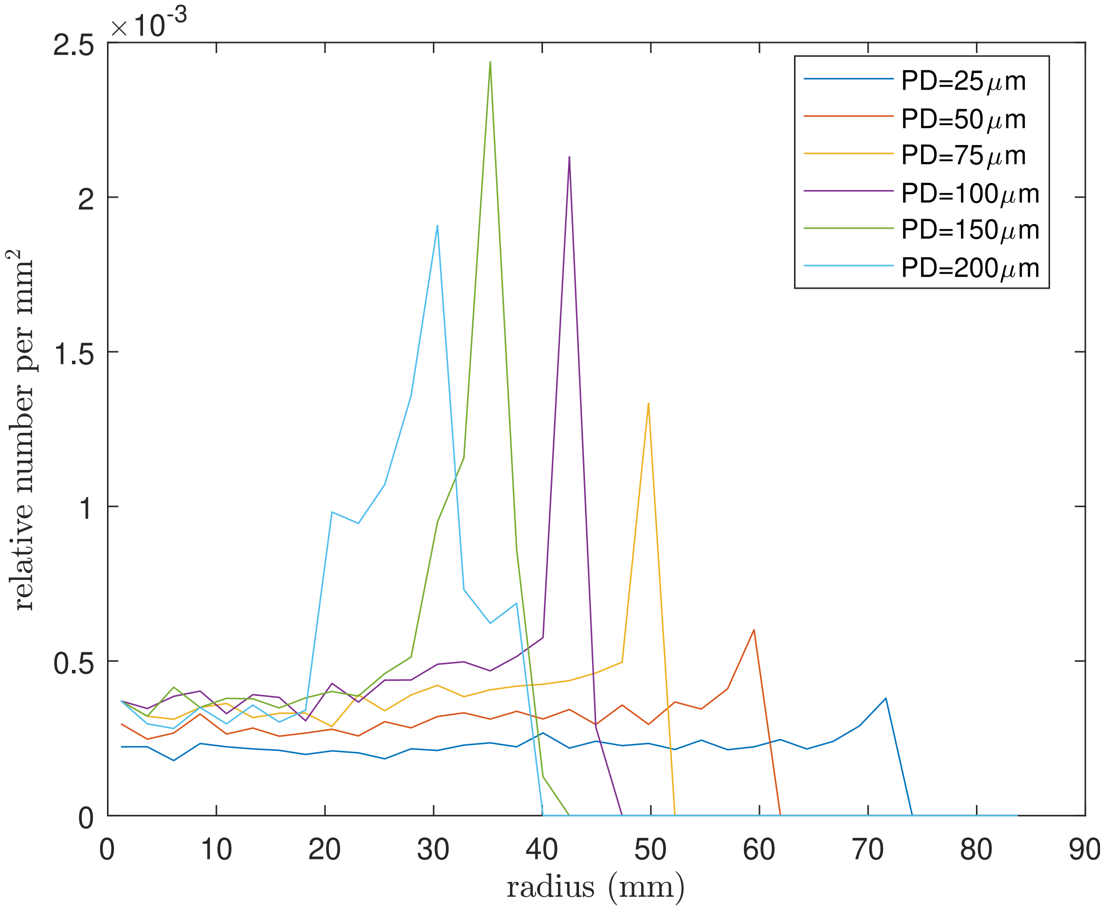


Figure 6.34: Concentration of the ice particles with the radial distance from the centreline at the icing jet nozzle exit plane for the reflected boundary condition simulations.

wall for different particle diameters. As the particle diameter increases the number of the trapped particles is significantly increased, and this can be linked with area of impingement illustrated in Figure 6.32. The simulated loss in the TWC for the contraction varies between 11.7 and 25 % as the particle diameter is varied from 50 to 100 $\mu$m.

Table 6.3: Simulated results of the percentage loss of the particles for the icing jet nozzle.

| Particle diameter PD ($\mu$m) | Total number of inlet particles $n_T$ | Number of trapped particles $n_t$ | $\frac{n_t}{n_T} \times 100\%$ |
|---|---|---|---|
| 25 | 2910 | 173 | 5.94 |
| 50 | 2910 | 341 | 11.7 |
| 75 | 2910 | 560 | 19.24 |
| 100 | 2910 | 727 | 24.98 |
| 150 | 2910 | 1082 | 37 |
| 200 | 2910 | 1356 | 46.6 |

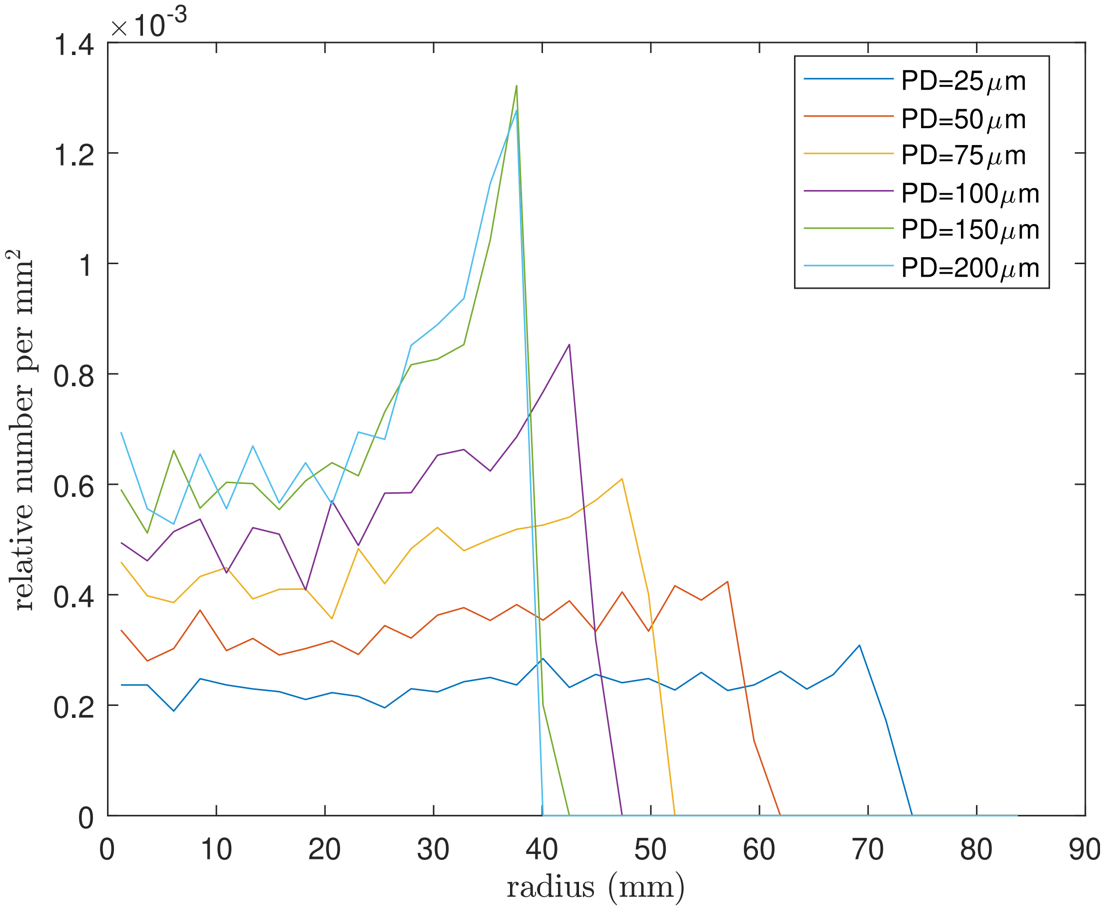


Figure 6.35: Concentration of the ice particles with the radial distance from the centreline at the icing jet nozzle exit plane for the trapped boundary condition simulations.

To investigate the quantity of TWC loss in the perforated diffuser, additional simulations were performed with the trapped boundary conditions for the perforated diffuser. The particles were injected from the perforated diffuser inlet, and Table 6.4 presents the total number of particles injected in the inlet plane of the perforated diffuser, the number of particles trapped on the diffuser wall, and the percentage losses of the particles for the different particle diameters. The loss due to particle trapping in the perforated diffuser was higher than the loss in the icing jet nozzle contraction (compare Table 6.4 with Table 6.3). Also, in the perforated diffuser case, the small particles have a greater tendency to be trapped whereas the opposite is the case in the icing jet nozzle contraction. The high turbulence intensity generated by the air orifices appears to bring the small particles into contact with the walls. The results show that the maximum simulated percentage loss in the perforated diffuser varies between 20 and 34 % for particle diameters between 50 and 100 $\mu$m.

Table 6.4: Simulated results of the percentage loss of the particles for the perforated diffuser.

| Particle diameter PD ($\mu$m) | Total number of inlet particles $n_T$ | Number of trapped particles $n_t$ | $\frac{n_t}{n_T}\times 100\%$ |
|---|---|---|---|
| 25 | 752 | 383 | 50.94 |
| 50 | 752 | 348 | 34 |
| 75 | 752 | 194 | 25.8 |
| 100 | 752 | 147 | 19.55 |
| 150 | 752 | 107 | 14.23 |
| 200 | 752 | 79 | 10.51 |

In the experiments reported in Section 5.5, the added water concentration measured by the IKP was around $2\,\mathrm{g/m^3}$ whereas the total concentration based on injection flow rates was around $20\,\mathrm{g/m^3}$. The combined simulated TWC loss in the perforated diffuser and icing jet nozzle is approximately 45 % for particle diameters from 50 to 100 $\mu$m. Therefore there is still a significant fraction of the water mass that has not been accounted for in the simulations. The most obvious source of this discrepancy is the water mass trapped in the spray guide pipe which was observed to be significant in the experiments but has not been included in the simulations.

## 6.7 Conclusion

Computational simulations were initially performed to aid in the hardware design process. But following the development of the hardware (presented in Chapter 4), simulations of the wind tunnel, icing jet generator, and the combination of the wind tunnel with the icing jet generator were also performed to further evaluate the experimental results presented in Chapter 5, and assess the facility performance.

Two cases for the original wind tunnel configuration – with- and without screens and honeycomb – were simulated in order to validate the present application of the CFD tools prior to application in proposed design modifications. For both cases, the CFD results are in good agreement with static pressure data from the experiments with the largest difference in static pressures occuring in the test section: the static pressure data is 100 Pa higher than the simulations in the case of screens and honeycomb, and 70 Pa higher than the simulations in the case with no screens and honeycomb. The experimental velocity profile across the test section (derived from pitot-static data) also agreed well with the simulations: over the core flow region ($-0.13 \leq x \leq 0.13\,\mathrm{m}$), the mean difference between the experiments and the simulation was $0.2\,\mathrm{m/s}$ in the screens and honeycomb case (at a flow speed of approximately $42.5\,\mathrm{m/s}$), and $1.6\,\mathrm{m/s}$ in the case with no screens and honeycomb (at a flow speed of approximately $45.0\,\mathrm{m/s}$).

Having demonstrated a successful application of the computational tools in the simulation of the performance of existing hardware, CFD was then applied to the icing jet generator and the new icing bell-mouth design. For the icing jet generator, good uniformity in both the flow speed and flow temperature at the nozzle exit was simulated. For the icing bell-mouth, the CFD results indicate that at the entrance to the test section, the velocity profile has a slight variation amounting to a deviation of about $1\,\mathrm{m/s}$ across the core flow region, while further downstream, at approximately the middle of the test section, the velocity uniformity should be very good. The experimental data for the velocity at the entrance to the test section are in good agreement with CFD results in terms of both the magnitude and distribution of the velocity: over the core flow region ($-0.11 \leq x \leq 0.11\,\mathrm{m}$), the mean difference between the experiments and the simulation was $0.41\,\mathrm{m/s}$ at the test section entrance (at a flow speed of approximately $44.0\,\mathrm{m/s}$).

The combined system consisting of the icing jet generator and the icing wind tunnel operating together has also been simulated in CFD using experimentally-identified inlet conditions. The CFD simulations show: (1) a uniform flow speed of approximately $30\,\mathrm{m/s}$ in the icing jet nozzle exit core flow region ($-0.075 \leq x \leq 0.075\,\mathrm{m}$); and (2) a flow velocity in the co-flow region (in which the warm air flow is admitted to the test section by the icing bell-mouth) of approximately $47\,\mathrm{m/s}$. These CFD results are in good agreement with velocity data derived from the pitot-static probe traversed along a horizontal line at the test section entrance plane: at the test section entrance and over the core flow region ($-0.07 \leq x \leq 0.07\,\mathrm{m}$), the mean difference between the experiments and the simulation was $0.2\,\mathrm{m/s}$ (at a flow speed of approximately $28.5\,\mathrm{m/s}$), and over the co-flow region ($-0.11 \leq x \leq -0.085\,\mathrm{m}$, and $0.085 \leq x \leq 0.11\,\mathrm{m}$), the mean difference between the experiments and the simulation was $1.3\,\mathrm{m/s}$ (at a flow speed of approximately $46.5\,\mathrm{m/s}$). The CFD simulations and the experimental data for the temperature distribution in the icing jet nozzle flow have also been compared using a normalised form of presentation which demonstrates that the extent of the uniform core flow region of the icing jet is well simulated.

The effect of different perforated diffuser mass flow rates on the velocity and temperature distributions have been simulated. For the discussion of these results, a 'mixing ratio' was defined as the ratio of the mass flow rate of warm air introduced through the perforated diffuser to the mass flow rate of the cold air mixture entering the core of the diffuser. The temperatures on the axis of the jet icing exit for the different mixing ratios from CFD results are in good agreement with energy equation analysis. This outcome therefore offers another indication that essentially fully-mixed conditions should exist in the icing jet nozzle flow. For mixing ratios between 2.5 and 4.54, the icing jet nozzle exit flow should vary in temperature from from $-16.7\,^{\circ}\mathrm{C}$ to $-3\,^{\circ}\mathrm{C}$.

# Chapter 7

# Preliminary Testing

## 7.1 Introduction

Previous chapters have analysed the operating principles of the new facility, introduced the hardware components developed for the new facility, presented data to characterise the facility performance, and also assessed the facility performance through computational simulation. In this chapter, preliminary experiments on a test article – a cylindrical rod with an internal heating element – are described. The thermal performance of the article is characterised, and visualisation of the ice accretion is presented for glaciated conditions and for conditions with a non-zero melting ratio. A complete analysis of ice accretion results is not performed as further quantification of the actual flow conditions is needed for meaningful interpretation of the results. The results in this chapter are provided as an initial illustration of the utility of the new icing wind tunnel facility under representative flow conditions.

## 7.2 Test article

### 7.2.1 Configuration

The test article illustrated in Figure 7.1 was fabricated from a $\frac{1}{2}$" copper tube (the external diameter being 12.7 mm). The internal heating element was created by uniformly winding a nichrome heating wire (diameter of 0.6 mm) around a 2.75 mm diameter steel mandrel insulated by double layers of shrink tube. To enhance the heat transfer within

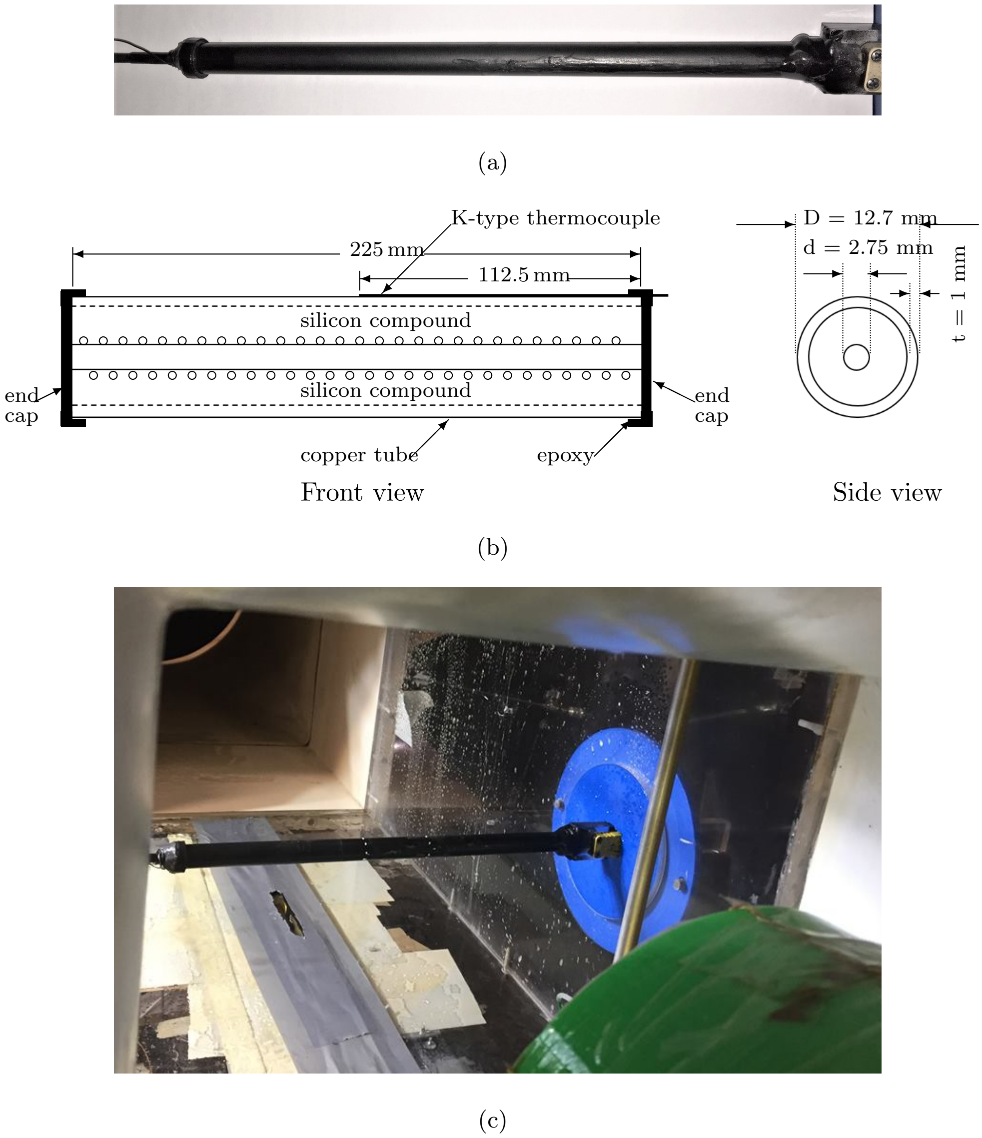


Figure 7.1: Illustration of the cylindrical test article. (a) Photograph of article; (b) Schematic diagram showing test article components; (c) Photograph of article installed in the wind tunnel test section, viewed from icing jet nozzle contraction.

the test article, the gap between the inner surface of the copper tube and the heater was filled with Silicone Heat Transfer Compound. The two ends of the copper tube were closed using plastic caps which were secured in place with epoxy.

A K-type foil thermocouple with thickness of 0.0005″ was bonded to the cylinder surface at the mid-span using cyanoacrylate cement. The surface of the cylinder was then painted black to enhance viewing of the ice accretion. The test article was installed perpendicular to the flow direction in the test section of the wind tunnel, with the aid of 3D printed circular base as illustrated in Figure 7.1.

### 7.2.2 Thermal analysis

#### 7.2.2.1 Convective heat transfer coefficients

To quantify the anticipated thermal performance of the test article, an assessment of heat transfer between the outer surface of the cylindrical test article and the test section flow is performed. The test article was positioned 150 mm from the test section entrance ($z$ =150 mm) and it was connected with one side wall in the test section. As the length of the test article is 225 mm, the article is longer than the icing jet exit diameter, but it does not fully span the width of the test section. As the test section flow has two characteristic velocities – one in the jet flow, and the other in the co-flow – the analysis proceeds by considering the possibility of two different heat transfer rates associated with these different velocities. Figure 7.2 illustrates the arrangement considered in the present analysis. To estimate the average heat transfer rate for each of the flow speeds, a correlation is applied for a cylinder at a uniform temperature $T_s$ in cross-flow as

$$\overline{Nu} = \frac{\overline{h}D}{k_\infty} = CRe_D^m Pr^n \left(\frac{Pr}{Pr_s}\right)^{0.25} \tag{7.1}$$

where $\overline{h}$ is the average heat transfer coefficient around the perimeter of the cylinder, $D$ is the cylinder diameter, $k_\infty$ is the thermal conductivity evaluated at the free stream temperature, $Re_D$ is Reynolds number based on diameter of the cylinder,

$$Re_D = \frac{\rho_\infty U_\infty D}{\mu_\infty}, \tag{7.2}$$

where $\rho_\infty$ is the free stream flow density, $U_\infty$ is the free stream flow velocity, and $\mu_\infty$ is the free stream flow dynamic viscosity. $Pr$ is the Prandtl number based on the free stream flow temperature, and $Pr_s$ is the Prandtl number based on the surface temperature of the cylinder.

The correlation constants $C$, $m$, and $n$ in Equation 7.1 depend on the flow conditions. For the present operating conditions which fall in the range $1 \times 10^3 \leq Re_D \leq 2 \times 10^5$, the appropriate values of the constants are $C = 0.26$ and $m = 0.6$, and for $Pr < 10$, $n = 0.37$ according to Žkauskas (1987). The difference in temperature between the flow and the test article will be relatively small, so we take $Pr = Pr_s$ and therefore we can re-write the correlation as

$$\overline{h} = 0.26 Re_D^{0.6} Pr^{0.37} \frac{k_\infty}{D} \tag{7.3}$$

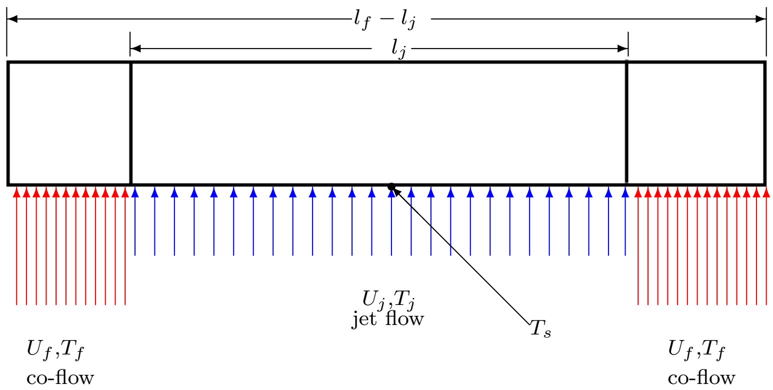


Figure 7.2: Illustration showing the test article subjected to jet and co-flow regions.

Equation 7.3 is applied separately to the jet and the co-flow since generally, these streams have different flow speeds and temperatures and thus, different heat transfer coefficient values are expected in the the jet $\overline{h}_j$ and the co-flowing streams $\overline{h}_{cf}$. At ambient temperature, in the jet at a flow speed of 28 m/s, $Re_D \approx$ 25,000 and in the co-flowing stream at a speed of 45 m/s, $Re_D \approx$ 40,000. Thus we expect a higher heat transfer coefficient in the co-flowing stream by a factor of $\overline{h}_{cf}/\overline{h}_j \approx 1.3$.

#### 7.2.2.2 Constant surface temperature model

If the surface temperature of the article is constant along its length and equal to $T_s$, then the convective heat transfer from the surface will be given by

$$\begin{aligned} Q_{conv} = Q_{cf} + Q_j &= \overline{h}_{cf} A_{cf} \left(T_s - T_{cf}\right) + \overline{h}_j A_j \left(T_s - T_j\right) \\ &= \overline{h}_{cf} \pi D l_{cf} \left(T_s - T_{cf}\right) + \overline{h}_j \pi D l_j \left(T_s - T_j\right) \end{aligned} \quad (7.4)$$

where $Q_{cf}$ is the heat transfer from the portion of the cylinder which is in the co-flow, $Q_j$ is the heat transfer from the part of the cylinder which is in the jet flow, $\overline{h}_{cf}$ is the average heat transfer coefficient around the cylinder in the co-flow region, $\overline{h}_j$ is the average heat transfer coefficient around the cylinder in the jet-flow region, $l_j$ is the length of the cylinder in the jet flow region and is assumed equal to the diameter of the nozzle exit (170 mm), and $l_{cf}$ is the remaining length of the test article (80 mm).

The constant surface temperature model might be reasonable in cases where the temperatures of the jet and the co-flowing streams are similar, and the heat transfer coefficient in each stream is similar. Having good heat conduction along the length of the article will also tend to make the surface temperatures along the length of the cylinder more uniform.

In the present case, the heat transfer coefficient in each stream differs by only about 30 %, the test article has a copper surface, and initial testing of the article was performed with an ambient temperature jet flow. Under such conditions, the constant surface temperature assumption seems reasonable. The validity of the constant surface temperature assumption can be tested through further analysis and ultimately, though experimentation.

#### 7.2.2.3 Constant heat flux model

To assess the validity of the constant surface temperature model suggested above, an alternative approach – based on the constant heat flux model – can be used. Justification for the constant heat flux model is derived from the fact that the heating wire was uniformly wound on the mandrel spanning the entire model length. Under these conditions, we can write

$$q_{conv} = \frac{Q_{elec}}{A_{total}} = \overline{h}_{cf}\left(T_{s,cf} - T_{cf}\right) = \overline{h}_{j}\left(T_{s,j} - T_{j}\right). \tag{7.5}$$

The ratio of the difference in the surface and flow temperatures in the different zones on the test article will therefore be given by

$$\frac{\overline{h}_{cf}}{\overline{h}_{j}} = \frac{T_{s,cf} - T_{cf}}{T_{s,j} - T_{j}}. \tag{7.6}$$

Consider first a case where ambient temperature conditions exist in both the jet and the co-flow: $T_j = T_{cf} = 20°\text{C}$, and the surface temperature of the article exposed to the jet is $T_{s,j} = 25°\text{C}$. Since $\overline{h}_{cf}/\overline{h}_j \approx 1.3$, we deduce from Equation 7.6 that in this case, $T_{s,cf} \approx 26.5°\text{C}$ so the difference in the surface temperature across the test article would be around 1.5°C only. While such a variation in surface temperature would be detectable, its magnitude is only about the same as the difference in temperature that exists between the jet flow and the co-flow when the jet is operated at nominally ambient conditions, see Section 5.4. Therefore, the constant surface temperature model appears justifiable if the article is operated in the jet flow at ambient temperature.

Consider now a case where the temperature in the jet is $T_j = -10°\text{C}$ and the temperature in the co-flow is $T_{cf} = 20°\text{C}$, and suppose the surface temperature of the article exposed to the jet is $T_{s,j} = 5°\text{C}$. If we again apply the approximation $\overline{h}_{cf}/\overline{h}_j \approx 1.3$, we deduce from Equation 7.6 that in this case, $T_{s,cf} \approx 39.5°\text{C}$ so the difference in the surface temperature across the test article would be 34.5°C. Therefore we cannot expect the constant surface temperature model to apply in this case.

### 7.2.3 Thermal measurements

Experiments have been conducted to measure the temperature of the test article when it was heated internally by the electrical resistance heater and operated in the facility with the jet and co-flowing streams, but without using liquid nitrogen to cool the icing jet flow. The following flow conditions prevailed in the jet and co-flow streams: $U_j \approx 28\,\text{m/s}$, $T_j \approx 21.5\,°\text{C}$; and $U_{cf} \approx 45\,\text{m/s}$, $T_{cf} \approx 20.3\,°\text{C}$.

The experiments involved establishing a range of steady-state heating conditions with a different electrical input power and recording the surface temperature indicated by the thermocouple bonded on to the mid-span point of the test article in each case. Table 7.1 presents the results in each case. Also included in the table are calculation of heat transfer rates based on the constant surface temperature model, using Equations 7.3 and 7.4, and the measured temperatures. The average heat transfer coefficients obtained from Equation 7.3 was $\overline{h}_j \approx 191\,\mathrm{W/m^2.°C}$ for the jet flow, and $\overline{h}_{cf} \approx 254\,\mathrm{W/m^2.°C}$ for the co-flow region.

The results in Table 7.1 show that the heat transfer calculated using the correlation and the constant surface temperature model is less than the measured electrical power for all operating conditions by between about 21 and 32 %, and the difference increases with increasing power and thus, with surface temperature. Under-estimation of the total convective heat transfer in this case is probably a consequence of the constant surface temperature model which treats the surface temperature of the portion of the test article in the co-flow as being the same as the surface temperature of the portion of the article in the jet flow. If constant heat flux conditions actually prevailed, the surface temperature in the co-flow region would be higher than in the jet flow region, thus causing additional convective heat transfer from the surface relative to the constant surface temperature model.

Table 7.1: Test article in ambient temperature jet flow experiments

| set | $T_s$ (°C) | $V$ (V) | $I$ (A) | $Q_{elec}$ (W) | $Q_j$ (W) | $Q_{cf}$ (W) | $Q_{conv}$ (W) | $\frac{Q_{conv}}{Q_{elec}} - 1$ |
|---|---|---|---|---|---|---|---|---|
| 1 | 23.3 | 9.4 | 0.69 | 6.49 | 2.65 | 2.45 | 5.10 | -0.21 |
| 2 | 26.0 | 13.7 | 1.02 | 14.0 | 6.30 | 4.73 | 11.0 | -0.21 |
| 3 | 26.5 | 14.4 | 1.06 | 15.3 | 6.96 | 5.14 | 12.1 | -0.21 |
| 4 | 27.8 | 17.0 | 1.26 | 21.4 | 8.62 | 6.18 | 14.8 | -0.31 |
| 5 | 29.5 | 19.2 | 1.42 | 27.3 | 10.9 | 7.64 | 18.6 | -0.32 |
| 6 | 32.8 | 22.5 | 1.66 | 37.4 | 15.3 | 10.3 | 25.6 | -0.32 |

Thermal imaging using an IR camera (FLIR C2) has also been performed to measure the distribution of surface temperature along the length of the test article. Results from this imaging are presented in Figure 7.3 for two cases: (a) the article was operated in the jet and co-flow with the jet operated at approximately 25 °C; and (b) the article was operated in the jet and co-flow with the jet operated at approximately −10 °C. In both cases, the electrical supply was adjusted to provide approximately 36.2 W of heating power to the test article. The temperature of the co-flow was approximately 24 °C for both cases. The red and blue solid lines in the top portion of Figure 7.3 show the variation in the average temperature deduced from the zones depicted as the broken red and blue lines in the images from the IR camera.

In the first case – the article operating in the ambient temperature jet flow, Figure 7.3(a) – the imaging detects some nonuniformity in the temperature distribution. Surface temperatures in the jet flow region are serveral degrees Celcius lower than the surface temperatures in the co-flow region. Unfortunately the measured temperature across the article is not particularly symmetric and the results are further complicated by a thermal disturbance associated with the foil thermocouple bonded to the copper surface. Taking the surface temperature of the article in the jet flow as being $T_{s,j} = 30°\text{C}$ – a nominal value identified from Figure 7.3(a) – based on Equation 7.6 (the constant heat flux model) we expect $T_{s,cf} = (1.3)(30 - 25) + 24 = 30.5°\text{C}$, only marginally warmer than the surface temperature in the jet region.

In the second case – the article operating in the cold jet flow, Figure 7.3(b) – strong temperature nonuniformity is detected. Taking the surface temperature of the article in the jet flow as being $T_{s,j} = 6°\text{C}$ – a nominal value identified from Figure 7.3(b) – based on Equation 7.6 (the constant heat flux model) we expect $T_{s,cf} = (1.3)(6-(-10))+24 = 44.8°\text{C}$, substantially warmer than the surface temperature in the jet region, and well in excess of the highest temperature registered by the thermal imaging. The strong temperature gradients along the surface of the article in this case cause a significant heat flux in the axial direction of the model, so neither the constant surface temperature nor the constant heat flux model will be applicable. Nevertheless, it is noted that the central portion of the test article has a zone of reasonably uniform temperature for an axial length equivalent to several test article diameters, making it suitable for initial experiments in the icing wind tunnel facility.

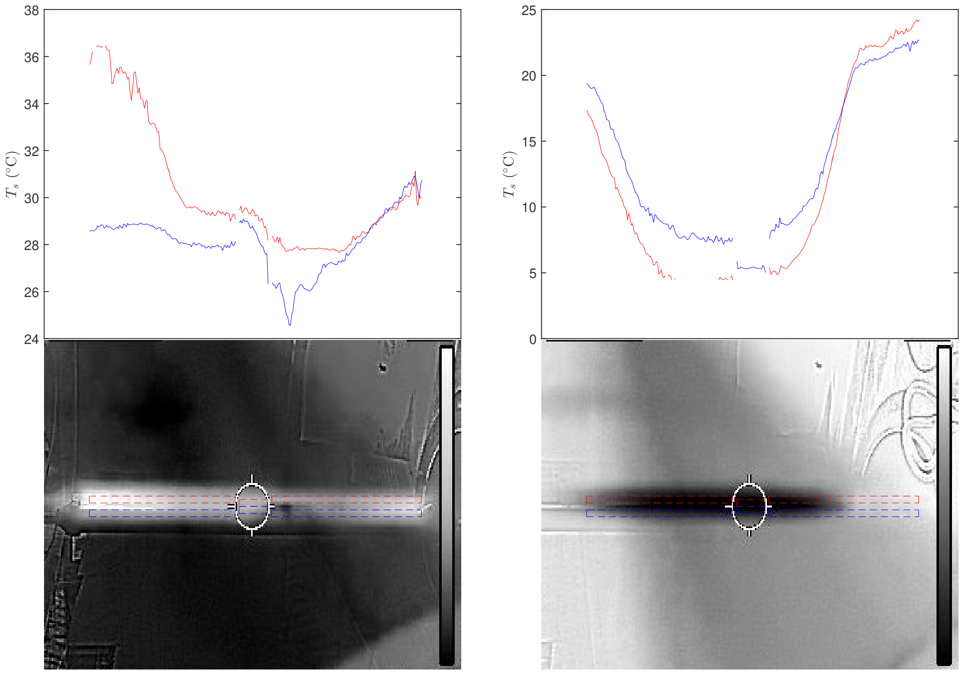


(a) (b)

Figure 7.3: Images from the IR camera showing surface temperature distributions the test article in (a) ambient temperature jet flow; (b) cold jet flow.

## 7.3 Preliminary ice accretion experiments

### 7.3.1 Experiment 1: Glaciated condition

Preliminary testing was performed to assess the performance of the icing wind tunnel under representative icing conditions. In this first test, approximately 15 litre of the liquid nitrogen was used with a valve-lift height of approximately 2.5 mm, resulting in an average icing jet nozzle exit flow temperature of approximately $-10$°C during the run time. The air was supplied to the atomiser nozzles at 5 bar, and the water pressure was at 4 bar. The heater was not actually used for the test article in this case. The wind tunnel fans were switched on and the nitrogen valve was opened prior to initiating the injection of the liquid water, which occurred after freezing temperatures were achieved in the icing jet nozzle exit flow, at approximately 30 seconds after initiation of the liquid nitrogen flow. The liquid nitrogen was exhausted approximately 98 s after initiation of the liquid nitrogen flow.

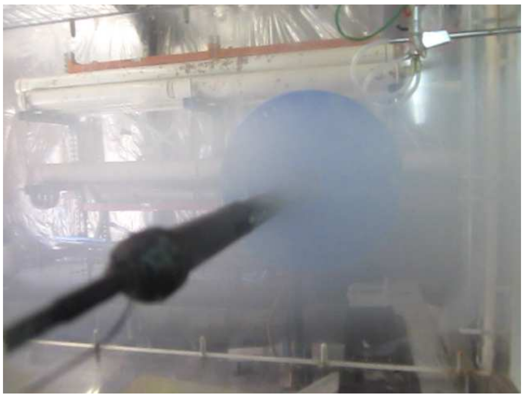

(a) t = 13 s.

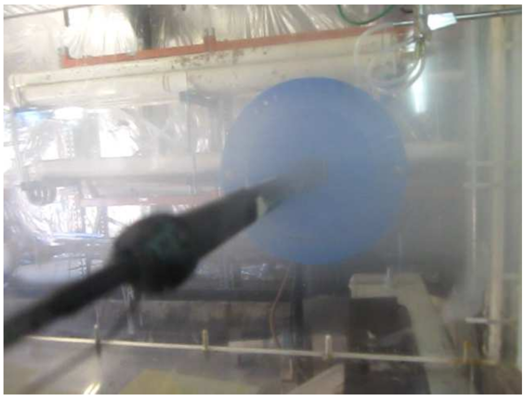

(b) t = 48 s.

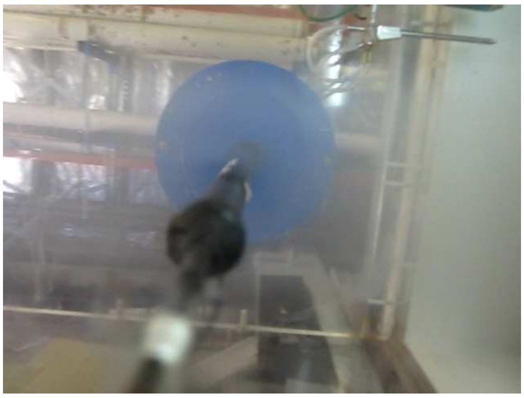

(c) t = 50 s.

(d) t = 57.33 s.

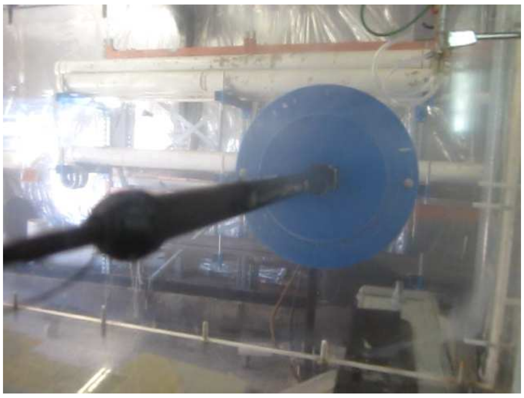

(e) t = 70 s.

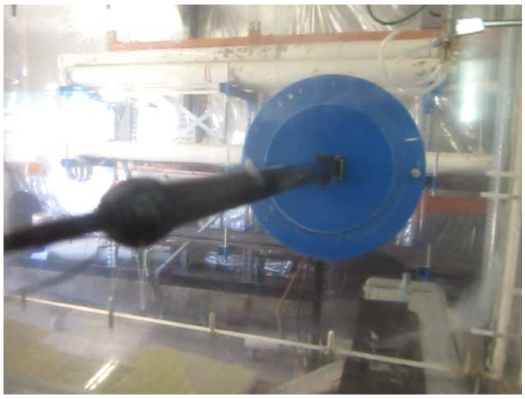

(f) t = 81 s.

Figure 7.4: Images showing development of ice accretion on the test article with time for a glaciated test flow condition. Flow is from right to left in each case.

Figure 7.4 shows the icing accretion progress on the test article surface in the test section. In this figure, the time values given in each sub-caption are relative to the initiation of water injection (ice generation) in the facility. The first signs of ice accretion were at approximately 13 s after the initiation of icing generation, Figure 7.4 (a), and occurred on the cylinder surface in a region near the perimeter of the icing jet nozzle – the region of the mixing layer. In this mixing layer region, the surface temperature of the test article, although not measured directly, would have been at least 10°C warmer than the test article surface temperature in the core flow of the icing jet, based on the results presented in Section 7.2.2. Visualisation was impeded due to the high fog density in the icing jet which arose because the humidity of the laboratory air drawn into the wind tunnel was high – the dew point temperature was around 15°C. By 48 s as shown in Figure 7.4(b), the visibility of the ice accretion in the vicinity of the mixing layer had increased. By 50 and 57 s (Figure 7.4(c) and (d)), accretion was visible across the width of the cylinder in the core flow on the leeward side of the test article and at approximately 90° around from the stagnation point. The images in Figure 7.4(e) and (f) were acquired after the nitrogen had been exhausted (and thus the fog density had reduced significantly), but the wind tunnel flow as still operating. Figure 7.4(e) illustrates a small amount of ice accretion had occurred across the width of the cylinder in the core flow region of the jet near the windward stagnation zone of the cylinder. Figure 7.4(f) captures the moment that the accretion zone in the vicinity of the mixing layer sheds from the test article.

### 7.3.2 Experiment 2: Melting ratio > 0 condition

For this experiment, the same test article was used and three atomiser nozzles were used in the spray guide pipe as usual, but a fourth nozzle of the same type was positioned near the exit of the icing jet nozzle to ensure that a non-zero melting ratio was achieved in the test flow. The air supply pressure for the three atomiser nozzles in the spray guide pipe was 6 bar, and the water pressure was 5 bar, while for the supplemental atomiser nozzle, the air pressure was 6 bar and the water pressure was 2 bar. The actual flow conditions at the test article generated by this liquid water injection arrangement have not been quantified. The purpose of the experiment was to illustrate, for the first time, the viability of the facility in the ice crystal icing context. Further work is required to quantify the actual flow conditions used in future experiments.

In this experiment, a liquid nitrogen volume of approximately 9 litre was used with a

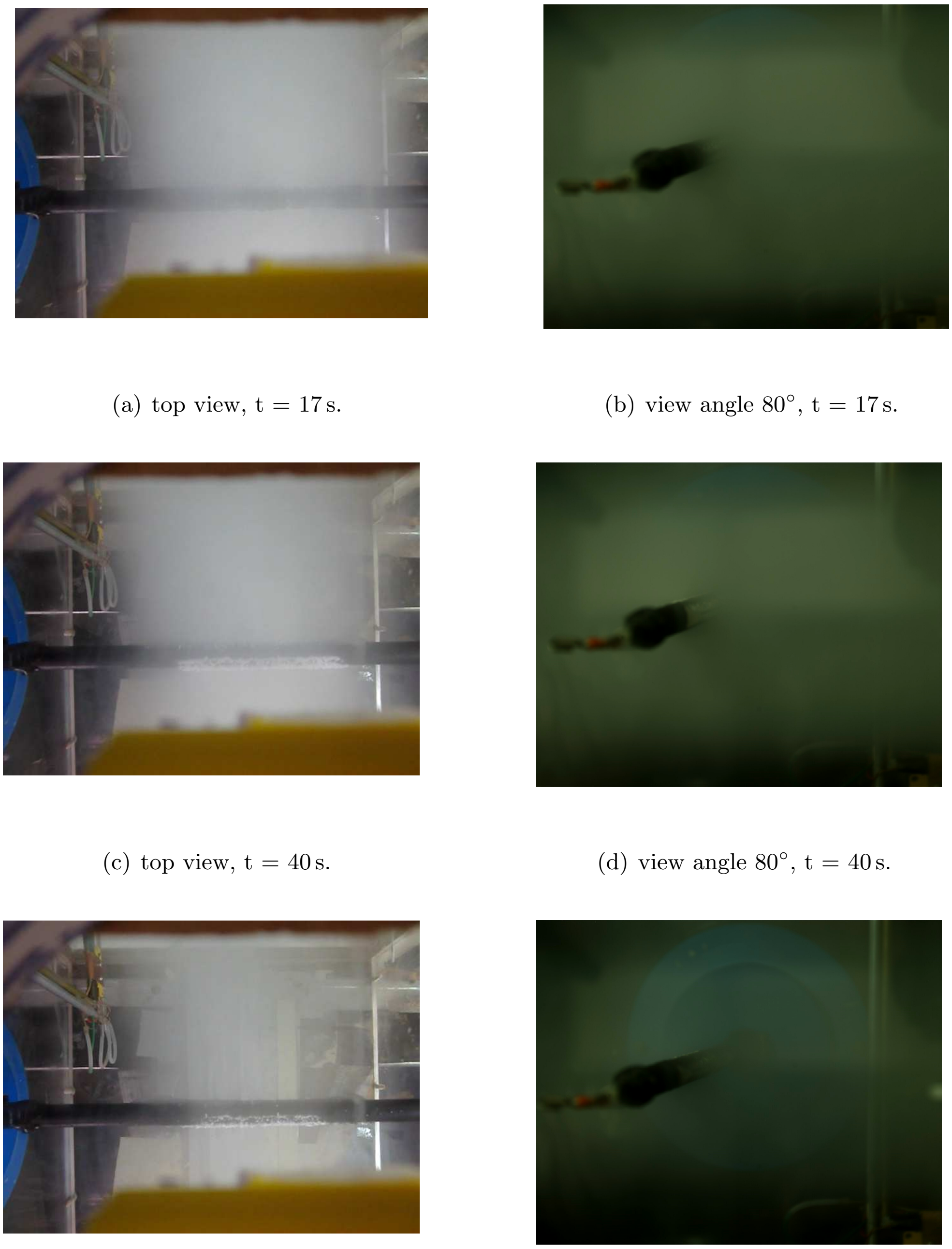

.

(a) top view, t = 17 s.

(b) view angle 80°, t = 17 s.

(c) top view, t = 40 s.

(d) view angle 80°, t = 40 s.

(e) top view, t = 47 s.

(f) view angle 80°, t = 47 s.

Figure 7.5: Images showing development of ice accretion on the test article with time for the case of $MR > 1$. Left column shows the top view with flow from top to bottom. Right column shows side view with flow from right to left.

valve-lift height of approximately 0.8 mm. The temperature of the flow at the icing jet nozzle exit was was approximately 0 °C during the nominally-steady run period of the facility. Two cameras were installed to record the ice accretion on the cylindrical test article: one was positioned on top of the test section viewing vertically downwards, and the second was positioned to give a side angle view of approximately 80°. The images in Figure 7.5 show the development of the ice accretion on the test article, and again, the indicated times are referenced to the start of water injection. The first signs of accretion were registered at approximately 17 s, and as shown in Figure 7.5(a) and (b), the accretion appears on the cylinder surface in the vicinity of the leading stagnation region of the test article. After 40 s from the initiation of the ice generation (Figure 7.5(c) and (d)), the accretion had increased in thickness on the windward surface, and light accretion on the leeward side of the test article was also evident. By 47 s (Figure 7.5(e) and (f)), the nitrogen was virtually exhausted, so viewing of the test article was made clearer as the fog density was reduced. Using the top view image taken at this time, and using the diameter of the test article (12.7 mm) as a reference, the thickness of the ice accretion on the windward surface was determined to be between 4 mm and 5 mm on the test article in the mixing layer region, and approximately 1 mm across the mid-span. Although the flow temperature in this case was higher than in the case of the glaciated conditions, the ice accretion was far more significant because of the relatively high liquid water content in the test flow.

## 7.4 Conclusion

Experiments conducted on a 12.7 mm diameter copper test article have demonstrated accretion in a nominally glaciated flow condition, and also in a flow condition having a simulated non-zero melting ratio. Significant accretion was registered on the windward side of the test article in the non-zero melting ratio case. However, further quantification of the flow and surface conditions is required before a meaningful analysis of such experiments can proceed.

# Chapter 8

# Conclusion

## 8.1 Motivation

Ice crystal ice accretion in the compressor of jet engines can occur when aircraft fly through clouds containing high concentrations of ice particles, such as those associated with tropical storm complexes. The ice accretion can cause partial blockage of the compressor over a short period of time and can generate significant effects such as loss of engine power, engine surge, stall, and even severe damage to the engine if large quantities of ice are suddenly dislodged from the compressor surfaces and ingested further into the engine. Ice accretion within aircraft engine compressors is a complex and poorly understood problem that represents a significant hazard for global aviation because of the increasing demand for flights, particularly in South-East Asia and the Pacific regions which are prone to tropical storms.

Ice accretion in compressors appears sensitive to many parameters including the shape of the surface, its roughness, wetting, temperature and other thermal characteristics, and flow parameters such as speed, pressure, temperature, humidity, melting ratio, total water content, particle size distribution, ice particle morphology. The interacting physical processes that govern the sensitivity of the compressor to ice accretion are not completely understood. Opportunities exist for researchers to contribute to the solution of such complex problems, but to develop reliable engineering models that can be used to aid the design and operation of compressors under icing conditions, further experimental data is needed.

A complete duplication of all of the possibly-relevant surface and flow and particle conditions is not currently achieved in any wind tunnel. Major icing wind tunnels around the globe can simultaneously duplicate many, though not all, of the relevant parameters. However, operating costs for these wind tunnels are typically very high, making these facilities difficult to access for instrument development activities and for fundamental experiments on compressor-relevant geometries at representative icing conditions.

## 8.2 Key Outcomes

An icing wind tunnel has been developed at the University of Southern Queensland to provide a facility that can be used for the development of new instrumentation and icing crystal icing measurement techniques, and for fundamental experiments on compressor-relevant geometries. The target was to develop a facility having both a modest size and operating cost, in order to enhance its appeal for use by university researchers and their collaborators.

The proposed wind tunnel concept involved: (1) evaporation of liquid nitrogen using air initially at ambient temperature in order to provide the cooling effect for freezing the water droplets; (2) dilution of the cold ice particle suspension through mixing with ambient-temperature air to partially melt the ice particles; (3) acceleration of the suspension through a nozzle contraction to provide an icing jet flow within a co-flowing stream.

It was recognised that the performance of the facility would be dictated largely by the supply of the liquid nitrogen. To achieve modest operating costs for the facility, the proposal specified a target maximum of 20 litre of liquid nitrogen per run in the wind tunnel facility which would have a duration of 2 minutes. The target operating conditions for the facility were a flow speed of $50\,\mathrm{m/s}$, temperatures around $0°\mathrm{C}$, and total water content up to $10\,\mathrm{g/m^3}$ with melting ratios up to 0.2.

A steady-flow conservation of energy analysis demonstrated the viability of the proposed icing wind tunnel arrangement within the constraints outlined above. Specific results from the conservation of energy analysis include the following. (i) A mixture temperature equal to the liquid nitrogen saturation temperature (approximately 77 K) can be achieved if the mass flow rate of evaporator air is approximately 0.92 times the mass flow rate of liquid nitrogen. (ii) An evaporator mass flow rate of air as high as 6.0 times the liquid nitrogen mass flow rate can still provide a flow at temperatures less than $-40°$C, which should be suitable for freezing the injected water droplets. (iii) The fully-mixed temperature in the test section achieves the ice melting temperature for total air mass flow rates (including the additional air introduced through the diffuser) of between 10 and 20 times the liquid nitrogen flow rates. (iv) For natural melting of the ice particles, the mass flow rate of warm laboratory air introduced through the diffuser should be tightly controlled because the melting ratio increases from zero to 0.2 for diffuser air mass flow rate changes of approximately 4.5 %. (v) The icing jet core diameter can be up to 228 mm for the target flow speed of 50 m/s and the specified liquid nitrogen delivery.

To provide flow durations longer than 2 minutes, which will be useful in some experiments, and for compatibility with the test section of the available wind tunnel (a flow cross-section size of 305 × 305 mm), an icing jet nozzle exit diameter of 170 mm was selected, somewhat smaller than the maximum of 228 mm specified from the conservation of energy analysis. The development of other hardware need to complete the apparatus proceeded through the application of engineering analysis, engineering and empirical design tools, computational simulations, and prototype development and testing.

CFD simulations, which were performed to assist in the design of the new hardware, indicated that the icing jet generator would have good uniformity of both the flow speed and flow temperature at the nozzle exit. For the icing bell-mouth inlet – a new component for the existing wind tunnel – the CFD simulations indicated that at the entrance to the test section, the velocity profile has a slight variation amounting to a deviation of about 1 m/s across the core flow region, while further downstream, at approximately the middle of the test section, the velocity uniformity should be very good. Simulations of the combined system consisting of the icing jet generator and the icing wind tunnel operating at experimentally-identified conditions, showed that a uniform flow speed of approximately 30 m/s should be generated in the icing jet nozzle exit core flow (having a diameter of 170 mm), and that flow velocity in the co-flow region (in which the warm air flow is admitted to the test section by the icing bell-mouth) would be approximately 47 m/s.

The performance of the facility has also been assessed through experiments. An isokinetic total water content probe, and a traversing system were also developed for use in the new wind tunnel facility. Results demonstrate that within the icing jet nozzle core flow diameter of 140 mm, the average flow speed was $28.1 \pm 1.1$ m/s. The air flow delivered through the perforated diffuser was at a temperature slightly higher than ambient, so it was possible to assess the thermal uniformity of the icing jet nozzle exit flow over a long period of time by operating the facility without liquid nitrogen evaporation. Under these conditions, very good temperature uniformity of the icing jet nozzle core flow was also demonstrated, the average temperature in the y-direction was $21 \pm 0.3\,^{\circ}$C, and the average temperature in the x-direction was $20.7 \pm 0.3\,^{\circ}$C. When the facility was operated with liquid nitrogen, the measured temperature uniformity was reasonable, but the fidelity of the measurements was compromised by the response of the instrumentation and the shorter testing period available for completion of the probe traverse across the nozzle exit flow. In one particular operating condition, the average temperature measured in the jet core flow was $-9.1 \pm 1.9\,^{\circ}$C. Different icing jet nozzle exit flow temperatures were achieved in the facility by setting different liquid nitrogen receiver valve-lift heights. Measurement of the total water content (TWC) distribution was performed when liquid water was injected into the facility when it was operated at ambient temperature. The isokinetic TWC probe was traversed along a vertical line passing through the axis of the nozzle and indicated a good degree of uniformity across core flow region in the vertical plane.

Initial testing in the facility was performed with a $\frac{1}{2}''$ heater cylinder positioned in the icing jet nozzle exit flow. Under fully-glaciated conditions with a flow temperature of approximately -10 °C, and with the cylinder operating at a surface temperature of approximately 12.3 °C, little accretion occurred on the windward side of the cylinder, except in the mixing layer region of the icing jet nozzle flow. Some accretion occurred on the leeward side of the cylinder in this fully-glaciated test. When the cylinder was tested at a surface temperature of approximately 7 °C, under partially-melted conditions generated through the introduction of a supplemental liquid water spray, accretion was observed on the windward side of the cylinder.

## 8.3 Future work

A new icing wind tunnel facility has been established and experiments have demonstrated sufficient uniformity of flow conditions to enable testing of compressor components and basic aerodynamic geometries to be performed in the future. However, before the outcomes of such testing can be meaningfully interpreted, some additional improvements in the facility operation should be made, and further quantification of flow conditions is needed.

1. *Humidity control.* The new icing wind tunnel currently introduces ambient laboratory air into the icing jet through both the liquid nitrogen evaporator and the diffuser. The humidity of this air is currently not controlled. The ice crystal icing process is known to be sensitive to the humidity because the production of liquid water (which is required for accretion) occurs through particle melting which is sensitive to humidity. Humidity control for the facility could be achieved by drawing the evaporator and diffuser air from a large flexible bag which contains the test air at a defined humidity. A desiccant-based or refrigeration-based dehumidification system could be designed for the flexible bag storage system and the humidity-controlled air could be accumulated within the bag over a period of time prior to the operation of the facility. Decreasing the humidity would also improve the visualisation of the icing process in the test section as currently the fog density is high and makes viewing test articles difficult.

2. *Melting ratio control.* The operation of the facility involves generating fully-glaciated conditions prior to the diffuser, and seeks to establish natural melting of the particles within the diffuser. To control the natural melting of the particles, tighter control of temperatures, humidity and flow rates will be required. An

alternative approach, which was trialled in the final demonstration experiment, involves the introduction of supplemental liquid water. In future work, this would be best achieved by positioning additional nozzles at the exit of the perforated diffuser, prior to flow acceleration through the icing jet nozzle contraction. Also, in future work, the humidity of the air added to the spray guide tube upstream of the evaporator and air added through the atomising nozzles can also be controlled. While the humidity of the air entering the test section through the wind tunnel bell mouth could affect the melting in the shear layer, effects are expected to be local and should not impact the portion of the test article within the core of the icing jet. Therefore it should not be necessary to control the humidity of the co-flowing air that enters the test section.

3. *Temperature control.* The thermal performance of the facility is dictated largely by the liquid nitrogen delivery and evaporation process. The liquid nitrogen flow rate is currently controlled manually by adjusting the lift-height of the valve in the liquid nitrogen receiver. To maintain a constant volume flow rate, the stepper motor which controls the valve position in the liquid nitrogen receiver could be adjusted based on measurements of the instantaneous liquid nitrogen volume flow rate. However, because the ultimate objective is to maintain the flow temperature constant, the stepper-motor which moves the valve could also be controlled based on the icing jet nozzle exit flow temperature through implementation of an automated feedback loop.

4. *Improved instrumentation.* Icing jet nozzle exit surveys of the flow conditions produced by the facility should be improved by developing faster-response instrumentation that can be confidently traversed through the icing jet during the steady run time of the facility. In particular, additional surveys of the total water content distribution will be required, so a fast-responding hygrometer is needed. Furthermore, to verify the melting ratio, an instrument for discriminating between the liquid and ice water content will be required. The IKP can be improved by increasing the heater area and performing calibrations to ensure that all ice particles are melted and fully vaporised within the available residence time. Improved insulation of the probe to maximise efficient heat delivery into the internal flow is also expected to have significant benefits. Further calibration and

testing of the IKP should be performed under both liquid and mixed phase flow conditions, possibly using a hot wire device as a reference for LWC measurement under fully-liquid operating conditions.

5. *Measurement of the Particle Size Distribution.* The particle size distribution within the test section should be measured. Computational simulations indicate that there may be significant non-uniformity in the distribution of the particle sizes across the icing jet nozzle exit. Reliable measurements of the particle size distribution are therefore required in order to quantify the conditions in the test section.

6. *CFD simulations.* Further computational simulations can also be performed to support the planned improvements in facility operation and instrumentation. For example, to estimate the degree of particle melting within the perforated diffuser as a function of different variables such as particle diameter, mixing ratio and residence time, further computational simulations will be required.

# References

Abel, S., Cotton, R., Barrett, P. and Vance, A. 2014, 'A comparison of ice water content measurement techniques on the faam bae-146 aircraft', *Atmospheric Measurement Techniques* **7**(9), 3007–3022.

AI-Khalil, K. and Salamon, L. 1998, Development of the cox icing research facility, *in* '36th Aerospace Science Meeting & Exhibit, AIAA - 98-0097', AIAA, Reno, NV.

Al-Khalil, K. 2003, Assessment of effects of mixed-phase icing conditions on thermal ice protection systems, Technical Report (No.DOT/FAA/AR-03/48).

Balakrishna, B. and Ketha, V. G. P. 2014, 'Validation of unsteady thermodynamic cfd simulations of aircraft wing anti-icing operation', *International Journal of Current Engineering and Technology* **2347 - 5161**.

Bansmer, S. E., Baumert, A., Sattler, S., Knop, I., Leroy, D., Schwarzenboeck, A., Jurkat-Witschas, T., Voigt, C., Pervier, H. and Esposito, B. 2018, 'Design, construction and commissioning of the Braunschweig icing wind tunnel', *Atmospheric Measurement Techniques* **11**(6), 3221–3249.

Baumert, A., Bansmer, S. E. and Bacher, M. 2015, Implementation of an innovative ice crystal generation system to the icing wind tunnel Braunschweig, *in* '53rd AIAA Aerospace Sciences Meeting', p. 1225.

Baumert, A., Bansmer, S., Sattler, S., Pervier, H. and Esposito, B. 2016, Simulating natural ice crystal cloud conditions for icing wind tunnel experiments-a review on the design, commissioning and calibration of the tu Braunschweig ice crystal generation system, *in* '8th AIAA Atmospheric and Space Environments Conference', p. 4053.

Bellucci, M. 2007, Cloud characterization in CIRA icing wind tunnel, PhD thesis, Università degli Studi di Napoli Federico II.

Bencic, T., Fagan, A., Van Zante, J. F., Kirkegaard, J. P., Rohler, D. P., Maniyedath, A. and Izen, S. H. 2013, Advanced optical diagnostics for ice crystal cloud measurements in the NASA Glenn propulsion systems laboratory, *in* '5th AIAA Atmospheric and Space Environments Conference', p. 2678.

Bond, T. H. and Anderson, D. N. 2004, 'Manual of scaling methods'.

Braga, R. C., Rosenfeld, D., Weigel, R., Jurkat, T., Andreae, M. O., Wendisch, M., Pöhlker, M. L., Klimach, T., Pöschl, U., Pöhlker, C. et al. 2017, 'Comparing parameterized versus measured microphysical properties of tropical convective cloud bases during the acridicon–chuva campaign', *Atmospheric Chemistry and Physics* **17**(12), 7365–7386.

Bravin, M., Strapp, J. W. and Mason, J. 2015, 'An investigation into location and convective lifecycle trends in an ice crystal icing engine event database', *SAE Technical Paper* 2015-01-2130.

Bucknell, A. J., McGilvray, M., Gillespie, D., Jones, G., Reed, A. and Collier, B. 2018, Experimental studies of ice crystal accretion on an axisymmetric body at engine-realistic conditions, *in* '2018 Atmospheric and Space Environments Conference', p. 4223.

Bucknell, A., McGilvray, M., Gillespie, D. R., Jones, G., Reed, A. and Buttsworth, D. R. 2018, 'Heat transfer in the core compressor under ice crystal icing conditions', *Journal of Engineering for Gas Turbines and Power* **140**(7), 071501.

Buttsworth, D., Davison, C., MacLeod, J. and Strapp, J. 2007, Evaporator design for an isokinetic total water content probe in a naturally aspirating configuration, *in* 'Proceedings of the 16th Australasian Fluid Mechanics Conference (AFMC 2007)', University of Queensland, pp. 825–830.

Cevik, F. 2010, Design of an axial flow fan for a vertical wind tunnel for paratroopers, Master's thesis, Middle East Technical University.

Chintamani, S., Delcarpio, D. and Langmeyer, G. 1997, Development of Boeing research aerodynamic icing tunnel circuit, *in* 'Symposium; 79th, Advisory Group for Aerospace Research and Development: Fluid Dynamics Panel: Aerodynamics of wind tunnel circuits and their components; 1996; Moscow', AGARD, pp. 8–1.

Clark, C., Orchard, D. M. and Chevrette, G. 2018, A guide creating sae as5562 ice crystal, mixed phase and rain conditions in a wind tunnel environment, *in* '2018 Atmospheric and Space Environments Conference', p. 3833.

Currie, T. C. and Fuleki, D. 2016, Experimental results for ice crystal icing on hemispherical and double wedge geometries at varying mach numbers and wet bulb temperatures, *in* '8th AIAA Atmospheric and Space Environments Conference', p. 3740.

Currie, T. C., Fuleki, D., Knezevici, D. C. and MacLeod, J. D. 2013, 'Altitude scaling of ice crystal accretion', *AIAA* **2677**, 24–25.

Currie, T. C., Fuleki, D. and Mahallati, A. 2014, Experimental studies of mixed-phase sticking efficiency for ice crystal accretion in jet engines, *in* '6th AIAA Atmospheric and Space Environments Conference', p. 3049.

Currie, T. C., Struk, P. M., Tsao, J.-C., Fuleki, D. and Knezevici, D. C. 2012, Fundamental study of mixed-phase icing with application to ice crystal accretion in aircraft jet engines, *in* '4th AIAA Atmospheric and Space Environments Conference', Vol. 10, pp. 6–2012.

Dally, J. W., Riley, W. F. and McConnell, K. G. 1993, *Instrumentation for engineering measurements*, Wiley New York.

Davison, C., MacLeod, J. and Strapp, J. 2009, Naturally aspirating isokinetic total water content probe: Evaporator design and testing, *in* '1st AIAA Atmospheric and Space Environments Conference', Fluid Dynamics and Co-located Conferences, American Institute of Aeronautics and Astronautics, p. 3861. doi:10.2514/6.2009-3861.

Davison, C., MacLeod, J., Strapp, J. and Buttsworth, D. 2008, Isokinetic total water content probe in a naturally aspirating configuration: Initial aerodynamic design and testing, *in* '46th AIAA Aerospace Sciences Meeting and Exhibit', p. 435.

Davison, C. R., Landreville, C. and Ratvasky, T. P. 2017, Validation of a compact isokinetic total water content probe for wind tunnel characterization at NASA Glenn icing research tunnel and at nrc ice crystal tunnel, *in* '9th AIAA Atmospheric and Space Environments Conference', p. 4088.

Dezitter, F., Grandin, A., Brenguier, J.-L., Hervy, F., Schlager, H., Villedieu, P. and Zalamansky, G. 2013, Haic-high altitude ice crystals, *in* '5th AIAA Atmospheric and Space Environments Conference', p. 2674.

Dixon, S. L. and Hall, C. 2013, *Fluid mechanics and thermodynamics of turbomachinery*, Butterworth-Heinemann.

Dong, W., Zhu, J., Zheng, M., Lei, G. and Zhou, Z. 2015, 'Experimental study on icing and anti-icing characteristics of engine inlet guide vanes', *Journal of Propulsion and Power* **31**(5), 1330–1337.

Gayet, J.-F., Shcherbakov, V., Bugliaro, L., Protat, A., Delanoë, J., Pelon, J. and Garnier, A. 2014, 'Microphysical properties and high ice water content in continental and oceanic mesoscale convective systems and potential implications for commercial aircraft at flight altitude', *Atmospheric Chemistry and Physics* **14**(2), 899–912.

Gent, R. W., Dart, N. P. and Cansdale, J. T. 2000, 'Aircraft icing', *Philosophical Transactions of the Royal Society of London. Series A: Mathematical, Physical and Engineering Sciences* **358**(1776), 2873–2911.

Gerber, H., Twohy, C. H., Gandrud, B., Heymsfield, A. J., McFarquhar, G. M., DeMott, P. J. and Rogers, D. C. 1998, 'Measurements of wave-cloud microphysical properties with two new aircraft probes', *Geophysical research letters* **25**(8), 1117–1120.

Goriachev, A., Zhulin, V., Goriachev, P., Grebenkov, S. and Savenkov, V. 2019, Experimental processing of methodical questions of modeling the atmospheric cloud containing ice crystals and mixed phase, Technical report, SAE Technical Paper 2019-01-1922.

Griffin, T. A., Lizanich, P. and Dicki, D. J. 2014, Psl icing facility upgrade overview, *in* '6th AIAA Atmospheric and Space Environments Conference', p. 2896.

Grzych, M. L. and Mason, J. G. 2010, Weather conditions associated with jet engine power loss and damage due to ingestion of ice particles: What we′ve learned through 2009, *in* '14th Conference on Aviation, Range, and Aerospace Meteorology'.

Gudmundsson, S. 2013, *General aviation aircraft design: Applied Methods and Procedures*, Butterworth-Heinemann.

Hauk, T., Bonaccurso, E., Roisman, I. and Tropea, C. 2015, 'Ice crystal impact onto a dry solid wall. particle fragmentation', *Proc. R. Soc. A* **471**(2181), 20150399.

Hervy, F. 2011, New sld icing capabilities at dga aero-engine testing, Technical report, SAE Technical Paper 2011-38-0086.

Hervy, F., Maguis, S., Virion, F., Esposito, B. and Pervier, H. 2015, 'Improvement of an altitude test facility capability in glaciated icing conditions at dga aero-engine testing', *SAE International Journal of Aerospace* **8**(2015-01-2154), 9–14.

Ide, R. F. 1999, Comparison of liquid water content measurement technquies in an icing wind tunnel, Technical report, DTIC Document.

Ide, R. F. and Sheldon, D. W. 2008, *2006 icing cloud calibration of the NASA Glenn Icing Research Tunnel*, National Aeronautics and Space Administration.

Jérôme, E., Hervy, F. and Maguis, S. 2016, 'Icing test capabilities at dga aero-engine testing', *International Journal of Engineering Systems Modelling and Simulation* **8**(2), 77–85.

Jones Jr, M. 2015, 'Pursuit of power: Nasa's propulsion systems laboratory no. 1 and 2', *Air & Space Power Journal* **29**(5), 111.

Knezevici, D. C., Fuleki, D., Currie, T., Galeote, B., Chalmers, J. and MacLeod, J. 2013, Particle size effects on ice crystal accretion–part ii, *in* '5th Atmospheric and Space Environments Conference'.

Knezevici, D., Fuleki, D., Currie, T. and MacLeod, J. 2012, Particle size effects on ice crystal accretion, *in* '4th AIAA Atmospheric and Space Environments Conference', p. 3039.

Kolodzie, J. P. and Van Winkle, M. 1957, 'Discharge coefficients through perforated plates', *AIChE Journal* **3**(3), 305–312.

Korolev, A., Strapp, J., Isaac, G. and Emery, E. 2013, 'Improved airborne hot-wire measurements of ice water content in clouds', *Journal of Atmospheric and Oceanic Technology* **30**(9), 2121–2131.

Lawson, R. P., Angus, L. J. and Heymsfield, A. J. 1998, 'Cloud particle measurements in thunderstorm anvils and possible weather threat to aviation', *Journal of Aircraft* **35**(1), 113–121.

Lindgren, B. and Johansson, A. V. 2002, 'Design and evaluation of a low-speed wind-tunnel with expanding corners', *Flow Facility Design and Experimental Studies of Wall-Bounded Turbulent Shear-Flows* **63**.

Mason, J. G., Chow, P. and Fuleki, D. M. 2011, 'Understanding ice crystal accretion and shedding phenomenon in jet engines using a rig test', *Journal of Engineering for Gas Turbines and Power* **133**(4), 041201.

Mason, J. G., Strapp, J. W. and Chow, P. 2006, The ice particle threat to engines in flight, *in* '44th AIAA Aerospace Sciences Meeting, Reno, Nevada', pp. 9–12.

Mingione, G., Barocco, M., Denti, E., Bindi, F. G. and French, D. 1997, 'Flight in icing conditions', *Direction gnrale de laviation civile, DGAC, Tech. Rep* .

Morel, T. 1975, 'Comprehensive design of axisymmetric wind tunnel contractions', *Journal of Fluids Engineering* **97**(2), 225–233.

Paraschivoiu, I. and Saeed, F. 2004, 'Aircraft icing'.

Politovich, M. K. 2000, 'Predicting glaze or rime ice growth on airfoils', *Journal of aircraft* **37**(1), 117–121.

Protat, A., Rauniyar, S., Kumar, V. and Strapp, J. 2014, 'Optimizing the probability of flying in high ice water content conditions in the tropics using a regional-scale climatology of convective cell properties', *Journal of Applied Meteorology and Climatology* **53**(11), 2438–2456.

Riley, J. T. 1999, Mixed-phase icing conditions: A survey of simulation capabilities, *in* '37th AIAA Aerospace Sciences Meeting and Exhibit'.

Rios Pabon, M. A. 2012, Ice crystal ingestion by turbofans, PhD thesis, Drexel University.

Rudoff, R., Bachalo, E., Bachalo, W. and Oldenburg, J. 1993, Liquid water content measurements using the phase doppler particle analyzer in the NASA Lewis icing research tunnel, *in* '31st Aerospace Sciences Meeting', p. 298.

Saleh, K. H. 2013, Initial development of ice crystal ice accretion at conditions related to turbofan operation at high Altitude, PhD thesis, University of Southern Queensland.

Salter, C., Warsap, J. and Goodman, D. G. 1962, 'A discussion of pitot-static tubes and of their calibration factors with a description of various versions of a new design', *Brit. ARC R&M* **3365**.

Schnoes, M., Voß, C. and Nicke, E. 2018, 'Design optimization of a multi-stage axial compressor using throughflow and a database of optimal airfoils', *Journal of the Global Power and Propulsion Society* **2**, 516–528.

Shields, D. 2011, A modeling study of ice accretion on a NACA 4412 airfoil, Master's thesis, Rensselaer Polytechnic Institute.

Steen, L. E., Ide, R. F., Van Zante, J. F. and Acosta, W. J. 2015, 'NASA Glenn icing research tunnel: 2014 and 2015 cloud calibration procedures and results'.

Struk, P., Bartkus, T., Tsao, J.-C., Currie, T. and Fuleki, D. 2015, 'Ice accretion measurements on an airfoil and wedge in mixed-phase conditions', *SAE Technical Paper* 2015-01-2116.

Struk, P., Broeren, A., Tsao, J., Vargas, M., Wright, W., Currie, T., Knezevici, D. and Fuleki, D. 2012, Fundamental ice crystal accretion physics studies, Technical Report NASA/TM-2012-217429.

Struk, P. M., King, M. C., Bartkus, T. P., Tsao, J.-C., Fuleki, D., Neuteboom, M. and Chalmers, J. 2018, Ice crystal icing physics study using a NACA 0012 airfoil at the national research council of canadas research altitude test facility, *in* '2018 Atmospheric and Space Environments Conference', p. 4224.

Tsao, J.-C. 2019, Scaling evaluation of ice-crystal icing on a modern turbofan engine in PSL using the COMDES-MELT code, Technical report, SAE Technical Paper 2019-01-1920.

Van Zante, J. F., Ratvasky, T. P., Bencic, T. J., Challis, C. C., Timko, E. N. and Woike, M. R. 2018, Update on the NASA Glenn propulsion systems lab icing and ice crystal cloud characterization-2017, *in* '2018 Atmospheric and Space Environments Conference', p. 3969.

Vecchione, L. and De Matteis, P. 2003, An overview of the CIRA icing wind tunnel, *in* '41st Aerospace Sciences Meeting and Exhibit', p. 900.

Wendisch, M., Pöschl, U., Andreae, M. O., Machado, L. A., Albrecht, R., Schlager, H., Rosenfeld, D., Martin, S. T., Abdelmonem, A., Afchine, A. et al. 2016, 'Acridicon–chuva campaign: studying tropical deep convective clouds and precipitation over amazonia using the new german research aircraft halo', *Bulletin of the American Meteorological Society* **97**(10), 1885–1908.

Žkauskas, A. 1987, Heat transfer from tubes in crossflow, *in* 'Advances in heat transfer', Vol. 18, Elsevier, pp. 87–159.

# Appendix A

# Small-scale Icing Wind Tunnel Prototype

## A.1 Introduction

This appendix describes a small version of the icing wind tunnel and presents experimental results that were obtained prior to establishing the full scale apparatus. The prototype was built to assess the likely capability of the full scale apparatus, and in particular, the values and the uniformity of both velocity and temperature at the exit plane of the cold jet. The experiments investigated the measurement and control of the air mass flow rate, mixing ratio, temperatures, and the liquid nitrogen consumption.

## A.2 Prototype hardware

A small prototype of scale 1/6 was built as illustrated in Figure A.1. The scale was chosen as suitable for creating the prototype parts using 3d printing. Many parts of the prototype were generated via solid modelling software (Creo). The main body of the prototype was the conical diffuser connected with the contraction nozzle in an arrangement similar to the full-scale device that was ultimately constructed, as described in Chapter 4 (Section 4.2.1). The conical diffuser has multiple ports on its wall to inject the air at approximately room temperature into the cold core flow. The body was assembled with a PVC shell as shown in Figure A.1. Two blowers were attached to the shell region to supply the air into the shell and a variable speed fan was attached at different locations depending on the configuration of interest as illustrated in Figure A.2. A small insulated tank (2 litre capacity) was connected at the prototype entrance and was used to supply the liquid nitrogen to the apparatus. The insulated tank was 3d printed and was insulated using expanding foam and aluminium foil. The liquid nitrogen was fed into the cold core flow pipe of the prototype by a valve arrangement similar to that used in the full scale apparatus as described in Chapter 4 (Section 4.2.6). A prototype show some features of the prototype valve is shown in Figure A.3. The valve was designed to control the volume flow rate of nitrogen while the liquid nitrogen level in the insulated tank was dropping during a run. Open loop control was achieved by performing a calibration test and by adjusting the valve aperture with the stepper motor based on the time relative to the start of the experiment. In the experiments with the small prototype, the evaporated nitrogen was used as a refrigerant to cool down the air only and was not used to produce any ice particles because dimension limitations made the injection of atomizing water impractical.

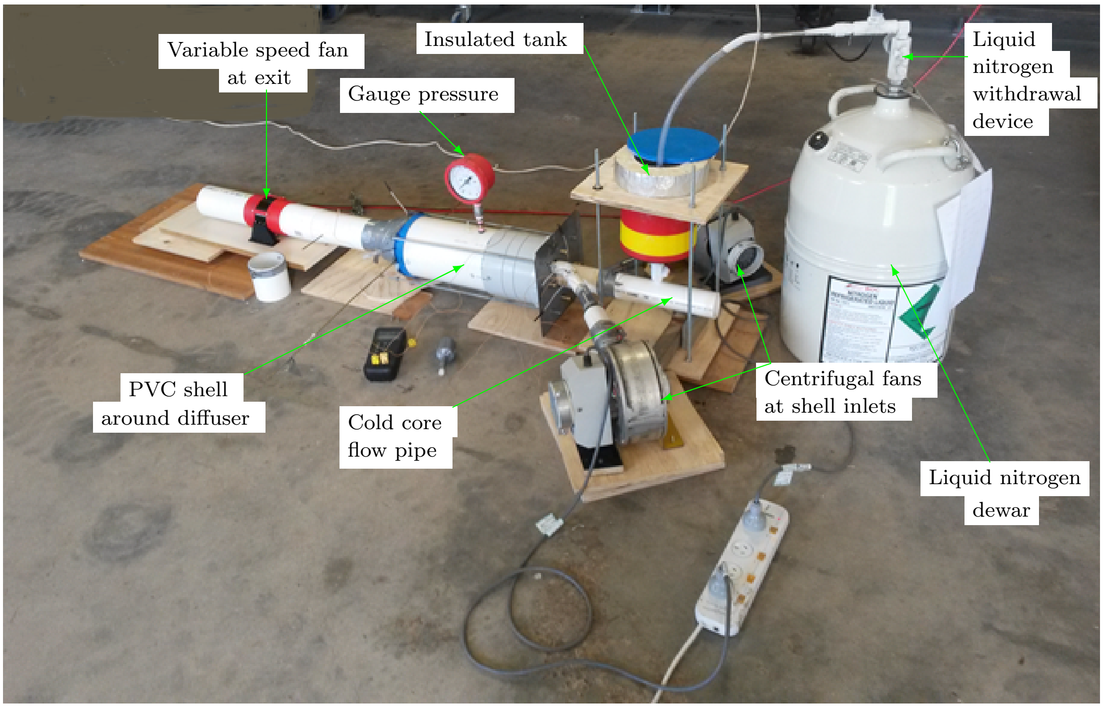


Figure A.1: Photograph showing the experimental icing jet generator prototype of 1/6 scale size.

## A.3 Arrangement of hardware

Three arrangements of the fan and blowers were tested as illustrated in Figure A.2. In Arrangement 1, two blowers were positioned at the shell inlets and the variable speed fan was positioned at the evaporator inlet. In Arrangement 2, the variable speed fan was positioned at the cold jet outlet. In Arrangement 3, the variable speed fan was positioned at the cold jet outlet, the evaporator inlet was closed, and the blowers were not used. In Arrangement 1, the variable speed fan did not have sufficient capacity when both blowers where operating, and this resulted in egress of some of the evaporated liquid nitrogen through the evaporator inlet. Arrangement 2 worked better than Arrangement 1, but ice deposition (frosting) from the ambient air accumulated on the valve of the liquid nitrogen passage and this reduced the liquid nitrogen flow rate, and caused temperature fluctuations at the nozzle exit. Configuration 3 was not subject to the icing problem because the evaporator inlet was closed. In arrangement 3, evaporation of the liquid nitrogen was achieved preliminary through conduction heat transfer from the duct walls.

The instrumentation used in these tests included several type K thermocouples for the temperature measurements at different points, and a pitot tube positioned at the inlet and outlet of the contraction nozzle. Pressure differences were measured with a U-tube water manometer. The survey of the temperature at the inlet of the contraction was performed manually.

## A.4 Preliminary results

The results from Arrangement 3 are presented in Figure A.4 and A.5. For these experiments 1.2, litres of liquid nitrogen was used in a period of 60 second, and approximately 0.079 kg/s of air at a temperature of 20 °C was drawn into the apparatus. This provided a cold flow at the exit of the nozzle contraction exit with a total mass flow rate of 0.0898 kg/s corresponding to the exit flow speed of 14.5 m/s and temperature between -15 and -20 °C.

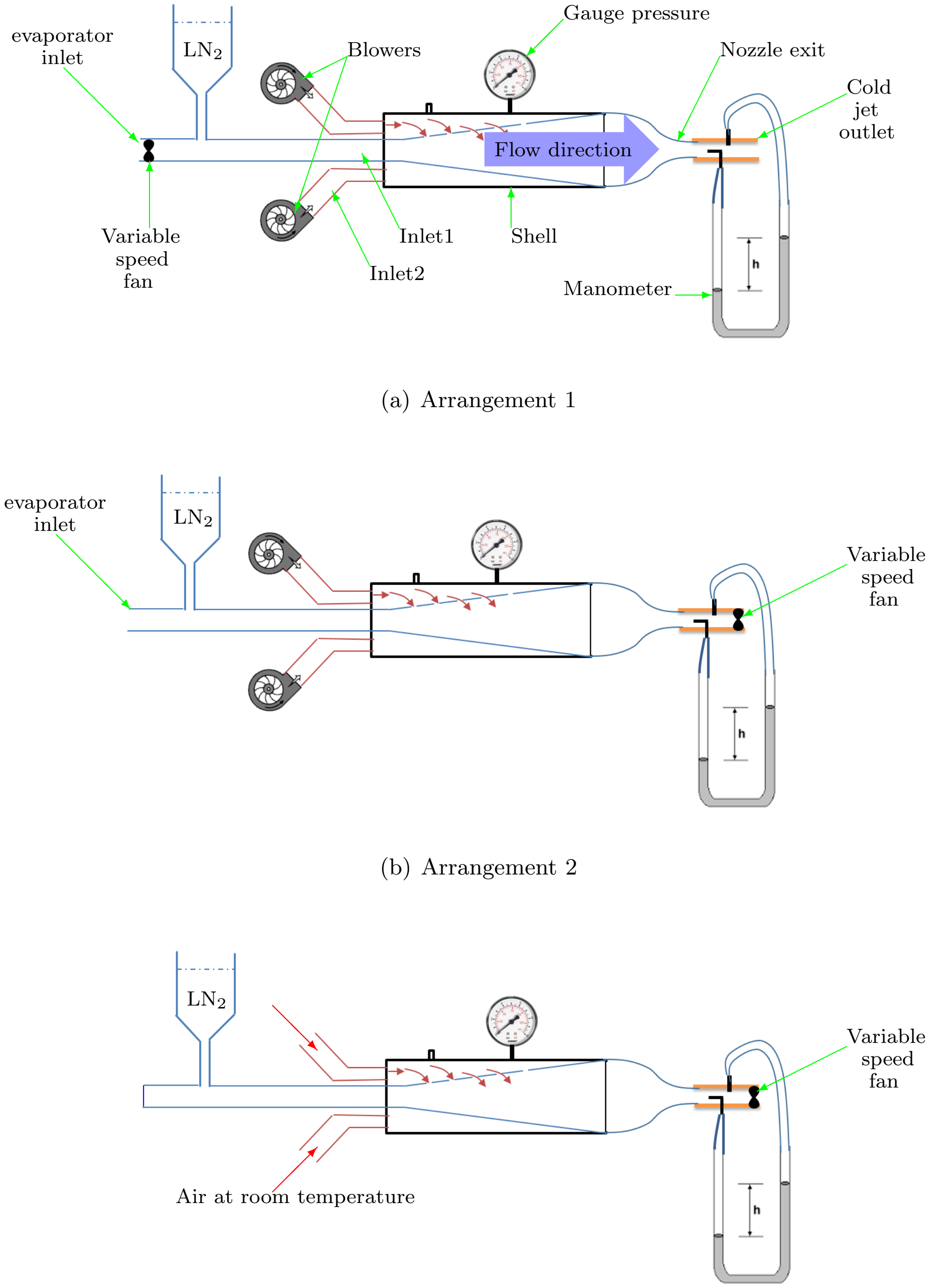


(a) Arrangement 1

(b) Arrangement 2

(c) Arrangement 3

Figure A.2: Schematic diagram of small-scaling icing wind tunnel prototype arrangements. (a) Arrangement 1: two blowers at diffuser shell inlet and one fan at the evaporator inlet; (b) Arrangement 2: two blowers at the at diffuser shell inlet and one fan at the nozzle exit; and (c) Arrangement 3: one fan at the nozzle exit with the evaporator inlet sealed.

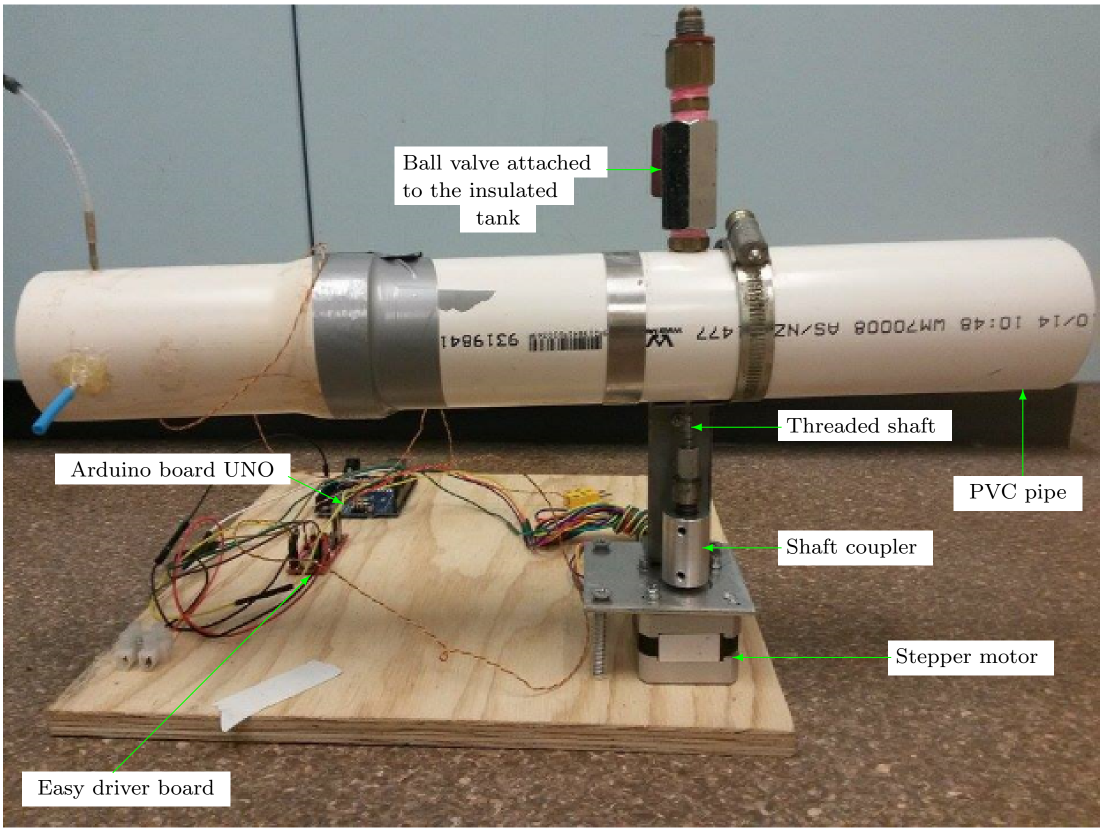


Figure A.3: Photograph showing the valve hardware used to adjust the liquid nitrogen flow rate. The valve is attached at the bottom of the insulated tank.

Figure A.4 shows the recorded temperature variation with time at both the evaporator inlet and the nozzle exit in Arrangement 3. As shown in Figure A.4, once the valve of the nitrogen tank started opening, the temperature dropped quickly at the inlet region and the nozzle exit, taking a time of around 10 seconds to achieve a stable state at a temperature of $-172\,^{\circ}\mathrm{C}$. The temperature at the nozzle outlet follows a similar behaviour to that of the evaporator inlet and quickly drops to a temperature of approximately $-20\,^{\circ}\mathrm{C}$. Over the test period between 70 and 100 seconds, the nozzle exit temperature varies from $-17.3\,^{\circ}\mathrm{C}$ to $-20\,^{\circ}\mathrm{C}$.

Figure A.5 shows manual temperature surveys at different 10 points across the contraction nozzle inlet. As shown in Figure A.5, the temperatures distribution is reasonably uniform across the contraction nozzle inlet over the survey periods of approximately 10 seconds. Surveys performed at later times display slightly improved spatial uniformity. The differences in values between each survey period are attributed to transient thermal effects associated with establishing steady state flow rate of the liquid nitrogen. The results show that the flow temperatures are decreasing slightly with time and improving in spatial uniformity with time.

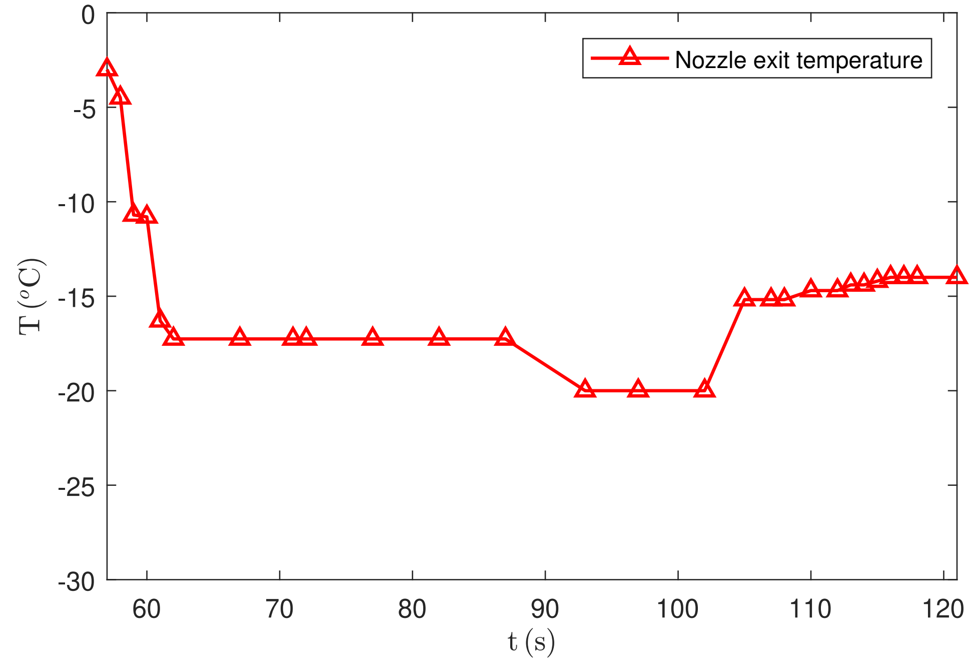


(a)

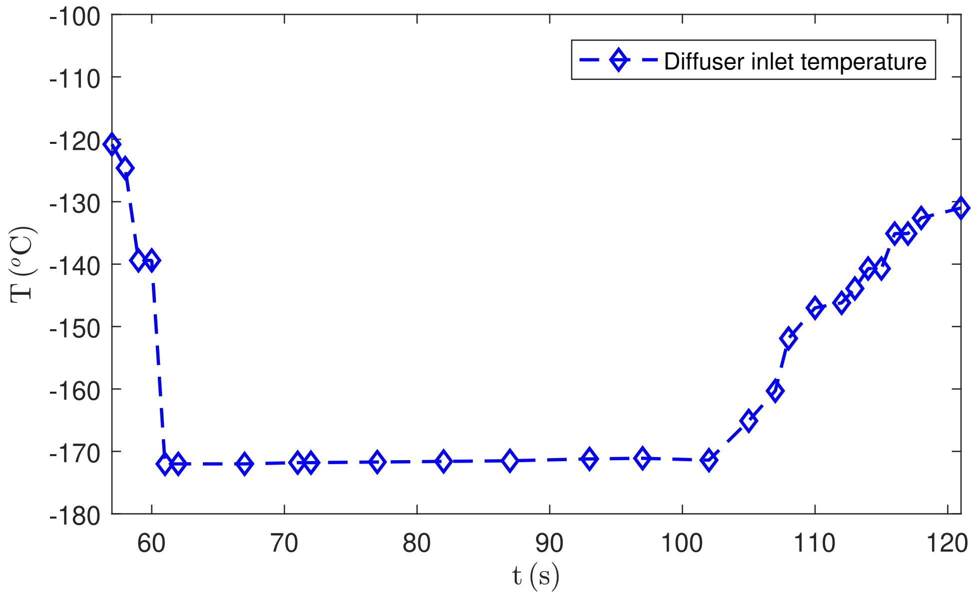


(b)

Figure A.4: Experimental temperature data variation with time of the icing jet prototype: (a) Nozzle exit; (b) diffuser inlet.

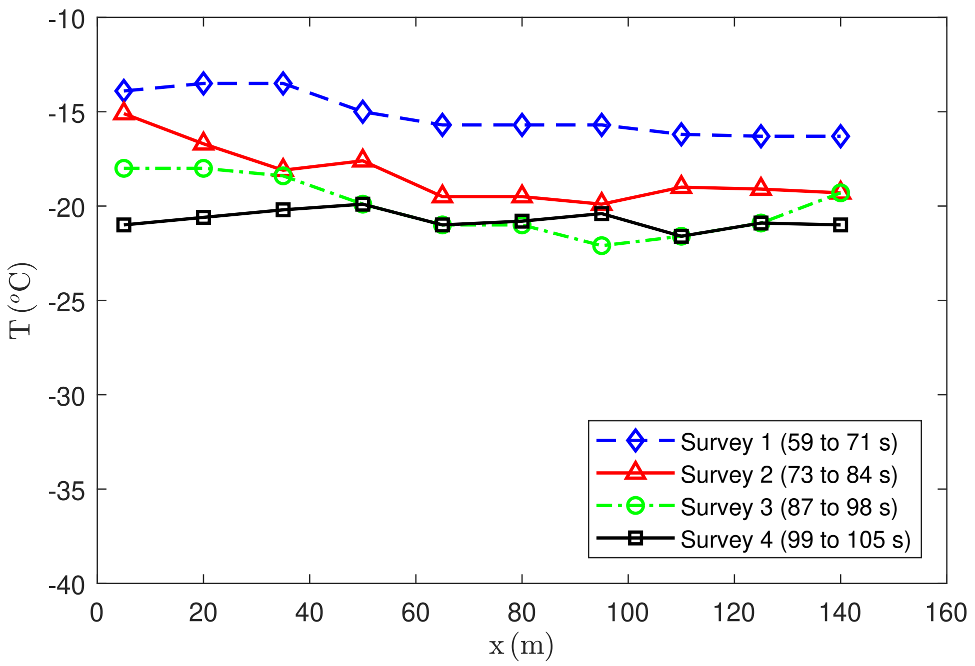


Figure A.5: Experimental temperature distribution along a horizontal line at the inlet to the contraction nozzle.

# Appendix B

# Conical Diffuser Design and Fabrication

## B.1 Design

The purpose of the conical diffuser is to dilute and warm the suspension of the very cold ice particles prior to acceleration in the nozzle contraction. The general arrangement is illustrated in Figure B.1. The diffuser has been designed to mix the cold core flow suspension with the warm air entering through the perforated conical surface. The intention was not to necessarily reduce the axial speed of the cold core-flow and therefore, the diffuser is not a conventional subsonic flow-deceleration device. Mixing should occur at approximately constant pressure conditions, thus reducing the possibility of large scale recirculation zones in the cold core flow. The reward-facing geometry of the diffuser is important because it reduces the possibility of ice particle impact on the diffuser surface. Furthermore, the injection of approximately room temperature air through the diffuser should minimise transient thermal effects associated with possible changes to the diffuser surface temperature.

So that the cold-flow is neither accelerated nor decelerated by the action of shear stresses associated with a velocity difference between the core-flow and the injected stream, the cross-sectional flow area introduced by the cone angle $\theta$ must be completely filled with the injected stream, which should travel axially at the speed of the core flow. Considering the configuration illustrated in Figure B.2, to achieve this condition under uniform flow density conditions, the following equation must be satisfied

$$n_j u_j \frac{\pi}{4} d_j^2 = u_\infty \pi (r_{i+}^2 - r_{i-}^2) \tag{B.1}$$

where:

$n_j$ is number of jet orifices at location $x$,

$u_j$ is flow velocity through each orifice,

$d_j$ is the orifice diameter,

$u_\infty$ is the core flow velocity, and

$r_{i+}$ and $r_{i-}$ represent the radii of the downstream and upstream extent of the diffuser area covered by the injection at station $x$.

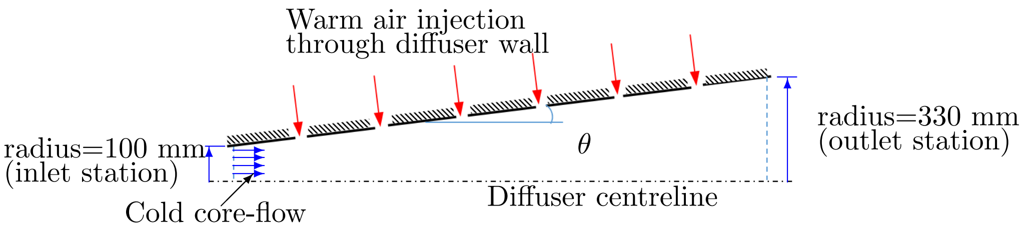


Figure B.1: Schematic diagram of diffuser and the injection orifices.

The left hand side of Equation B.1 represents the total volume flow rate through a certain axial location of multiple ports, while the right hand side refers to the volume flow rate required to cover the flow region between main core and the wall of the cone.

If there is a uniform azimuthal distribution of orifices, the injected flux will be dissipated through turbulent mixing. To maximize flow uniformity for acceleration through the nozzle contraction positioned downstream of the diffuser, the axial flux should be chosen so it matches that of the core-flow. To achieve this matching, the following equality should be satisfied

$$n_j u_j^2 \sin\theta \left(\frac{\pi}{4} d_j^2\right) = u_\infty^2 \pi \left(r_{i+}^2 - r_{i-}^2\right) \tag{B.2}$$

From Equation B.1 the ratio of core flow to orifice velocity is

$$\frac{u_\infty}{u_j} = \frac{n_j d_j^2}{4\left(r_{i+}^2 - r_{i-}^2\right)}, \tag{B.3}$$

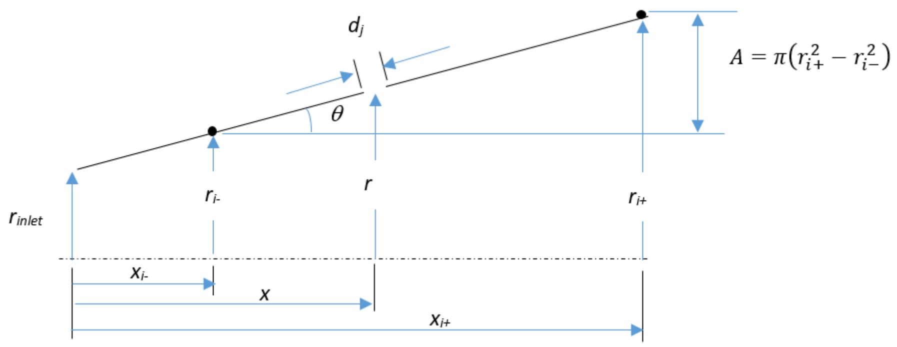


Figure B.2: Schematic diagram of showing distribution of orifices on the cone wall.

whereas from Equation B.2, the square of this ratio is given by

$$\left(\frac{u_\infty}{u_j}\right)^2 \frac{1}{\sin\theta} = \frac{n_j d_j^2}{4\left(r_{i+}^2 - r_{i-}^2\right)} \tag{B.4}$$

Conditions given by equation B.3 and B.4, can only be simultaneously satisfied is

$$\sin\theta = \frac{u_\infty}{u_j} \tag{B.5}$$

The conical half-angle of the diffuser was chosen to be $\theta = 7.5°$. This then specified the required ratio $u_\infty/u_j$ (Equation B.5) which defined the relationship between the number of orifices ($n_j$), the diameter of each orifice ($d_j$), and the spacing between adjacent rows according to Equation B.3. For ease of fabrication, the orifice diameter was chosen to be $d_j = 6\,\text{mm}$ throughout the diffuser. According to the mass flow calculations in Chapter 4, the flow speed was specified to be $u_\infty = 5.5\,\text{m/s}$ at inlet of the diffuser. According to the Equation B.5, the flow velocity at each orifice should be $u_j = 42\,\text{m/s}$, and the total number of orifices associated with these conditions should be 400 orifices distributed on the diffuser wall.

## B.2 Fabrication and assembly the conical diffuser

Solid modelling software was used to generate the conical diffuser. The diffuser orifice pattern in this design was defined from the approach described in Section B.1. To generate the conical perforated diffuser, two longitudinal sheet metal (0.7 mm) strips as shown in Figure B.3 were formed. The 6 mm diameter orifices were distributed on the two halves. Additional holes of 4 mm diameter were drilled in the sheet metal to attach supported rings around the conical shell to maintain a circular cross section in different positions along the conical length. The two sheet metal plates were rolled as shown in Figure B.4 and assembled together to get the final shape of the conical diffuser as shown in Figure B.5.

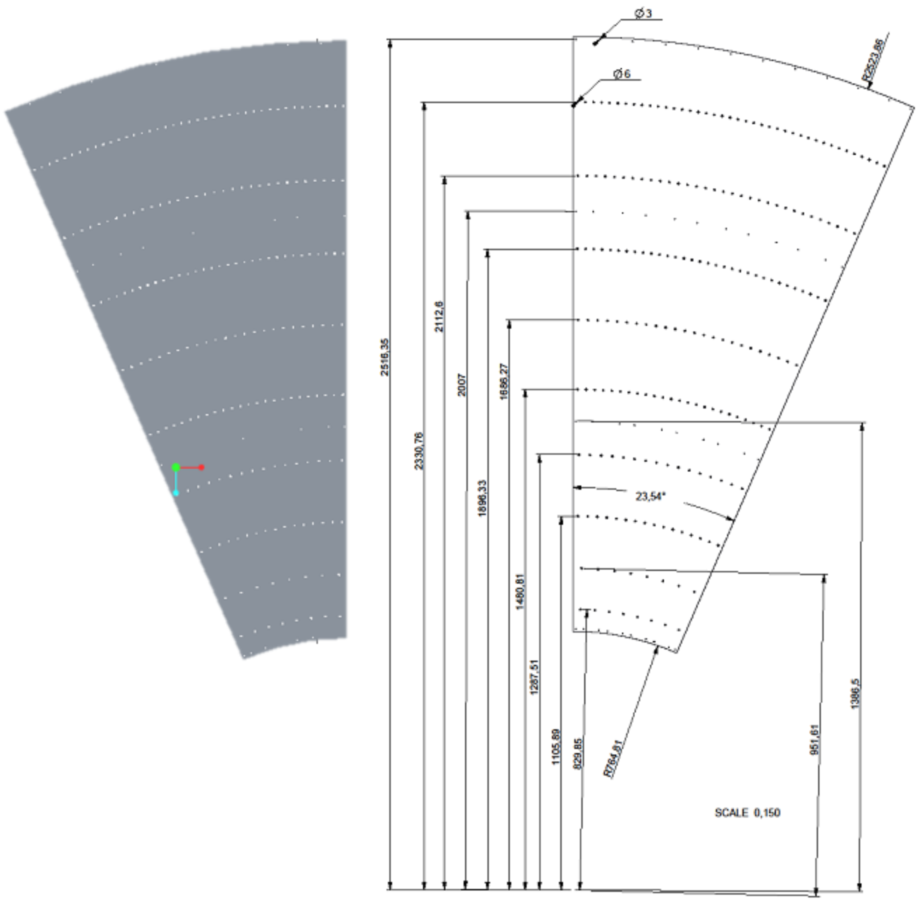


Figure B.3: Schematic diagram of one half of the conical diffuser prior to rolling.

After generating the geometry, the file was exported to the water jet cutting machine in to cut the sheet metal of thickness 0.7 mm for creating the two longitudinal strips. Four rings also were generated in the same manner but from sheet of wood of thickness

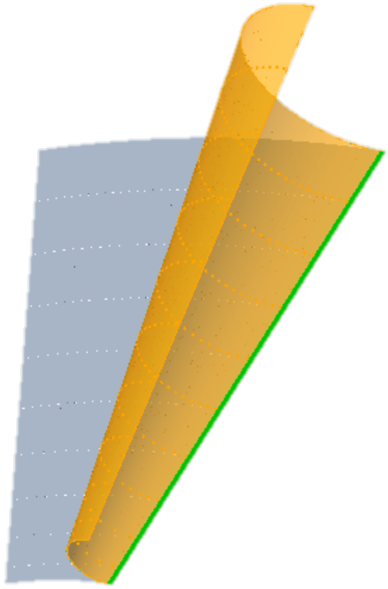

Figure B.4: Solid model illustration of one of the sheet metal strips before and after rolling.

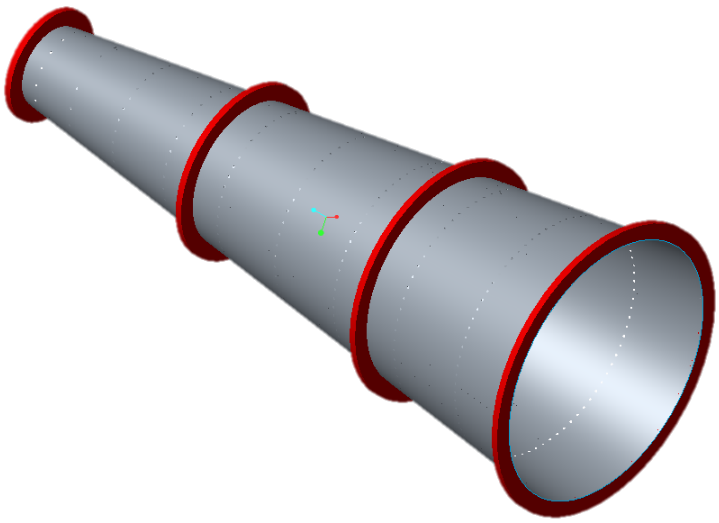

Figure B.5: Solid model illustration of the conical diffuser assembly.

17 mm. Then all parts have been assembled together as shown in Figure B.6.

For increased support and improved symmetry, three additional rings and two longitudinal wooden bars were added as shown in Figure B.7.

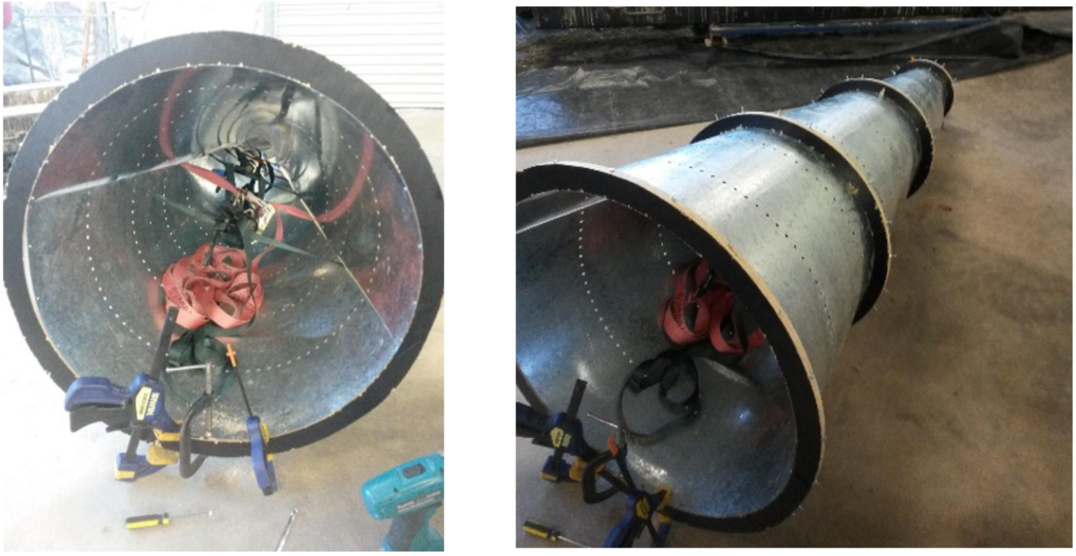

(a) (b)

Figure B.6: Photographs showing the conical diffuser during assembly.

Figure B.7: Photograph of the completed conical diffuser assembly.

# Appendix C

# Design and Fabrication of Contraction Nozzle

## C.1 Internal contraction shape

Key parameters in the nozzle contraction design are the area contraction ratio (CR), the contour shape, and contraction length. The primary design criterion is flow uniformity at contraction outlet, but other criteria such as available space and cost also have an impact on the design.

The largest contraction ratio handled by Morel (1975) is 25. In the current work, the CR has been chosen as 15. Higher contraction ratios can improve the uniformity of the exit velocity. The selection of this contraction ratio provides the necessary transition from the diffuser outlet diameter of 660 mm, to the nozzle exit diameter of 170 mm.

Two cubic arcs have been selected to create the internal wall contour of the contraction as shown in Figure C.1, following the Morel (1975) study. The profile has been formed by using two non-dimensional wall shape functions $f$ to generate two reverse cubic arcs, as specified in Equations C.1 and C.2.

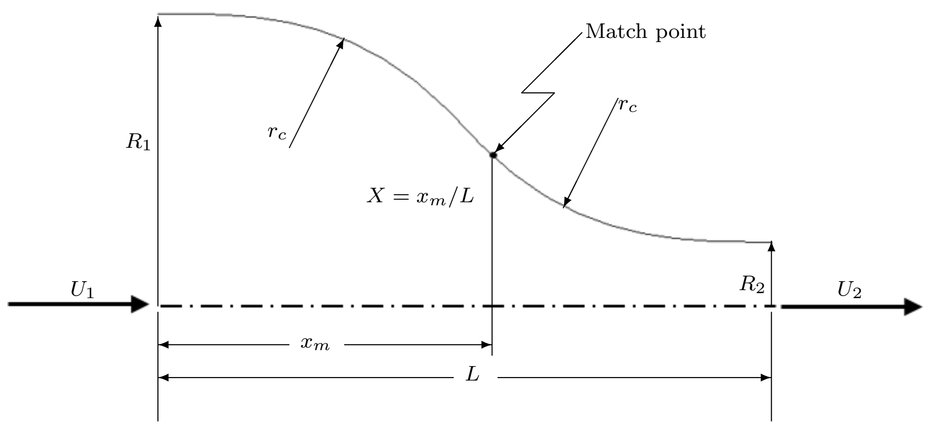


Figure C.1: Schematic diagram showing nozzle wall contour constructed by two matched cubic arcs (adapted from Morel 1975).

$$f = 1 - \frac{1}{X^2}\frac{x^3}{L} \quad \text{for} \quad x/L \leq X \tag{C.1}$$

$$f = 1 - \frac{1}{(1-X)^2}\left(1 - \frac{x^3}{L}\right) \qquad \text{for} \quad x/L > X \tag{C.2}$$

where $X$ represents, the dimensionless position of the matching point and is equal to $x_m/L$ as shown in Figure C.1.

The none-dimensional function $f$ is defined as

$$f\,(x/L) = \frac{D - D_2}{D_1 - D_2} \tag{C.3}$$

Selecting a contraction length is a compromise: it is known that too long a contraction yields thicker boundary layers at the contraction outlet, but too short a contraction causes flow separation problems. According to Morel (1975), $L/D_1$ between 0.75 and 1.25 are most popular in wind tunnels applications. In addition, the numerical results of Morel (1975) demonstrate that this range gives satisfactory values of wall the pressure coefficients $C_{pi}$ and $C_{pe}$ which are defined as

$$C_{pi} = 1 - (V_i/U_{1,\infty})^2 \tag{C.4}$$

$$C_{pe} = 1 - (U_{2,\infty}/V_e)^2 \tag{C.5}$$

where $V$ is the wall velocity, $U_{1,\infty}$ and $U_{2,\infty}$ are velocities in regions away from the wall at the inlet and the outlet respectively, and subscripts $i$ and $e$ refer to the lowest and highest wall velocity. For the present design, an intermediate contraction length of $L/D_1 = 1.0$ has been adopted.

Morel (1975) indicates that separation of boundary layer at the inlet is governed by $C_{pi}$. An small value of $C_{pi} = 0.3$ has been selected for the present design to avoid separation near the inlet.

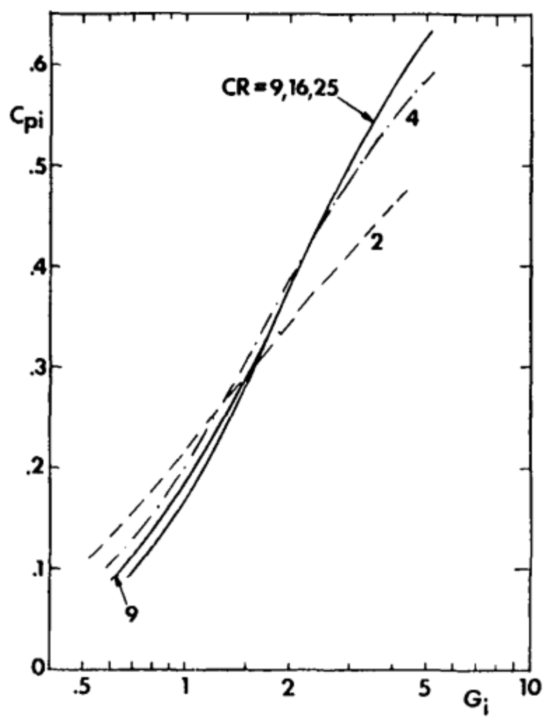


Figure C.2: Dependence of $C_{pi}$ on the dimensionless parameter $G_i$ (adopted from Morel 1975).

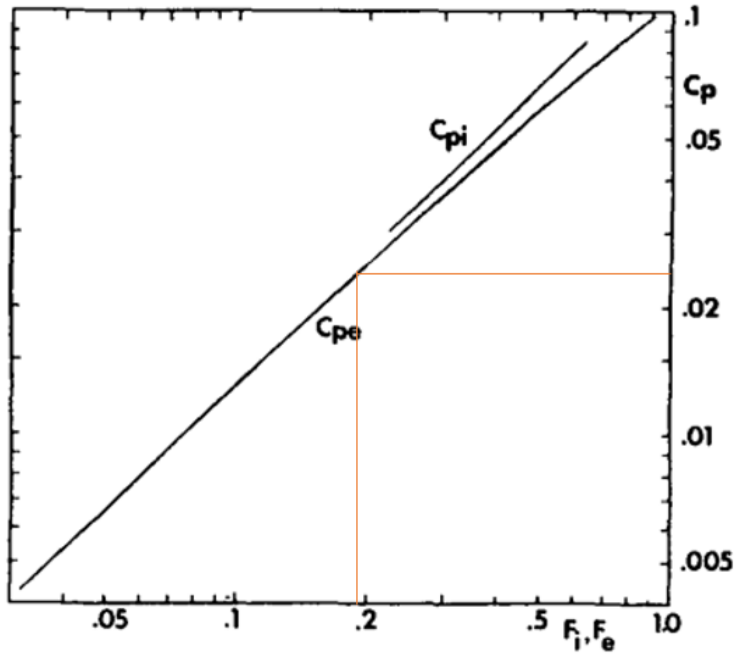


Figure C.3: Dependence of $C_{pi}$ and $C_{pe}$ on the dimensionless parameters $F_i$ and $F_e$ respectively (adopted from Morel 1975).

For $C_{pi} = 0.3$, Figure C.2 (from Morel, 1975) gives a value of $G_i \approx 1.5$. $G_i$ is a dimensionless function as shown in Equation C.6

$$G_i = \frac{m-1}{m} X^{-1} \left(\frac{L}{D_1}\right)^{-2} \tag{C.6}$$

where $m = D_1/D_2$ and equals 3.882 for the chosen contraction design. By applying Equation C.6, the $X$ value is approximately 0.495.

Another important parameter is defined as

$$F_e = \frac{m-1}{m^3} (1-X)^{-2} \left(\frac{L}{D_1}\right)^{-3} \tag{C.7}$$

Substituting values of $X$, $m$, and $L/D_1$ in Equation C.7, gives $F_e = 0.197$. For $F_e = 0.197$, Figure C.3 gives $C_{pe} = 0.025$ which suggests the boundary layer near the contraction exit is far from the separating, and thus the flow uniformity should be very good (better than about 1 % in velocity). For cubic contractions and in many applications, the non-uniformity is required to be less than 2 percent. According to the

Morel (1975) the non uniformity at the nozzle exit $\tilde{u}_2$ can be defined as

$$\tilde{u}_2 = (V - U_c)_2 \,/ U_{2,\infty} \tag{C.8}$$

where $V$ is the velocity near to the wall, $U_c$ is the velocity at centreline, $U_{2,\infty}$ is the velocity far downstream, and subscript 2 refers to the flow conditions on the nozzle exit plane. Therefore, $C_{pe} \leq 0.06$ because the non-uniformity in this case is approximately of $\tilde{u}_2 \approx 0.35\, C_{pe}$ (Morel, 1975).

The nozzle wall contour defined from this analysis is shown in Figure C.4.

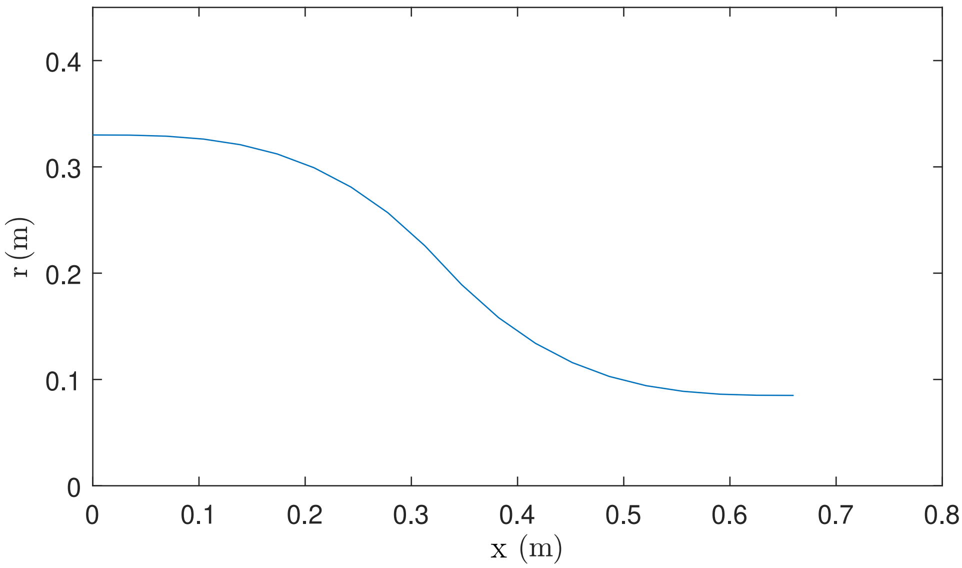


Figure C.4: Nozzle wall profile generated by two reverse cubic arcs: the y-axis represents the radius of the nozzle and the x-axis represents the axial length.

## C.2 Design of nozzle components

The contraction profile obtained in Section C.1 is illustrated in Figure C.4 and this represents the internal surface of the contraction nozzle. The outer surface of the nozzle was then obtained by translating the internal surface profile in the outward direction in a manner that provided an overall thickness of the section at the inlet of 50 mm while retaining a thin trailing edge at the nozzle lip as shown in Figure C.5. The internal and external profiles were defined in Matlab scripts and data points along these profiles were transferred to the solid modelling software (Creo). The nozzle lip as

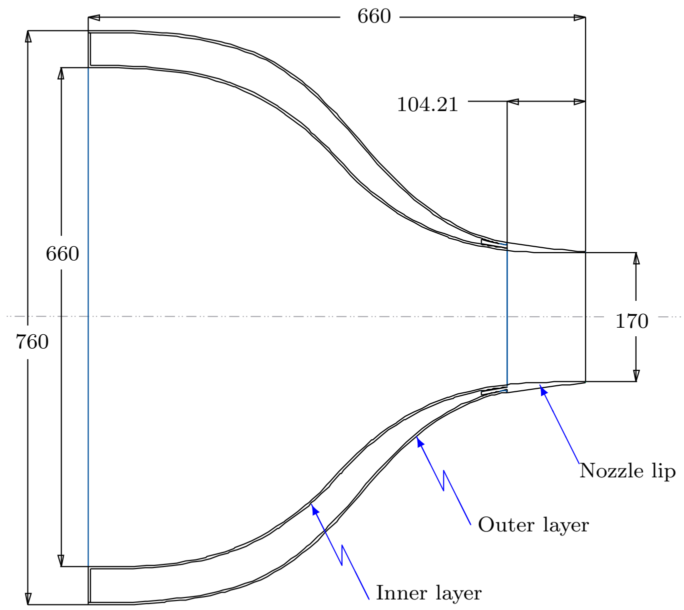


Figure C.5: Illustration of nozzle component arrangement and dimensions.

illustrated in Figure C.5 was a 3D printed component, and it enables the outer layer and the inner layer to be connected together with a relative thin trailing edge. Two moulds, one for the inner contraction and one for the outer profile, were required to generate fibreglass layers.

## C.3 Design and fabrication of nozzle moulds

### C.3.1 Solid modelling

Moulds for the fibreglass layup were designed using solid modelling software. Each mould was divided into four quarters as illustrated in Figure C.6 and Figure C.7. The moulds were fabricated from polystyrene using four quarters because of the travel limitations of the CNC machine.

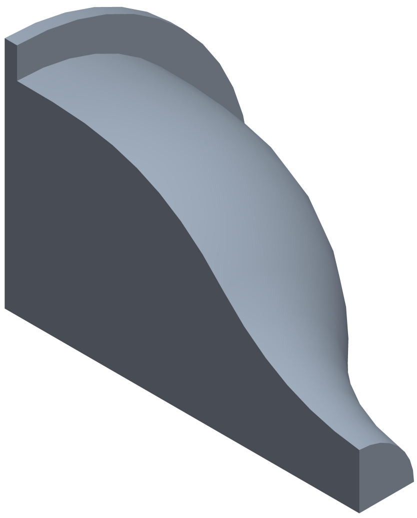

(a) Inner mould.

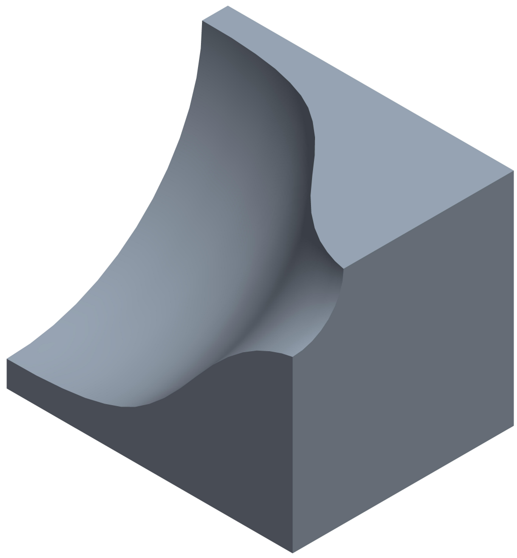

(b) outer mould.

Figure C.6: Nozzle Contraction moulds generated by solid modelling (quarter).

### C.3.2 Creating nozzle moulds by cutting process

The mould files in .igs format were delivered to the CNC milling machine in the USQ mechanical workshop. High density polystyrene foam was used for the moulds. The dimensions of foam required for each inner quarter mould was $400 \times 400 \times 576$ mm, and for outer quarter mould was $430 \times 430 \times 556$ mm. Photographs of the fabricated polystyrene mould shapes are shown in Figure C.8.

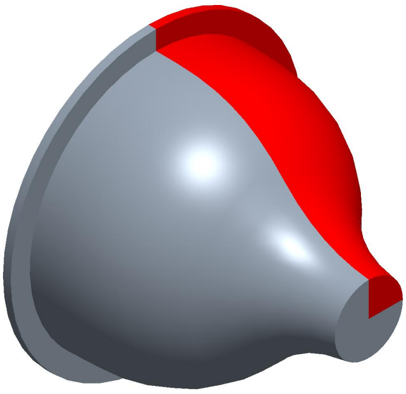

(a) Inner mould.

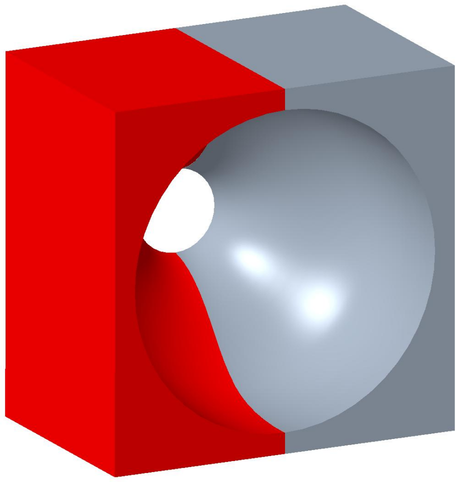

(b) outer mould.

Figure C.7: Nozzle contraction moulds each assembled from the four quarters.

### C.3.3 Fibreglass work

Fibreglass lay-up work requires moulds with smooth surfaces. The moulds were prepared firstly by assembling the quarters together by using a cement (TechGrip Bond). Then, the moulds were painted with a resin material (Epoxy Laminating) to prevent the polystyrene surfaces from dissolving when the MEKP material is applied to provide the surface with adequate toughness for the sanding process. The peaks which existed on the mould surfaces were eliminated with multiple grades of wet and dry sand papers until the roughness reached approximately 15.3 $\mu$m. The mould surfaces were then coated with a filler (mixture of resin and Qcell), and then the mould was polished again. The last two process were repeated many times to get a very smooth surface finish. Figure C.9 shows resin material on the moulds.

Two materials were used for mould release: wax and PVA mould release (a special formula release agent for the fibreglass industry). Six wax layers with polishing between application of each layer were used to produce a high gloss surface. Following the wax application and polishing, the moulds were coated with a thin layer of PVA using a spray gun with results as shown in Figure C.10.

A layer of Gel Coat was then applied to make smooth surfaces on the inside and outside

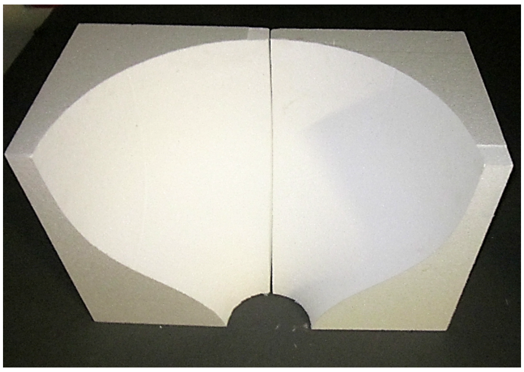

(a) half outer mould.

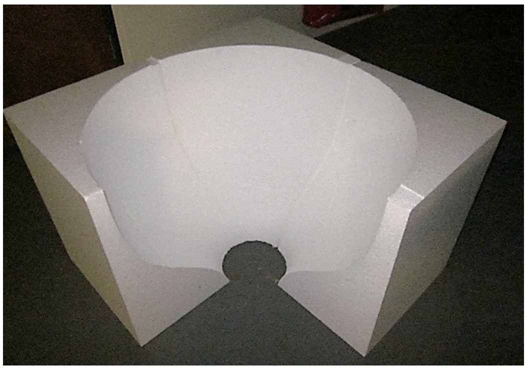

(b) three-quarters outer mould.

(c) half inner mould.

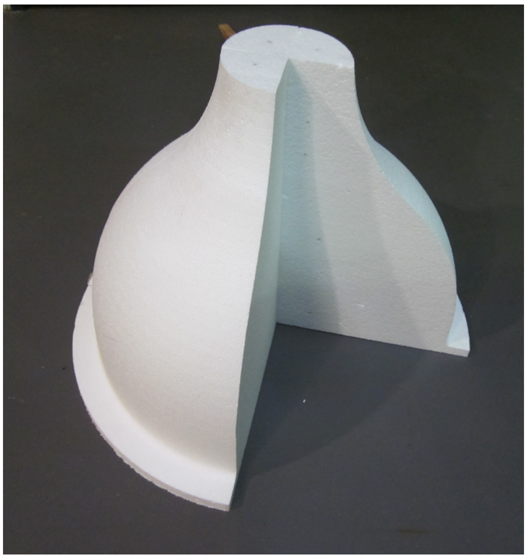

(d) three-quarters inner mould.

Figure C.8: Photographs showing the nozzle polystyrene moulds generated by the milling machine.

of the nozzle as shown in Figure C.11. The moulds were coated with segments cut from sheet fibreglass called chopped strand mat (woven into a fabric). The process involved brushing sheets of material with resin and placing them on the mould with additional resin and squashing them together layer after layer. Four layers were used for both moulds as shown in Figure C.12. The results of fibreglass work are two layers nozzle with a suitable smooth surface as shown in Figure C.12. To finish the fabrication of the contraction nozzle, the inner and outer components were pressed out of the moulds as shown in Figure C.13, and then assembled together with the nozzle lip. The assembled contraction component is shown in Figure C.14.

(a) inner mould.

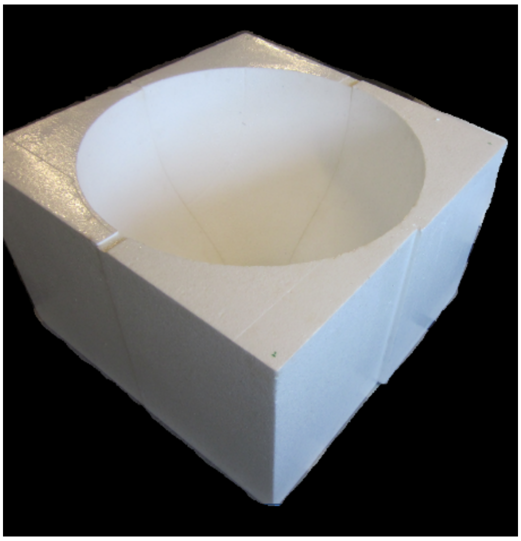

(b) outer mould.

Figure C.9: Photographs showing the nozzle polystyrene moulds painted with the resin material.

(a) inner mould.

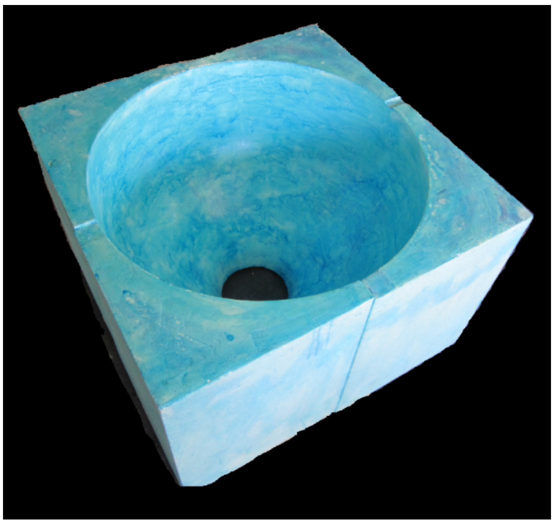

(b) outer mould.

Figure C.10: Photographs showing the nozzle polystyrene moulds coated with PVA mould release.

(a)

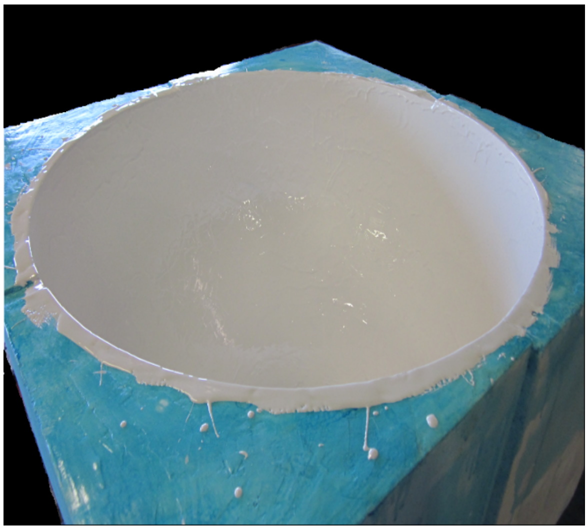

(b)

Figure C.11: Photographs showing the nozzle polystyrene moulds coated with Gel Coat. (a) Inner mould; and (b) outer mould.

(a) Inner mould.

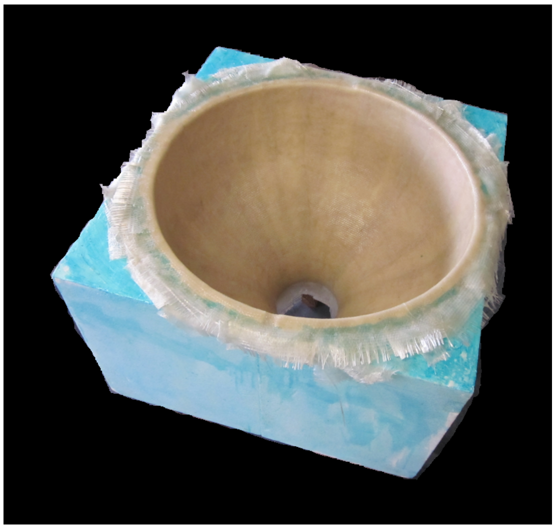

(b) outer mould.

Figure C.12: Photographs showing the layers of fibreglass on the nozzle polystyrene moulds.

(a) Inner layer. (b) outer layer.

Figure C.13: Photographs showing the fibreglass nozzle layers after drying and releasing from their moulds.

Figure C.14: Photograph showing the assembled nozzle contraction.

# Appendix D

# Fan and Diffuser Performance Assessment

This appendix presents a performance assessment of the fan and perforated diffuser operating in conjunction with the facility. Figure D.1 presents the performance of the fan showing the relationship of the static pressure, the air flow rate, and the motor current at different operation conditions. As shown in Figure D.1, the fan has options to operate in three speed modes: low, medium, and high. In the current study, the high speed mode was used. During wind tunnel testing, the static pressure in the diffuser shell region, which is representative of the static pressure downstream of the fan was measured to be approximately 451 Pa. The motor current was also measured in the same test and was approximately 3.3 amps. Based on these measurements, the fan performance curve (Figure D.1) indicates the volumetric flow rate for the fan $\dot{V}_{a,f}$ is approximately 558 litre/s. The air mass flow rate for the fan can be calculated as:

$$\dot{m}_{a,f} = \rho_a \dot{V}_{a,f} \approx 0.608\,\mathrm{kg/s} \tag{D.1}$$

for $\rho_a$=1.09 kg/m$^3$ which is an indicative value for the local laboratory conditions. The air mass flow rate delivered through the perforated diffuser surface can be estimated by first measuring the pressure difference between the static pressure in the shell and the static pressure in the core region of the diffuser. When this is done, the static pressure drop through the perforated diffuser is calculated as

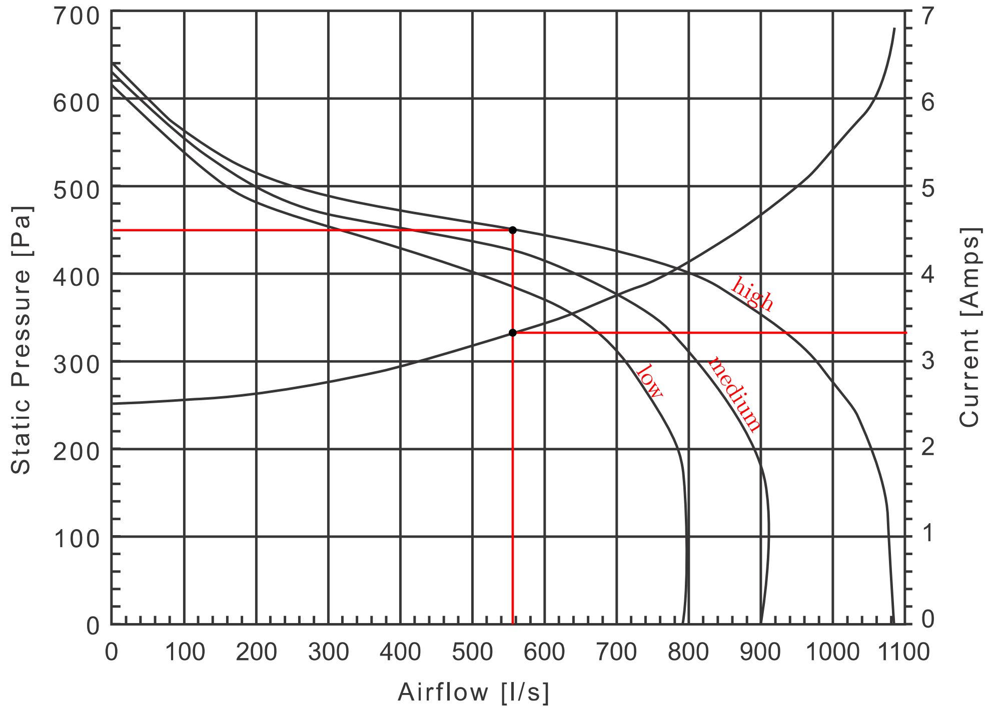


Figure D.1: Theoretical Fan static pressure and motor current variation with air volumetric flow rate. (Figure adapted from Direct Drive Blowers - Torin Manual)

$$\Delta P_{d,wall} = 1.2\,\mathrm{kPa} \tag{D.2}$$

On the assumption that there is no recovery of the dynamic pressure of the flow through each hole, the velocity through each hole is

$$V_h = \sqrt{\frac{2\Delta P_{d,wall}}{\rho_a}} = 46.9\,\mathrm{m/s} \tag{D.3}$$

The combined air flow passing through the 400 orifices, each with a 6 mm hole diameter, effectively passes through a total area given by

$$A_h = \frac{\pi}{4} d_h^2 N_h \tag{D.4}$$

where $d_h$ is the hole diameter and $N_h$ is the holes number. In this case, total area is equal to $A_h = 0.0133\,\mathrm{m}^2$.

The total air mass flow rate through the diffuser holes then can be calculated:

$$\dot{m}_{a,d} = C_d \rho_a V_h A_h \tag{D.5}$$

where $C_d$ is the discharge coefficient for the perforated plate. According to Kolodzie and Van Winkle (1957), the perforated plate discharge coefficient is correlated using

$$C_d = K\left(\frac{d_h}{Ph}\right)^{0.1} \tag{D.6}$$

where $K$ is a constant depending on the Reynolds number of flow through the holes and the ratio of the perforated plate thickness $T_p$ to the hole diameter $d_h$. $Ph$ represents the hole pitch. The Reynolds number corresponding to the diffuser holes can be defined as

$$Re_d = \frac{\rho_a V_h d_h}{\mu_a} \tag{D.7}$$

where $\mu_a$ is the dynamic viscosity of the air.

For the velocity $V_{holes} = 46.9\,\mathrm{m/s}$, $Re_d =$ 19300, and in the present application $T_p/d_h =$ 0.15, so the $K$ value according to the Kolodzie and Van Winkle (1957) correlation is approximately 0.74 and as a result, $C_d \approx$ 0.72. Now using Equation D.5, the mass flow rate through the perforated diffuser wall is approximately $\dot{m}_{a,d} \approx$ 0.49 kg/s.

This value of mass flow rate differs from the value derived from the fan performance curve by about 20 %. This is reasonable result given the likely uncertainties in the installed performance of the fan and the uncertainties in the discharge coefficient of the perforated diffuser.

# Appendix E

# Pressure Drop Measurement for Perforated Entrance Plate

The pressure drop ($\Delta P_i$) at entrance was measured using a water manometer at the normal facility operating condition and was found to be approximately 736 Pa. The flow velocity through the holes can be estimated using

$$V_i = \sqrt{\frac{2\Delta P_i}{\rho_a}} = 36.5\,\mathrm{m/s}, \tag{E.1}$$

and the total open area at the entrance is

$$A_i = \frac{\pi}{4} d_h^2 N_h \tag{E.2}$$

where $d_h$ is the hole diameter ($d_h = 12\,\mathrm{mm}$), and $N_h = 44$, the number of the holes in the plate. Therefore $A_i = 0.00498\,\mathrm{m}^2$ and the mass flow rate of air evaporator can be found from

$$\dot{m}_{air,e} = C_d \rho_a V_i A_i, \tag{E.3}$$

again $C_d$ is the discharge coefficient for the perforated plate and can be determined from Equation D.6. For the chosen perforated plate geometry, $T_p = 10\,\mathrm{mm}$, and $P_h = 20\,\mathrm{mm}$.

For the velocity $V_i = 36.5\,\mathrm{m/s}$, the Re = 26,900 and the ratio of $T_p/d_h = 0.833$, according to the Kolodzie and Van Winkle 1957 correlation, $K \approx 0.94$. By substitution of the $K$ value and $d_h/P_h = 0.6$ in Equation D.6, $C_d \approx 0.893$. The mass flow rate of air evaporator can be calculated from Equation E.3 and is found to be $\dot{m}_{air,e} = 0.177\,\mathrm{kg/s}$.

# Appendix F

# Ultrasonic Nozzle Data Sheet

The atomizer nozzle type MAD 0331 B1 was used in the experiments. Figure F.1 shows the details of atomizer nozzle and its fittings.

www.pnr-nozzles.com

# ULTRASONIC ATOMIZERS

## ATOMIZERS AND FITTINGS

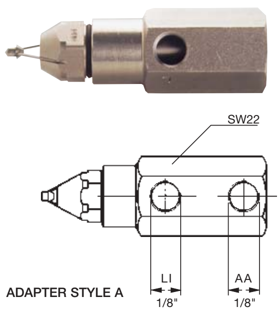


Ultrasonic atomizers produce the finest sprays available with air assistance for industrial processes, with a narrow angle full cone jet.
Water and air do not mix in a confined volume before leaving the nozzle and therefore their feed pressures can be adjusted independently without influencing each other: this allows for a very wide regulation range on the liquid capacity and makes it easier to reach the desired operating conditions.

Please note that the code given in the table only refers to the atomizing head and must be completed with the identification for one of the four connection adapters available, as shown below in the page.
The drawing beside shows an atomizing head assembled onto one A type adapter.

| Materials | Atomizing head | B1 AISI 303 Stainless steel |
|---|---|---|
| | Adapter | B1 AISI 303 Stainless steel |
| | | T1 Brass |

WM = Water capacity (l/min)
AH = Air capacity (Ncm/h)

### IDENTIFICATION CODES

**ATOMIZING HEAD**
The codes given in the table refer to the atomizing head only, and can be used to order the head as a separate part.

**ADAPTERS**
Can be ordered separately using the codes below, please replace
XX = B1 for AISI 303
XX = T1 for brass

**COMPLETE ATOMIZERS**
To identify a complete atomizer, please add to the head code the three suffix letters describing the adapter material and the adapter style according to the information below.

MAD 0801 B1 X Y Z

Adapter Material
A = T1 Brass
B = B1 AISI 303

Adapter style
A = XMA 0103 xx
B = XMA 0101 xx
C = XMA 0102 xx
D = XMA 0100 xx

Connection
B = BSP F
N = NPT F

| Angle | Set-up Code | Air pressure (bar) | WM (0,5) | AH (0,5) | WM (0,7) | AH (0,7) | WM (1,0) | AH (1,0) | WM (2,0) | AH (2,0) | WM (3,0) | AH (3,0) |
|---|---|---|---|---|---|---|---|---|---|---|---|---|
| 25° | MAD 0331 B1 | 2 | 0,10 | 3,1 | 0,12 | 3,0 | 0,15 | 3,1 | 0,27 | 2,7 | - | - |
| | | 3 | 0,05 | 3,7 | 0,10 | 3,1 | 0,12 | 3,6 | 0,20 | 3,7 | 0,32 | 2,9 |
| | | 4 | 0,02 | 4,7 | 0,05 | 4,8 | 0,08 | 4,4 | 0,18 | 4,4 | 0,25 | 4,2 |
| | | 5 | - | - | 0,02 | 5,3 | 0,05 | 5,3 | 0,13 | 5,5 | 0,22 | 5,2 |
| | | 6 | - | - | - | - | 0,02 | 6,1 | 0,12 | 6,0 | 0,18 | 5,8 |
| | MAD 0801 B1 | 2 | 0,23 | 2,7 | 0,28 | 2,9 | 0,37 | 2,7 | 0,72 | 2,2 | - | - |
| | | 3 | 0,22 | 3,6 | 0,27 | 3,6 | 0,32 | 3,5 | 0,52 | 3,2 | 0,82 | 2,7 |
| | | 4 | 0,18 | 4,5 | 0,22 | 4,4 | 0,28 | 4,6 | 0,45 | 4,6 | 0,62 | 4,7 |
| | | 5 | 0,12 | 5,4 | 0,18 | 5,3 | 0,25 | 5,6 | 0,40 | 5,4 | 0,53 | 5,4 |
| | | 6 | 0,07 | 6,2 | 0,13 | 6,3 | 0,22 | 6,2 | 0,35 | 6,3 | 0,50 | 6,2 |
| | MAD 1131 B1 | 2 | 0,50 | 7,3 | 0,60 | 6,6 | 0,73 | 6,9 | 1,15 | 5,6 | - | - |
| | | 3 | 0,40 | 9,7 | 0,50 | 9,5 | 0,65 | 9,4 | 0,96 | 9,3 | 1,35 | 7,9 |
| | | 4 | 0,27 | 11,6 | 0,37 | 11,9 | 0,55 | 11,8 | 0,93 | 12,1 | 1,20 | 11,5 |
| | | 5 | 0,13 | 13,9 | 0,23 | 13,8 | 0,38 | 14,0 | 0,87 | 14,1 | 1,15 | 13,8 |
| | | 6 | 0,07 | 18,6 | 0,13 | 18,7 | 0,27 | 8,7 | 0,72 | 18,9 | 1,10 | 19,0 |
| 40° | MAL 0800 B1 | 2 | 0,18 | 2,7 | 0,23 | 2,7 | 0,32 | 2,9 | 0,73 | 2,1 | - | - |
| | | 3 | 0,15 | 3,7 | 0,18 | 3,9 | 0,25 | 3,5 | 0,50 | 3,7 | 0,85 | 2,6 |
| | | 4 | 0,10 | 4,5 | 0,17 | 4,6 | 0,22 | 4,9 | 0,33 | 4,8 | 0,53 | 4,4 |
| | | 5 | 0,03 | 5,4 | 0,10 | 5,6 | 0,18 | 5,4 | 0,30 | 5,4 | 0,45 | 5,3 |
| | | 6 | - | - | 0,03 | 6,2 | 0,12 | 6,3 | 0,27 | 6,2 | 0,38 | 6,3 |
| | MAL 1130 B1 | 2 | 0,46 | 7,3 | 0,52 | 7,2 | 0,68 | 6,8 | 1,13 | 5,7 | - | - |
| | | 3 | 0,38 | 9,5 | 0,47 | 9,7 | 0,65 | 10,2 | 0,95 | 9,4 | 1,27 | 7,7 |
| | | 4 | 0,23 | 11,8 | 0,35 | 11,8 | 0,50 | 11,9 | 0,88 | 12,1 | 1,15 | 11,8 |
| | | 5 | 0,13 | 13,5 | 0,23 | 13,9 | 0,37 | 14,0 | 0,82 | 14,1 | 1,10 | 14,2 |
| | | 6 | 0,07 | 16,0 | 0,13 | 16,2 | 0,27 | 16,2 | 0,63 | 16,2 | 1,03 | 16,3 |
| | MAL 1300 B1 | 2 | 0,95 | 14,6 | 1,12 | 16,5 | 1,40 | 16,3 | 2,42 | 10,4 | - | - |
| | | 3 | 0,80 | 19,3 | 1,00 | 20,0 | 1,26 | 22,2 | 1,90 | 19,2 | 2,87 | 14,5 |
| | | 4 | 0,60 | 24,7 | 0,80 | 24,7 | 1,08 | 25,0 | 1,80 | 25,0 | 2,40 | 23,2 |
| | | 5 | 0,42 | 29,9 | 0,60 | 30,3 | 0,90 | 30,4 | 1,70 | 30,5 | 2,27 | 29,9 |
| | | 6 | 0,23 | 35,6 | 0,40 | 36,0 | 0,67 | 35,6 | 1,55 | 36,2 | 2,15 | 35,2 |

Liquid pressure (bar): 0,5 / 0,7 / 1,0 / 2,0 / 3,0

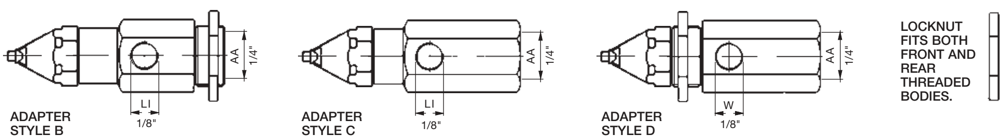


B and D adapter style allow for mounting the atomizer through a wall or the side of a duct.
In this case do not forget to order the VAC 0021 B1 locknut, which fits both, to hold the adapter in place.

Figure F.1: Data sheet for the ultrasonic nozzle used in experiments.

# Appendix G

# Pitot Tube Details and Pressure Sensors Data Sheets

## G.1 Ardupilot Arduplane Pitot static tube

The Ardupilot Arduplane Pitot static tube (APM−2.5/2.6) with ellipsoid nose has been used. Four holes of 0.5 mm diameter are distributed around the tube perimeter. The holes are designed to receive the local static pressure, while the upstream facing hole of 1 mm diameter, which is located on the tip of the pitot probe, is designed to receive the total pressure of the flow. The profile and the dimensions of pitot tube are illustrated in Figure G.1, and a photograph of the pitot probe installed on the traversing system is presented in Figure 4.21.

For the pitot static pressure probe, the pressure difference between the central hole and the static pressure measured around the perimeter of the probe downstream can be defined as

$$p_t - p_s = \frac{\rho u_\infty^2}{2} \tag{G.1}$$

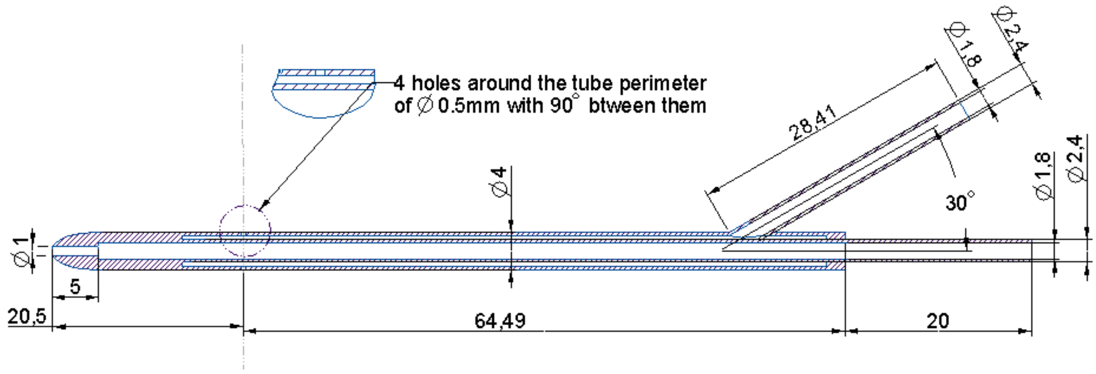


Figure G.1: Schematic diagram of pitot-static pressure probe head.

## G.2 MPXV7002DP

The calibration equation of the sensor (MPXV7002DP) as specified by the manufacturer is

$$V_{out} = V_s\,(0.2P + 0.5) \pm 6.25\% V_{FSS} \tag{G.2}$$

where $V_{out}$ is the voltage signal, $V_s$ is the source voltage (5.0 volt was used), $P$ is the pressure in kPa, and $V_{FSS}$ is calculated from the algebraic difference between the output voltage at full rated pressure and the output voltage at the minimum rated pressure.

Figure G.3 illustrates the electronic circuit and wiring. The circuit can be used either with a mini SD card or with a direct connection to a computer. The system produced encouraging results, however the data acquisition rate was slow (1 reading per second). Because of the slow response of Arduino board system, the Arduino was replaced by a LabVIEW data acquisition system and a SDX transducer (as described in Section G.3).

## G.3 SDX01D4-A

The calibration of the SDX01D4-A sensor was performed with reference to the digital manometer in different points along the wall of the wind tunnel. The data are presented

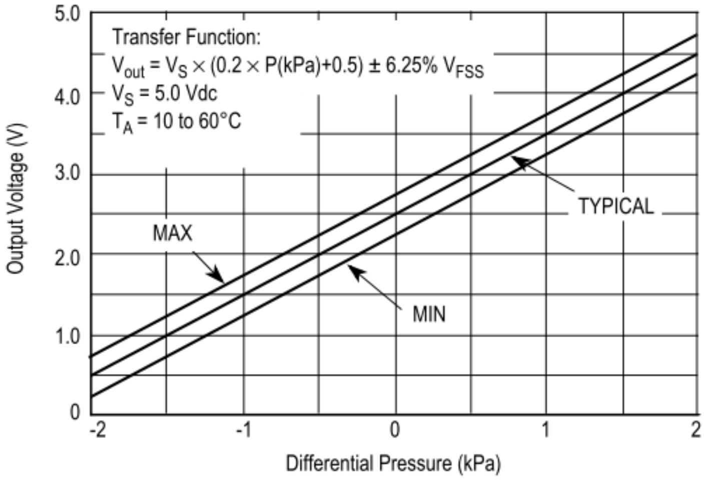


Figure G.2: Output voltage versus pressure differential (adopted from pressure sensor data sheet).

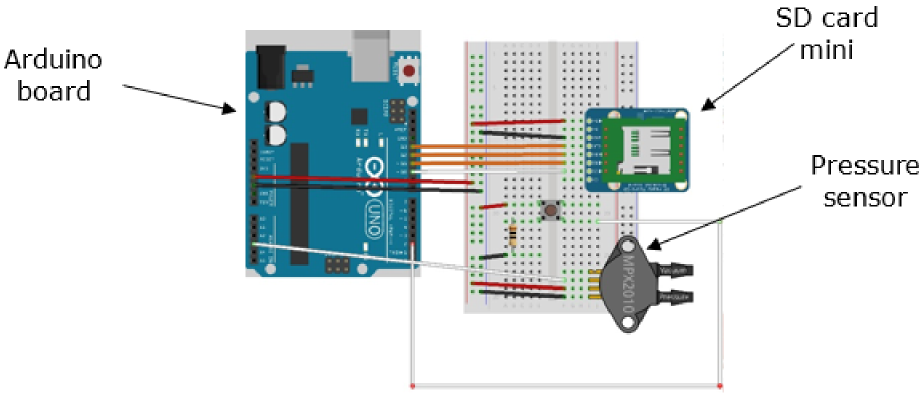


Figure G.3: Illustration showing electronic circuit and wiring connections for the pressure sensor with the Arduino board.

in Table G.1, and the calibration correlation is shown in Figure G.4

Table G.1: Calibration data for SDX transducer.

| P (Pa) | $V_r$ (V) |
|---|---|
| 0 | $0.5861 (= V_i)$ |
| 871 | 0.6722 |
| 1378 | 0.722 |
| 1515 | 0.7345 |
| 1597 | 0.7422 |

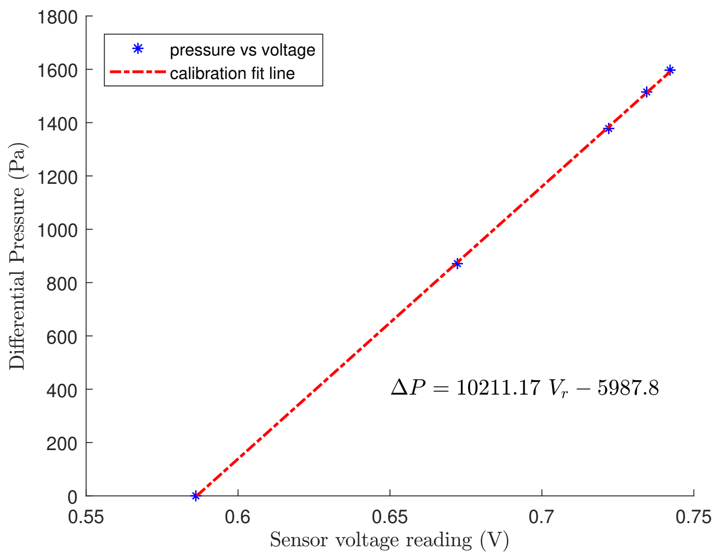


Figure G.4: Digital pressure manometer readings variation with sensor voltage readings.

Honeywell

# Microstructure Pressure Sensors
# Low Cost, Compensated, DIP Package
0 psi to 1 psi up to 0 psi to 100 psi

*SDX Series*

**FEATURES**
- Low Cost DIP
- Precision Temperature Compensation
- Calibrated Zero & Span
- Small Size
- Low Noise
- High Impedance for Low Power Applications
- Prime Grade Available (SDXxxxyy-A)

**TYPICAL APPLICATIONS**
- Medical Equipment
- Computer Peripherals
- Pneumatic Controls
- HVAC

**⚠ WARNING**

**PERSONAL INJURY**

DO NOT USE these products as safety or emergency stop devices or in any other application where failure of the product could result in personal injury.

**Failure to comply with these instructions could result in death or serious injury.**

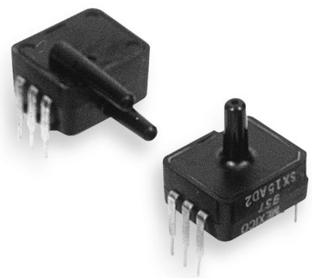

The SDX series sensors provide a very cost effective solution for pressure applications that require small size plus performance. These calibrated and temperature compensated sensors give an accurate and stable output over a 0 °C to 50 °C [32 °F to 122 °F] temperature range. This series is intended for use with non-corrosive, non-ionic working fluids such as air, dry gases and the like.

Devices are available to measure absolute and gage pressures from 1 psi (SDX01) up to 100 psi (SDX100). The absolute devices have an internal vacuum reference and an output voltage proportional to absolute pressure.

The SDX devices are available in standard commercial and prime grades (SDCxxxyy – A) to allow optimization of accuracy and cost in any given application.

The SDX devices feature an integrated circuit (IC) sensor element and laser trimmed thick film ceramic housed in a compact solvent resistant case. The package is a double-wide (i.e. 0.600 inches lead spacing) dual-inline package (DIP). This is the same familiar package used by IC manufacturers except it is only 11,94 mm [0.470 in] long and has a pressure port(s). The pc board area used by each DIP is approximately 0.26 in$^2$. This extremely small size enables the use of multiple sensors in limited available space. The DIP provides excellent corrosion resistance and isolation to external package stress.

The DIP mounts on a pc board like a standard IC with through-hole pins. The pins anchor the pressure sensor to the pc board and provide a more secure and stable unit than other types of packages.

The output of the bridge is ratiometric to the supply voltage and operation from any dc supply voltage up to 20 Vdc is acceptable.

Contact your local honeywell representative or go to Honeywell's website at www.honeywell.com/sensing for additional details.

**⚠ WARNING**

**MISUSE OF DOCUMENTATION**
- The information presented in this product sheet is for reference only. Do not use this document as a product installation guide.
- Complete installation, operation, and maintenance information is provided in the instructions supplied with each product.

**Failure to comply with these instructions could result in death or serious injury.**



Figure G.5: Data sheet for Honeywell sensor SDX series. General features.

# Microstructure Pressure Sensors

## Low Cost, Compensated, DIP Package

0 psi to 1 psi up to 0 psi to 100 psi

*SDX Series*

**PRESSURE RANGE SPECIFICATIONS**

| Model No*, Pressure Connection, Pressure Type | | | Operating Pressure | Proof Pressure (2) | Full-Scale Span (1) | | |
|---|---|---|---|---|---|---|---|
| ***Gage*** | ***Diff/Gage*** | ***Absolute*** | | | **Min.** | **Typ.** | **Max.** |
| SDX01G2 | SDX01D4 | -- | 0 psid to 1 psid | 20 psid | 17.37 mV | 18.00 mV | 18.63 mV |
| SDX01G2-A | SDX01D4-A | -- | | | 17.82 mV | 18.00 mV | 18.80 mV |
| SDX05G2 | SDX05D4 | -- | 0 psid to 5 psid | 20 psid | 57.90 mV | 60.00 mV | 62.10 mV |
| SDX05G2-A | SDX05D4-A | -- | | | 59.40 mV | 60.00 mV | 60.60 mV |
| SDX15G2 | SDX15D4 | -- | 0 psid to 15 psid | 30 psid | 86.85 mV | 90.00 mV | 93.15 mV |
| SDX15G2-A | SDX15D4-A | -- | | | 89.10 mV | 90.00 mV | 90.90 mV |
| | | SDX15A2 | 0 psia to 15 psia | 30 psia | 86.85 mV | 90.00 mV | 93.15 mV |
| | | SDX15A4 | | | 86.85 mV | 90.00 mV | 93.15 mV |
| | | SDX15A2-A | | | 89.10 mV | 90.00 mV | 90.90 mV |
| | | SDX15A4-A | | | 89.10 mV | 90.00 mV | 90.90 mV |
| SDX30G2 | SDX30D4 | -- | 0 psid to 30 psid | 60 psid | 86.85 mV | 90.00 mV | 93.15 mV |
| SDX30G2-A | SDX30D4-A | -- | | | 89.10 mV | 90.00 mV | 90.90 mV |
| | | SDX30A2 | 0 psia to 30 psia | 60 psia | 86.85 mV | 90.00 mV | 93.15 mV |
| | | SDX30A4 | | | 86.85 mV | 90.00 mV | 93.15 mV |
| | | SDX30A2-A | | | 89.10 mV | 90.00 mV | 90.90 mV |
| | | SDX30A4-A | | | 89.10 mV | 90.00 mV | 90.90 mV |
| SDX100G2 | SDX100D4 | -- | 0 psid to 100 psid | 150 psid | 96.50 mV | 100.00 mV | 103.5 mV |
| SDX100G2-A | SDX100D4-A | -- | | | 99.00 mV | 100.00 mV | 101.0 mV |
| | | SDX100A2 | 0 psia to 100 psia | 150 psia | 96.50 mV | 100.00 mV | 103.5 mV |
| | | SDX100A4 | | | 96.50 mV | 100.00 mV | 103.5 mV |
| | | SDX100A2-A | | | 99.00 mV | 100.00 mV | 101.0 mV |
| | | SDX100A4-A | | | 99.00 mV | 100.00 mV | 101.0 mV |

* Ordering information: Order model number. (-A) = Prime Grade

Pressure Connection and Pressure Type

- G2 = “D2” DIP Package, Temperature Compensated Gage Sensor
- G2-A = “D2” DIP Package, Prime Grade, Temperature Compensated Gage Sensor
- D4 = “D4” DIP Package, Temperature Compensated Differential Sensor
- D4-A = “D4” DIP Package, Prime Grade, Temperature Compensated Differential Sensor
- A2 = “D2” DIP Package, Temperature Compensated Absolute Sensor
- A2-A = “D2” DIP Package, Prime Grade, Temperature Compensated Absolute Sensor
- A4 = “D4” DIP Package, Temperature Compensated Absolute Sensor
- A4-A = “D4” DIP Package, Prime Grade, Temperature Compensated Absolute Sensor

**GENERAL SPECIFICATIONS**

| Characteristic | Description (Maximum Ratings) All Devices |
|---|---|
| Supply Voltage (Vs) | 20 Vdc |
| Common Mode Pressure | 150 psig |
| Lead Soldering Temperature (2 seconds to 4 seconds) | 250 °C [482 °F] |

**ENVIRONMENTAL SPECIFICATIONS**

| Characteristic | Description (Maximum Ratings) All Devices |
|---|---|
| Compensated Operating Temperature | 0 °C to 50 °C [32 °F to 122 °F] |
| Operating Temperature | -40 °C to 85 °C [-40 °F to 185 °F] |
| Storage Temperature | -55 °C to 125 °C [-67 °F to 257 °F] |
| Humidity Limits | 0 % RH to 100 % RH |



Figure G.6: Data sheet for Honeywell sensor SDX series. Pressure range specifications.

# Appendix H

# Screen loss coefficients calculation

The screens of the original wind tunnel were treated as a porous medium which produces a pressure drop. Details of the porous medium option in the Fluent are provided in the Fluent manual. For the present work the pressure jump approach was selected. To include this option in the current simulation, the calculation of the pressure jump coefficient ($C_2$), and viscous resistance coefficient ($C_1$) are required. The pressure drop in the porous medium is calculated using

$$\Delta p = -\left(\frac{\mu}{\alpha}v + C_2\frac{1}{2}\rho v^2\right)\Delta m \tag{H.1}$$

where $\mu$ is flow dynamic viscosity, $\alpha$ is flow thermal diffusivity, $C_2$ is pressure jump coefficient and $\Delta m$ is the thickness of medium. The coefficient $C_2$ is given by

$$C_2 = \frac{K_L'}{\Delta m} \tag{H.2}$$

where $K_L'$ is an adjusted losses factor which is given by

$$K_L' = K_L\frac{V^2_{@\,open\ area}}{V^2_{@\,100\%\,open\ area}} \tag{H.3}$$

where $K_L$ is a loss factor. The loss factor $K_L$ was calculated according to the literature (Cevik, 2010; Lindgren and Johansson, 2002) using

$$K_L = K_{mesh}K_{Rn}\sigma_s + \frac{\sigma_s^2}{\beta_s^2} \tag{H.4}$$

where $K_{mesh}$ is parameter relevant to the mesh material, and for metal wires it can be selected between 1.0 and 1.3, $\beta_s$ is a mesh porosity and is defined as

$$\beta_s = \left(1 - \frac{d_w}{M_w}\right)^2 \tag{H.5}$$

where $d_w$ is the wire diameter of the screen and $M_w$ is the width of the one cell of the screen measured from centre to centre between two wires. $\sigma_s$ is the screen solidity which is

$$\sigma_s = (1 - \beta_s) \tag{H.6}$$

$K_{Rn}$ is the Reynolds effect coefficient and is given by:

$$K_{Rn} = \left\{\begin{matrix} 0.78\left(1 - \frac{Re_w}{354}\right) & 0 \leq Re_w \leq 400 \\ 1 & 400 \leq Re_w \end{matrix}\right\} \tag{H.7}$$

where $Re_w$ is Reynolds number based on the wire diameter of the mesh and is given by

$$Re_w = \frac{\rho V_s d_w}{\mu} \tag{H.8}$$

where $V_s$ is the velocity that the air flow would have at the mesh location if the fractional open area was 100%. For the flow speed of 42.6 m/s at the test section of the wind tunnel and with the contraction ratio of the original bell-mouth of 6.4, the velocity at the screen section is around 6.656 m/s, and this will produce $Re_w = 97$. For this Reynolds number the Reynolds effect coefficient is $K_{Rn} = 1.3625$. The porosity of the actual screens was measured around 0.735 and solidity around 0.265, and the $K_{mesh}$ was taken as 1.3. From these assumptions the internal resistance coefficients were obtained as $K_L = 0.598$, $K'_L = 1.107$, $C_2 = 1107$. The viscous resistance coefficient $C_1$ was obtained from

$$C_1 = \frac{1}{\beta_s} = 1.36. \tag{H.9}$$